Shear Performance of Reinforced Concrete (RC) Beams Strengthened with Mortar-based Composites under Monotonic and Fatigue Loading

Thesis submitted to the University of Nottingham for the degree of

Doctor of Philosophy

June 2025

Xiangsheng Liu

Supervisors: Dr. Georgia E. Thermou and Dr. Fangying Wang

Department of Civil Engineering

University of Nottingham

Abstract

Reinforced concrete (RC) beams form the backbone of modern structures, yet their performance is increasingly compromised by aging, environmental degradation, outdated design standards, unauthorised modifications, increased load demands, impact damage, poor construction quality, and corrosion. These challenges have significantly heightened the demand for effective structural maintenance and strengthening strategies. While fibre-reinforced polymers (FRPs) are widely adopted due to their high strength-to-weight ratio and design flexibility, their limitations—such as poor fire resistance, environmental toxicity, and incompatibility with concrete substrates—restrict their applicability. In this context, mortar-based composites, including Steel-Reinforced Grout (SRG) and High-Performance Fibre-Reinforced Concrete (HPFRC), have emerged as promising alternatives for enhancing the shear capacity of RC beams. Despite their potential, research on SRG and HPFRC systems remains limited, particularly under cyclic and fatigue loading conditions.

This study aims to evaluate the application of SRG and HPFRC jacketing for the shear strengthening of RC beams. The research begins with a comprehensive literature review and the establishment of a database containing 218 samples of RC beams strengthened with mortar-based composites. This database facilitates the analysis of key design parameters influencing shear strengthening performance and assesses the accuracy of traditional empirical models for shear capacity prediction.

Subsequently, experimental investigations evaluate the static and fatigue performance of SRG-strengthened beams, with comparative analyses including Carbon Fabric Reinforced Cementitious Matrix (CFRCM) and Steel-Reinforced Polymer (SRP) systems. Unlike these systems, HPFRC, which lacks textile reinforcements, is studied independently to account for its unique mechanical properties. Key parameters, such as shear span-to-depth ratio (*a/d*), textile density, jacket configuration, and mortar properties, are systematically explored. Results confirm the effectiveness of all strengthening systems in enhancing shear capacity, with fully wrapped SRG systems uniquely capable of transforming failure modes from brittle shear to ductile flexural behaviour. Predictive models for shear capacity and

fatigue life were developed for SRG and HPFRC systems based on experimental findings.

In addition, nine machine learning (ML) models were developed to predict the shear capacity of FRCM-strengthened beams, with XGBoost achieving the highest accuracy and stability. Shapley Additive Explanations (SHAP) and Partial Dependence Plots (PDP) were employed to enhance model interpretability and identify key factors influencing shear capacity, such as beam depth, concrete compressive strength, and mortar thickness. A novel finite element analysis (FEA) model for SRG systems was also proposed, addressing limitations in existing methods by independently modelling the behaviours of mortar and textile components. This innovation enables accurate simulation of premature delamination in high-density SRG systems, providing a robust framework for future design optimization.

This research validates the efficacy of mortar-based composites for shear strengthening of RC beams, advancing understanding and application in both static and fatigue contexts. The findings bridge critical knowledge gaps in the performance of SRG and HPFRC systems, enhance the predictive accuracy of design models, and offer innovative tools and methodologies to improve the resilience of aging infrastructure.

Acknowledgement

This PhD research was conducted under the supervision of Professor Georgia E. Thermou and Professor Fangying Wang at the Centre for Structural Engineering and Informatics (CSEI), University of Nottingham.

I would like to express my deepest gratitude to my principal supervisor, Professor Georgia E. Thermou, for her unwavering support, patience, and invaluable guidance throughout my PhD journey. Her mentorship has been instrumental in shaping my ability to think critically, approach challenges with confidence, and grow as a researcher. I would also like to sincerely thank my second supervisor, Professor Fangying Wang, for her support, particularly in finite element modelling. Although she joined my supervisory team at a later stage, her insights and expertise were valuable in refining aspects of my numerical work.

I would also like to sincerely thank Professor Grazziela Figueredo and Professor George Gordon for their invaluable guidance in machine learning. Their expertise and constructive feedback have greatly contributed to the depth and quality of this work, enhancing my understanding of the application of machine learning techniques in structural engineering research.

I extend my heartfelt thanks to the L2 laboratory team at the University of Nottingham for their essential support in the experimental phase of this research. Special thanks go to Mr. Mike Langford, L2 Laboratory Manager; Mr. Nigel Rook, L2 Chief Technician; and technicians Mr. Ali Palmer and Mr. Gary Davies, for their technical assistance, problem-solving skills, and tireless efforts that ensured the experiments ran smoothly.

I am deeply indebted to my family and my girlfriend for their constant belief in me and their unwavering support throughout this journey. Despite being miles away, they have always felt close to me, offering encouragement and strength during challenging times.

Lastly, I cherish the unforgettable moments spent with new friends at Nottingham, who have enriched my experience and provided me with lasting memories. Their companionship has made this journey both fulfilling and joyful.

Contents

List of Figures

List of Tables

List of Abbreviations

ACI	American Concrete Institute
ANN	Artificial Neural Network
B	Basalt Fibre
BFRP	Basalt Fibre Reinforced Polymer
BFRCM	Basalt Fabric Reinforced Cementitious Mortar
C	Carbon Fibre
CFRCM	Carbon Fabric Reinforced Cementitious Mortar
CFRP	Carbon Fibre Reinforced Polymer
DIC	Digital Image Correlation
DT	Decision Tree
ECC	Engineered Cementitious Composite
FE	Finite Element
FEA	Finite Element Analysis
FW	Fully Wrapped Jackets
FRC	Fibre Reinforced Concrete
FRCM	Fabric Reinforced Cementitious Mortar
FRP	Fibre Reinforced Polymer
G	Glass Fibre
GFRCM	Glass Fabric Reinforced Cementitious Mortar
GFRP	Glass Fibre Reinforced Polymer
HPFRC	High Performance Fibre Reinforced Concrete
JSCE	Japan Society of Civil Engineers
KNN	*K* Nearest Neighbour
LGBoost	Light Gradient Boosting
LR	Linear Regression

LVDT	Linear Variable Differential Transducer
ML	Machine Learning
MLP	Multilayer Perceptron
MVS	Minimum Variance Sampling
NSM	Near Surface Mounted
P	Poliparafenilen Benzobisoxazole Fibre
PBO	Poliparafenilen Benzobisoxazole
PDP	Partial Dependence Plots
PFRCM	PBO Fabric-Reinforced Cementitious Mortar
RBF	Radial Basis Function
RC	Reinforced Concrete
RF	Random Forest
S	Steel Fibre
SB	Side Bonded Jackets
SC	Strengthening Configuration of FRCM System
SFRC	Steel Fiber Reinforced Concrete
SHAP	Shapley Additive Explanations
SMCFT	Simplified Modified Compression Field Theory
SRG	Steel-Reinforced Grout
SRP	Steel-Reinforced Polymer
STL	Statistical Learning Theory
SVM	Support Vector Machine
SVR	Support Vector Machine
TRM	Textile-Reinforced Mortar
TRC	Textile-Reinforced Concrete
TT	Training Time
U	U-Shaped Jackets
UHPFRC	Ultra-High Performance Fibre Reinforced Concrete
UHTSS	Ultra-High Tensile Strength Steel
XGBoost	Extreme Gradient Boosting

List of Notations

a	Length of shear critical span
a/d	Shear-span ratio
A_f	Reinforced area of textiles
A_{sl}	Section area of tension reinforcement
A_w	Area of stirrups
A_w/s	Area of stirrups to spacing ratio
b_w	Width of the beam's cross section
$b_{w,FRC}$	Width of the FRC jacket
CoV	Standard Deviation
d	Effective depth of the cross section
D_f	Stress distribution coefficient
DAF	Dynamic amplification factor in fatigue testing
E_a	Elastic modulus of adhesive
E_f	Elastic modulus of fabric
E_{FRCM}	Elastic modulus of FRCM composite
f_b	Bond strength of matrix
f_c	Cylindrical compressive strength of concrete
f_c'	Cubic compressive strength of concrete
f_{cm}	Compressive strength of the mortar
f_{cmt}	Tensile strength of the mortar
f_f	Flexural strength of matrix
f_{fu}	Ultimate strength of the beam
$f_{fu,f}$	Ultimate strength of fabric
$f_{fu,jac}$	Ultimate stress of jackets
f_{fv}	Design tensile strength of the FRCM system

f_{fed}	Effective stress of SRG/FRCM at failure
$f_{fed,max}$	Maximum design stress of the jackets
f_t	Tensile strength of concrete
$f_{y,L}$	Yield strength of tension reinforcement
f_{yw}	Mean yield strength of stirrups
f_{ywd}	Design yield strength of stirrups
G_c	Shear modulus of concrete
G_f	Fracture energy
G_F	Fracture energy associated with the debonding phenomenon under quasi-static monotonic loading
$G_F^{Fatigue}$	Energy release associated with the maximum load of the cycle
h_f	Effective depth of the jacket
h_{fe}	Effective hight of the jacket
k	Factor that considers the size effect
K_0	Initial stiffness
K_n	Stiffness of each cycle in fatigue testing
L_e	Effective bond length of FRCM/SRG
L_{max}	Available bond length of FRCM/SRG
MAE	Mean Absolute Error
n	Number of layers of textiles
N	Fatigue life of the tested beam
N_s	Number of FRCM strips
P_h	Maximum load in fatigue testing
P_l	Minimum load in fatigue testing
P_{max}	Peak load of the tested beam
P_{ref}	Design static shear ultimate strength of beams
P_u	Ultimate load of the tested beam
R^2	coefficient of determination
R_c	Influence factors of *a/d* on the beam
R_f	Influence factors of *a/d* on the SRG jacket
RMSE	Root Mean Square Error
s	Slip corresponding to τ

s_0	Slip at which the bond strength is achieved
s_f	Slip value at which the interface shear stress reduces to zero
s_u	Ultimate interface slip
S	Cyclic stress level of the tested beam
S_f	Axial stiffness of the textile
SD	Standard Deviation
t_a	Ideal thickness of adhesive
t_{cm}	Thickness of mortar
t_f	Equivalent thickness based on the 'smeared distribution of fibres' approach
v_{FRC}^{exp}	Experimental normalised shear stress of the FRCM jackets
v_{FRC}^{pred}	Predicted normalised shear stress of the FRC jackets
v_{FRC}^{exp}	Experimental normalised shear stress of the FRC jackets
v_{FRC}^{pred}	Predicted normalised shear stress of the FRC jackets
V_c	Shear strength contributed form the concrete
V_C^{ACI}	Shear strength contributed form the concrete, according to ACI
V_C^{EC2}	Shear strength contributed form the concrete, according to EC
V_C^{JSCE}	Shear strength contributed form the concrete, according to JSCE
V_{CON}	Shear strength provided by the plain beam
V_{exp}	Experimental shear capacity provided by strengthened beams
V_{JAC}	Shear strength provided by the mortar-based composite jacket
V_{FRC}	Shear strength contributed form the FRC jacket
V_{FRC}^{exp}	Experimental shear strength provided by FRC jackets
V_{FRC}^{pred}	Predicted the shear strength provided by FRC jacket
V_{FRCM}	Shear strength contributed form the FRCM jacket
V_{FRCM}^{exp}	Experimental shear strength provided by FRCM jackets
V_{FRCM}^{pred}	Predicted the shear strength provided by FRCM jacket
V_f	Shear strength contributed form the textile
V_F	Shear strength contributed form the fibre
V_m	Shear strength contributed form the mortar
V_{pred}	Predicted shear capacity provided by strengthened beams
V_{RET}	Shear strength of mortar-based composite strengthened beams

V_s	Shear strength contributed form the transverse reinforcement
V_{shear}	Shear strength of strengthened RC beams
V_{SRG}	Shear strength contributed form the SRG jacket
w_f	Width of the FRCM strips
s_f	FRCM strip spacing
z	Inner lever arm
z_b	Co-ordinates of the bottom ends of the effective FRCM/SRG
z_t	Co-ordinates of the top ends of the effective FRCM/SRG
α_0	Angle between the fibres and the beam axis perpendicular to the shear force
β	Stiffness degradation of the tested beam in fatigue testing
β_l	Effective bond length ratio of FRCM/SRG
β_w	Concrete width ratio of FRCM/SRG
δ	Total displacement of the tested beam in fatigue testing
δ_{max}	Displacement of the tested beam at the peak load
δ_u	Displacement of the tested beam at the ultimate load
δ_y	Displacement of the tested beam at the yield load
ε_c	Concrete compressive strain when compressive stress reaches σ_c
$\varepsilon_{c,r}$	Concrete compressive strain corresponding to σ_{cu}
ε_{cu}	Ultimate compressive strain of the concrete
ε_{eff}	Effective strain of textiles
ε_{eff}^{exp}	Experimental value of textile's effective strain
ε_{fu}	Ultimate strain of textiles
ε_t	Concrete tensile strain when compressive stress reaches σ_t
$\varepsilon_{t,r}$	Concrete tensile strain corresponding to σ_{tu}
ε_{tu}	Ultimate tensile strain of the concrete
ε_{FRCM}	Ultimate strain of FRCM composite
ε_{SRG}	Ultimate strain of SRG composite
ΔP_{max}	Shear strength increase of the retrofitted beams
θ	Angle between the concrete compression strut and the beam axis perpendicular to the shear force
λ	Maximum bond length parameter

μ_p	Average value
μ_δ	Displacement ductility of the tested beam
ρ_c	parameter values of the descending section of the stress–strain curve under uniaxial compression
$\rho_{long,b}$	Area ratio of the tensile reinforcement
ρ_w	Stirrup reinforcement ratio
ρ_f	Fibre reinforcement ratio
σ_c	Compressive stress of concrete
σ_{cm}	Uniaxial compressive strength of mortar
σ_{cu}	Ultimate compressive stress of concrete
σ_t	Tensile stress of concrete
σ_{tu}	Ultimate tensile stress of concrete
τ	Local interface shear stress
τ_{max}	Shear bond strength
χ	Interface roughness parameter
Ψ	Energy absorption of the tested beam
Ψ_{CON}	Energy absorption of the control beam
Ψ_d	Energy dissipation of the tested beam
Ψ_{JAC}	Energy absorption provided by the strengthening jacket
Ψ_{RET}	Energy absorption provided by the strengthened beam

Chapter 1

Introduction

1.1 Background

Reinforced concrete (RC) structures are integral to modern structures, yet their performance is increasingly compromised due to various factors, including outdated design standards, environmental degradation, unauthorised design modifications, aging, increased loads, impact damage, poor construction quality, and corrosion. These issues have accelerated the demand for structural maintenance and strengthening. For instance, the 2020 Aegean Sea earthquake near Samos Island revealed significant damage in buildings constructed before 2010, while those built to newer standards demonstrated greater resilience (Çetin et al., 2020). Similarly, in the UK, nearly 60% of residential buildings were constructed before 1960, highlighting the aging infrastructure's vulnerability and the growing need for retrofitting solutions (Department for Communities and Local Government, 2012).

A critical concern in RC structures is their susceptibility to brittle failure, particularly shear failure, which often leads to catastrophic collapse. Shear failure, typically caused by inadequate transverse reinforcement or poor material quality, can rapidly propagate and compromise structural integrity. For example, during the 2010 Haiti earthquake, the widespread collapse of UNIH university buildings was attributed to shear deficiencies in critical structural elements (Eberhard et al., 2010). Such failures are particularly hazardous during seismic events, where the combination of lateral and cyclic loads further amplifies the risk of brittle behaviour. Figure 1.1

illustrates inadequate reinforcement in beams and columns, such as insufficient stirrups and longitudinal reinforcement, leading to shear failure and structural collapse. Similarly, as shown in Fig. 1.2, in the earthquake of Samos Island, the cantilever beams also showed very obvious shear cracks; although the whole buildings did not collapse, they could no longer be used because of the impossibility of repairment (Çetin et al., 2020).

Fig. 1.1. Steel bar in the collapsed structures at the UNIH University in Haiti earthquake (Eberhard et al., 2010).

Fig. 1.2. Overhang damages in Samos Island Earthquake (Çetin et al., 2020).

Fatigue loading presents another significant challenge, particularly for infrastructure such as bridges subjected to repeated vehicle loads. According to Ryall (2008), increased traffic volumes and heavier axle weights have accelerated fatigue-induced deterioration in RC bridges, with load limits in the UK rising from 12 tons in 1904 to 44 tons in 1996 (Fig. 1.3). Repeated cyclic loading, whether from traffic or seismic events, degrades the bond and stiffness of RC elements, redistributes stresses unpredictably, and accelerates crack propagation. This compromises the long-term durability and safety of RC structures, necessitating effective strengthening methods.

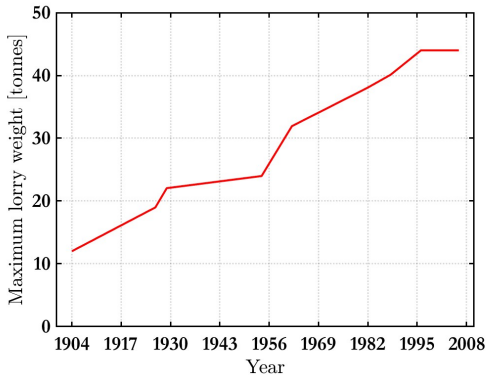

Fig. 1.3. Variation of heavy vehicle load with time (Ryall 2008).

To address these challenges, the development of innovative and reliable strengthening systems has become a critical focus in structural engineering. Fibre-reinforced polymers (FRPs) have emerged as a widely adopted solution due to their high strength-to-weight ratio and design flexibility. However, their resin-based matrices exhibit poor high-temperature performance, low fire resistance, and environmental toxicity, limiting their application in certain scenarios (Graeff et al., 2012; Sakr et al., 2018). As an alternative, mortar-based composites have gained attention for their superior durability, fire resistance, and compatibility with existing concrete structures (Laterza et al., 2017; Roberts et al., 2006). Among these materials, two relatively new options—Steel Reinforced Grout (SRG) and High-Performance Fibre Reinforced Concrete (HPFRC)—have demonstrated significant potential for shear strengthening of RC beams. However, research on the shear behaviour of RC beams strengthened with SRG and HPFRC is limited, particularly under cyclic and fatigue loading conditions. Bridging these knowledge gaps is crucial for advancing the application of these innovative materials in structural strengthening and enhancing the resilience of aging structures.

1.2 Aim and Objectives

This study aims to investigate the shear performance of RC beams strengthened with mortar-based composites under static and fatigue conditions, focusing on SRG and HPFRC. To comprehensively evaluate the performance of SRG systems, the study also examines Carbon Fabric Reinforced Cementitious Matrix (CFRCM,) which belongs to the same Fabric Reinforced Cementitious Matrix (FRCM) category, and Steel Reinforced Polymer (SRP), which utilises the same type of textile. In contrast, HPFRC

is investigated separately, due to its absence of textile reinforcements. The research objectives are as follows:

a. **Comprehensive Literature Review**

   Conduct a detailed review of the latest research on the shear performance of RC beams strengthened with mortar-based composites. Establish an experimental database to evaluate the influence of critical design parameters on strengthening efficiency and to assess the performance of existing design models in predicting the shear contribution of mortar-based composites.

b. **Experimental Investigation of SRG-Strengthened Beams**

   Evaluate the shear enhancement provided by SRG systems under both monotonic and fatigue loading through experimental testing on 29 full-scale RC beams. Develop predictive models for the shear strength of SRG strengthened beams. Establish a predictive model for fatigue life based on fracture mechanics.

c. Experimental Investigation of HPFRC-Strengthened Beams

   Assess the shear enhancement provided by HPFRC systems under monotonic and fatigue loading through experimental testing on 10 full-scale RC beams. Develop fatigue life prediction models based on *S-N* curves of strengthened beams.

d. **Machine Learning Based Shear Strength Prediction of FRCM Strengthened Beams**

   Develop machine learning models for predicting the shear strength of FRCM-strengthened beams. Evaluate the accuracy and robustness of these models and compare them against conventional empirical design models.

e. **Finite Element Models of SRG Strengthened Beams**

   Develop finite element models in ABAQUS to simulate the behaviour of SRG-strengthened beams with shear deficiencies.

The research methodology to achieve these objectives is summarised in Fig. 1.4.

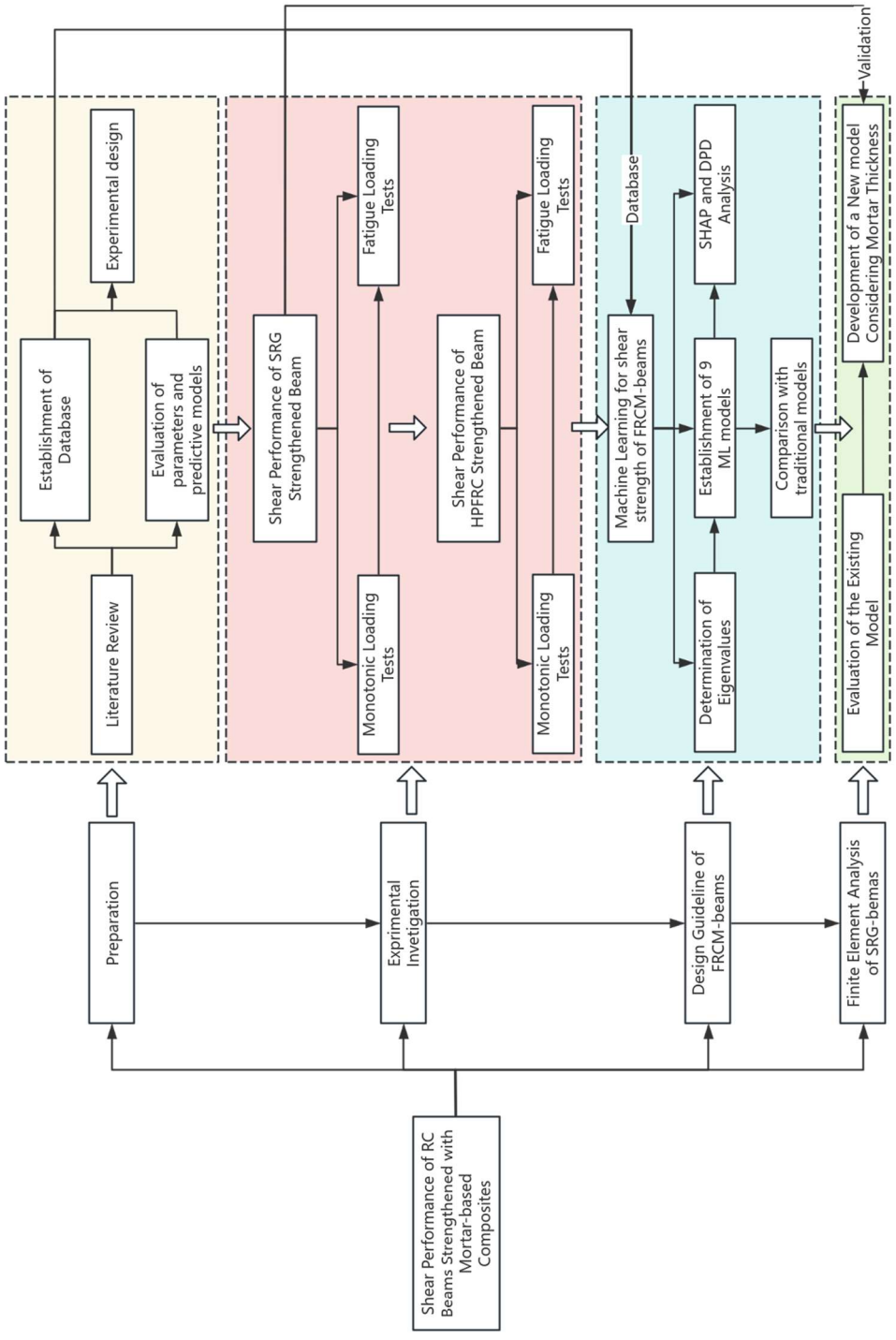

Fig. 1.4. Research methodology in this project

1.3 Thesis Layout

This thesis is organised into eight chapters, with Chapter 1 serving as the introduction.

Chapter 2 provides a detailed description of mortar-based composites and includes a comprehensive literature review on their application for strengthening RC beams. Furthermore, a database comprising 218 strengthened beams is established to evaluate the parameters influencing strengthening performance and to assess existing shear strength prediction models.

Chapter 3 presents the experimental work conducted on SRG-strengthened beams under monotonic loading and proposes a design model that incorporates shear span ratio for predicting the shear strength of strengthened beams.

Chapter 4 focuses on the experimental investigation of SRG-strengthened beams under fatigue loading and develops a fatigue life prediction model based on fracture mechanics.

Chapter 5 explores the performance of HPFRC-strengthened beams under both static and fatigue loading, proposing a fatigue life prediction model based on *S-N* curves.

Chapter 6 compares nine machine learning models developed to predict the shear strength of strengthened beams, evaluating their performance against each other.

Chapter 7 introduces a novel finite element model for SRG-strengthened beams, considering the effects of mortar thickness.

Chapter 8 summarises the main conclusions of this research and recommendations for future work.

Chapter 2

Literature Review

This chapter provides a systematic review of research on the shear performance of RC beams strengthened with mortar-based composites. It begins with an introduction to mortar-based composites. A detailed review of the current state of research on mortar-based composite-strengthened beams under static and fatigue loading, particularly concerning shear performance, is then presented. Subsequently, the established database is analysed to identify the influence of various design parameters on the shear strengthening effectiveness of these systems. Existing empirical models for predicting the shear strength of strengthened beams are also collected and evaluated using the database. Finally, the chapter concludes with a summary of the existing literature, highlighting research gaps and providing the foundation for the direction of this study.

2.1 Shear Strengthening of RC Beams using Mortar-Based Composite Jackets

2.1.1 Mortar-Based Composites

With the aging of structures, environmental degradation, lack of maintenance, and the need to meet updated design requirements, structural strengthening has become increasingly important. Among the advancements in materials, Fibre-Reinforced Polymers (FRP) have gained popularity due to their high strength-to-weight ratio, excellent corrosion resistance, and durability against environmental degradation (Tetta et al., 2016). FRP systems, composed of high-strength fabrics bonded with resin, offer

several advantages: (i) maintenance-free with a long lifecycle, (ii) superior bending performance that fully utilises the compressive strength of concrete and the tensile strength of FRP composites, (iii) ease of transportation and installation due to their lightweight nature, and (iv) high durability in corrosive environments (Gonzalez-Libreros et al., 2017b).

However, the epoxy resin matrix of FRP presents significant limitations, including poor high-temperature performance, incompatibility with wet surfaces, and inadequate adhesion to substrates such as concrete or masonry (Tetta et al., 2015). To address these challenges, researchers have increasingly turned to mortar-based composites for structural strengthening (Tetta and Bournas, 2016; Ombres, 2015b). Among these, the Fabric Reinforced Cementitious Matrix (FRCM) which replaces resin with mortar as the binding matrix for fabrics, has garnered considerable attention. According to Gonzalez-Libreros et al. (2017a), the term FRCM encompasses several systems: (i) Textile-Reinforced Mortar (TRM), which employs textiles made of carbon (CFRCM), glass (GFRCM), or basalt (BFRCM); (ii) PBO-FRCM (PFRCM), which uses Poliparafenilen Benzobisoxazole (PBO) textiles; and (iii) Steel-Reinforced Grout (SRG), which incorporates Ultra-High Tensile Strength Steel (UHTSS) textiles. As illustrated in Fig. 2.1, commonly used textiles in FRCM systems include carbon, glass, basalt, PBO, and UHTSS fibres. This material offers several advantages, including lower cost, compatibility with labour-intensive construction practices, better fire resistance, and improved adhesion to substrates such as concrete and masonry (Marcinczak and Trapko, 2019a). Additionally, they can be applied to wet surfaces or under low-temperature conditions, making them a versatile solution for structural strengthening (Wakjira and Ebead, 2019b).

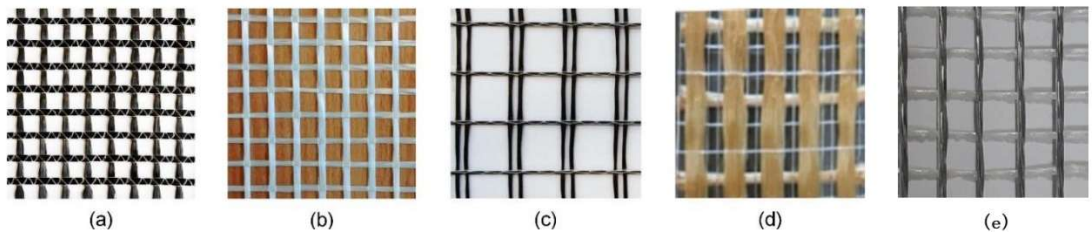

Fig. 2.1. Textiles: (a) carbon-fibre textile (Tetta et al., 2018a); (b) glass-fibre textile (Tetta et al., 2018a); (c) basalt-fibre textile (Tetta et al., 2018a); (d) PBO-fibre textile (Tetta et al., 2018a); (e) UHTSS textile (Wakjira and Ebead, 2019a).

In addition, High-Performance Fibre Reinforced Concrete (HPFRC) and Ultra-high Performance Fibre Reinforced Concrete (UHPFRC), as other mortar-based composite materials, have also emerged as promising solutions for structural strengthening (Jongvivatsakul et al., 2016; Savino et al., 2018). The characteristics of ordinary concrete include lower tensile strength and ductility, which can be enhanced by incorporating steel fibres into the matrix (Savino et al., 2018). UHPFRC and HPFRC exhibit remarkably similar mechanical properties (Buttignol et al., 2017). They utilise fine powders (silica fume), low water-binder ratios, and superplasticisers, resulting in a dense matrix with enhanced homogeneity and lower permeability than conventional concrete (Kang et al., 2010; Ren et al., 2021). The reduced permeability enhances resistance against ingress of harmful chemicals, leading to superior corrosion resistance and durability (Amin et al., 2021). HPFRC/UHPFRC exhibits excellent resistance to damage from freeze-thaw cycles and high temperatures, and the shrinkage can be minimised to zero through proper heat treatment, thus enhancing durability against aging (Huang et al., 2022). In addition, the low coarse aggregate content and high fibre fraction (typically around 2%) improve the stiffness and ductility of structures (Said et al., 2022). HPFRC/UHPFRC demonstrate superior compressive strengths over ordinary concrete, with HPFRC values spanning 90-120 MPa and UHPFRC exceeding 120 MPa (Sohail et al., 2021; Nunes et al., 2022). Therefore, these properties make HPFRC/UHPFRC an ideal material for strengthening beams as a jacketing device.

2.1.2 Shear Strengthening under Monotonic Loading

In aging RC structures, the shear strengthening of RC beams is one of the most critical requirements when assessing structural integrity. This necessity arises from several factors, including insufficient shear reinforcement, corrosion of existing steel reinforcement, low concrete strength, and/or increased applied loads. The following sections provide a detailed review of published studies on the use of FRCM, UHPFRC, HPFRC for the shear strengthening of RC beams.

The earliest research employing similar materials for structural strengthening was conducted by Basunbul et al. (1990), who reinforced simply supported beams with rectangular cross-sections using thin layers of steel mesh mortar and concrete. Their findings demonstrated superior performance for steel mesh mortar compared to concrete: the first-crack load increased by 24%, mid-span deflection was reduced by

10%, and the ultimate load of beams strengthened with steel mesh mortar was 28% higher than that of unstrengthened beams. Similarly, Paramasivam et al. (1994) investigated the use of thin steel wire mesh mortar layers for strengthening T-shaped beams. Their results confirmed the effectiveness of this technique, provided proper treatment was applied to the interface between new and existing materials. The first-crack load, stiffness, and ultimate load capacity were significantly improved.

Brückner et al. (2008) conducted shear strengthening tests on 12 T-beams using multiaxial GFRCM. Three unstrengthened beams were used as controls, while the remaining beams were strengthened with two, four, or six textile layers. Additionally, six of the strengthened beams incorporated mechanical anchorage systems to delay debonding of the TRM jackets. The study found that, without anchorage, the TRM jackets increased the shear capacity of the T-beams by 7%. When anchorage was applied, the effectiveness improved significantly, with shear capacity enhancements reaching 14%, demonstrating the importance of anchorage systems in improving the performance of TRM jackets.

Larbi et al. (2010) investigated the shear strengthening capacity of textile reinforced concrete (TRC) plates bonded to small-scale rectangular RC beams. Eight tests were conducted using TRC plates made of three different mortar compositions: hydraulic mortar with glass fibres, inorganic phosphate cement, and ultra-high-performance mortar with short metallic fibres. The plates were bonded to the beams with epoxy resin, excluding debonding mechanisms from their evaluation. Results showed that TRC plates made with inorganic phosphate cement-glass fibres or ultra-high-performance metallic fibres effectively improved shear capacity, highlighting the potential of these advanced materials in structural retrofitting.

Al Salloum et al. (2012) examined the effectiveness of BFRCM jackets in shear strengthening of small-scale rectangular RC beams. Their experimental program included ten beams and varied parameters such as mortar type (cementitious versus polymer-modified), the number of TRM layers (two or four), and textile orientation (0°/90° or ±45°). Results indicated shear capacity improvements ranging from 36% to 88%, with gains increasing with the number of textile layers. The ±45° textile orientation outperformed the 0°/90° configuration, while polymer-modified mortar was more effective than cementitious mortar. However, all samples in this study failed

due to shear-compression mechanisms, limiting the full utilization of CFRCM's strengthening potential.

Azam et al. (2014) explored the shear strengthening effects of carbon and glass FRCM systems. Through three-point bending tests on rectangular beams, they observed that side-bonded and U-wrapped FRCM systems exhibited comparable performance in terms of strength and failure modes, suggesting that U-wrapping may be unnecessary when the bond between FRCM and the concrete surface is sufficient. Additionally, when using a single layer of fabric, no significant differences in shear capacity improvement were observed between carbon and glass FRCM systems. However, for carbon FRCM, the strengthening effect was markedly enhanced with two layers of fabric, regardless of the configuration (shear capacity increased by 26% for side-bonded and 23% for U-wrapped systems), compared to the single-layer systems (9% and 5%, respectively).

Tetta and Bournas (2016) evaluated the shear strengthening effects of FRCM systems (light carbon fibre, heavy carbon fibre, and glass fibre) and FRP systems on RC beams under varying temperatures. Strengthening configurations included full wrapping, U-wrapping, and side bonding, with different numbers of textile layers. Their three-point bending tests revealed that FRCM systems improved the shear capacity of strengthened beams by 20%–195%, irrespective of temperature. At elevated temperatures, the performance of FRCM systems significantly surpassed that of FRP systems. For instance, as the temperature increased from 100°C to 150°C, the shear capacity of FRP systems dropped sharply, whereas FRCM systems were only slightly affected. Among the configurations, full wrapping provided the greatest improvement in shear capacity, while side bonding was the least effective.

Aljazaeri and Myers (2017) investigated the use of PFRCM jackets to strengthen rectangular beams with or without internal stirrups. As shown in Fig. 2.2, the FRCM system was applied in two configurations: U-wrapped continuous and U-wrapped strips. Results from four-point bending tests indicated that the continuous FRCM system outperformed the strip configuration under identical conditions. Moreover, for beams without stirrups, the shear strengthening effect of PBO-FRCM was less significant than for beams with stirrups. The authors attributed this to the non-uniform properties of concrete, which, in the absence of internal shear reinforcement, resulted

in unpredictable crack paths and larger crack widths, thereby reducing the effectiveness of the PFRCM system. However, this conclusion contrasts with findings from other studies, such as Gonzalez-Libreros et al. (2017a), who reported that FRCM systems were more effective for beams without stirrups. A detailed discussion on this discrepancy is provided in Section 2.2.

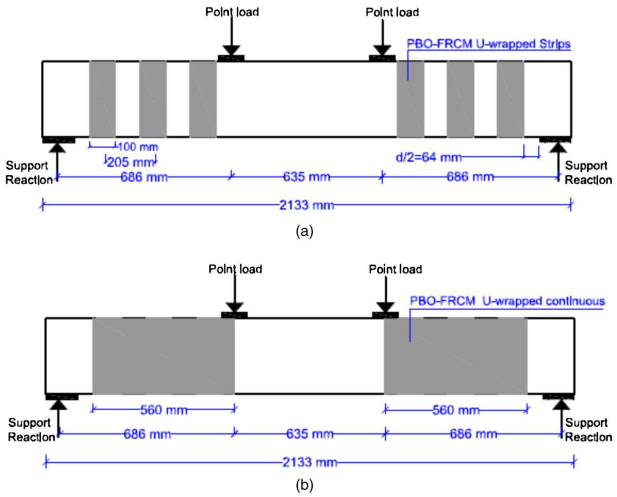

Fig. 2.2. Shear strengthening configurations: (a) U-wrapped strips; (b) U-wrapped continuous (Aljazaeri and Myers, 2017)

Hung and Cheng (2016) investigated the shear strengthening effects of RC rectangular beams using UHPFRC as a matrix, with or without steel mesh reinforcement. For comparison, they also strengthened beams with a mortar matrix. The results indicated that all jackets enhanced shear capacity, with improvements ranging from 20% to 167%. The UHPFRC-based composite with a single-layer steel mesh exhibited the best transformation performance. While mortar-based ferrocement jackets improved the mechanical properties of the original beams, they exhibited significant detachment when the shear capacity increased by only 6%. Replacing mortar with UHPFRC effectively mitigated this issue. Moreover, the study highlighted that UHPFRC -based jackets reduced average crack widths by more than half during all loading stages compared to mortar-based jackets. However, the dense steel mesh required in ferrocement systems compromised construction quality, ultimately affecting the mechanical properties of the strengthened beams. In contrast, UHPFRC jackets without steel mesh simplified the construction process and outperformed mortar-based ferrocement jackets in preventing cracks under intermediate damage conditions.

Younis et al. (2017) primarily explored the influence of textile types on the shear strengthening effect of FRCM systems. Three textile materials were tested: PBO fibre, carbon fibre, and glass fibre. All FRCM systems demonstrated significant improvements in shear performance, with the shear capacity of strengthened beams increasing by an average of 51% compared to unstrengthened beams. The failure deflection of the strengthened beams reached 2.4 times that of the unstrengthened counterparts. Among the tested systems, carbon FRCM exhibited the best performance, while PBO-FRCM showed the lowest enhancement.

Sakr et al. (2018) investigated the shear strengthening effects of UHPFRC plates bonded to one or both sides of RC beams. Their findings demonstrated that UHPFRC jackets effectively suppressed diagonal shear cracks on the reinforced surfaces, although diagonal cracks on non-reinforced surfaces became more pronounced. Beams strengthened with a single 60 mm UHPFRC plate on one side showed a 34% increase in maximum load-bearing capacity compared to the control beam, while beams strengthened with two 30 mm UHPFRC plates bonded on both sides achieved a 145% increase. These results highlight the significant potential of UHPFRC for improving shear capacity in RC beams.

Sark et al. (2019) further studied the shear behaviour of UHPFRC strengthened beams. As shown in Fig. 2.3, there were four reinforcement configurations: (a) UHPFRC plates with a thickness of 30mm on both sides, (b) a plate with a thickness of 60mm on one side, (c) 30mm plates on both sides with steel anchors and (d) a 60mm plate on one side with a steel anchor. Under the four-point bending test, the shear load enhancement values of the strengthened beams were 145%, 34%, 188% and 120%, respectively. They found that the effectiveness of a beam strengthened on both sides was always better than that of a beam bonded on one side. They also found that adding additional steel anchors greatly enhanced the effectiveness of a beam. For example, the UHPFRC plate with a thickness of 60mm on one side suffered from premature debonding, which made it unable to play a complete role, but a steel anchor was able to prevent this debonding.

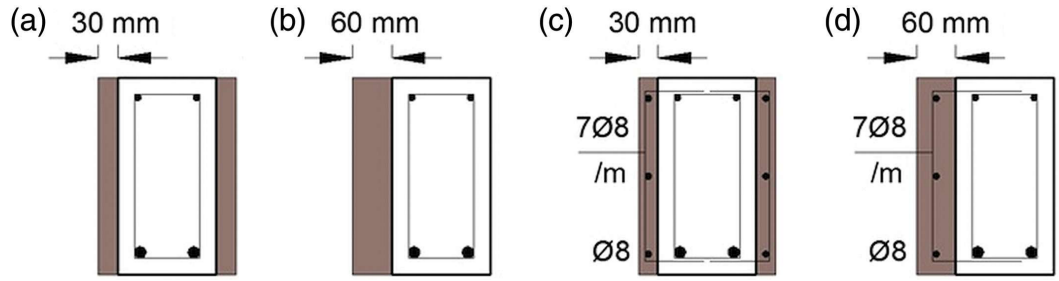

Fig. 2.3. Strengthening configurations: (a) the tensile zone, (b) the compressive zone, and (c) U-shape (Sark et al., 2019).

Marcinczak et al. (2019) evaluated the shear strengthening capacity of PFRCM systems applied to T-beams with various anchorage configurations, as shown in Fig. 2.4. Three anchoring methods were used: (a) wrapping the PBO fabric around a GFRP grid and embedding it into pre-drilled holes, (b) inserting ropes made of PBO fibre and special mineral mortar into pre-drilled holes, and (c) attaching a 150-mm-wide PBO strip. The study found that the PFRCM system increased shear strength by 10–27%. However, sliding between the fibres and the matrix required proper anchorage to prevent premature debonding of the mesh. The best strengthening effect was achieved with anchorage method (c), attributed to the higher axial stiffness of the composite, as the anchorage provided continuous reinforcement along the beam's length.

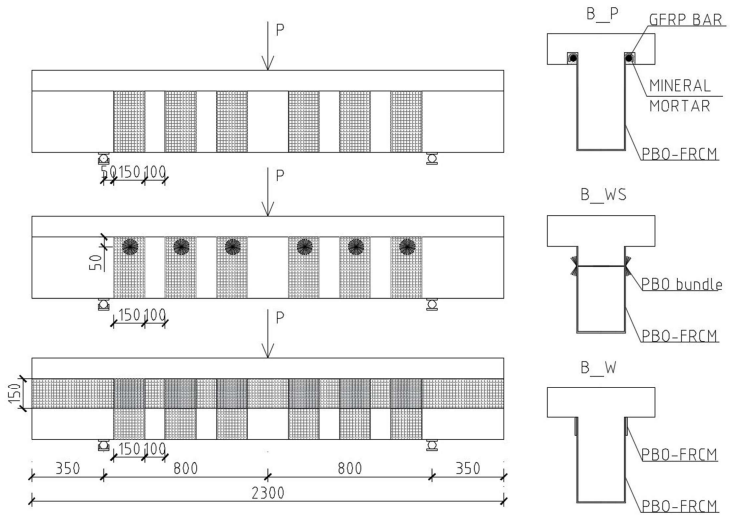

Fig. 2.4. Shear strengthening configurations: (a) PBO fabric was wrapped around a GFRP composite grid and then placed in pre-drilled holes, (b) ropes made of PBO fibre and special mineral mortar were inserted into pre-drilled holes and (c) a 150 mm wide PBO strip was pasted (Marcinczak et al., 2019)

Thermou et al. (2019) investigated the behaviour of SRG-strengthened shear-critical RC beams. Results from three-point bending tests demonstrated that SRG jacketing

effectively prevents shear failure by transforming the failure mode from brittle to ductile, achieving a shear strength increase of 114–160%. This highlights the potential of SRG jacketing as an effective shear reinforcement technique for RC beams, though the interaction between the SRG jacket and the RC beam requires further exploration. Additionally, for U-wrapped configurations, beams with a mechanical anchorage system exhibited higher load-bearing capacity than those without anchorage. The study also refined the effective strain expressions proposed by Escrig et al. (2015), aligning the theoretical predictions more closely with experimental results.

Wakjira and Ebead (2019a) conducted three-point bending tests on shear-critical T-beams strengthened with SRG jackets. Two configurations were examined: U-wrapped and side-bonded. Their findings revealed that SRG jacketing increased shear capacity by 10% to 71%, with the U-wrapped system proving more effective than side bonding. Beams reinforced with high-density steel textiles (3.14 cords/cm) demonstrated greater shear capacity improvement (average 45%) compared to those with low-density textiles (1.57 cords/cm, average 36%).

In a subsequent study, they further examined U-wrapped SRG-reinforced T-beams, focusing on the effects of shear span-to-depth ratio (*a/d*) and textile density (Wakjira and Ebead, 2020). Using a similar experimental setup as their 2019 study, they found that SRG jacketing increased shear capacity by 21–133%, with an average improvement of 78%. However, the strengthening effect decreased as *a/d* increased. SRG jacketing also delayed the formation of the first crack. For beams reinforced with high-density SRG textiles, shear failure was caused by fibre-matrix interface and mortar layer detachment. In contrast, low-density SRG textile failures were due to debonding between the SRG jacket and the concrete cover. The authors proposed an analytical model for predicting the shear capacity of SRG-reinforced beams, incorporating the effects of the shear span-to-depth ratio.

He et al. (2020) investigated the shear performance of RC beams strengthened with side-bonded BFRCM jackets. Ten beams were tested under four-point bending, with parameters such as shear span ratio, interface material, reinforcement type, and BFRP grid installation angle being varied. Results showed that BFRCM effectively enhanced ultimate load capacity, with shear span ratio having minimal impact on their contribution. Beams strengthened with 45° basalt grids performed better in limiting

diagonal crack propagation and mitigating stiffness degradation compared to those with 0° grids. Additionally, the reliable interface performance between the BFRP grid and concrete ensured consistent shear failure in all basalt grid-strengthened beams, while beams strengthened with basalt plates exhibited localised debonding and lower ductility.

Ramezani and Esfahani (2023) explored the use of industrial waste as a replacement for mortar in FRCM systems to shear-strengthen RC beams. To evaluate the performance of this novel CFRCM system, they compared it with beams strengthened using FRP systems. Their findings indicated that the shear capacity of strengthened beams improved by 21.3% with FRP and 23.1% with FRCM strips. The comparable performance of FRP and FRCM systems was attributed to the similar axial stiffness of the fabrics used in both systems. Additionally, the study highlighted that when a/d was 2.5, all strengthening systems performed better than when a/d was 3.5.

Jo et al. (2024) conducted four-point bending tests on 12 RC rectangular beams to investigate the effects of textile axial stiffness, internal transverse reinforcement ratio (0.19% and 0.285%), and application methods (side-bonded and U-wrapped) on the performance of CFRCM-strengthened beams. The results revealed that the shear strengthening effectiveness of CFRCM increased with higher textile axial stiffness. Beams with lower internal transverse reinforcement ratios exhibited greater shear capacity enhancement. However, no significant performance differences were observed between the side-bonded and U-wrapped configurations.

The literature review in this part indicates that research on mortar-based shear strengthening of RC beams has predominantly focused on CFRCM systems. As relatively newer materials, studies on SRG and HPFRC remain scarce. Furthermore, the limited research available on SRG lacks comprehensive comparisons with other strengthening materials. Current findings also reveal several contradictions, such as the interaction effects between FRCM systems and internal stirrups and the effectiveness of different strengthening configurations. These inconsistencies highlight the need for further investigation into the contribution of mortar-based composite systems like SRG and HPFRC to shear capacity enhancement.

2.1.3 Shear Strengthening under Fatigue Loading

Research on the shear strengthening of RC beams using mortar-based composites under static loading is already limited, and studies on their behaviour under fatigue loading are even scarcer. In particular, SRG and HPFRC systems have yet to be investigated in the context of the shear fatigue behaviour of RC beams. Given this lack of research and the material similarities, this section includes a review of the shear fatigue behaviour of RC members strengthened with FRP systems to provide context and insight into this domain.

Mazumdar and Mallick (1998) found that the relationship between the fatigue strength and the ultimate bearing capacity was proportional to the bond length through the glass fibre-reinforced polymer (GFRP) single-side lap test. In addition, the ratio of the ultimate bearing capacity to the fatigue strength was fixed even if the bond length was different. In contrast, Jen and Ko (2010), through single shear tests, concluded that fatigue strength was inversely proportional to bond length when the adhesive layer thickness was 1 mm or 1.5 mm.

Xu et al. (1996) observed an opposing trend, noting that increasing adhesive layer thickness slowed fatigue crack propagation, suggesting a more gradual degradation process. Conversely, Tamura et al. (2009) expanded on this by examining the influence of adhesive layer thickness on the fatigue behaviour of FRP-concrete interfaces. Their results showed that while the static ultimate capacity increased with adhesive layer thickness, fatigue life was inversely related to it.

These conflicting conclusions have driven further in-depth research into the shear performance of FRP-strengthened beams. Czaderski and Motavalli (2004) conducted an experimental study on the fatigue performance of T-beams strengthened with prefabricated L-shaped CFRP plates. Their results indicated that CFRP strain primarily accumulated during the early stages of fatigue and gradually increased with prolonged fatigue loading.

Williams and Higgins (2008) focused on the shear fatigue behaviour of T-shaped RC beams strengthened with CFRP. Their experimental results demonstrated that U-shaped CFRP jacketing effectively reduced stirrup stress but had no significant effect on the stress in bending reinforcement. They also observed that while diagonal cracks propagated under fatigue loading, the rate of propagation increased with higher load

amplitudes. However, lower fatigue loads did not significantly affect the shear capacity of the beams under subsequent static loading.

Chaallal et al. (2010) investigated the fatigue shear behaviour of CFRP-strengthened T-beams using three-point bending tests. Specimens were subjected to fatigue loading for up to 5 million cycles at a frequency of 2 Hz, with a load range between 35% and 65% of the ultimate static load. If no failure occurred after the fatigue test, monotonic loading was applied until failure. By the end of the experiment, specimens strengthened with one layer of CFRP survived 5 million cycles, with some showing no visible signs of damage. This highlighted the effectiveness of CFRP strengthening in extending fatigue life.

Ferrier et al. (2011) developed a calculation method for accurately predicting the internal forces and deformations of FRP-strengthened beams under fatigue loading. This model, grounded in the fundamental theory of beam-section mechanics, aligned closely with experimental results. They concluded that the fatigue-bearing capacity of strengthened beams was primarily limited by the strength of the concrete and reinforcement, rather than the strength of the FRP or bonding layer.

Dong et al. (2012) examined the fatigue performance of rectangular beams strengthened with U-wrapped CFRP and GFRP strips using four-point bending tests. As shown in Fig. 2.5, each beam was first subjected to two preliminary load cycles to verify the testing system, followed by sine wave fatigue loads at a frequency of 5 Hz. The maximum and minimum fatigue loads were 40% and 15% of the ultimate static load of the reference beam, respectively. The results demonstrated that both CFRP and GFRP systems significantly improved initial crack load, ultimate strength, crack inhibition, and rigidity. CFRP-strengthened beams exhibited the highest ultimate strength and lowest deflection. After 1,000,000 fatigue cycles, FRP-strengthened beams showed 18–70% lower ultimate deflection compared to unreinforced beams. However, stiffness degradation in CFRP-strengthened beams was more pronounced than in GFRP-strengthened beams after prolonged fatigue loading.

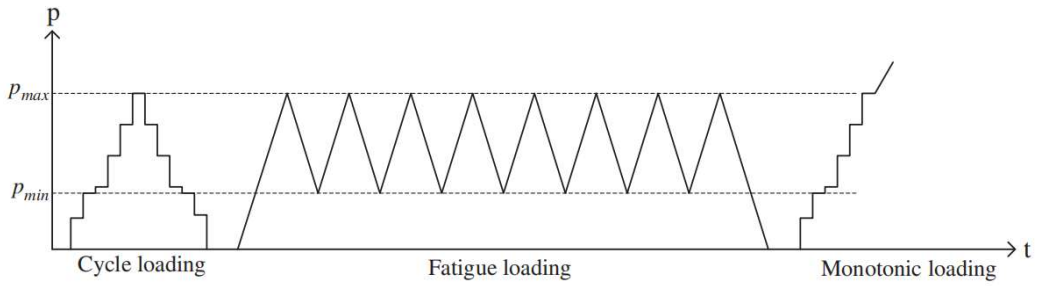

Fig. 2.5. Loading schemes for beams tested (Dong et al, 2012)

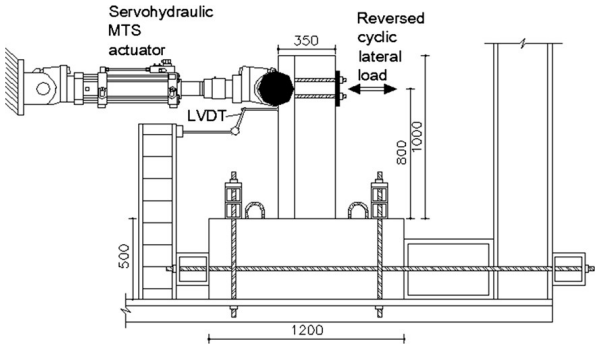

Fig. 2.6. Test set-up (Tzoura and Triantafillou, 2016)

Tzoura and Triantafillou (2016) investigated the shear strengthening effects of carbon FRCM systems under cyclic loading. The experimental setup, illustrated in Fig. 2.6, involved U-wrapped FRCM jackets applied to T-shaped beam sections. The load was cyclic and increased incrementally, with displacement amplitudes of 2 mm or 5 mm at a rate of 0.2 mm/s. Results showed that the effectiveness of the FRCM system did not scale proportionally with the number of fabric layers. Notably, one layer of fabric provided better performance than two layers in terms of the total fibre volume fraction. Moreover, increasing the displacement amplitude from 2 mm to 5 mm had no significant impact on the system's performance.

Pino et al. (2017) evaluated the fatigue performance of beams strengthened with PBO-FRCM systems using three-point bending tests, though their study was not limited to shear behaviour. They concluded that the FRCM system improved the fatigue performance of beams, with the degree of improvement depending on the number of FRCM layers. However, fatigue life decreased as peak loads increased. Residual strength tests showed that all strengthened specimens retained at least 95% of the static ultimate load capacity after fatigue loading.

Elghazy et al. (2018) studied the fatigue performance of corrosion-damaged RC beams strengthened with FRCM composite systems. Accelerated corrosion techniques were used to degrade the tensile steel bars, employing salted concrete as the electrolyte and creating a dry-wet cycle of three wet days followed by three dry days. After 140 days, the tensile steel bars experienced a theoretical weight loss of 20%. The FRCM systems tested included carbon and PBO fibres. Four-point bending tests revealed that the FRCM systems significantly improved the flexural response of corroded beams, restoring or even exceeding their original load-bearing capacity. The ultimate load of PBO-FRCM-strengthened beams ranged from 107% to 129% of the control beam's capacity, while carbon-FRCM-strengthened beams achieved an increase of up to 155%.

Akbari et al. (2018) conducted similar experiments on beams strengthened with carbon-FRCM jackets. They found that the fatigue endurance limit of the strengthened beams was approximately 65% of the yield strength of the steel reinforcement (PSY), and beams subjected to 2 million fatigue cycles retained at least 95% of their monotonic load capacity. Failure in all strengthened beams was attributed to fatigue fractures in the steel reinforcement, with no significant damage observed in the FRCM layers. Although the FRCM system extended the fatigue life of the beams, its direct impact on fatigue behaviour remained inconclusive.

In a subsequent study, Akbari and Nanni (2020) examined the fatigue behaviour of beams strengthened with glass-FRCM systems, focusing on the tensile stress limits of reinforced steel under fatigue loading. The results challenged the ACI 549.4R-13 guideline, which limits tensile stress in steel bars under service loads to 0.8 PSY. Their experiments demonstrated that fatigue fractures could occur at lower stress levels (0.7 PSY), suggesting the need for revised standards to ensure safety.

The limited studies on the fatigue performance of FRP-shear-strengthened RC beams have generally confirmed the effectiveness of such systems in enhancing fatigue resistance. However, conflicting conclusions frequently arise, highlighting inconsistencies in understanding the mechanisms involved. Notably, no research currently exists on the shear fatigue behaviour of RC beams strengthened with SRG or HPFRC systems. This significant gap underscores the urgent need for in-depth investigations in this area to advance the understanding of these materials' fatigue performance. By addressing this knowledge gap, research on SRG and HPFRC

systems can contribute to developing effective retrofitting solutions, improving structural resilience, and extending the service life of aging infrastructure.

2.2 Evaluation of Design Parameters Affecting the Strengthening Effectiveness

The literature review above highlights a lack of systematic discussion on the design parameters affecting the effectiveness of mortar-based composite strengthening. To address this gap, this section presents a detailed review of the factors influencing the shear performance of RC beams strengthened with mortar-based composite jacketing. A comprehensive database was compiled to examine how beam design parameters impact shear strength enhancement.

2.2.1 Experimental Database

An overview of the studies considered for the development of the experimental database is presented in Table 2.1 (218 beams from 36 experimental studies), including FRCM (TRM, PFRCM, SRG) and FRC (SFRC, HPFRC, UHPFRC, ECC, ECC-R) jacketing systems. Among them, 'ECC-R' represents a system that embedded FRP grids or welded bar meshes. The literature is sorted based on the publication year, from the most recent to the oldest. The data range of the strengthening system (SS), the concrete compressive strength (f_c), the shear span ratio (a/d), as well as the mode of failure as typical parameters influencing shear performance in each literature are also presented in Table 2.1. The detailed database compiled for the known mortar-based composites is shown in Table A of Appendix.

Table 2.1. Summary of the studies included in the database.

No.	Reference	SS	f_c (MPa)	a/d	Number of strengthened beams	Failure mode	
						Shear	Flexural
1	(Wakjira and Ebead, 2020)	FRCM	34.0	1.6-3.1	8	8	
2	(Wang et al., 2020a)	FRC	28.3	2.6	1	1	
3	(Wang et al., 2020b)	FRC	30.0	1.5, 2.5	4	4	
4	(Yang et al., 2020)	FRC	26.3	2.3, 3.0	3	3	
5	(Attar et al., 2020)	FRC	30.0	4.5	4	4	
6	(Thermou et al., 2019)	FRCM	28.0, 23.0	2.2	9	3	6

7	(Marcinczak et al., 2019)	FRCM	39.0	2.4	9	9	
8	(Wakjira and Ebead, 2019a)	FRCM	34.0	2.8	8	8	
9	(Jongvivatsakul et al., 2019)	FRC	32.4, 36.7	2.8	7	7	
10	(Garg et al., 2019)	FRC	28.6	1.6	2	2	
11	(Wang et al., 2019)	FRC	44.8	2.0, 3.0	8	8	
12	(Wakjira and Ebead, 2019b)	FRCM	25.8	2.0	6	6	
13	(Zhang et al., 2019)	FRCM	34.0	2.6	8	8	
14	(Wei et al., 2020)	FRC	26.6	2.0, 3.0	4	4	
15	(Sakr et al., 2019)	FRC	30.0	2.1	2	1	1
16	(Marcinczak and Trapko, 2019b)	FRCM	36.0	2.4	4	4	
17	(Marcinczak and Trapko, 2019a)	FRCM	39.0	2.4	1	1	
18	(Azam et al., 2018a)	FRCM	61.0	3.2	3	3	
19	(Tetta et al., 2018a)	FRCM	16.8-20.0	1.6-3.6	19	19	
20	(Ebead and Wakjira, 2018)	FRCM	30.0	2.0	6	6	
21	(Younis and Ebead, 2018)	FRCM	30.0	1.8	6	5	1
22	(Azam et al., 2018b)	FRCM	61.0	1.6	2	2	
23	(Sakr et al., 2018)	FRC	30.0	2.1	2	1	1
24	(Yang et al., 2017)	FRC	35.0	2.2	3	3	
25	(Gonzalez-Libreros et al., 2017b)	FRCM	21.0-25.0	3.3	6	6	
26	(Younis et al., 2017)	FRCM	30.0	2.0	15	15	
27	(Aljazaeri and Myers, 2017)	FRCM	45.0	2.5	6	6	
28	(Tetta et al., 2016)	FRCM	16.0-18.0	3.2	9	9	
29	(Hung and Chen, 2016)	FRC	24.4-25.2	3.3	5	5	
30	(Awani et al., 2016)	FRCM	36.0	3.0	6	6	
31	(Tetta and Bournas, 2016)	FRCM	11.0-20.0	2.3, 2.6	20	19	1
32	(Tzoura and Triantafillou, 2016)	FRCM	11.0-20.0	1.6	9	10	
33	(Azam and Soudki, 2014)	FRCM	38.0	2.2	4	4	
34	(Ruano et al., 2014)	FRC	26.3	1.8	9	9	

Total	218	208	10

The database, apart from the details of the beams and the applied mortar-based composites, presents the failure modes observed during testing as well as the shear strength provided by the mortar-based composite jacket V_{JAC} ($= V_{RET} - V_{CON}$; where V_{RET} and V_{CON} are the shear strength of the strengthened and the corresponding reference beam (control beam)). The ratio V_{JAC}/V_{CON} reflects the contribution of the mortar-based composite on the strength increase of the control beams. In the following, graphs are developed which illustrate the impact of the mechanical and geometrical properties of the strengthened beams on V_{JAC}/V_{CON}. The data are grouped based on their mode of failure using the classification proposed by Gonzalez-Libreros et al. (2017a). The shear strengthened beams failed in three distinct modes: i) flexural failure where concrete crushing follows the longitudinal steel bar yielding; ii) shear failure where failure is caused by diagonal tension, fabric rupture, etc.; and iii) shear-detachment where shear failure occurs when detachment occurs either between the composite and the beam substrate or within the mortar layer (mostly in the case of multi-layered composite jackets). In some cases, the application of the mortar-based composite jackets (fully wrapped) modified the mode of failure from brittle to ductile flexural failure. The beams that present flexural failure can be considered as the lower bound of the strengthening capacity (Gonzalez-Libreros et al., 2017a).

In general, the addition of mortar-based composite jacketing systems substantially improved the shear behaviour of the RC beams (up to 196%), as presented in Fig. 2.7 (The purple curve indicates the percentage of the beams (see the secondary axis) of the database that corresponds to the data related to each abscissa interval). For FRCM systems, the shear strength of RC beam was increased by 61% on average, 196% on the maximum and 4% on the minimum. The average strengthening effect of FRC systems (80%) was slightly better than that of FRCM system, and the shear strength of RC beam can be increased from 4% to 190% in the data collected. There is a large variation of V_{JAC}/V_{CON} depending on the system applied and the mode of failure. Most of the beams were strengthened using FRCM systems (72% of the beams of the database) and among them the CFRCM is the dominant one (36% of the jacketed beams). SRG and ECC systems were applied equally to 15% of the beams of the

database. The less investigated systems seem to be the UHPFRC (2%), SFRC (6%) and ECC-R (5%) jacketing.

The variation in the observed strengthening efficiency among different mortar-based composite systems can be attributed to differences in material composition, jacketing configuration, bond mechanisms, and failure modes. For FRCM systems, the effectiveness is particularly dependent on the bond quality between the textile and mortar, as well as the adequacy of mechanical anchorage. Inadequate interfacial bonding often results in premature debonding or fibre rupture, limiting the contribution of the composite jacket to overall shear resistance. Moreover, differences within FRCM systems themselves can be traced to the mechanical properties of the textiles and their compatibility with the surrounding mortar. Systems using stiffer textiles with better interfacial adhesion tend to demonstrate superior performance, while those with poor bond quality or insufficient anchorage are more susceptible to inefficient stress transfer and failure. By contrast, FRC systems rely on the homogeneous distribution of short fibres within the cementitious matrix, enabling enhanced crack-bridging, improved ductility, and greater resistance to localised delamination. This integrated mechanism often results in more stable and effective shear strengthening, provided that the fibre content, orientation, and matrix consistency are well controlled.

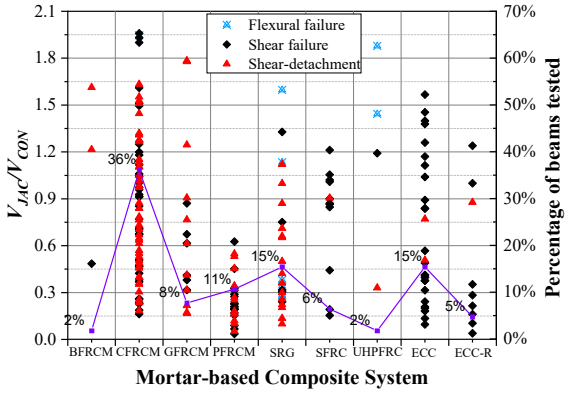

Fig. 2.7. Variation of V_{JAC}/V_{CON} as a function of the various mortar-based composite systems.

2.2.2 Design Parameters of the Strengthened RC Beams

In this section, the variation of V_{JAC}/V_{CON} as a function of the design parameters of the beams such as the shear span ratio, a/d, the mean cylindrical concrete compressive strength, f_c, the tensile longitudinal steel reinforcement ratio, $\rho_{long,b}(= A_{sl}/b_w d)$, and

the stirrup reinforcement ratio, $\rho_w (= A_w/b_w s)$ (where s is the stirrups spacing; b_w is the beam width; A_{sl} is the sectional area of the tensile reinforcement; A_w is the sectional area of the stirrups) is presented in Fig. 2.8.

Most of the tested beams have a shear span ratio, a/d, between 2 and 3 (71%) which corresponds to the 'shear failure valley', that is, the transition zone between shear compression failure and oblique tension failure (Kani, 1964). The variation of V_{JAC}/V_{CON} as well as the mode of failure seems to be independent from a/d. The variation of V_{JAC}/V_{CON} with the concrete compressive strength, f_c, is presented in Fig. 2.8(b). The highest values of strength increase are observed for f_c values up to 20MPa (24%), which are considered representative of old type construction. As observed in Fig. 2.8(b), there is a trend the effectiveness of the mortar-based composite systems to decrease as the concrete compressive strength increases.

Regarding the reinforcement detailing of the beams, most of the beams (64%) have a longitudinal steel reinforcement ratio, $\rho_{long,b}$, higher than 0.02, which in some cases exceed the maximum reinforcement ratio, ρ_{max}, to avoid flexural failure (Fig. 2.8(c)). The stirrup reinforcement ratio, ρ_w, seems to influence the effectiveness of the mortar-based composite jackets (Fig. 2.8d). Excluding the case of $\rho_w = 0$ (no presence of stirrups in the shear critical region), for ρ_w values up to 0.0025, which corresponds to beams strengthened with FRCM systems, the effectiveness of the jacket is reduced with the increase of the shear reinforcement (i.e. closely spaced stirrups). This is mainly attributed to the interaction between the internal and external shear reinforcement (Gonzalez-Libreros et al., 2017a). The beams with ρ_w between 0.0030 and 0.0035 seem not to follow this trend, which mainly corresponds to the beams strengthened with FRC jackets. A detailed analysis on the impact of the external shear reinforcement FRCM system follows in section 2.2.3.

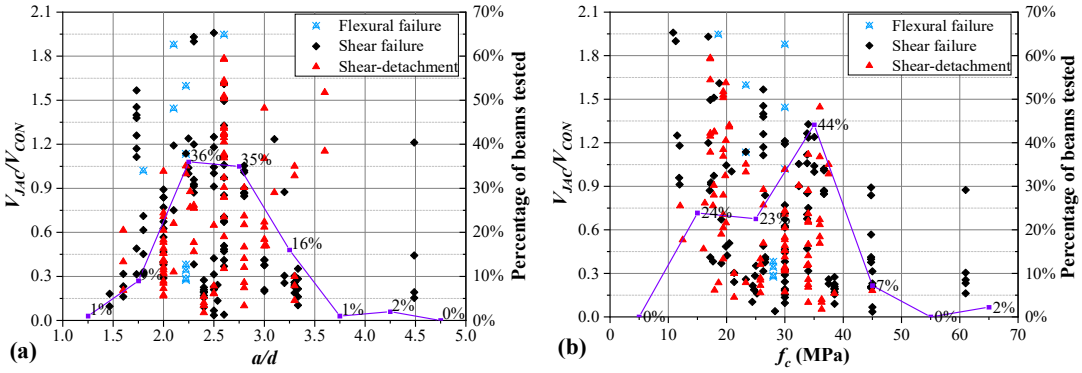

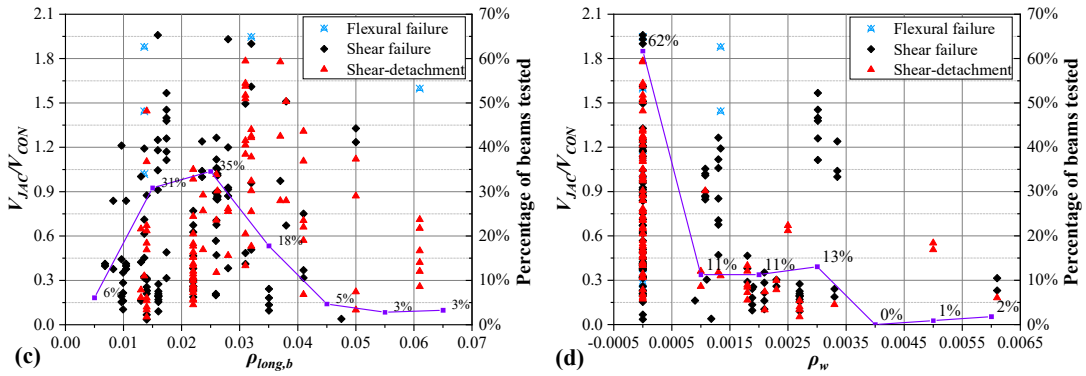

Fig. 2.8. Variation of V_{JAC}/V_{CON} with (a) a/d, (b) f_c, (c) $\rho_{long,b}$, (d) ρ_w.

2.2.3 Design Parameters of FRCM Jacketing Systems

2.2.3.1 Strengthening Configuration

The database contains 164 collected beams strengthened by FRCM systems. The variation of V_{JAC}/V_{CON} as a function of FRCM jacket configuration is presented in Fig. 2.9a. Regarding the notation given to the alternative jackets, 'FW' and 'U' stand for the fully wrapped and U-shaped jackets, respectively, whereas 'SB' for the side bonded. 'C' and 'S' correspond to continuous textiles and textile strips, respectively. 'A' indicates the presence of a mechanical anchorage system. U-shaped jackets were applied to 74% of the strengthened beams from which 12% and 48% used continuous textiles with and without mechanical anchorage, respectively. The rest used textile strips with (8%) and without mechanical anchorage (6%). Side bonded jackets with continuous textiles and textiles strips were applied to 14% and 8% of the database beams, respectively. By excluding the fully wrapped beams (4%), in general the U-shaped FRCM jackets seem to be more effective when compared to the side bonded ones. As observed in Fig. 2.9a, the most common mode of failure is shear detachment (49%), which was observed even in the beams that mechanical anchorage was used (23%).

The mechanical anchorage systems used in 40 out of 164 beams of the database for the application of the FRCM jackets are the following: i) metallic (steel or aluminium) anchors; ii) FRCM/FRP insertion anchors; iii) near surface mounted (NSM) anchors; and iv) horizontal FRCM laminate anchors. Details about the aforementioned mechanical anchorage systems can be found in the research conducted by Godat et al., (2020).

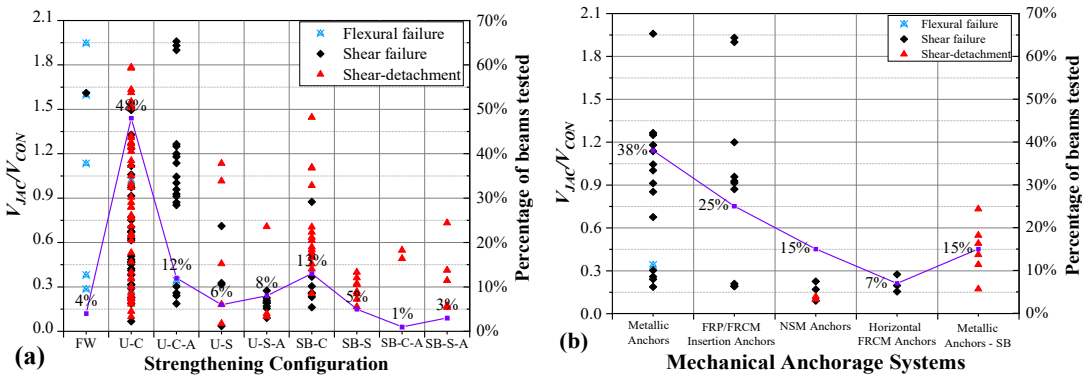

Fig. 2.9. Variation of V_{JAC}/V_{CON} with (a) strengthening configuration and (b) mechanical anchorage systems

Fig. 2.9b presents the relationship between the failure modes of the strengthened beams when the mechanical anchorage systems were adopted. For U-wrapped strengthened beams, except for NSM anchors, the other three methods can improve the adhesion between the FRCM system and the concrete surface. Metallic (steel or aluminium) anchors are an effective method to prevent debonding of the system significantly, but Aljazaeri and Myers (2017) illustrated that it is ineffective in preventing the fibre from sliding in the matrix. No detachment failure mode can be found for FRCM/FRP insertion and horizontal FRCM laminate anchors. In the research carried by Tetta et al. (2016), T-beams strengthened with the 2-layered carbon TRM jacket using FRCM/FRP insertion anchors had similar behaviour to the 4-layered carbon TRM jacketed beams without anchorage system, thus demonstrating the need of using anchorage systems in providing a more cost-effective strengthening solution. However, according to Baggio et al. (2014), the use FRCM/FRP insertion anchors in U-shaped FRCM jacketed rectangular beams increased strength by only 3% compared with beams without anchors.

As observed by Wang et al. (2019) the lack of effectiveness of such an anchorage system may be related to the fact that the anchors are intended to restrain out-of-plane peeling of the composite and do not restrain the in-plane fibre slippage. Moreover, Gonzalez-Libreros et al. (2017a) demonstrated that although beams with and without anchors exhibited diagonal tension shear failure, the presence of anchors slightly changed the inclination of shear cracks around the anchors. In the collected data, only 50% of the samples with NSM anchorage prevented detachment. It is worth noting that all these detached NSM anchorage samples refer to the U-shaped strip configuration. However, Marcinczak and Trapko (2019b) demonstrated that NSM

system was still effective compared with the non-anchored ones, since they had higher shear capacity and delayed the occurrence of detachment. The failure mode observed was the gradual crack's development, leading eventually to jacket debonding. In the case of side-bonded jacketing, metallic anchors could not prevent the detachment of the jackets (Fig. 2.9b).

2.2.3.2 Failure Modes

In this section, the failure modes of the FRCM strengthened beams under the various jacketing configurations are discussed. Figure 2.9a shows the observed failure modes for each scheme, and the corresponding schematics are presented in Figure 2.10. Additionally, Fig. 2.11 illustrates the typical failure modes attributed to fibre rupture or detachment of the jacket.

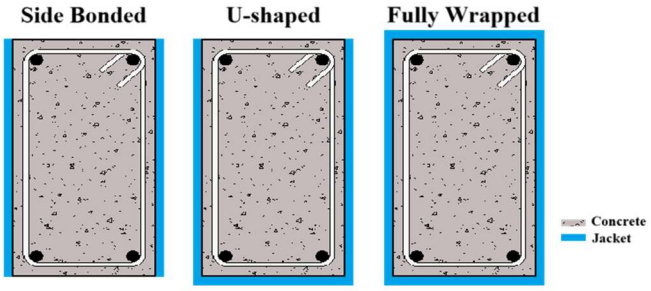

Fig. 2.10. Cross-sectional strengthening schemes.

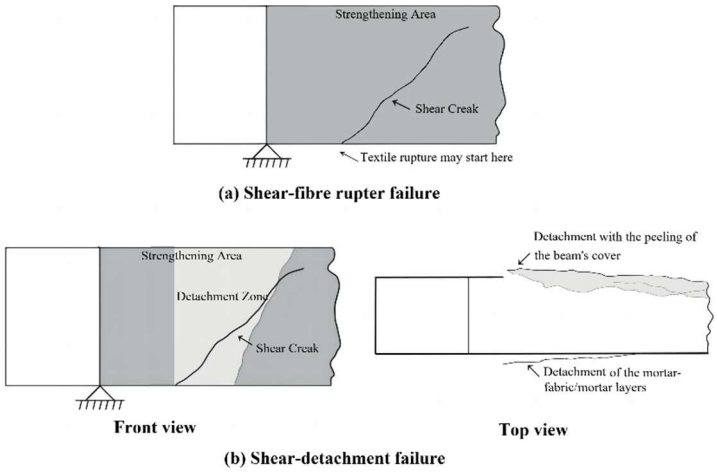

Fig. 2.11. Failure modes: (a) shear-fibre rupture; (b) shear-detachment.

Fully wrapped beams: In most cases, failure occurred due to fibre rupture. Although debonding is most likely to happen first, shear capacity is controlled by the rupture of the textile (Tetta and Bournas, 2016; Thermou et al., 2019). The fully

wrapped configuration creates a larger contact area and bonding strength between the jacket and substrate, enhancing the interface friction and transfer of frictional forces between the strengthening system and concrete. Furthermore, the fully wrapped configuration creates a tight wrapping layer that serves as a protective barrier for the concrete surface, reducing the risk of surface delamination and damage. These factors make the mortar-based composite jacket less prone to premature detachment and increase the likelihood of transforming the beam's response from shear to flexural failure. In case of shear failure, noticeable diagonal cracks can be observed on the jacket, especially near the supports and load application points, with fibre rupture commonly occurring at the crack initiation location at the bottom of the beam (National Research Council, 2004). Fig. 2.11(a) illustrates a typical shear failure mode caused by fibre rupture.

U-shaped beams: Most U-wrapped beams without mechanical anchorage systems failed due to detachment of the composite, which can be further classified as follows: (a) detachment of the textile from the jacket-beam interface accompanied by the peeling of the beam's cover; (b) complete extraction of some fibres in the textile; (c) detachment of the jacket itself accompanied by the detachment of the mortar-fabric/mortar layers or the delaminated or slipped multi-layer textiles. Fig. 2.11(b) illustrates the potential detachment mode in this failure scenario, with the left side presenting the frontal view and the right side showing the top view. It is worth noting that in this failure mode, shear diagonal cracks on beams can be observed after the jacket is removed. In general, the detachment of mortar-based composite jacketing does not affect the concrete surface of RC beams (Thermou et al., 2019; Wakjira and Ebead, 2019a), but a few researchers mention that the concrete cover peels off (Awani et al., 2016; Tetta et al., 2015). In addition, Younis et al. (2017) observed that fibre slippage was more likely to occur in fabrics with higher density since the closely spaced fibres may prevent the uninhibited flow of the mortar, leading thus to a reduced bond quality. The beams failing in this mode often demonstrate significantly constrained ductility (National Research Council, 2004). Another key failure mode similar to that of a fully wrapped reinforcement configuration is the rupture of the fibre (Zhang et al., 2019); this appears to be more common in systems with anchors. In the case of U-wrapped jackets with anchors, there is another failure mode in which the anchorage is separated, or the surrounding area of the anchorage is damaged (Tetta et

al., 2016; Marcinczak et al., 2019). This phenomenon is also common in FRP systems (Chen and Teng, 2003a).

Side bonded beams: Detachment was the mode of failure observed for the side bonded beams. Almost all specimens had 45° diagonal cracks at the load location when failure occurred (Wakjira and Ebead, 2019b). Younis et al. (2017) observed the following detachment patterns: (i) longitudinal stripping of the jacket at the top; (ii) debonding of the jacket in the vertical direction, that is, the detachment along with the whole depth of the beam at the load position; (iii) longitudinal peeling of mortar-based composite system at the bottom; and (iv) the peeling of the jacket in the inclined direction, which is more common on the inclined mortar-based composite system strips. Based on the data collected, anchoring does not have a significant impact on the failure mode of side bonded jackets. Therefore, to avoid premature detachment of the strengthened beams, certain design codes for externally bonded FRP composite materials design prohibit using side bonded jackets (National Research Council, 2004). Based on the review, this approach may need to be adopted also for the case of FRCM systems.

In addition to the influence of the strengthening configuration on the failure mode, the reinforcement ratio of longitudinal and transverse bars ($\rho_{long,b}$ and ρ_w) in the beam also has an impact. As shown in Fig. 2.8(c) and (d), increasing $\rho_{long,b}$ and ρ_w leads to a slight decrease in the probability of detachment of the strengthening jacket. This decrease can be attributed to the fact that a higher reinforcement ratio enhances the load transfer mechanisms within the beam, thereby reducing localised stress concentrations. This improved load transfer capacity reduces the strain and stress on the strengthening jacket, thereby reducing the risk of detachment. Furthermore, a higher $\rho_{long,b}$ and ρ_w contributes to better control of deflection and crack development in the beam, which enhances the overall structural integrity and limiting concrete's cover peeling. The reduced deflection also mitigates the discrepancy in load displacement response between the strengthening system and the substrate, thereby further preventing detachment.

2.2.3.3 Design parameters of the FRCM system

The variation of V_{JAC}/V_{CON} with the nominal ultimate strain of the textiles as provided by the manufacturer (ε_{fu}), the web reinforcement ratio of the textile (ρ_f), the axial

rigidity of the textile ($E_f\rho_f$), the FRCM reinforcement ratio (ρ_{cm}), and f_{cm}/f_c (where f_{cm} is compressive strength of the mortar) is depicted in Fig. 2.12. The web reinforcement ratio (ρ_f) and the FRCM reinforcement ratio (ρ_{cm}) are defined as follows (Gonzalez-Libreros et al., 2017a):

$$\rho_f = 2nt_f w_f / b_w s_f \quad (2\text{-}1)$$

$$\rho_{cm} = 2t_{cm} w_f / b_w s_f \quad (2\text{-}2)$$

where n is the number of textile layers applied; t_f is the thickness of the textile; $t_{cm}(= (n+1)t_m)$ is the total thickness of the FRCM composite (t_m is the nominal thickness of a single mortar layer); w_f is the width of FRCM strips; and s_f is the longitudinal distance of FRCM strips (if the textiles are applied as continuous, then $w_f = s_f = 1$).

Regarding ε_{fu}, apart from glass and basalt fibre, the rest of the materials have two or more different values for ε_{fu}. Most of the beams (53%) were strengthened with textiles that had ε_{fu} in the range of 1.5-2.0% (Fig. 2.12(a)). 87% of the strengthened beams had a web reinforcement ratio $\rho_f < 0.0045$ and 48% had $\rho_f < 0.0015$ (Fig. 2.12(b)). The variation of V_{JAC}/V_{CON} seems not to be directly related to the amount of web reinforcement confirming similar observations made in other studies (Escrig et al., 2015; Ombers, 2015a). The increase of ρ_f has a slight impact on the CFRCM jacket shear strength ($average: V_{JAC}/V_{CON} = 0.86$), a significant impact on the B- and GFRCM jacket shear strength ($average: V_{JAC}/V_{CON} = 1.10$ and 0.69) and almost no effect on the PFRCM and SRG ($average: V_{JAC}/V_{CON} = 0.25$ and 0.62).

The interaction between internal transverse steel reinforcement (stirrups) and the externally bonded FRCM jackets has not been studied in detail. Similar to the approach adopted for FRP jacketing (Ary and Kang, 2012), the ratio of the axial stiffness of the transverse steel reinforcement to that of the FRCM composite ($E_S\rho_W/E_f\rho_f$; where $E_f\rho_f$, is axial rigidity of the textile index of FRCM composites; E_f is the elastic modulus of the textile fibres in GPa; E_s is the elastic modulus of steel reinforcement) is used to evaluate the interaction between stirrups and the FRCM system. In Figs. 2.12(c) and (d), the relationship between $E_f\rho_f$ and $E_S\rho_W/E_f\rho_f$ with V_{JAC}/V_{CON} is presented, respectively. The $E_f\rho_f$, which expresses the axial rigidity of the textile, for most of the jackets lies between 0.052-1 (89% of the beams). For similar axial rigidity

values, the PFRCM system seems less effective than the rest of the FRCM systems (C-, G-, BFRCM and SRG). When internal shear reinforcement is present, the increase of $E_S\rho_W/E_f\rho_f$ (i.e., more stirrups for the beam) renders the contribution of the FRCM system less effective. Using the experimental data shown in Fig. 2.12d, and after applying exponential curve fitting to the data (51 beams), the following empirical expression is derived:

$$V_{FRCM}/V_{CON} = 0.383\left(E_s\rho_w/E_f\rho_f\right)^{-0.3} \quad (2\text{-}3)$$

Equation (2-3) should be treated with caution since it is based on a limited amount of data.

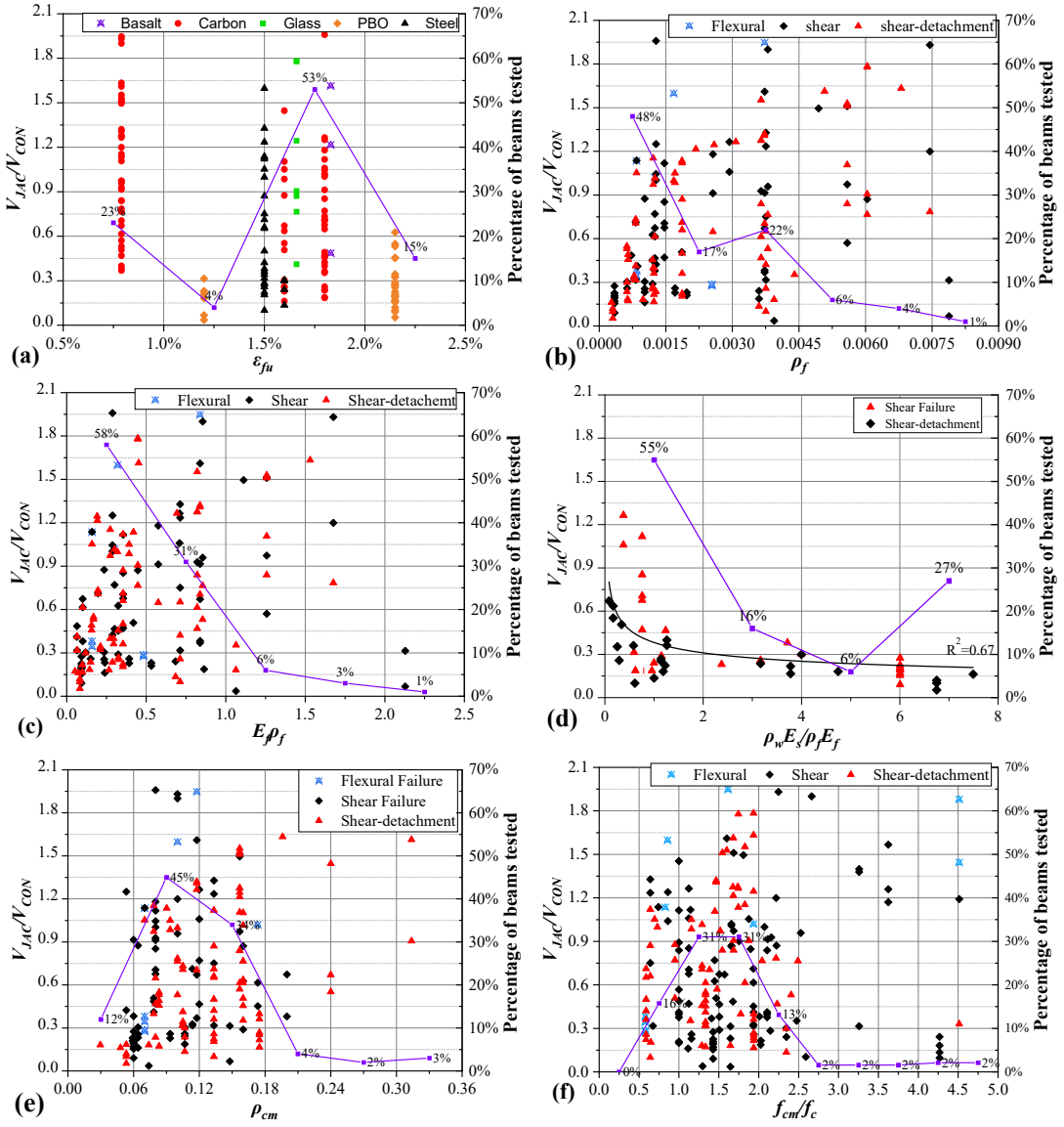

Fig. 2.12. Variation of V_{JAC}/V_{CON} with (a) ε_{fu}, (b) ρ_f, (c) $E_f\rho_f$, (d) $E_s\rho_w/E_f\rho_f$ (e) ρ_{cm}, (f) f_{cm}/f_c

Regarding the FRCM reinforcement ratio, most of the specimens (79%) receive ρ_{cm} values between 0.06-0.18 (Fig. 2.12e). In general, the increase of ρ_{cm} leads to increased shear capacity for the beams. This is attributed to the fact that an increase in ρ_{cm} corresponds to an increase in the thickness of the FRCM mortar, which increases the cross-sectional area (especially the width) of the RC beam, thereby improving the shear capacity of the beam. The impact of the cementitious matrix compressive strength, f_{cm}, on V_{JAC}/V_{CON} is presented in Fig. 2.12f. 91% of the studies used f_{cm}/f_c between 0.5-2.5. As observed in the Fig. 2.12f, there is not direct correlation between f_{cm}/f_c to V_{JAC}/V_{CON}.

2.2.4 Design Parameters of FRC Jacketing Systems

The database presented in Table A contains 54 collected beams strengthened by the FRC (ECC, ECC-R, SFRC HPFRC and UHPFRC) systems. Figures 2.13(a) and (b) present the variation of V_{JAC}/V_{CON} with the fibre type and the fibres' volume fraction. Since some studies do not provide information on the specific fibre types and volume fractions, only the specimens for which full details are provided are presented in Figs. 2.13a and 2.13b (46 and 31 beams were used in Figs. 2.13a and 2.13b, respectively). Most FRC systems use steel fibres (57%), followed by PVA and PE fibres (28% and 15%, respectively). A smaller percentage of FRC jacketed beams, especially in the cases that steel or PVA fibres are used, fails due to detachment compared with FRCM strengthened beams. Tanarslan et al. (2021) demonstrated that the FRC system can offer a better bonding effect with the beam surface to prevent the occurrence of partial detachment. As seen in Fig. 2.13a, the shear strength increases for PE, PVA and steel fibre systems ranges between 5% to 88%, 10% to 89% and 15% to 187%, respectively. Most studies use a volume fraction of fibres between 1.5-2.0% (83% of the samples in Fig. 2.13b). Although the number of specimens is small, it seems that there is a trend between the increase in strength as the volume fraction of fibres increases.

Fig. 2.13c shows the variation of V_{JAC}/V_{CON} with the type of jacketing configuration. The most common strengthening configuration in FRC system is side bonding (SB), which accounts for 65% of the beams, whereas 8% correspond to one side bonding and the rest (57%) to two side bonding. SB (two sides) jackets have a greater potential to improve shear strength, and V_{JAC}/V_{CON} increase by up to187%, while for SB (one

side) jackets, the strength increased ranges between 33% and 124%. For U-wrapped beams (35% of the samples), V_{JAC}/V_{CON} ranges from 13 to 157%.

The impact of the ratio of the width of the jacket to the width of the beam, $b_{w,FRC}/b_w$, on V_{JAC}/V_{CON} is presented in Fig. 2.13d. The term $b_{w,FRC}$ refers to the width of the FRC jacket, which corresponds to the total width of the two sides. 64% of the studies used $b_{w,FRC}/b_w$ between 0.2-0.6. Detachment failure is observed for $b_{w,FRC}/b_w$ less than 0.4. Due to the limited number of data and the large dispersion of the results no solid conclusions can be drawn about the impact of $b_{w,FRC}$ on the shear strength increase.

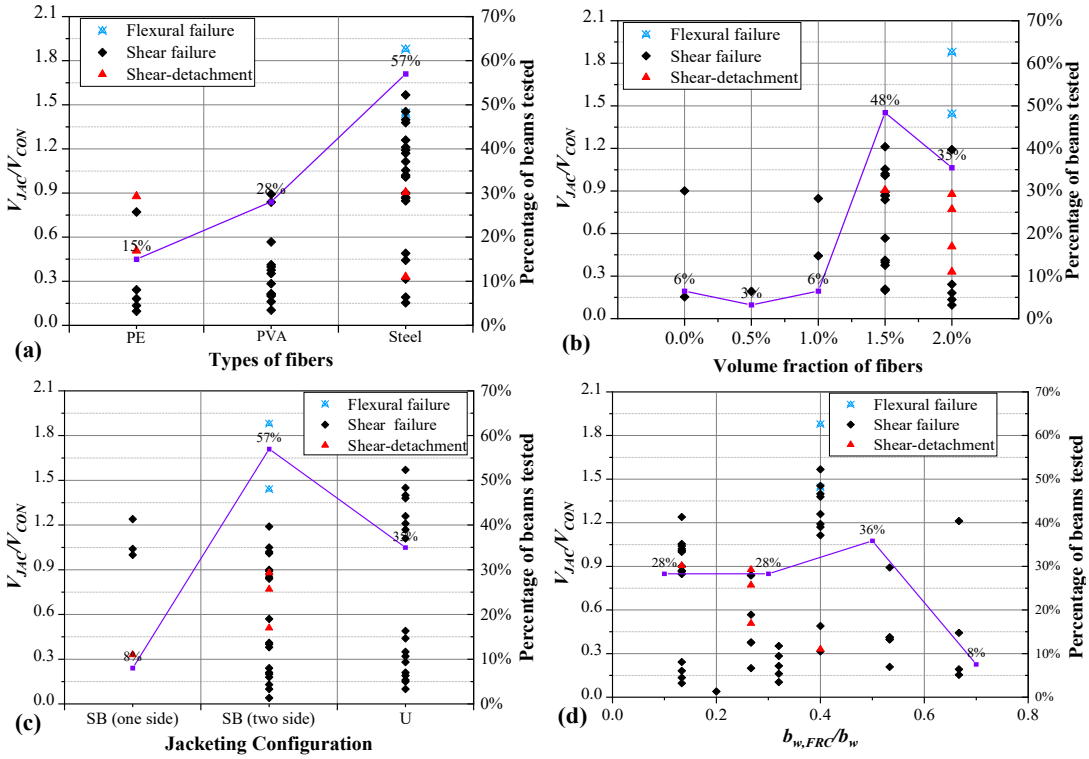

Fig. 2.13 Variation of V_{JAC}/V_{CON} with (a) fibre type, (b) volume fraction of fibres, and (c) jacketing configuration and (d) $b_{w,FRC}/b_w$

2.3 Shear Resistance of Beams Retrofitted with Mortar-Based Composites

2.3.1 Analytical Models for FRCM Jacketing Systems

The total shear strength of FRCM strengthened RC beams (V_{shear}) comprises shear strength contributions from concrete (V_C), steel stirrups (V_s) and FRCM jacket (V_{FRCM}):

$$V_{shear} = V_C + V_s + V_{FRCM} \leq V_{Rd,max} \quad (2\text{-}4)$$

V_{shear} shall not exceed the shear limit value ($V_{Rd,max}$), which corresponds to the crushing of diagonal compression columns in the web of the member (Eurocode 2, 2005).

According to Eurocode 2 (2005) and ACI 318 (2008), the shear strength contribution from concrete (V_C) is:

$$\begin{aligned} V_C^{EC2} &= 0.12k\left(100\rho_{long,b}f_c\right)^{1/3}b_w d \\ &\geq 0.035k^{3/2}{f_c}^{2/3}b_w d \end{aligned} \quad (2\text{-}5)$$

$$V_C^{ACI} = 0.167\sqrt{f_c}b_w d \quad (2\text{-}6)$$

where $k = 1 + \sqrt{(200/d)} \leq 2.0$ (with d in mm) is a factor that considers the size effect. According to EC2 (Eurocode, 2004), the shear strength contribution from stirrup (V_s) can be calculated as:

$$V_s = \frac{A_w}{s} z f_{ywd} \quad (2\text{-}7)$$

where f_{ywd} is the design yield strength of the shear reinforcement, A_w is the shear reinforcement area, $z = 0.9d$ is the inner lever arm, and s is the stirrup spacing.

The shear strength contribution of the FRCM jacket, V_{FRCM}, can be calculated using the analytical models presented in Tables 2.2. These models can be categorised into two types: those based on the characteristics of the fibres and those based on the properties of the FRCM composite as a whole.

Specifically, models 1-4 (Triantafillou and Papanicolaou, 2006; Escrig et al., 2015; Thermou et al., 2019; Tetta et al., 2018b) are based on fibre's properties. Model 1 (Triantafillou and Papanicolaou, 2006) initially proposed a truss analogy model to predict the shear strength of FRP jackets, calibrated with experimental data specifically for fully wrapped FRCM-strengthened rectangular beams, and later extended it to other configurations such as U-shaped wraps (Gonzalez-Libreros et al., 2017a). In this model, the effective fibre strain (ε_{eff}) is assumed to be 0.5 times the ultimate strain (ε_{fu}), without considering potential performance differences across configurations. To address this limitation, Model 2 (Escrig et al., 2015) refined the model by introducing distinct ε_{eff} expressions based on strengthening configuration, linking ε_{eff} to concrete compressive strength (f_c), fibre modulus (E_f), and fibre reinforcement ratio

(ρ_f). Model 3 (Thermou et al., 2019) further adjusted the model experimentally, adding an additional term for undamaged textiles to improve the accuracy of the ε_{eff} expression. Additionally, Model 4 (Tetta et al., 2018b) improved on Chen and Teng's FRP model (2023) by eliminating the need for fibre modulus (E_f), addressing challenges in selecting an appropriate modulus when predicting the shear strength provided by FRCM. Compared to the models proposed by Models 1-3, this revised model removes the influence of ε_{eff} and instead introduces the design value of the effective stress in the jackets.

In contrast, models 5-7 (ACI, 2013; Younis et al., 2017; Ombres, 2015b) that focus on composite properties aim to synthesize the collective behaviours of textiles and mortar. Model 5 is provided by ACI 549.4R-13 (2013), which is only standard considering the shear strength contribution of continuous FRCM U-wrapped or fully wrapped systems, although it is acknowledged that the standard was developed based on an insufficient amount of experimental data. This model sets 0.004 as the effective composite strain. However, this limit has yet to be comprehensively validated experimentally. Model 6 (Younis et al., 2017) adopted ACI's approach, using ε_{eff} = 0.004 and estimating FRCM shear strength by summing the contributions of textiles and mortar. Model 7 (Ombres, 2015b) used a model initially designed for FRP systems, applying an effectiveness coefficient (k_e) of 0.5 to account for reductions when used in FRCM, highlighting dependencies on debonding strength, composite modulus, and optimal bond length.

The analytical models were implemented in the database presented in Table A. For all the beams of the database, the angle between the concrete compression strut and the beam axis is perpendicular to the shear force is considered $\theta = 45^0$, whereas the angle between the fibres and the beam axis is perpendicular to the shear force in all the applications is $\alpha = 90^0$. In addition, the expression for the each model's experimental value of the effective strain (ε_{eff}^{exp}) that is calculated from the experimental shear strength appears in Tables 2.2 and 2.3, except for Model 4 which does not depend on ε_{eff}^{exp}. Due to limitations imposed by the analytical models, the strengthened beams with anchorage systems and/or flexural failure are not considered in the analysis (Gonzalez-Libreros et al., 2017a).

The experimental and the predicted normalised shear stress of the FRCM jacketing system, v_{FRCM}^{exp} and v_{FRCM}^{pred}, are calculated from:

$$v_{FRCM}^{exp} = \frac{V_{FRCM}^{exp}}{b_w d f_c}\ ;\ v_{FRCM}^{pred} = \frac{V_{FRCM}^{pred}}{b_w d f_c} \tag{2-8}$$

where $V_{FRCM}^{exp}(= V_{JAC}$ see Table A) is the experimental shear strength provided by FRCM jackets; V_{FRCM}^{pred} is predicted the shear strength provided by FRCM jacket which is calculated by the different models.

Table 2.2. Analytical models for the shear strength contribution of the FRCM jacket.

Reference	$\boldsymbol{V_{FRCM}}$
Model 1 (Triantafillou & Papanicolaou1 2006);	$V_{FRCM} = 2nt_f h_f \frac{w_f}{s_f}\varepsilon_{eff}E_f(cot\theta + cot\alpha_0)sin\alpha_0$ $V_{FRCM} = 2nt_f h_f \frac{w_f}{s_f}\varepsilon_{eff}E_f = \rho_f h_f b_w \varepsilon_{eff}E_f; \theta = 45^{\circ}; \alpha_0 = 90^{\circ}$ **For Model 1**: $\varepsilon_{eff} = 0.5\varepsilon_{fu}$
Model 2 (Escrig et al., 2015);	**For Model 2**: For fully wrapped: $\varepsilon_{eff} = 0.035\left(\frac{f_c^{2/3}}{\rho_f E_f}\right)^{0.65}\varepsilon_{fu}$ For side bonding or U-wrapped: $\varepsilon_{eff} = 0.020\left(\frac{f_c^{2/3}}{\rho_f E_f}\right)^{0.55}\varepsilon_{fu}$
Model 3 (Thermou et al., 2019)	**For model 3**: For textile without damage: $\varepsilon_{eff} = 0.010\left(\frac{f_c'^{2/3}}{\rho_f E_f}\right)^{0.47}\varepsilon_{fu}$ For fully wrapped: $\varepsilon_{eff} = 0.066\left(\frac{f_c^{2/3}}{\rho_f E_f}\right)^{0.59}\varepsilon_{fu}$ For side bonding or U-wrapped: $\varepsilon_{eff} = 0.015\left(\frac{f_c^{2/3}}{\rho_f E_f}\right)^{0.94}\varepsilon_{fu}$ **Experimental value of effective strain**: $\varepsilon_{eff}^{exp} = \frac{V_{FRCM}^{exp}}{2nt_f h_f (w_f/s_f)E_f}$
Model 4 (Tetta et al., 2018b)*	$V_{FRCM} = 2nt_f b_w h_f \frac{w_f}{s_f} f_{fed}(cot\theta sin\alpha_0 + cos\alpha_0)$; $V_{FRCM} = 2nt_f b_w h_f \frac{w_f}{s_f} f_{fed} = \rho_f b_w^2 h_f f_{fed}; \theta = 45^0; a = 90^0;$ $f_{fed} = D_f f_{fed,max}$ $f_{fed,max} = 8.67\beta_l\beta_w\sqrt{\frac{1000\sqrt{f_c}}{nt_f}}$; $\beta_l = \begin{cases} 1, \lambda \geq 1 \\ sin\left(\frac{\pi\lambda}{2}\right), \lambda < 1 \end{cases}$; $\beta_w = \sqrt{\frac{2 - w_f/(s_f sin\alpha)}{1 + w_f/(s_f sin\alpha)}}$ $D_f = \begin{cases} \frac{2}{\pi\lambda}\left(\frac{1 - cos\left(\frac{\pi\lambda}{2}\right)}{sin\left(\frac{\pi\lambda}{2}\right)}\right), \lambda \leq 1 \\ 1 - \frac{\pi - 2}{\pi\lambda}, \lambda > 1 \end{cases}; \lambda = L_{max}/L_e$ $L_{max} = \begin{cases} h_f/sin\alpha \text{ ,for U-wrapped jackets} \\ h_f/2sin\alpha \text{ ,for side bonding jackets} \end{cases}; L_e = 15\sqrt{\frac{1000nt_f}{\sqrt{f_c'}}}$ $h_{fe} = z_b - z_t; z_b = h_f - (h - d_{fb}); z_t = d_{ft}$
Model 5 (ACI, 2013)	$V_{FRCM} = nA_f f_{fv} h_f = \rho_f b_w f_{fv} d;$ $A_f = 2t_f\, w_f/s_f; f_{fv} = E_{FRCM}\varepsilon_{eff}; \varepsilon_{eff} = \varepsilon_{FRCM} \leq 0.004$ **Experimental value of effective strain:** $\varepsilon_{eff}^{exp} = \frac{V_{FRCM}^{exp}}{nA_f E_{FRCM} d}$

Model 6 (Younis et al., 2017)**	$V_{FRCM} = k_e \varepsilon_{eff} E_{FRCM} \rho_f b_w d(cot\theta + cot\alpha_0) sin\alpha_0$; $V_{FRCM} = k_e \varepsilon_{eff} E_{FRCM} \rho_f b_w d; \theta = 45^0; \alpha_0 = 90^0$; $\varepsilon_{eff} = \frac{f_{fdd}}{E_{FRCM}} \left[1 - \frac{1}{3} \frac{l_e sin\alpha}{min(0.9d; h_f)}\right]$; $f_{fdd} = \frac{0.24}{\gamma_{fd}\sqrt{\gamma_c}} \sqrt{\frac{E_{FRCM} k_b \sqrt{f'_{ck} f'_{ctm}}}{t_f}}$; $f'_{ctm} = 0.30 f'^{2/3}_{ck}$ $k_b = \left(\frac{2 - w_f/b}{1 - w_f/400}\right)^{0.5}$; $l_e = \left(\frac{E_{FRCM} t_f}{2 f_{ctm}}\right)^{0.5}$; $k_e = 0.5$ $b = \begin{cases} s_f, & \text{for strips} \\ 0.9d sin(\theta + \alpha_0)/sin\alpha_0, & \text{for continous} \end{cases}$ **Experimental value of effective strain:** $\varepsilon_{eff}^{exp} = \frac{V_{FRCM}^{exp}}{k_e E_{FRCM} \rho_f b_w d}$
Model 7 (Ombres, 2015b)***	$V_{FRCM} = F_z(V_m + V_{fb})$; $F_z = \frac{N_f w_f}{a} V_m = 2(0.17\sqrt{f'_{cm}} t_m d)$; $V_f = 2nA_f f_{fv} d = 2\rho_f b_w f_{fv} d$ $f_{fv} = E_{FRCM} \varepsilon_{eff}$; $\varepsilon_{eff} = \varepsilon_{FRCM} \leq 0.004$ **Experimental value of effective strain:** $\varepsilon_{eff}^{exp} = \frac{(V_{FRCM}^{exp}/F_z - V_m)}{2nA_f E_{FRCM} d}$

* D_f is the stress distribution coefficient; $f_{fed,max}$ is the maximum design stress of the jackets; β_l and β_w reflect the effect of the effective bond length and the concrete width ratio of the jacket; λ is the maximum bond length parameter; L_{max} and L_e are the available bond length and the effective bond length respectively; d_f is the effective height of the FRCM; z_b and zz_t are the co-ordinates of the top and bottom ends of the effective FRCM; d_{fb} is the distance from the compression face to the top edge of the FRCM; d_{ft} is the distance from the compression face to the lower edge of the jacket.

** k_e is the 'effectiveness coefficient', take 0.5; f_{fdd} is debonding strength; f'_{ck} is concrete characteristic cylindrical strength; f'_{ctm} is average tensile strength of concrete; γ_{fd} and γ_c are partial safety factor, which are taken as 1 in this chapter; k_b is the geometric coefficient; l_e is optimal bond length.

*** F_z is the ratio of the total length of the strengthened zone to the critical shear span; N_s is number of FRCM strips; a is the length of shear critical span.

2.3.1.1 Assessment of the Analytical Models for FRCM Jacketing Systems

The accuracy of the six models in predicting the shear strength of the composite system is assessed using the following statistical indices: the Average Value (μ_p), Standard Deviation (SD) and Coefficient of Variation (COV) of $v_{FRCM}^{exp}/v_{FRCM}^{pred}$, Mean Absolute Error (MAE) and Root Mean Square Error (RMSE) between v_{FRCM}^{exp} and v_{FRCM}^{pred}. The calculated m, SD, COV, RMSE, and MAE values for the models are presented in Table 2.3. COV, MAE and RMSE are calculated as follows:

$$\text{COV} = \frac{SD}{\mu_p} \tag{2-9}$$

$$\text{MAE} = \frac{\sum_{i=1}^{x} \left| v_{FRCM}^{pred}/v_{FRCM}^{exp} - 1 \right|}{N} \tag{2-10}$$

$$\text{RMSE} = \sqrt{\frac{\sum_{i=1}^{x} \left(v_{FRCM}^{pred}/v_{FRCM}^{exp} - 1 \right)^2}{N}} \tag{2-11}$$

Table 2.3. Results of the assessment of the analytical models 1-7 based on the selected statistical indices.

Type	Formula	Failure mode	No.	$v_{FRCM}^{exp}/v_{FRCM}^{pred}$			$v_{FRCM}^{pred}/v_{FRCM}^{exp} - 1$	
				μ_p	SD	COV	MAE	RMSE
Fibre-properties-based	Model 1	No detachment	20	0.60	0.35	0.58	1.22	1.58
		Detachment	75	0.84	1.06	1.26	1.95	3.21
		Total	95	0.79	0.96	1.19	1.80	2.95
	Model 2	No detachment	20	1.19	0.82	0.69	0.49	0.54
		Detachment	75	3.12	2.02	0.65	0.67	0.93
		Total	95	2.71	1.98	0.73	0.64	0.87
	Model 3	No detachment	20	1.18	1.11	0.94	0.73	1.01
		Detachment	75	8.06	5.43	0.67	0.75	0.79
		Total	95	6.64	5.61	0.84	0.75	0.85
	Model 4	No detachment	20	0.58	0.19	0.32	0.99	1.16
		Detachment	75	0.70	0.41	0.59	1.09	1.68
		Total	95	0.67	0.38	0.57	1.09	1.60
Composite-properties-based	Model 5	No detachment	14	2.12	2.80	1.32	1.00	2.01
		Detachment	45	2.61	1.30	0.50	0.54	0.58
		Total	59	2.50	2.05	0.83	0.65	1.10
	Model 6	No detachment	14	1.78	0.87	0.49	1.08	2.54
		Detachment	45	2.36	0.90	0.38	0.52	0.56
		Total	59	2.22	0.91	0.41	0.65	1.33
	Model 7	No detachment	14	1.05	2.80	2.67	1.43	3.32
		Detachment	45	1.61	0.93	0.58	0.60	0.74
		Total	59	1.47	2.05	1.39	0.79	1.74

2.3.1.2 Models Based on Fibre Properties

Figure 2.14 illustrates the relationship between v_{FRCM}^{pred} and v_{FRCM}^{exp} obtained by Models 1-4. Model 1 consistently overestimates the shear strength contribution of the FRCM jacket (μ_p = 0.79, SD = 0.96, COV = 1.19), regardless of whether failure is due to jacket detachment. This overestimation poses safety concerns for shear design, as it may result in unsafe structures. Moreover, Model 1 exhibits the highest Mean Absolute Error (MAE = 1.80) and Root Mean Square Error (RMSE = 2.95), indicating poor predictive performance. In contrast, Model 2 underestimates the shear contribution (μ_p = 2.71, SD = 1.98, COV = 0.73), which ensures structural safety but leads to inefficient designs, increasing material waste and costs. Notably, the average $v_{FRCM}^{exp}/v_{FRCM}^{pred}$ for beams with detachment (1.19) is lower than for those without detachment (3.12), highlighting reduced accuracy for the former failure mode. Model 3, developed as an improvement to Model 2 based on experimental data, was intended to address the

overestimation of shear strength observed in the previous model. However, the results revealed that the underestimation issue not only persisted but was further exacerbated. Consequently, this model exhibited the poorest predictive performance among the evaluated models (μ_p=6.64).The average value of $v_{FRCM}^{exp}/v_{FRCM}^{pred}$ for Model 4 is the smallest (0.67) among the 4 models, leading to an overestimation of the strength which is unconservative. However, the predicted values for the CFRCM strengthened beams that failed due to detachment are very close to the experimental ones (Fig. 2.14d).

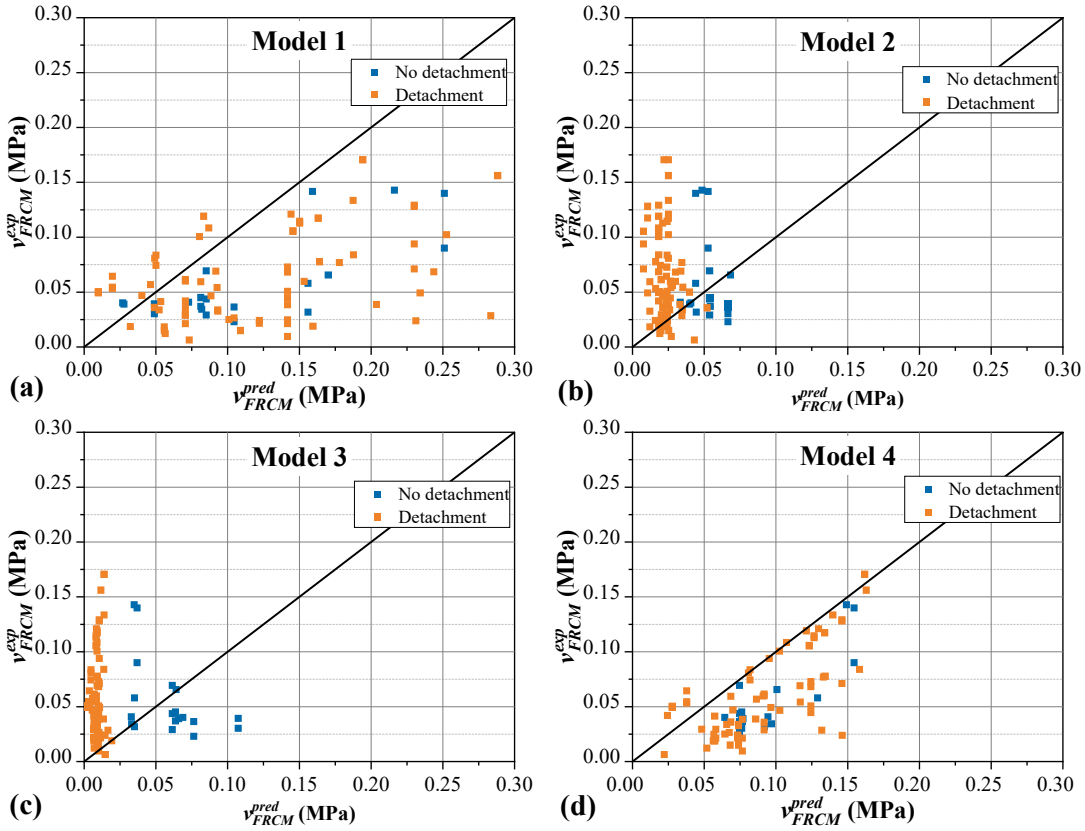

Fig. 2.14 Comparison between experimental, v_{FRCM}^{exp}, and predicted, v_{FRCM}^{pred}, shear strength for: (a) Model 1; (b) Model 2; (c) Model 3; (d) Model 4.

Figure 2.15 presents the experimental value of the fibre effective strain ε_{eff}^{exp} versus the predicted value of strain ε_{eff}^{pred} for Models 1-3, as well as their normalised experimental value of effective strain $\varepsilon_{eff}^{exp}/\varepsilon_{fu}$ versus $\rho_f E_f/f'^{2/3}_c$. Model 4 is not included since it is not based on ε_{eff}. Regarding ε_{eff}^{exp} versus ε_{eff}^{pred}, the effective strain of most beams in Model 1 is underestimated (Fig. 2.15a), which implies that ε_{eff} should be larger than $0.5\varepsilon_{fu}$. Although Model 2 used more detailed equations for ε_{eff},

the predicted values of effective strain are underestimated. Model 3 exacerbates this underestimation, aligning with its poor performance in predicting V_{FRCM}.

Since Models 1-3 share a same calculation model of ε_{eff}^{exp}, their normalised experimental effective strain values are identical. As shown in Fig. 2.15d, $\varepsilon_{eff}^{exp}/\varepsilon_{fu}$ has a remarkably decreasing trend as $\rho_f E_f / f'^{2/3}_c$ increases. Interestingly, for a small number of beams $\varepsilon_{eff}^{exp}/\varepsilon_{fu}$ exceeds 1, which implies that the effective strain is larger than the rupture strain which is not realistic since ε_{eff}^{exp} should be a portion of ε_{fu}. This is attributed to the fact that ε_{eff}^{exp} is not measured but it results after the implementation of Models 1-3 for $V_{FRCM}^{exp} (= V_{JAC}$ see Table A).

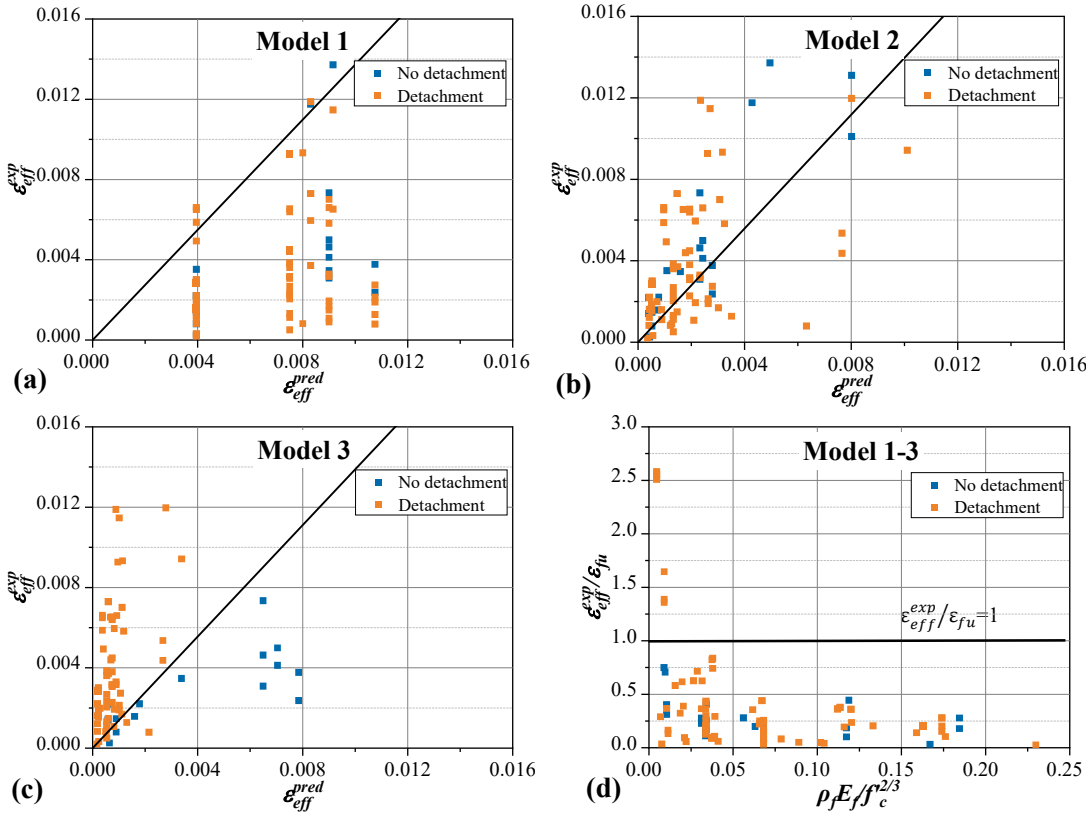

Fig. 2.15. ε_{eff}^{exp} versus ε_{eff}^{pred}: (a) Model 1, (b) Model 2, (c) Model 3; (d) Normalised experimental effective strain, $\varepsilon_{eff}^{exp}/\varepsilon_{fu}$ versus $\rho_f E_f / f'^{2/3}_c$

In summary, Model 1 overestimates the shear strength contribution of the FRCM jacket, resulting in the highest MAE and RMSE values among all models. Model 4 also overestimates shear strength but achieves more accurate predictions for beams failing due to detachment. Models 2 and 3, on the other hand, underestimate the FRCM shear contribution. While this ensures structural safety, it results in inefficient designs,

leading to unnecessary material use and increased costs. Model 3, despite being an attempted improvement, demonstrated the poorest predictive performance overall, emphasizing the need for further refinement in these models.

2.3.1.3 Models Based on FRCM Composite Properties

Since many of the studies included in the database do not provide information on the elastic modulus of the FRCM composite, only 59 beams from the database are used to compare the experimental, v_{FRCM}^{exp}, with the predicted shear stress values, v_{FRCM}^{pred}, using Models 5-7 (Table 2.2) as shown in Fig. 2.16.

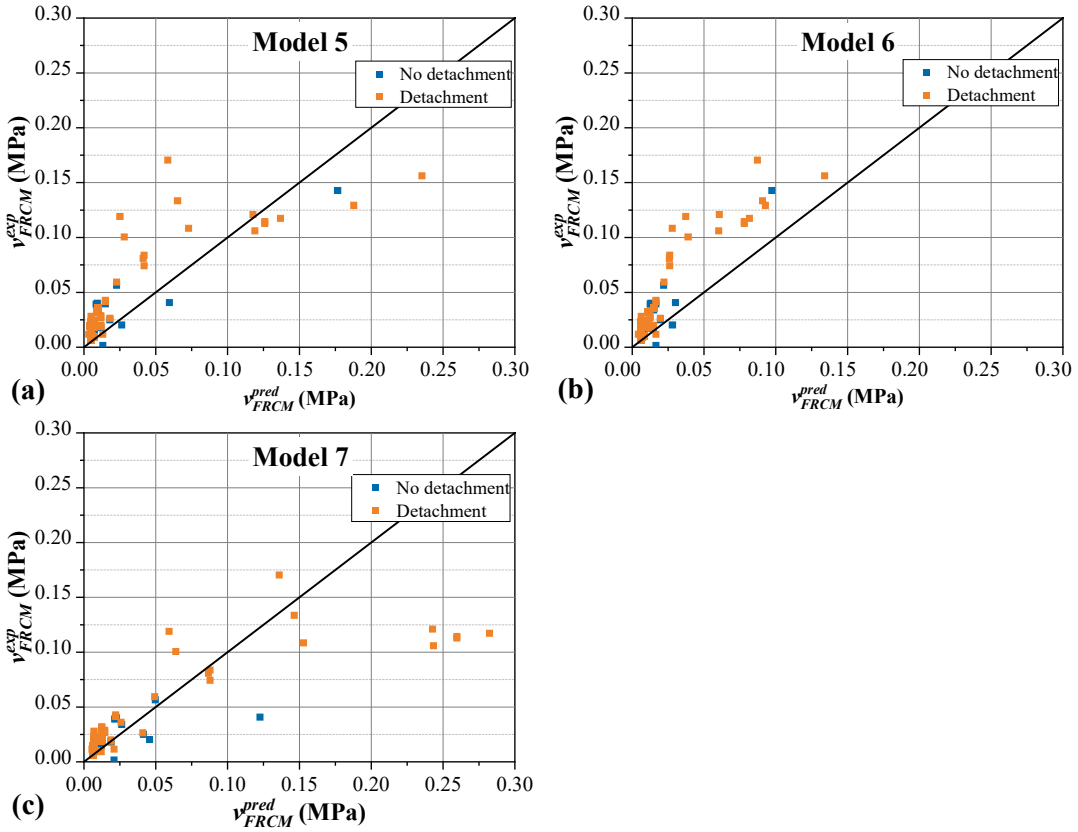

Fig. 2.16. Comparison between experimental, v_{FRCM}^{exp}, and predicted, v_{FRCM}^{pred}, shear strength for: (a) Model 5; (b) Model 6; (c) Model 7.

As observed in Table 2.3, Model 5 reaches average $v_{FRCM}^{exp}/v_{FRCM}^{pred}$ ratio (μ_p) of 2.50, SD of 2.05, and COV of 0.83. Fig. 2.16a demonstrates that Model 4underestimates the predicted shear strength. This may be attributed to the low value of the effective strain of the fibre considered (limited to $\varepsilon_{eff}^{pred} = 0.004$, see also Fig. 2.17a where ε_{eff}^{exp} is compared to ε_{eff}^{pred}). Model 7 illustrates the shear strength provided by FRCM system can be calculated by summarizing the contribution of the textile and

the associated mortar. Model 6 has μ_p of 1.48, SD of 2.05 and COV 1.39. As seen in Fig. 2.16c, in most of the cases the model underestimates the shear strength of the strengthened beams. Model 6 has a similar behaviour with Models 5 and 7.

Figure 2.17 depicts the experimental value of the fibre effective strain, ε_{eff}^{exp}, versus the predicted value, ε_{eff}^{pred}, as well as the normalised experimental value of effective strain $\varepsilon_{eff}^{exp}/\varepsilon_{fu}$ versus $\rho_f E_f / f'^{2/3}_c$ for Models 5-7 Fig. 2.17(d-f) suggests similar to Models 1 and 2 that, $\varepsilon_{eff}^{exp}/\varepsilon_{fu}$ decreases with the increase of $\rho_f E_{FRCM}/f'^{2/3}_c$. $\varepsilon_{eff}^{exp}/\varepsilon_{fu}$ is almost always greater than 0.25 and $\rho_f E_{FRCM}/f'^{2/3}_c$ is less than 0.05 for nearly all non-detachment failed beams. The high consistency of these models verifies that $\rho_f E_{FRCM}/f'^{2/3}_c$ has an influence on ε_{eff}, which is also affected by the failure mode of the beam. The strengthened beams with $\varepsilon_{eff}^{exp}/\varepsilon_{fu}$>1 correspond to 8.4%, 55.9% and 22.0% (5, 33 and 13 beams) in case of Models 5-7. As discussed in section 3.1.1.1, ε_{eff}^{exp} is not measured but it is defined after implementing Models 5-7 for V_{FRCM}^{exp}(= V_{JAC} see Table A).

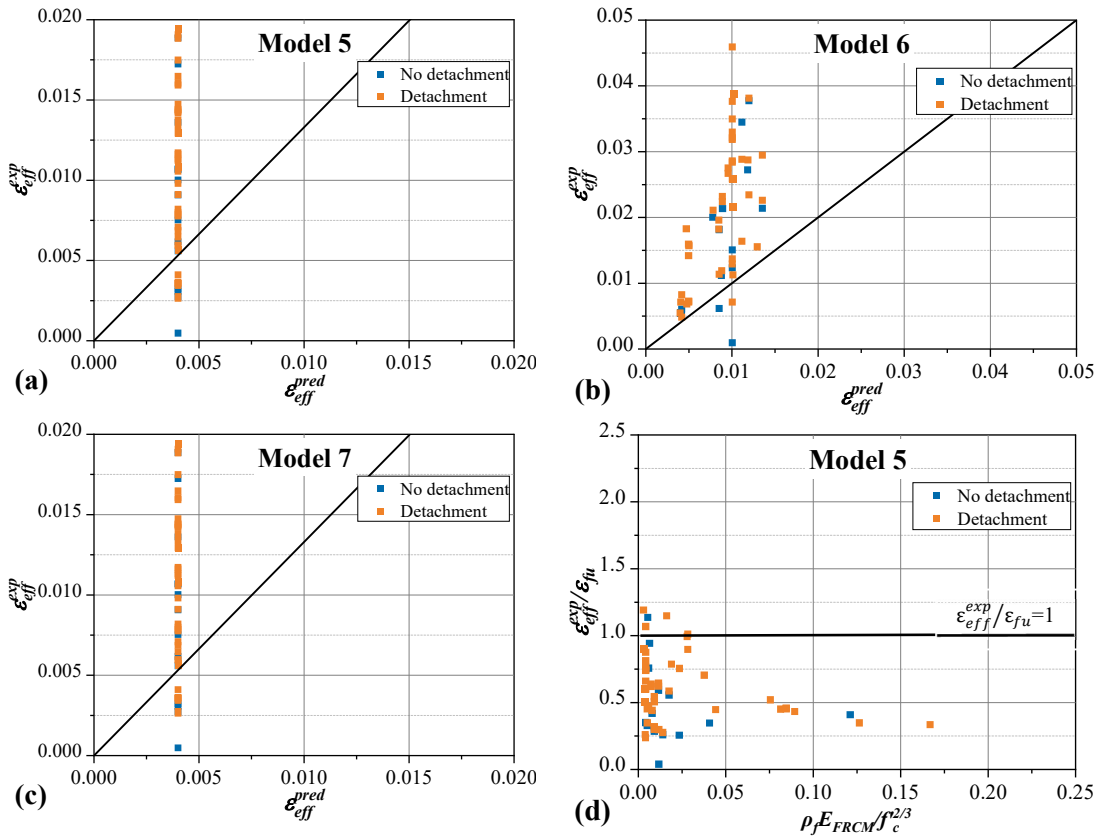

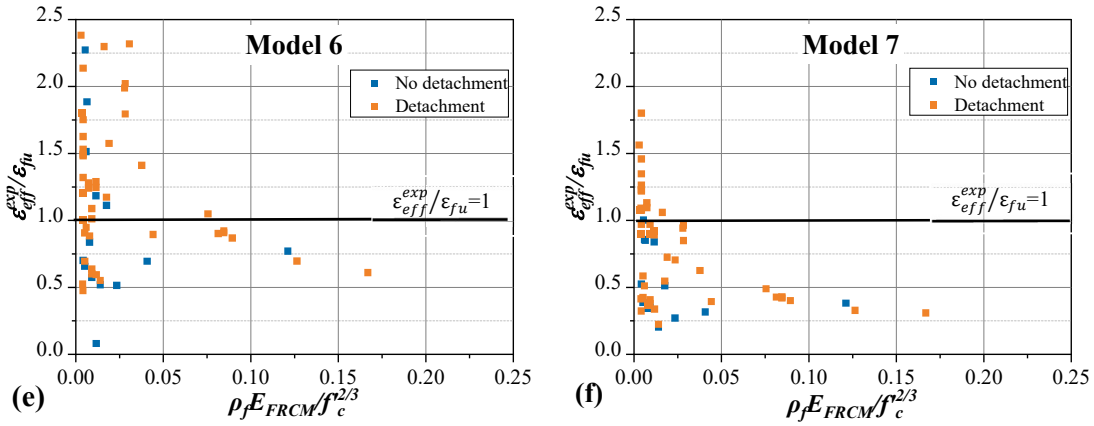

Fig. 2.17. ε_{eff}^{exp} verse ε_{eff}^{pred}: (a) Model 5, (b) Model 6, (c) Model 7; Normalised experimental effective strain, $\varepsilon_{eff}^{exp}/\varepsilon_{fu}$, versus $\rho_f E_{FRCM}/f'^{2/3}_c$: (d) Model 5, (e) Model 6, (f) Model 7.

When v_{FRCM}^{exp} is less than 0.5, Figures 2.16 and 2.17 highlight that Models 5-7, which are based on the properties of the composite material, outperform Models 1-4, which rely on fibre properties. This is particularly evident when the detachment failure occurs. However, when considering the entire range, Models 5-7 do not exhibit a significant advantage over Models 1-4 in terms of MAE and RMSE. Consequently, the existing models are unable to provide accurate predictions for the shear strength contribution of FRCM.

2.3.2 Analytical Models for FRC Jacketing Systems

The total shear strength of fibre-reinforced-cement system strengthened RC beams (V_{shear}) comprises shear strength contributions from concrete (V_C), steel stirrups (V_S) and FRC jacket (V_{FRC}):

$$V_{shear} = V_C + V_s + V_{FRC} \tag{2-12}$$

V_{FRC} is calculated according to ACI 544 (2018), *fib* Model Code (2010) and the Japan Society of Civil Engineers (JSCE) (2007) design codes that are presented in Table 2.4. The same models can also be found in Yin et al. (2018). In case of Models 8 and 9, V_C is defined by Eqs. 2-5 and 2-6, respectively, whereas V_s is defined according to Eq. 2-7. For Model 10, V_c is given by JSCE (2006):

$$V_C^{JSCE} = \beta_d \beta_p \beta_n f_{vcd} b_w d/\gamma_b \tag{2-13}$$

where $f_{vd,FRC} = 0.3f_{c,FRC}^{2/3}/\gamma_c$ is the design average tensile strength perpendicular to diagonal cracks; $f_{vcd} = 0.2\sqrt{f_c}$; $\beta_d = \sqrt[4]{\frac{1000}{d}} \leq 1.5$; $\beta_p = \sqrt[3]{100\rho_{long}} \leq 1.5$; $\beta_n = 1$ for the member without axial compressive force.

The experimental and the predicted normalised shear stress of the FRC jacketing system, v_{FRC}^{exp} and v_{FRC}^{pred}, are calculated from:

$$v_{FRC}^{exp} = \frac{V_{FRC}^{exp}}{b_w d f_c'}; v_{FRC}^{pred} = \frac{V_{FRC}^{pred}}{b_w d f_c'} \quad (2\text{-}13)$$

where $V_{FRC}^{exp} (= V_{JAC}$ see Table A) is the experimental shear strength provided by FRC jackets; V_{FRC}^{pred} is predicted the shear strength provided by FRCM jacket which is calculated by Models 8-10.

Table 2.4. Analytical models to predict $\boldsymbol{V_{FRC}}$

Reference	Formula
Model 8 (ACI 554, 2018)*	$V_{FRC} = \frac{2}{3} f_{ct,FRC} \left(\frac{a}{d}\right)^{0.25} b_{w,FRC} d_{FRC}$
Model 9 (*fib* Code, 2010)**	$V_{FRC} = 18 b_{w,FRC} d_{FRC} k \left[100\rho_{long}\left(1 + 7.5\,\frac{f_{Ftuk}}{f_{ct,FRC}}\right) f'_{c,FRC}\right]^{1/3}$
Model 10 (JSCE, 2007)***	$V_{FRC} = V_m + V_F = \frac{0.18\sqrt{f'_{c,FRC}} b_{w,FRC} d_{FRC}}{\gamma_b} + \frac{(f_{vd,FRC}/\tan\alpha) b_{w,FRC} z}{\gamma_b}$

*Where $f_{ct,FRC}$ is the tensile strength of FRC jacket, taken as $0.3f'^{2/3}_{c,FRC}$; $f'_{c,FRC}$ is the compressive strength of FRC jacket; $b_{w,FRC}$ is the width of the jacket; d_{FRC} is the effective depth of the jacket;
**k is the is the size effect factor, taken as $1 + \sqrt{200/d_{FRC}} \leq 2.0$; f_{Ftuk} is the characteristic value of the final residual tensile strength of FRC obtained from the crack opening (1.5mm), and $f_{Ftuk}/f_{ct,FRC}$ would be taken as 0.62 (Gowripalan and Gilbert, 2000);
***where $V_{c,FRC}$ is shear strength contributions from concrete in FRC; $V_{f,FRC}$ is shear strength contributions from fibre in FRC; Where $f_{vd,FRC} = 0.3f_{c,FRC}^{2/3}/\gamma_c$ is the design average tensile strength perpendicular to diagonal cracks.

In the case of the ECC-R jacketed beams (13 specimens), Models 8-10 cannot be used to assess this system (Bywalski et al., 2020). Additionally, due to missing information, the beams in the research of Garg et al. (2019), Sakr et al. (2018), and Sakr et al. (2019) were not used. In total 39 beams were used to calculate m, SD, COV

of $v_{FRC}^{exp}/v_{FRC}^{pred}$, as well as MAE, RMSE of $v_{FRC}^{pred} - v_{FRC}^{exp}$ as presented in Table 2.5. Figure 2.18 illustrates the relationship between v_{FRC}^{pred} and v_{FRC}^{exp} for Models 8-10.

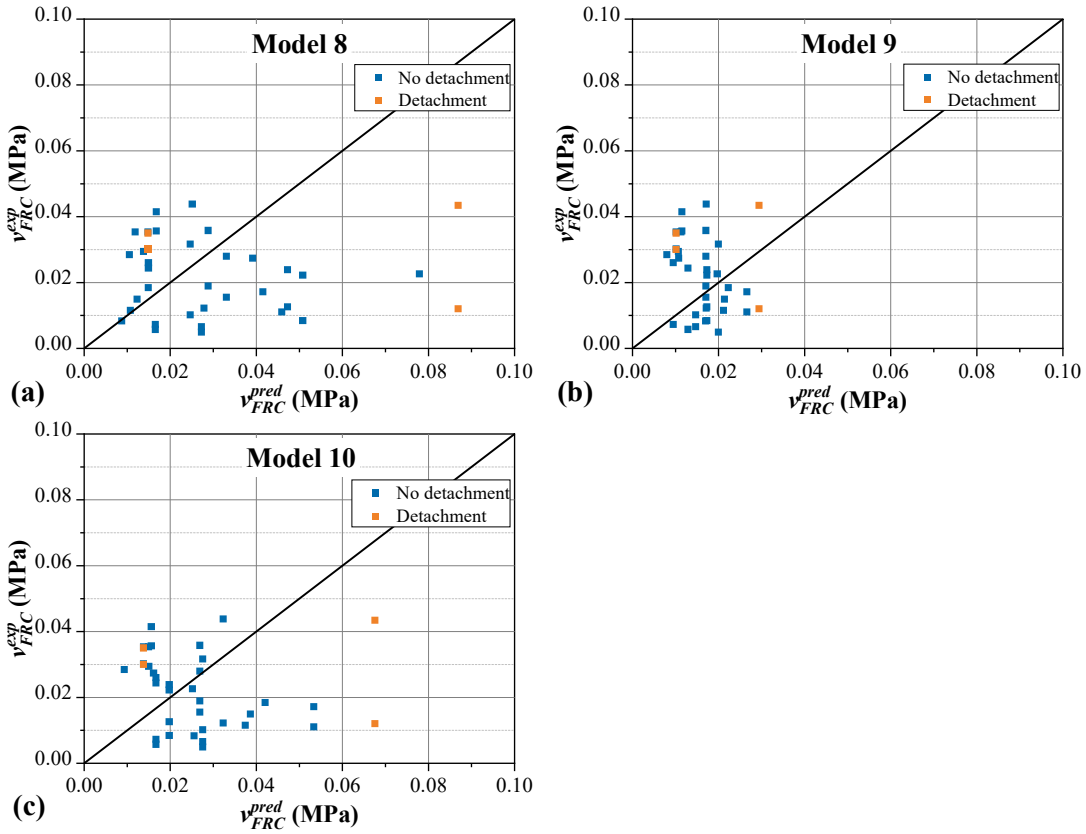

Fig. 2.18. Comparison between experimental, v_{FRC}^{exp} and predicted, v_{FRC}^{pred}, shear strength for: (a) Model 8; (b) Model 9; (c) Model 10.

Table 2.5. Results of the assessment of the analytical Models 8-10 based on the selected statistical indices.

Model	Number	$v_{FRC}^{exp}/v_{FRC}^{pred}$			$v_{FRC}^{pred}/v_{FRC}^{exp} - 1$	
		m	SD	COV	MAE	RMSE
Model 7	39	1.11	0.84	0.76	1.20	1.86
Model 8	39	1.63	1.11	0.68	0.63	0.82
Model 9	39	1.13	0.85	0.75	1.10	1.61

Each of Models 8, 9, 10 rely on a different parameter to assess the shear strength contributed by the FRC system. Specifically, Model 8 considers the influence of the shear span ratio, Model 9 introduces the characteristic value of the final residual tensile strength of the FRC obtained by considering a crack opening equal to 1.5mm, and Model 10 considers that the shear strength of the FRC comprises the shear strength of concrete and the shear strength of the fibres. Even though μ is larger than 1 in all models, still there is a certain number of beams where v_{FRC}^{exp}<v_{FRC}^{pred} (Model 8: 20 beams,

Model 9: 16 beams, Model 10: 18). Models 8 and 10 seem to be equivalent. However, the dispersion is high in all models, leaving much room for the development of more reliable formulas for the various FRC strengthening systems.

Building upon the preceding discussion, Table 2.6 summarises the fundamental assumptions and configuration sensitivity of Models 1–10. This comparative analysis underscores the necessity for developing balanced models capable of simultaneously accounting for both jacketing configuration and bond-dependent behaviour.

Table 2.6. Key assumptions and performance trends of Models 1–10.

	Model	Reference	Key Distinction	Performance
FRCM	1	Triantafillou & Papanicolaou (2006)	Truss analogy; constant $\varepsilon_{eff} = 0.5\varepsilon_{fu}$; no configuration sensitivity.	Overestimation
	2	Escrig et al. (2015)	Fibre property-based; ε_{eff} depends on f_c, E_f , an ρ_f ; considers different wrap configurations.	Underestimation
	3	Thermou et al. (2019)	Fibre property-based; refines Model 2 by adding term for undamaged textiles; considers wrap types.	Significant underestimation
	4	Tetta et al. (2018b)	Fibre property-based; replaces ε_{eff} with jacket stress; wrap type not explicitly included.	Slight overestimation
	5	ACI 549.4R-13 (2013)	Composite property-based; constant ε_{eff} = 0.004; applies to continuous wraps only	Underestimation
	6	Younis et al. (2017)	Composite property-based; adds bond length and effectiveness factor; wrap type considered.	Underestimation
	7	Ombres (2015b)	Composite property-based; expands on Model 5 by explicitly accounting for debonding strength and optimal bond length.	Slight Underestimation
FRC	8	ACI 544 (2018)	Uses empirical formula incorporating a/d and tensile strength of FRC.	Slight Underestimation
	9	fib Model Code (2010)	Includes fibre residual strength and compressive strength.	Underestimation
	10	JSCE (2007)	Combines concrete and fibre contributions with β-coefficients for geometry and reinforcement.	Slight Underestimation

2.4 Conclusions and Research Gaps

This chapter has systematically reviewed the current state of research on mortar-based composites for shear strengthening of RC beams. The findings confirm that mortar-based composites can effectively improve the shear strength of beams and serve as reinforcement materials for beams. Among them, FRCM jacketing systems have been shown to increase shear strength by 4% to 196% (average: 61%), while other mortar-based composite systems demonstrate enhancements ranging from 4% to 190%

(average: 80%). Among these, CFRCM systems are the most commonly used, accounting for over 50% of tested beams, with a maximum reported shear strength improvement of 196%. Comparatively, PFRCM systems exhibit lower effectiveness under similar axial stiffness conditions.

U-shaped jacketing is the most widely adopted configuration (74% of beams), with delamination of the jacket being the predominant failure mode. Alternative anchorage systems discussed in the literature effectively mitigate delamination for most configurations, though near-surface-mounted (NSM) anchoring appears to be less effective. For side-bonded beams, even with anchorage systems, delamination remains the primary failure mode. Conversely, fully wrapped jackets not only prevent delamination but also shift the failure mode from shear to flexural, often resulting in fibre rupture.

Despite these advancements, significant research gaps remain. The majority of studies have focused on CFRCM systems under static loading conditions, with limited exploration of alternative materials such as SRG and HPFRC. Critical parameters influencing the performance of these materials, including textile density, mortar properties, and reinforcement configurations, have not been comprehensively investigated. Additionally, there is a lack of comparative studies evaluating the performance of SRG and HPFRC systems against other FRCM materials, hindering a holistic understanding of their relative efficiency and application potential.

Another notable gap lies in the absence of research on the fatigue performance of mortar-based composites. While durability under cyclic loading is a critical factor for infrastructure such as bridges, the fatigue behaviour of FRCM systems remains largely unexplored. This lack of understanding limits their application in environments where long-term performance under repeated loading is essential.

Existing predictive models for the shear capacity contribution of FRCM systems also exhibit substantial limitations. Many models fail to incorporate key parameters such as the shear span-to-depth ratio, mortar thickness, and the interaction between internal and external reinforcement systems. These factors have been shown to significantly influence strengthening performance, and their omission results in inconsistent predictions and reduced reliability. Furthermore, while effective strain limits for fibres are recognised as a critical parameter for defining failure mechanisms,

such as fibre rupture or delamination, they remain insufficiently defined in the current models. This restricts the development of accurate and robust predictive tools for practical design applications.

Addressing these gaps will advance the understanding and application of mortar-based composite systems for RC beam strengthening, particularly under varying loading conditions. Future research should focus on these areas to enhance the reliability and efficiency of these innovative strengthening techniques.

Chapter 3

Effectiveness of SRG Jackets in Shear Strengthening of RC Beams under Monotonic Loading

As discussed in Chapter 2, research on the shear performance of Steel Reinforced Grout (SRG) strengthened beams remains limited, particularly in terms of comprehensive comparisons with other strengthening systems. The effects of SRG on failure mode transitions and energy dissipation have yet to be thoroughly investigated, leaving gaps in understanding its full potential and limitations.

Furthermore, considering the significant role of the shear span-to-depth ratio (*a/d*) in influencing shear transfer mechanisms, failure modes, and retrofitting efficiency—and the conflicting findings in existing literature—this chapter investigates the efficiency of SRG jacketing in enhancing the shear strength of deficient deep (*a/d* = 2) and slender (*a/d* = 3.5) RC beams under monotonic loading. For comparison, the performance of Carbon Fiber Reinforced Cementitious Matrix (CFRCM) and Steel Reinforced Polymer (SRP) strengthening systems is also evaluated.

The experimental program involves 17 asymmetrically loaded beams, with key parameters studied including *a/d* (2 and 3.5), matrix type (resin or mortar), textile type

(steel and carbon), number of textile layers (1-3 layers), density of UHTSS textile (1.57 and 3.14 cords/cm) and jacketing configurations (U-shaped and fully wrapped). Results indicate that all strengthening systems are effective, with fully wrapped SRP and SRG systems being particularly successful in shifting the failure mode from shear to flexure.

3.1 Experimental Programme

3.1.1 Specimen Details

The experiments included 17 rectangular RC beams tested under three-point bending monotonic loading using a simply supported configuration. In contrast to four-point bending, which generates a region of pure bending between the loading points, the three-point setup concentrates shear forces within a single shear span, making it more appropriate for investigating shear-related failure mechanisms. This configuration also produces a maximum bending moment at mid-span, allowing precise observation of crack initiation and propagation at a critical location. In addition, the simplified load path and test arrangement enhance repeatability, while the clearer stress distribution facilitates the interpretation of shear-dominated responses. This simplification further aids in decoupling shear effects from flexural behaviour, enabling a more accurate assessment of the beam's shear performance (Mujika, 2007).

The total length is 1677 mm (660 inch), the effective span is 1100 mm, and the breadth × height is 102 mm × 203 mm (40 inch × 80 inch). Two different shear span ratios (a/d) of 2.0 and 3.5 were investigated (Beam series A and B, respectively). Beams with $a/d \leq 2.5$ fall into the classification of deep beams, whereas those exceeding 2.5 are categorised as slender beams (Shear and Torsion, 1998; Shafieifar et al., 2018; Jung and Kim, 2008). To directly evaluate the effectiveness of the SRG and other jacketing systems (such as SRP and CFRCM) considered in this study, no internal transverse reinforcement was included in the critical span (a=350 mm for Series A and a=620 mm for Series B). The remaining span contained 8 mm diameter stirrups spaced at 140 mm and 40 mm for Series A and Series B beams, respectively (Fig. 3.1a). Based on cross-sectional analysis and moment distribution considerations, it was ensured that the shear failure load in the unstrengthened region significantly exceeds the corresponding flexural capacity, thus preventing premature shear failure

outside the strengthened zones. All beams had tensile and compressive longitudinal reinforcements equal to 2 ∅16 and 2 ∅10, respectively (Fig. 3.1b).

The specimen dimensions were selected considering laboratory constraints and established scaling principles for reinforced concrete beam testing, informed by previous studies under comparable conditions (e.g., Tetta et al., 2018a; Wang et al., 2020b). Although these beams were scaled down compared to structural members used in practical applications, literature indicates that maintaining geometric similarity enables observed failure modes, crack patterns, and shear mechanisms in scaled tests to remain relevant to full-scale behaviour, despite inherent size effects related to energy dissipation, fracture mechanics, and aggregate interlock mechanisms (Bazant and Yu, 2005; Carpinteri et al., 1999). Therefore, the present experimental results provide valuable insights into the shear strengthening mechanisms of reinforced concrete beams, facilitating meaningful extrapolation to predict the shear performance of larger, full-scale structural components.

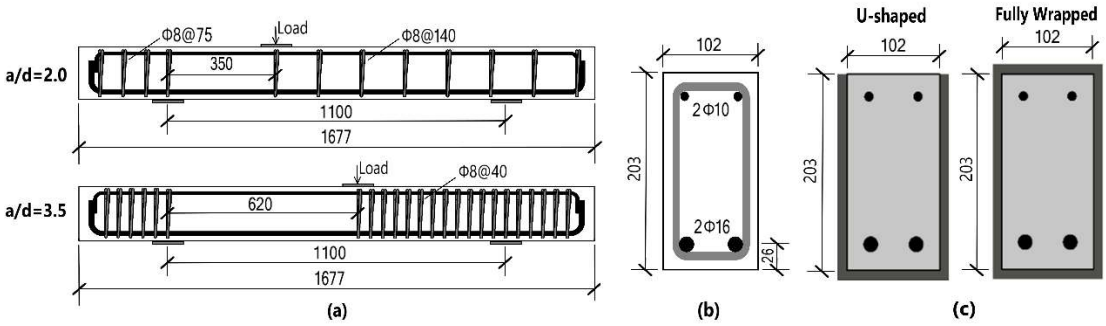

Fig. 3.1. (a) Layout of the reinforcement; (b) Cross section; (c) Jacket configurations.

The key parameters of this study include the: (i) shear span-to-depth ratios (2.0 and 3.5), (ii) composite strengthening systems, namely SRG, SRP, CFRCM, (iii) density of ultra-high tensile strength steel (UHTSS) textiles, 1.57 and 3.14 cords/in (low density and high density, respectively), (iv) number of textile layers (1-3 layers), and (v) strengthening configuration (fully wrapped and U-wrapped jackets) (Fig. 3.1c).

The details of the beams tested are shown in Table 3.1. The code name given to the specimens corresponds to X-YZ-Qi, where 'X' is equal to A or B corresponding to the beam with a/d = 2 or 3.5, respectively. 'Y' indicates the material used for the beam jacketing with N corresponding to non-strengthening, 'G' to SRG jacketing, 'P' to SRP jacketing, and 'C' to CFRCM jacketing. In case of SRP and SRG jacketing, 'Z' is equal

to 'L' or 'H' which corresponds to the low- (1.57 cords/cm) or high-density (3.14 cords/cm) UHTSS textiles, respectively. 'Q' refers to the jacket configuration ('U' and 'W' for U-shaped and fully wrapped jackets, respectively) and 'in' to the number of layers ('1', '2', and '3' for 1, 2 and 3 layers, respectively). For example, B-GH-U2 is a beam with *a/d* = 3.5 strengthened with two-layered U-shaped SRG jackets of 3.14 cords/cm density textile.

The comparison of shear strengthening performance among different systems can rely on their axial stiffness which is defined as (Mandor and El Refai, 2022; Al-Jaberi and Myers, 2023; Cakir et al., 2023):

$$S_f = \rho_f E_f \tag{3-1}$$

where ρ_f $(= 2nt_f w_f / b_w s_f)$ is the fibre reinforcement ratio; n is the number of textile layers applied; t_f is the thickness of the textile; w_f is the width of FRCM strips; and s_f is the longitudinal distance of FRCM strips; b_w is the width of the cross-section; and E_f is the elastic modulus of the textile.

As shown in Table 3.1, all SRG and SRP systems, whether high or low density UHTSS textiles were used, had almost identical axial stiffness, allowing direct comparison between them. In addition, the two-layered CFRCM exhibited lower S_f than SRGs, whereas in case of the three-layered CFRCM is higher.

Table 3.1. Specimen details

Specimens	f'_c (MPa)	Strengthening System	Strengthening Configuration	n	ρ_f (‰)	E_f (GPa)	S_f (MPa)
Series A (*a/d* = 2.0)							
A-N	26.4	Control beam	-	-	-	-	-
A-GL-U2	26.7	SRG	U	2	3.29	190	625.10
A-GL-W2	26.6	SRG	FW	2	3.29	190	625.10
A-GH-U1	28.5	SRG	U	1	3.31	190	628.90
A-GH-W1	27.3	SRG	FW	1	3.31	190	628.90
A-PH-U1	28.2	SRP	U	1	3.31	190	628.90
A-PH-W1	25.7	SRP	FW	1	3.31	190	628.90
A-C-U2	29.4	CFRCM	U	2	1.88	252	473.76
A-C-W2	30.5	CFRCM	FW	2	1.88	252	473.76
A-C-U3	33.3	CFRCM	U	3	2.82	252	710.64
A-C-W3	32.0	CFRCM	FW	3	2.82	252	710.64
Series B (*a/d* = 3.5)							
B-N	24.2	Control beam	-	-	-	-	-
B-GL-U2	24.7	SRG	U	2	3.29	190	625.10
B-GH-U1	26.3	SRG	U	1	3.31	190	628.90
B-PH-U1	25.0	SRP	U	1	3.31	190	628.90

B-C-U2	26.0	CFRCM	U	2	1.88	252	473.76
B-C-U3	25.9	CFRCM	U	3	2.82	252	710.64

Note: f_c = concrete compressive strength on the test day; n = number of textile layers; ρ_f = fibre reinforcement ratio, $2nt_f w_f / b_w s_f$; t_f = textile thickness; w_f is the width of FRCM strips; $s_f$is the longitudinal distance of FRCM strips; E_f = elastic modulus of bare fibres; $\rho_f E_f$ = axial stiffness of strengthening systems.

3.1.2 Material Properties

The specimens were all cast using the same concrete grade. To determine the concrete compressive strength, three 150 mm concrete cubes were tested on the day of beam testing, and the average value was taken. The concrete compressive strength testing was conducted in accordance with BS EN 12390-3 (2013). Table 3.1 presents the concrete compression strength for each specimen. In the beams, the yield stresses for the 16 mm- and 10 mm-diameter longitudinal bars were 508 MPa and 538 MPa, respectively. Additionally, the yield stress of the 8 mm-diameter stirrups was measured at 326 MPa. The tensile strength of the steel reinforcement was determined based on ISO 15630–1 (2019) and ISO 6892–1 (2009). The representative tensile stress-strain curves for the tested reinforcement bars (16 mm-, 10 mm-diameter longitudinal bars, and 8 mm-diameter stirrups) are presented in Fig. 3.2.

The same inorganic binder was used in both SRG and FRCM systems which comprised an eco-friendly mineral geo-mortar with a crystalline reaction geo-binder base that only needs to be mixed with water (water-cement ratio 1:5) for use. Its 28-day average bending strength, compressive strength, and bond strength measured according to EN 196-1 (2005), EN 12190 (2013), and EN 1542 (1999a), respectively, were reported by the manufacturer to be 8 MPa, 5 MPa, and 2 MPa.

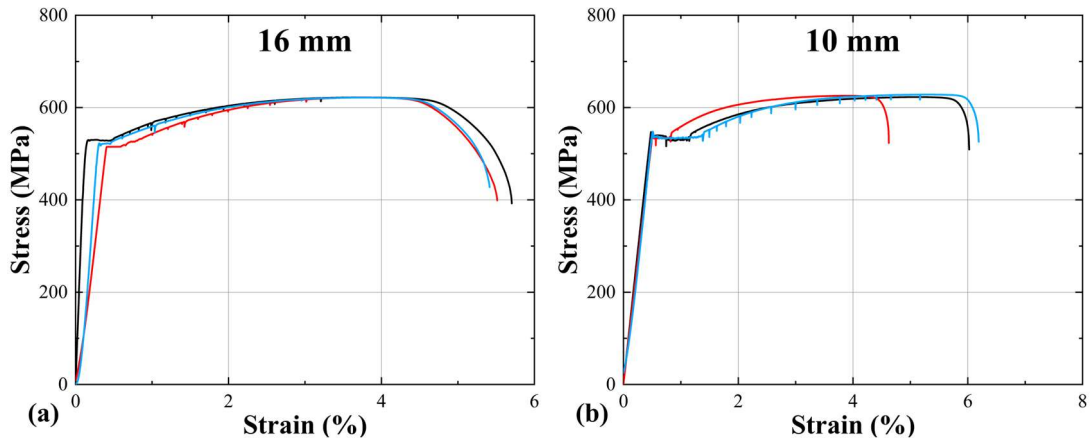

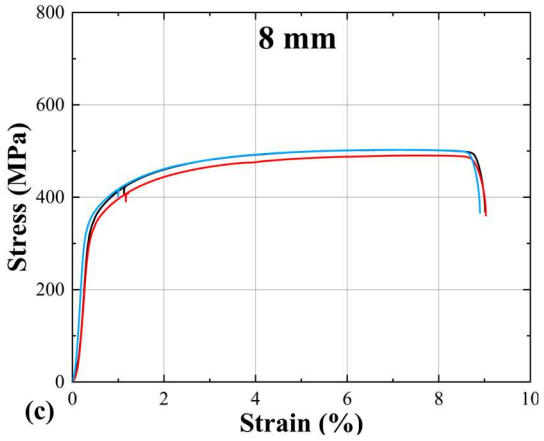

Fig. 3.2. Tensile stress-strain curves of steel reinforcement bars.

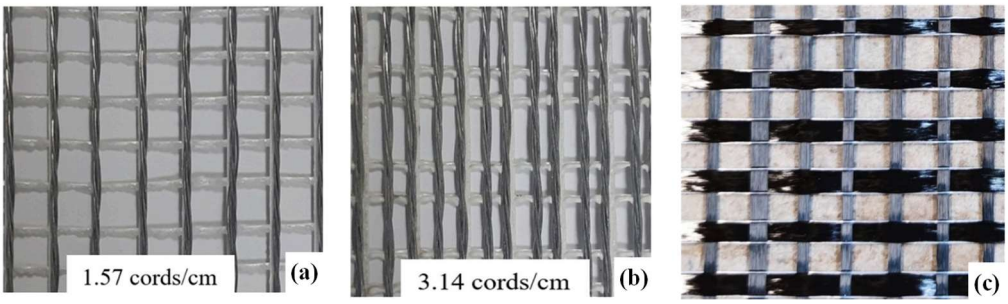

Fig. 3.3. The three types of textiles used in this study: (a) low-density UHTSS textile; (b) high-density UHTSS textile; (c) carbon textile.

Table 3.2. Properties of the textiles

	t_f (mm)	Weight (g/m^2)	A (mm^2)	Density (Cords/cm)	$f_{fu,f}$ (MPa)	E_f (GPa)	ε_{fu} (%)
Steel-Low density	0.084	670	0.538	3.14	3000	190	1.5
Steel-High density	0.169	1200	0.538	1.57	3000	190	1.5
Carbon (10mm×10mm)	0.048	170	-	-	-	252	2.0

A = cord area; $f_{fu,f}$ = tensile strength; ε_{fu} = fibre's strain to failure

Table 3.3. Properties of the mortars and resin

	Mixture Density (kg/cm^3)	f_{cm} (MPa)	f_f (MPa)	f_b (MPa)	E_f (GPa)
Mortar	2050	50	8	2	22
Resin	1600	-	-	14	5.3

f_{cm} = compressive strength (28 d); f_f = flexural strength (28 d); f_b = bond strength (28 d).

Galvanised unidirectional Ultra-high-tensile-strength steel (UHTSS) textiles were used which comprised high strength steel 3×2 cords attached to a fibreglass micromesh for easy installation. The fibreglass micromesh held the cords in place without adding strength to the composite system (Thermou et al., 2019). Each cord was made by five

twisted wires, among which two filaments wrapped three straight filaments at a high twist angle (see Fig. 3.3). The geometric and mechanical properties of a single cord are shown in Table 3.2 as provided by the manufacturer. This experimental study explored two different densities of 1.57 and 3.14 cords/cm, and the equivalent thicknesses per unit width of a single-layer steel fabric, t_f, were 0.084 mm and 0.169 mm respectively (see Table 3.2). The spacing between successive cords (i.e. density of the textile) is considered a key design parameter for the successful application of the SRG system, since it controls the flow of the cementitious grout through the steel textile and thus determines the quality of the bond between the textile and the matrix. The density should be such as to allow uninhibited flow of the cementitious grout through the steel textile. In case of the SRP systems, the matrix used was a high wettability epoxy mineral adhesive, consisting of two parts mixed in a ratio of 1:3. (Table 3.3). The carbon textile used in the CFRCM system was a square grid made of high-strength carbon fibre with a mesh size of 10×10mm and an equivalent thickness of 0.048 mm. The mechanical properties of the carbon textile utilised are presented in Table 3.2. According to the manufacturer, the compressive strength of the mortar was tested based on EN 12190 (1999b), and the tensile properties of the fabric were tested based on EN 2561 (1995).

3.1.3 Strengthening Procedure

Except for the control beams, the rest of the beams were strengthened in the shear critical region. Figure 3.4 presents the basic steps of the SRG jacketing application. The application procedure for the SRP and SRG/FRCM jacketing systems was similar, except for the critical region preparation step. In the case of SRG/FRCM application, the critical region was roughened before jacket installation, whereas this step was not required for SRP jacketing. U-shaped and fully wrapped jackets were applied, whereas the number of textile layers varied from 1 to 3 layers. It should be noted that in the fully wrapped jacket, the fabric was continuous; while in the U-shaped jacket, each layer was applied individually.

As shown in Fig. 3.4a, UHTSS textiles due to their high stiffness were pre-bent to facilitate the application. The edges of the beam's cross section were not rounded; hence the textile was bent at right angles (Thermou et al., 2019). Regarding the FRCM system, the surface of the beam was roughened, cleaned, and saturated with water prior

to mortar application (Fig. 3.4b). The mortar matrix was applied manually with a trowel directly onto the lateral surface of the specimens. Then, the textile was placed immediately after the application of the mortar. The mortar was squeezed out between the steel fibres by applying pressure manually. After applying the first layer of textile, the next layers were applied following the same procedure. To strengthen the beams, each layer of mortar was applied with a thickness of 2-3 mm, while the resin layer was applied with a thickness of approximately 1 mm. In case of FRCM and SRG applications, the strengthened area was wrapped with plastic film for curing.

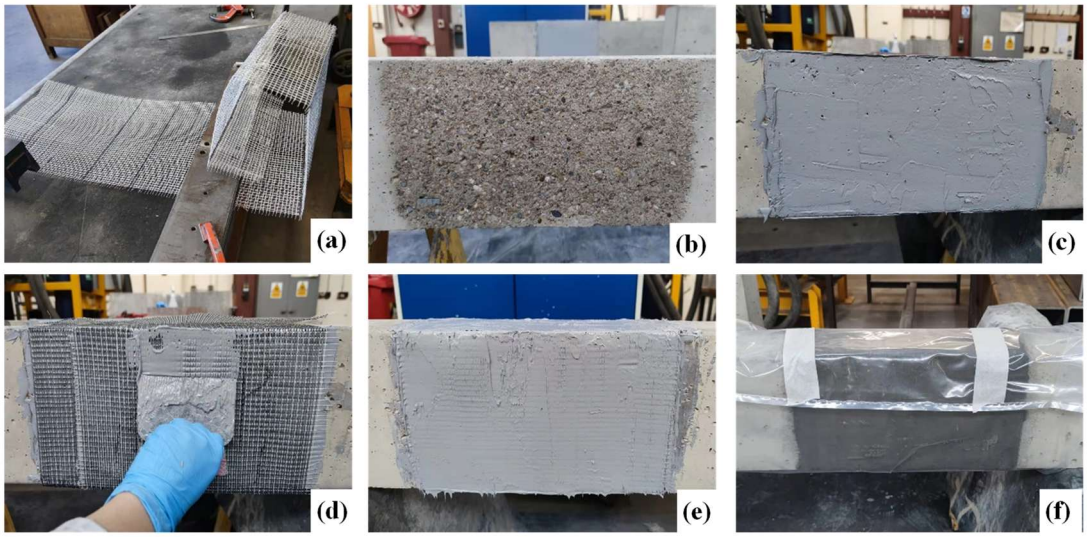

Fig. 3.4 Steps of the SRG jacketing application: (a) pre-bending the textile; (b) roughening and cleaning the surface in the shear critical zone; (c) applying the first matrix layer; (d) placing the textile; (e) repeating application process until complete; (f) curing the strengthened area.

3.1.4 Test Setup & Experimental Methodology

All beams were subjected to monotonic three-point loading using a stiff steel reaction frame. As shown in Fig. 3.5, the rectangular beams employed a vertically positioned servo-hydraulic actuator with a capacity of 500 kN, and the load was applied at a displacement rate of 0.02 mm/s. The beams were placed on two steel supports secured to a solid floor with threaded rods, which were subjected to monotonically increasing external loads until failure.

An external LVDT (Linear Variable Differential Transducer) was used to measure the vertical displacement of the beam at the load application position. The remaining two LVDTs were employed to monitor the settlement at the supports. Strain gauges

were not installed in the specimens. Instead, a non-contact Digital Image Correlation (DIC) system was employed to monitor full-field strain development in the shear-critical regions. DIC compares a sequence of digital images captured before and during loading, offering advantages such as low cost, ease of use, and robustness under varying environmental conditions. Its reliability in structural testing has been validated in prior studies (e.g., Cakir et al., 2023; Sharafisafa et al., 2020). The strengthened surface was prepared with a white matte base and black speckle pattern for tracking surface deformation. A high-resolution camera was positioned 1.5 m from the beam, capturing images at 0.5 Hz throughout loading. The images were processed using INSPECT Correlate 2023 (Zeiss, 2023), with a subset size of 64 × 64 pixels, following Dutton et al. (2013), who recommended a minimum of 36 × 64 pixels for accurate beam strain capture. This setup enabled detailed observation of strain localisation and crack development without the limitations of discrete strain gauges (Sharafisafa et al., 2014).

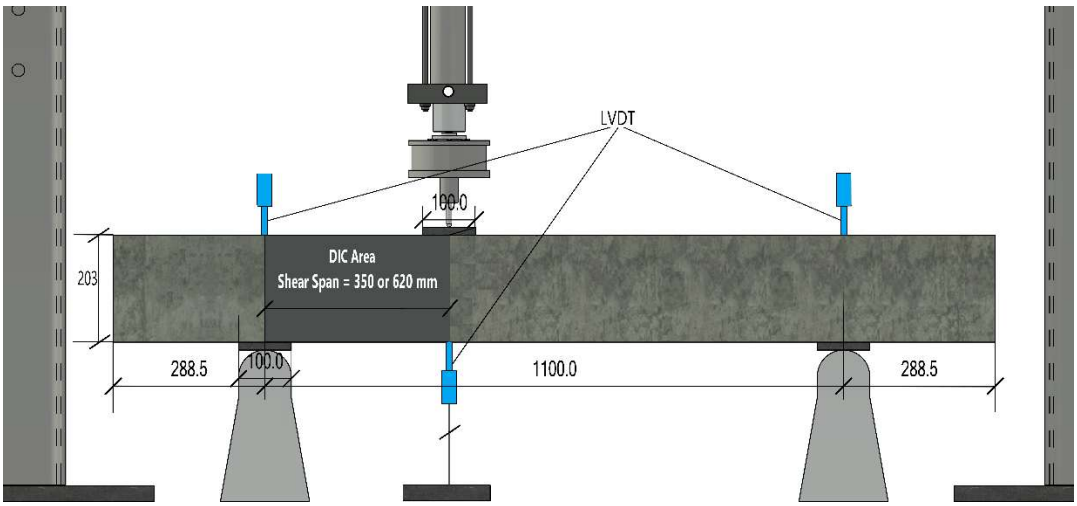

Fig. 3.5 Test setup, configuration of the DIC at the shear-critical span, and LVDTs positions.

3.2 Experimental Results and Discussion

Table 3.4 summarises the test results such as the peak load (P_{max}) and the corresponding displacement (δ_{max}); the strength increase of the retrofitted beams ($\Delta P_{max} = P_{RET} - P_{CON}$; where P_{RET} and P_{CON} are the peak load of the retrofitted and the corresponding control beam); the ultimate load P_u =(80% P_{max}) and the corresponding displacement δ_u; the shear strength of the critical shear span (*V;* for the

control specimen it is equal to V_{CON}; for the retrofitted specimens it is equal to V_{RET}); the shear strength provided by the strengthening system V_{JAC}(= $V_{RET} - V_{CON}$; where V_{RET} and V_{CON} are the shear strength of the retrofitted and the corresponding control beam); energy absorption, Ψ; and the failure mode. When no descending branch is present in the load–deflection curve, the ultimate deflection δ_u is defined as the last recorded data point. This follows standard practice for retrofitted elements, where failure is primarily governed by the externally bonded strengthening system (e.g., Thermou et al., 2019; *fib* Bulletin 90, 2019).

Table 3.4. Summary of test results

Series	Beam	P_{max} (kN)	ΔP_{max} (%)	P_u (kN)	δ_{max} (mm)	δ_u (mm)	V=V_{RET} (kN)	V_{JAC} (kN)	V_{JAC}/V_{RET} (%)	Ψ= Ψ_{RET} (kN·mm)	Failure Mode
A	A-N	51.3	-	41.1	2.50	3.96	35.0*	-	-	87.1**	S
	A-GL-U2	109.8	114	87.9	3.53	5.33	74.9	39.9	53.3	214.5	SD
	A-GH-U1	97.5	90	78.0	3.15	3.95	66.5	31.5	47.4	172.3	SD
	A-GL-W2	114.8	124	108.7	24.32	30.8	78.3	43.3	55.3	2636.9	FR
	A-GH-W1	107.7	110	85.6	9.51	9.73	73.4	38.5	52.5	773.7	SF
	A-PH-U1	112.5	119	90.0	3.89	4.33	76.7	41.7	54.4	250.6	SD
	A-PH-W1	141.5	176	113.2	17.70	31.6	96.5	61.5	63.7	3831.0	FR
	A-C-U2	106.7	107	85.3	3.96	4.42	72.8	37.8	51.9	268.1	SD
	A-C-U3	120.2	134	96.1	4.42	4.87	82.0	47.0	57.3	323.6	SD
	A-C-W2	133.8	161	107.1	5.76	6.41	91.2	56.3	61.7	471.6	SD
	A-C-W3	140.6	174	112.5	7.30	7.41	95.9	60.9	63.5	561.2	SD
B	B-N	38.8	-	31.1	1.41	1.50	16.9*	-	-	31.5**	S
	B-GL-U2	102.6	164	82.1	4.70	7.30	44.8	27.8	62.1	272.7	SD
	B-GH-U1	105.0	170	84.0	5.17	6.74	45.8	28.9	63.1	309.8	SD
	B-PH-U1	120.9	211	96.7	5.98	6.23	52.8	35.8	67.8	403.2	SD
	B-C-U2	117.9	204	94.3	5.82	6.70	51.4	34.5	67.1	385.0	SD
	B-C-U3	122.4	215	97.9	5.62	6.36	53.4	36.5	68.4	373.0	SD

* V=V_{CON} for the control specimen ** Ψ= Ψ_{CON} for the control specimen

In general, the experimental results demonstrated that the SRG, SRP and CFRCM systems can improve the shear capacity of RC beams. Additionally, as *a/d* increased, the shear strength of the jacketed beams (V_{RET}) decreased but the shear strength provided by the strengthening system across all strengthening systems (V_{JAC}/V_{RET}) was increased. The reduction in V_{JAC} can be attributed to three factors. As the beam transitions from deep to slender, the carrying mechanism shifts from arch action to a truss-like system, inherently decreasing the absolute shear resistance (Tetta et al., 2018a; Wakjira and Ebead, 2020). In addition, the larger shear span increases the likelihood of shear damage, impairing the bond between the jacket and substrate, facilitating detachment. The higher *a/d* ratio induces pronounced shear concentration

around beam ends (Lu et al., 2003; Jabbar et al., 2021), contributing to premature failure of the strengthening system and diminished shear enhancement, as evidenced by the DIC strain fields of Series B beams in Fig 3.7.

The failure modes are also presented in Table 3.4, where S is the failure caused by diagonal tension, fibre rupture; SD stands for shear-detachment failure, that is, shear failure occurs when detachment occurs either between the composite and the beam substrate or within the mortar layer; SF indicates shear-flexural failure, in which the beam exhibits some signs of flexural failure, but eventually shear failure occurs due to sudden detachment of the jacket; and FR represents flexural-rupture failure where concrete fracture follows the longitudinal steel bar yielding with fibre rupture.

3.2.1 Failure Modes and Crack Evolution Analysis

Series A beams: Figure 3.6 illustrates the failure modes of the Series A beams. The first column on the left shows the condition of each beam at the end of testing, while the remaining images present the horizontal and vertical strain fields at peak load, obtained via Digital Image Correlation (DIC). Note that specimen A-C-U2 is excluded from the DIC results due to a technical issue. The control beam, A-N, experienced diagonal tension failure as shown in Fig. 3.6a. A single inclined crack appeared initially, expanding with increasing load, leading to brittle shear failure.

The U-shaped SRG and SRP jacketed beams failed due to shear-detachment prior to flexural yielding (Figs. 3.6(b, d, f)). As the load increased, vertical cracks appeared at the bottom of the beam, followed by rapid deflection and eventual sudden detachment of the jacket, resulting in failure. Various failure modes were observed; A-GL-U2 experienced jacket detachment and slippage of the textile fibres, while A-GH-U1 displayed poor adhesion, leading to detachment between the textile and mortar. In contrast, the resin matrix in A-PH-U1 exhibited better adhesion, leading to the peeling of the concrete cover layer. This is because the mortar as a coarse matrix cannot penetrate the overly fine gaps of high-density fabrics, while the resin as a finer matrix can more effectively pass through these gaps and bond with the textile.

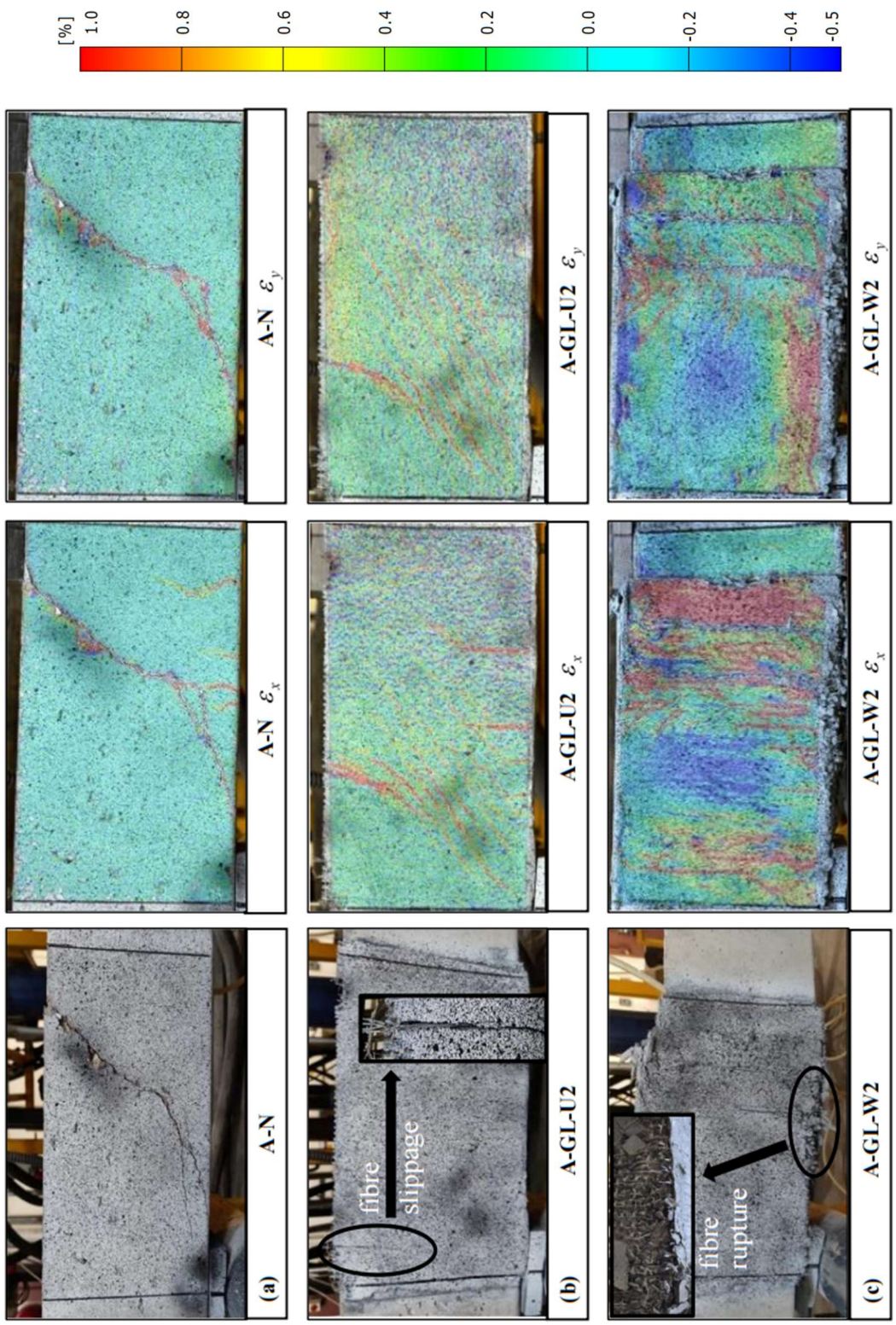
[%]
1.0
0.8
0.6
0.4
0.2
0.0
-0.2
-0.4
-0.5
A-N ε_y
A-GL-U2 ε_y
A-GL-W2 ε_y
A-N ε_x
A-GL-U2 ε_x
A-GL-W2 ε_x
(a) A-N
(b) A-GL-U2
fibre slippage
(c) A-GL-W2
fibre rupture

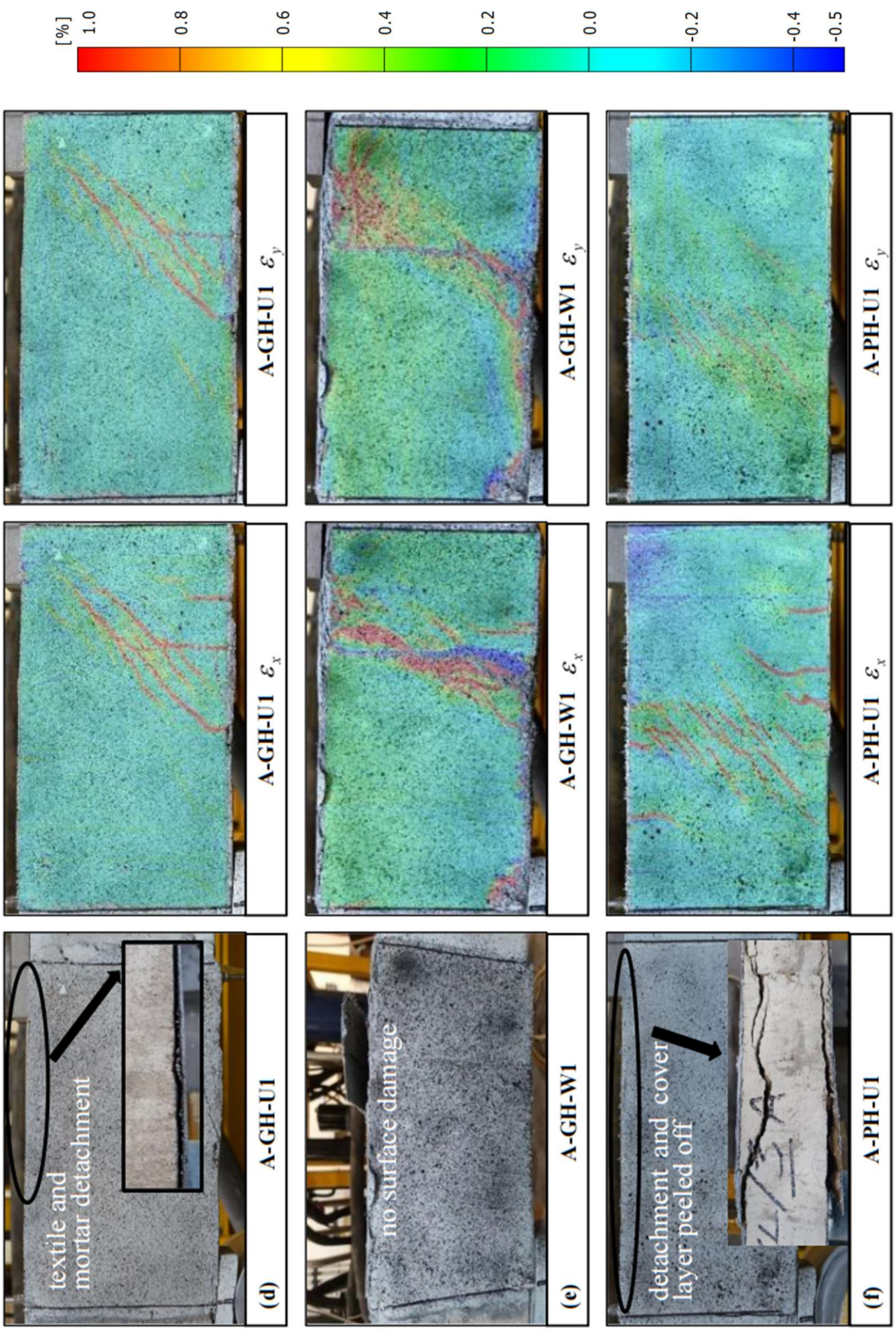
[%]
1.0
0.8
0.6
0.4
0.2
0.0
-0.2
-0.4
-0.5
A-GH-U1 ε_y
A-GH-W1 ε_y
A-PH-U1 ε_y
A-GH-U1 ε_x
A-GH-W1 ε_x
A-PH-U1 ε_x
textile and mortar detachment
no surface damage
detachment and cover layer peeled off
(d) A-GH-U1
(e) A-GH-W1
(f) A-PH-U1

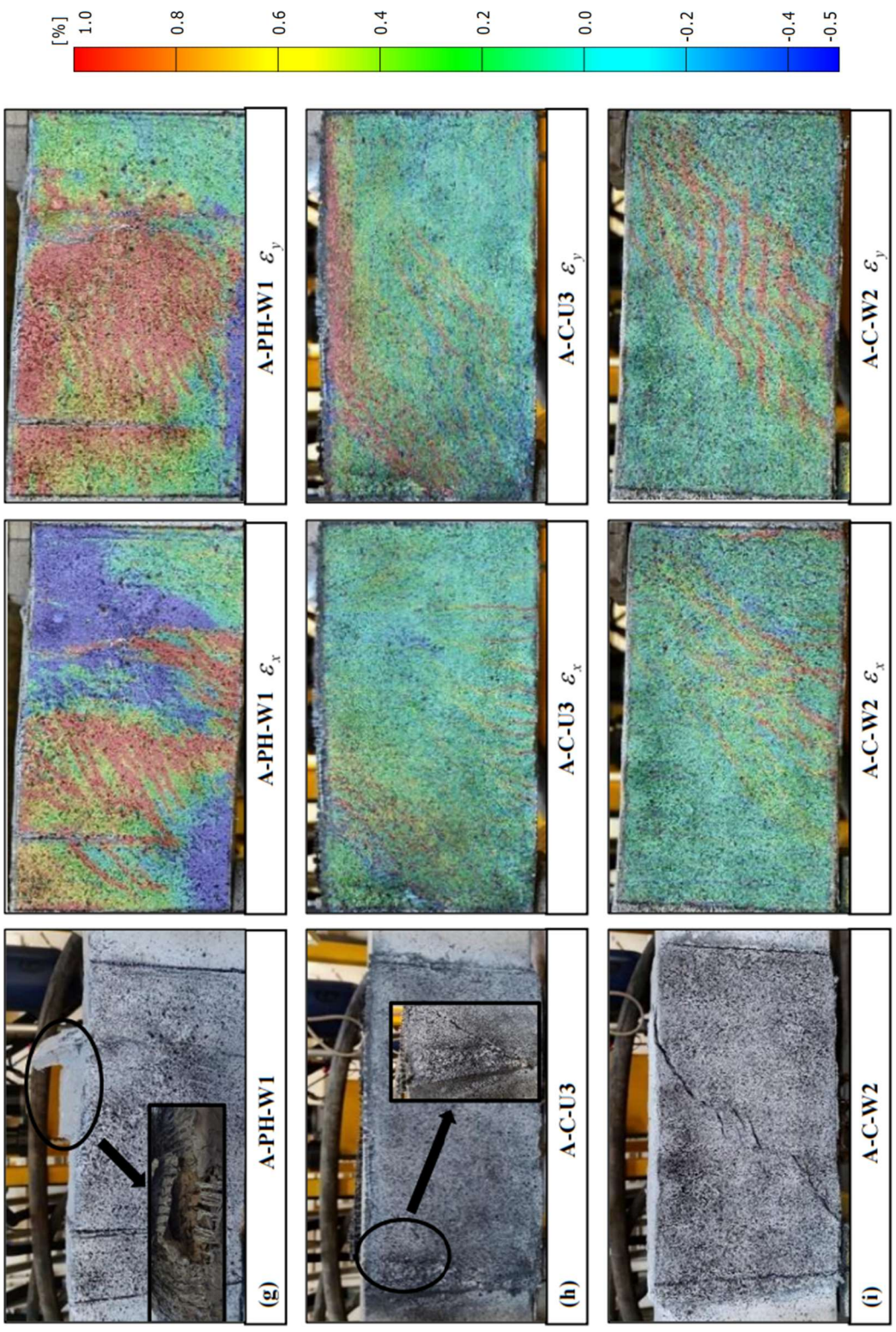
[%]
1.0
0.8
0.6
0.4
0.2
0.0
-0.2
-0.4
-0.5
A-PH-W1 ε_y
A-C-U3 ε_y
A-C-W2 ε_y
A-PH-W1 ε_x
A-C-U3 ε_x
A-C-W2 ε_x
(g) A-PH-W1
(h) A-C-U3
(i) A-C-W2

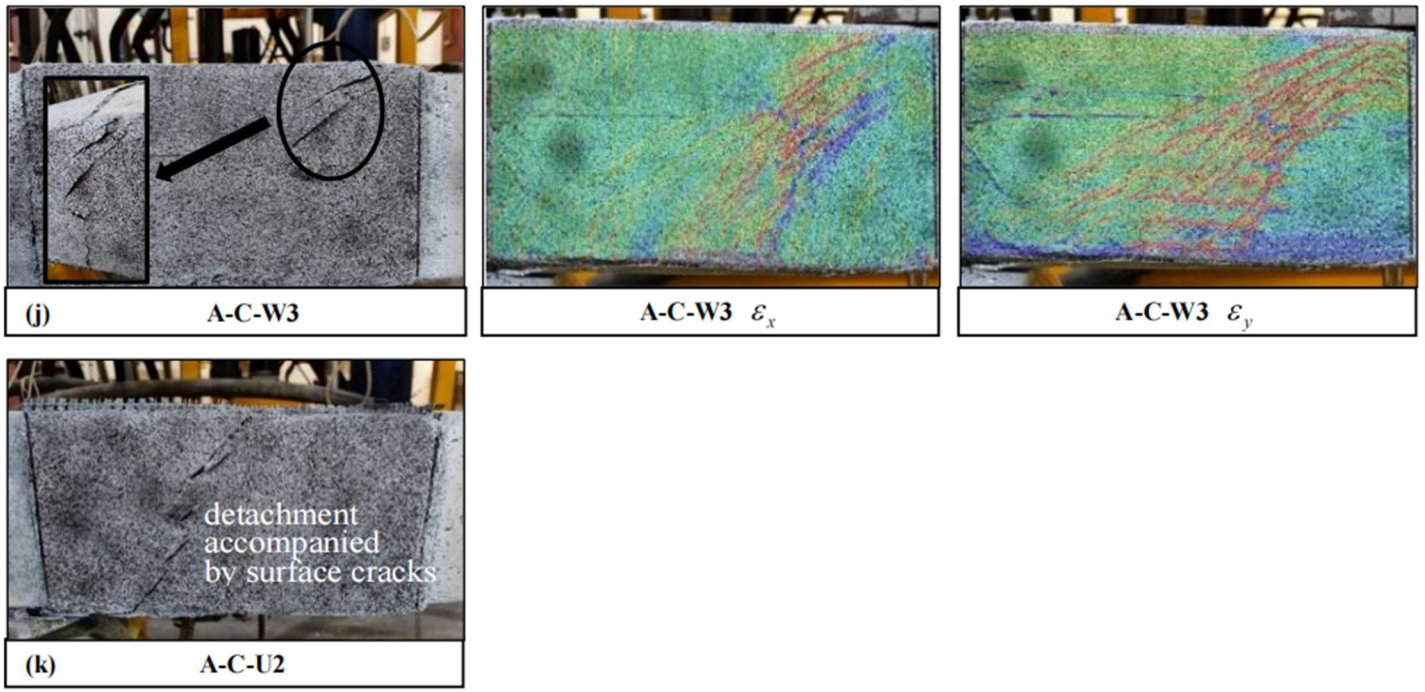

Fig. 3.6. Failure modes and strain contours in the critical shear span at failure of Series A beams: (a) A-N; (b) A-GL-U2; (c) A-GH-U1; (d) A-GL-w2; (e) A-GH-W1; (f) A-PH-U1; (g) A-PH-W1; (h) A-C-U3; (i) A-C-W2; (j) A-C-W3; (k) A-C-U2.

The fully wrapped SRG and SRP beams (A-GL-W2, A-GH-W1, A-PH-W1, Figs. 3.6(c, e, g)) displayed a ductile behaviour compared to the U-shaped jacketed beams. Flexural cracks formed, gradually widening until reaching the yielding point, with the SRG or SRP system allowing ongoing deformation. Specifically, A-GL-W2 and A-PH-W1 failed by fibre rupture after yielding of steel, while A-GH-W1 experienced sudden detachment of the jacket leading to shear failure.

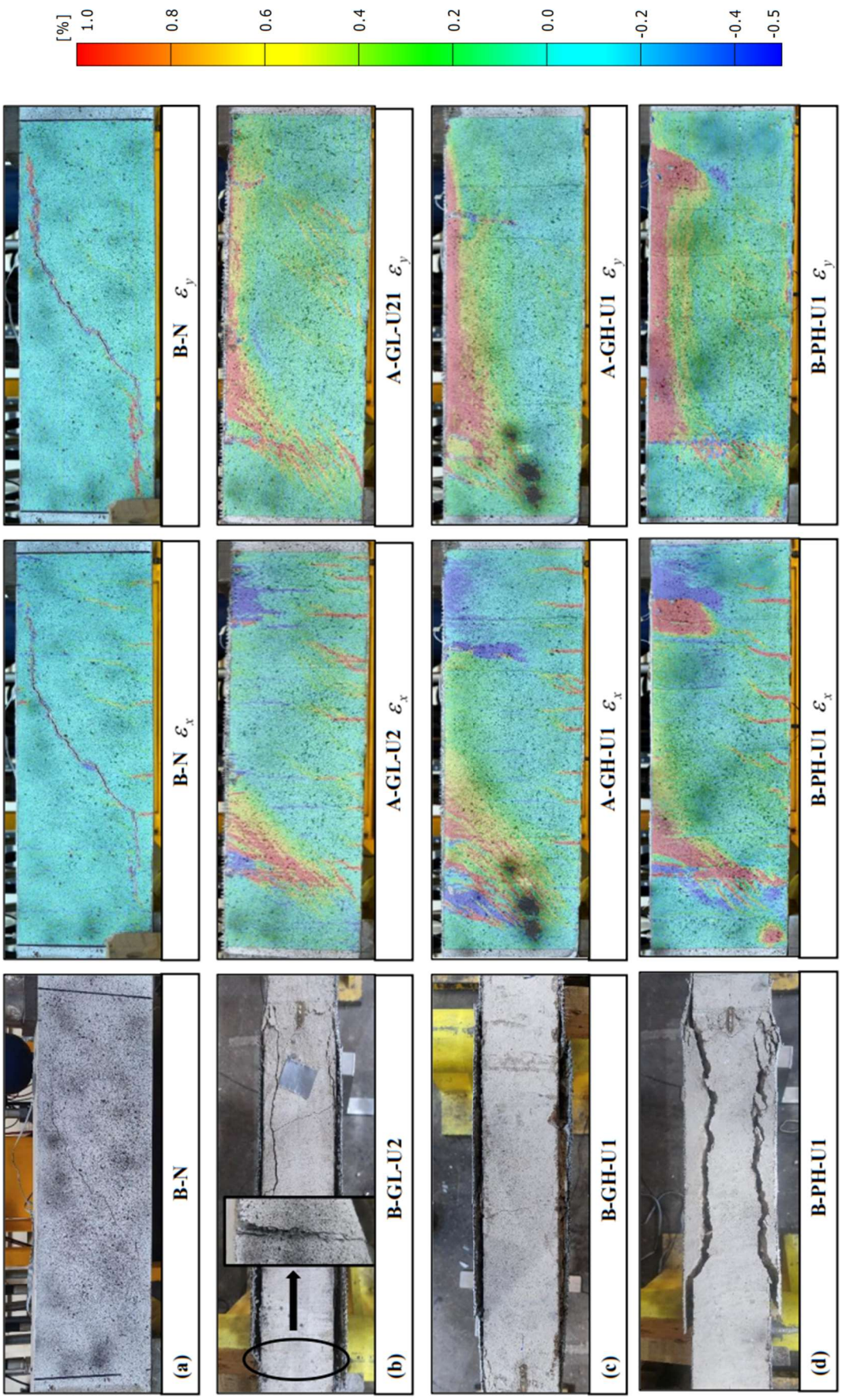
[%]
1.0
0.8
0.6
0.4
0.2
0.0
-0.2
-0.4
-0.5
B-N ε_y
A-GL-U21 ε_y
A-GH-U1 ε_y
B-PH-U1 ε_y
B-N ε_x
A-GL-U2 ε_x
A-GH-U1 ε_x
B-PH-U1 ε_x
(a) B-N
(b) B-GL-U2
(c) B-GH-U1
(d) B-PH-U1

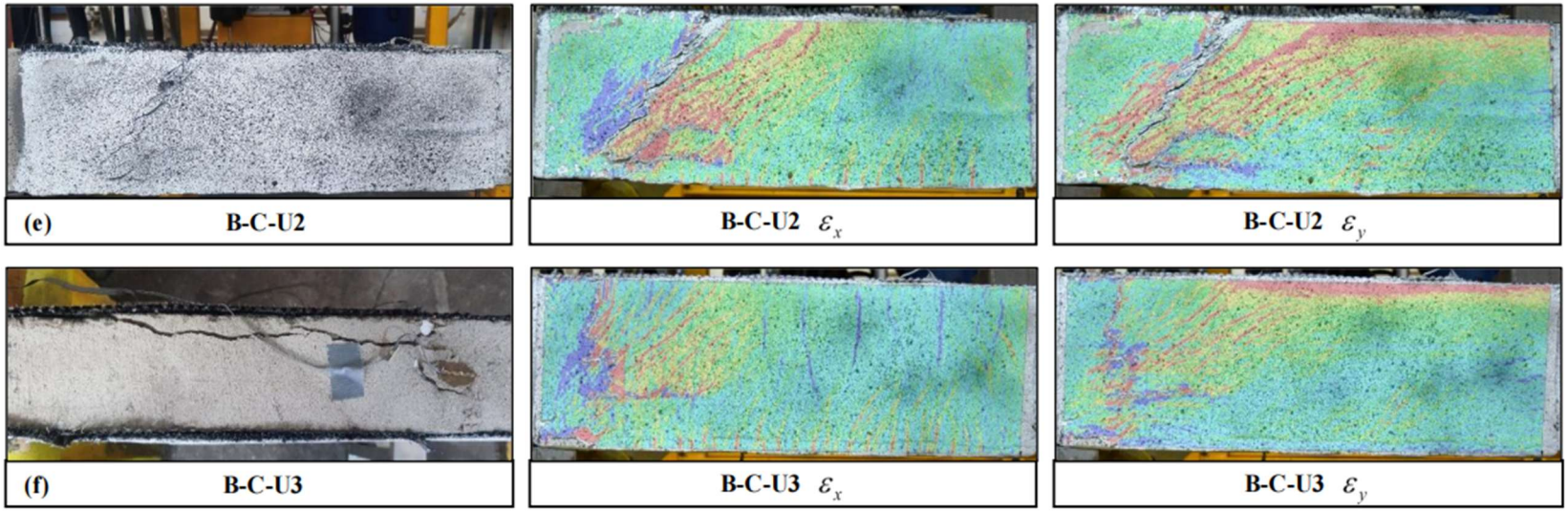

Fig. 3.7. Failure modes and strain contours in the critical shear span at failure of Series B beams: (a) B-N; (b) B-GL-U2; (c) B-GH-U1; (d) B-PH-U1; (e) B-C-U2; (f) B-C-U3.

For CFRCM-strengthened beams, both U-shaped and fully wrapped configurations exhibited shear-detachment failure, as depicted in Figs. 3.6(h-k). In the case of the two-layered systems (A-C-U2 and A-C-W2), cracks developed near the support and at the load application location as the load increased. Subsequently, the cracks progressed into a diagonal crack that that extended across the entire shear-critical region. The detachment of both the mortar and textile in the crack area ultimately resulted in the failure of the beam. In addition, a three-layer carbon fibre textile was employed to further increase the beam's stiffness and alter the stress transfer mechanism of A-C-U3 and A-C-W3, which eliminated the occurrence of cracks penetrating the entire surface. After detachment failure, the textile remained undamaged upon removing the mortar from the cracks. Interestingly, there was a slight variation in CFRCM system's failure modes when the U-shaped configuration was replaced with the fully wrapped configuration for the same number of layers.

In DIC diagrams, the control beam A-N displayed pronounced diagonal cracking in both horizontal and vertical directions, in addition to flexural cracks that were not fully developed. All strengthened beams exhibited extensive strain distribution within the critical region compared to the control beam. Notably, A-GL-W2 and A-GH-W1 which failed in flexure showed wider strain distribution, with the jacket preventing the formation of diagonal cracks. However, oblique cracks still formed in U-shaped SRG and SRP jacketed beams. Due to fact that UHTSS textiles comprise unidirectional cords, SRP- and SRG-strengthened beams presented considerable strains only in the horizontal direction, while CFRCM systems displayed larger vertical strains.

Series B beams: For the Series B beams (shear span-to-depth ratio of 3.5), the control beam B-N failed in a typical diagonal tension mode with sudden shear cracking and formation of large diagonal cracks (Fig. 3.7a). For the strengthened beams (Figs. 3.7b-f), shear failure occurred for all cases with detachment of the jacket from the substrate (including part of the concrete cover layer). The failure modes mirrored those of the corresponding specimens with a/d = 2.0. Among the SRG and SRP systems, B-GH-U1 peeled off the least amount of cover layer at failure while B-PH-U1 peeled off the most. This is because the epoxy resin provides higher adhesion compared to the mortar matrix, resulting in larger portions of the concrete cover being peeled off at failure. Regarding the CFRCM systems, no peeling off of the mortar portion from the CFRCM surface was observed for B-C-U3 at failure, while such partial phenomenon occurred for the two-layered CFRCM system (B-C-U2).

In order to better comparation, Figure 3.7 also illustrates the horizontal and vertical strain fields observed at peak load for the beams with $a/d=3.5$, obtained using DIC. The control beam, B-N, showed more incomplete vertical deformations than A-N at peak load. In contrast to Series A beams, Series B strengthened beams exhibited larger areal deformations, primarily on one side near the support. This can be attributed to the altered shear force distribution near the beam ends due to the end restraint effect of the supports. The higher shear span ratio in Series B led to more concentrated shear forces near the supports, causing easier damage in sections adjacent to them. For B-C-U2 and B-C-U3, it can be observed that increasing the number of fabric layers further optimised the stress distribution. The three-layered CFRCM jacketed beam showed smaller deformations at peak load without any mortar peel-off at the surface.

To summarise, the potential of closed SRG jackets to modify the response of shear deficient beams from brittle to ductile was demonstrated (i.e. A-GL-W2 and A-PH-W1). Irrespective of the jacketing system applied herein (i.e. SRG, SRP, CFRCM) and the shear-to-span ratio (*a/d* =2 and 3.5), all beams strengthened with U-shaped jackets failed due to shear-detachment.

3.2.2 Load-deflection Curves.

Figure 3.8 depicts the load-deflection responses of the series A beams (*a/d* = 2.0) strengthened by SRG, SRP, and CFRCM jackets. The control beam failed in shear at a peak load of 51.3kN (corresponding displacement of 2.5mm). All the U-shaped SRG jacketed beams failed in shear with a strength increase in a range of 90% to 114% (Fig. 3.8a). Regarding the fully wrapped jacketed beams, A-GL-W2 (low-density UHTSS fully wrapped jacketed beam) showed a small drop in strength at 75kN, which indicated some degree of textile detachment, while the SRG system still contributed to the shear resistance up to the peak load (124% higher than the control beam). However, A-GH-W1 (high-density UHTSS fully wrapped jacketed beam) failed due to detachment of the jacket (shear-detachment) at a load 110% higher than the control beam. In case of the U-shaped CFRCM strengthened beams, which all failed in shear, the strength increased by 58% and 77% for the two- and three-layered U-wrapped beams (A-C-U2 and A-C-U3), respectively. The fully wrapped A-C-W2 and A-C-W3 beams exhibited higher strength increase of 130% and 192%, respectively. Meanwhile, Fig. 3.8c shows that the SRP reinforced beams A-PH-U1 and A-PH-W1 had different results, with A-PH-U1 failing in shear due to jacket detachment, while increasing strength by 119%. The SRP fully wrapped beam, A-PH-W1, showed a transition from brittle to ductile failure mode, with strength and deflection increasing by 176% and 608%, respectively.

Figure 3.9 depict the load-deflection responses of the strengthened beams, using identical jacket configurations for *a/d* = 2.0 and 3.5. In beams with *a/d*=2.0 (deep beams), the predominant mechanism governing the shear resistance is that of the arch action, whereas for the beams with *a/d*=3.5 (slender beams), the dominant mechanism shifts towards beam action, resembling a truss analogy mechanism. The peak loads of series B strengthened beams (except B-GL-U2) demonstrated a slight increase compared to the Series A beams. This increase is because the slender beams distribute

a smaller portion of shear force across the strengthened region under the same load, thereby delaying shear failures to some extent. Furthermore, the strengthened beams in Series B exhibited substantially larger deflections and lower stiffness compared to Series A beams due to increased moments associated with the higher *a/d* (Wakjira and Ebead, 2020).

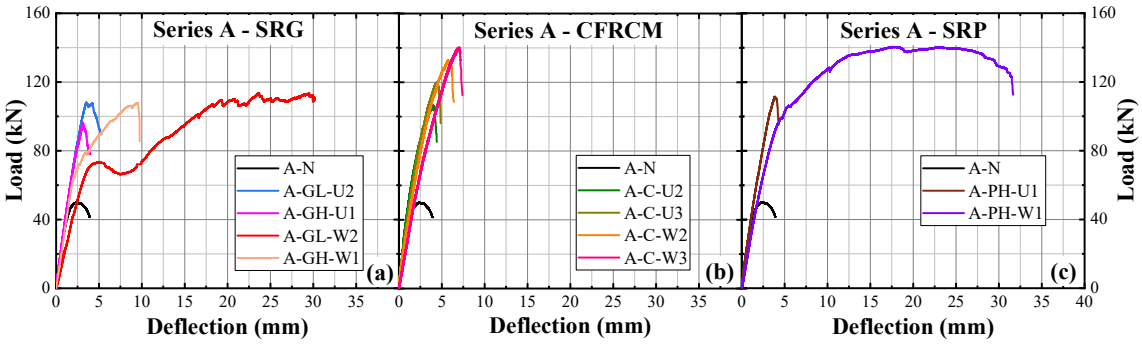

Fig. 3.8. Load-deflection curves for all tested specimens with *a/d=2* (Series A beams): (a) SRG; (b) CFRCM; (c) SRP strengthened beams.

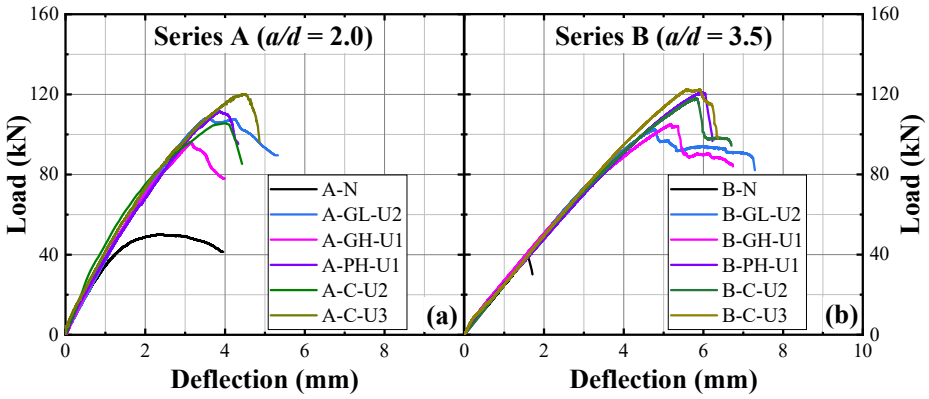

Fig. 3.9. Effect of *a/d* on the load–deflection response of beams: (a) Series A (*a/d* = 2.0); (b) Series B (*a/d* = 3.5).

3.2.3 Energy Absorption

The energy absorption (Ψ) of the strengthened beams was defined as the area under the load-displacement curve of the beam up to the point of failure (Ebead, 2015). For beams that failed in shear, the Ψ value was calculated up to the peak load, while for beams with ductile performance (i.e. flexural failure), Ψ was calculated up to the ultimate point (80% of the peak load). The Ψ results for all tested beams are presented in Table 3.4. Additionally, the relationship between the energy absorbed by the jacket (Ψ_{JAC}) (i.e. difference between the energy absorption of the strengthened beam (Ψ_{RET})

and that of the control beam (Ψ_{CON})), and the beam's textile axial stiffness ($\rho_f E_f$) is presented in Fig. 3.10.

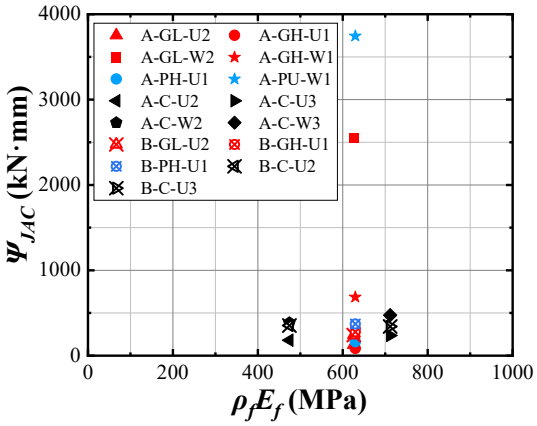

Fig. 3.10. Energy absorption vs axial stiffness for the strengthened beams.

With an increase in the *a/d* ratio, the B series strengthening systems exhibited greater energy absorption compared to the A series. Notably, for beams failing in a ductile mode (such as A-GL-W2 and A-PH-W1), the Ψ_{JAC} values surpassed those associated with beams failing due to shear-detachment. In comparison to the control A-N, the energy absorption of these beams increased by up to 4298%. This indicates that fully wrapped SRG and SRP jackets can significantly enhance the resilience of shear-deficient RC beams. Moreover, no significant differences were observed between the U-shaped SRP and SRG systems, irrespective of whether they belonged to the A or B series. Additionally, the energy absorption of CFRCM showed a proportional increase with the axial stiffness of the fabric. Both fully wrapped and U-shaped configurations displayed a consistent linear increase in slope, aligning with previous findings (Lu et al., 2024). In summary, the fully wrapped SRP and low-density SRG systems, particularly SRP, exhibited remarkable ductility, suggesting their potential effectiveness in reinforcing structures to withstand seismic and other high-intensity loads in practical engineering applications.

3.3 Parameters Affecting the Performance of the Strengthened Beams

3.3.1 Effect of the Shear Span-to-depth Ratio

Figure 3.11 depicts the impact of *a/d* on the enhancement of shear strength (V_{JAC}/V_{CON}) for all jacketed beams. As observed, V_{JAC}/V_{CON} increases as *a/d* increases. The strength increase in the B-PH-U1 surpasses that of A-PH-U1 by 102%. The smallest increment is observed in the two-layer low-density SRG system (B-GL-U2 vs A-GL-U2), albeit still reaching 50%.

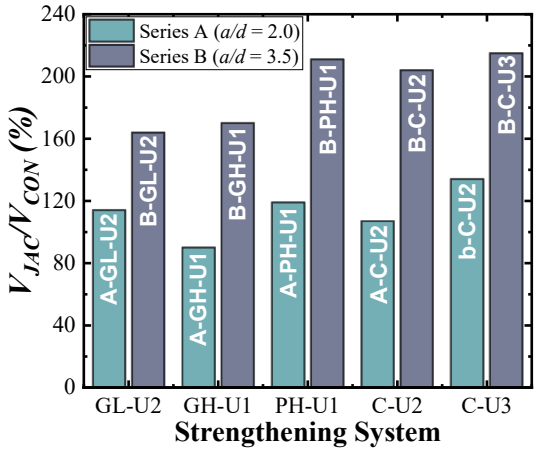

Fig. 3.11. Effect of the *a/d* ratio on V_{JAC}/V_{CON}.

For Series A beams (*a/d=2,* deep beams), after the formation of diagonal cracks, arch action predominates. The majority of the load is directly transferred from the load application point to the support through diagonal compressed struts, meaning the load is primarily carried by diagonal compressed struts (Wakjira and Ebead, 2020). The influence of arch action diminishes with the increase in the *a/d* ratio, reducing the concrete's contribution to shear strength. However, this is offset by an increase in the contribution of the strengthening system acting as lateral reinforcement on the beam (Tan et al., 2008). Moreover, for deep beams, inclined cracks are oriented more obliquely relative to the fibre alignment (vertical direction) of the fabrics. Hence, stresses along the fibre orientation are less effective in impeding crack propagation and widening. With increasing shear span-depth ratio, the angle between the fibres and crack opening direction is reduced, decreasing the proportion of shear force undertaken horizontally by the fabrics, which thereby elevates the percentage of shear contribution

provided by the strengthening system (Li and Leung, 2016). Overall, the fundamental mechanism governing this behaviour lies in the transition from arch action to truss action as the a/d ratio increases. This shift reduces the direct contribution of compressive struts within the concrete to shear resistance, thereby increasing the reliance on the effectiveness of the external strengthening system for shear force transfer.

3.3.2 UHTSS: Effect of the Textile Density and the Matrix Type

The impact of the UHTSS density on V_{JAC}/V_{CON} of beams strengthened with UHTSS textiles' systems is shown in Fig. 3.12a. In Series A beams, the V_{JAC}/V_{CON} of the low-density U-shaped SRG jacketed beam (A-GL-U2) was 24% higher than that of the high-density counterpart (A-GH-U1), while the fully wrapped low-density SRG exhibited a 14% higher shear strength. These findings suggest that a UHTSS density of 3.14 cords/cm obstructed the passage of mortar, resulting in reduced adhesion of the textile to the matrix and poor strengthening performance. This low adhesion also caused debonding at the interface between the textile and matrix, as well as delamination of the internal mortar layer, leading to decreased composite integrity and premature detachment of jackets (Wakjira and Ebead, 2020; Wakjira and Ebead, 2019a). However, both B-GL-U2 and B-GH-U1 highlighted nearly identical shear strength enhancement. The deficient performance of B-GL-U2 may be attributed to defects in the strengthening application. Hence, it can be concluded that in case of the SRG strengthening system, the use of high-density (>3.14 cords/in) UHTSS textiles results in poor adhesion. This is in agreement with previous research where it was concluded that due to the small gaps between the cords in case of the 4.72 cords/cm density UHTSS textiles imposed difficulties in the penetration of the mortar. Thus, it is recommended to use a UHTSS textile density of less than 3.14 cords/cm (4 cords/in) for optimal results in the SRG system.

With respect to the matrix influence on high-density UHTSS systems (Fig. 3.12b), the resin-based system (SRPs) showed greater shear strength enhancement than the mortar-based system (SRGs), irrespective of the series. This implies that the fine resin substrate could impregnate the gaps in the high-density UHTSS textiles more effectively than the coarser mortar, thereby providing superior adhesion.

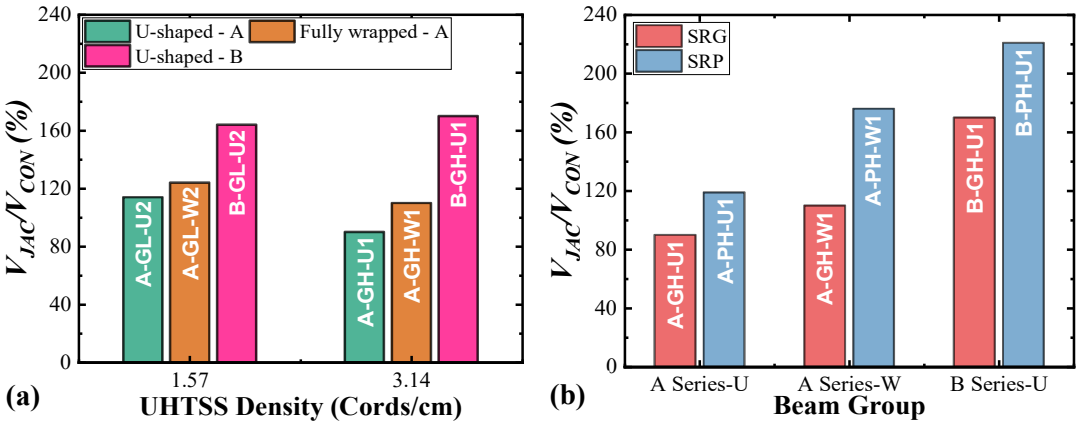

Fig. 3.12. Effect of the UHTSS textile density and the system matrix.

The inverse relationship between textile density and strengthening effectiveness can be attributed to matrix infiltration mechanics and interfacial bonding behaviour. When the textile density exceeds a critical threshold (e.g., >3.14 cords/cm), a "barrier effect" occurs, in which the tightly packed cords form narrow micro-channels that impede the penetration of mortar. This insufficient matrix impregnation leads to the formation of voids and inter-yarn discontinuities, which act as stress concentrators and reduce the mechanical interlock between the textile and the surrounding matrix. As a result, the effective contact area is diminished, decreasing the interfacial shear transfer capacity and compromising the composite action. These local weaknesses can trigger premature debonding or delamination under shear, ultimately reducing the overall effectiveness of the strengthening system.

3.3.3 Effect of the Fibre Type and Number of Layers of Textile

To assess the impact of different fibre types and the number of textile layers, Fig. 3.13 illustrates the V_{JAC}/V_{CON} of varied CFRCM and SRG in A series, grouped based on distinct strengthening configurations. Among the tested setups, A-C-W3 demonstrated the most significant improvement in shear strength, reaching up to 174%, while A-GH-U1 exhibited the least favorable result at only 90%. Despite the lower axial stiffness of the two-layered CFRCM compared to SRG, it can still achieve similar or even superior shear strength enhancement. However, Fig. 3.8b indicates that the CFRCM system lacks the ability of the SRG jacket to induce a ductile failure mode in the beam. Additionally, the three-layer CFRCM, designed to mitigate shear failure, still manifested shear-detachment failure. Concerning the impact of the number of layers, two- and three-layered U-wrapped beams demonstrated strength increases of

58% and 77%, respectively. In contrast, fully wrapped beams with two- and three-layered CFRCM jackets exhibited even higher strength increases, at 130% and 192%, respectively. Therefore, an increase in the number of textile layers contributes to enhancing the shear strengthening effectiveness of the FRCM system.

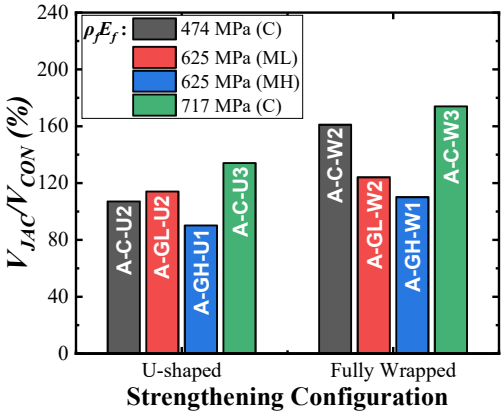

Fig. 3.13 Effect of the fibre type and layers of textile.

Therefore, the performance variations observed among different fibre types and configurations can be attributed to differences in mechanical properties, interfacial bonding capacity, and stress distribution efficiency. The relationship between the number of textile layers and strengthening effectiveness follows composite mechanics principles, whereby multilayer systems promote a more distributed stress field and mitigate localised stress concentrations that could otherwise lead to premature failure. In addition, layered systems provide redundancy, meaning that failure of a single layer does not compromise the integrity of the entire strengthening system.

3.4 Prediction of the Shear Strength of SRG-Jacketed Beams

The shear span-to-depth ratio has a significant impact on the shear strength of RC beams. However, existing models rarely consider the influence of shear span-to-depth ratio, especially in the case of SRG jacketing. Wakjira and Ebead (2020) developed a model to predict the shear strength of U-shaped jacketed SRG beams considering the effect of *a/d*. This model, however, does not account for side bonding, full wrapping, and fibre rupture failure. Additionally, Wakjira and Ebead's model (2020) requires the knowledge of the longitudinal reinforcement strains, which may impose challenges in the implementation of the model.

Therefore, a model is developed to predict the shear strength of SRG-strengthened beams with no transverse reinforcement. This model could be also applied in cases of sparsely spaced and corroded links, considering that the contribution of the internal transverse reinforcement is negligible. To develop and validate the model, an experimental database was compiled using experimental results from this study and existing literature (i.e. Thermou et al., 2019, Wakjira and Ebead, 2020, Wakjira and Ebead, 2019a, Ombres and Verre, 2021). The strengthened beams included in the database did not have any anchoring mechanisms and transverse reinforcement, and all experienced shear failure.

Table 3.5 presents the main mechanical properties, experimental results, and predicted results of 25 SRG-strengthened beams in the database. The model uses Eurocode 2 to calculate the shear strength provided by the concrete beam (V_c) and estimates the shear strength provided by the SRG (V_{SRG}) based on the model of Chen & Teng (2003a). The shear span-to-depth impact factors R_c and R_f for V_c and V_{JAC}, respectively, were introduced through Wakjira and Ebead's model (2020). This model eliminates the need for longitudinal steel strain in calculations, and incorporates side bonding, full wrapping, and fibre rupture failure of SRG jackets. The shear strength of the strengthened beams (V) can be calculated as:

$$V = R_c V_c + R_f V_{SRG} \tag{3-2}$$

The shear strength contributed by the concrete beam is typically calculated using the model in EC2 (2005):

$$V_C^{EC2} = 0.18k\left(100\rho_{long,b} f_c\right)^{1/3} b_w d \tag{3-3}$$

where, f_c is the compressive strength of concrete obtained from cylinders; d is the depth of the cross-section; $\rho_{long,b}$ is the area ratio of the tensile reinforcement; and $k = 1 + \sqrt{(200/d)} \leq 2.0$ (with d in mm) is a factor that considers the size effect.

The shear strength of SRG jackets (V_{SRG}) is calculated by the model proposed by Chen & Teng (2003a and 2003b). This model initially developed for FRP systems, but existing research (Wakjira and Ebead, 2020, Rossi et al., 2022, Tetta et al., 2018b) has demonstrated its applicability to FRCM systems. The V_{JAC} can be calculated as:

$$V_{SRG} = 2nt_f b_w h_{fe} \frac{w_f}{s_f} f_{fed}(cot\theta sin\alpha_0 + cos\alpha_0) \tag{3-4}$$

where α_0 is the angle between the fibres and the beam axis perpendicular to the shear force, taken as 90°; θ is the angle of the critical shear cracks to x-axis, taken as 45°. f_{fed} is the effective stress of SRG at failure; h_{fe} is effective hight of SRG , $= z_b - z_t$; $z_b = 0.9d - (h - d_{fb})$; $z_t = d_{ft}$, in which z_b and z_t are the co-ordinates of the top and bottom ends of the effective FRCM; d_{fb} is the distance from the compression face to the top edge of the FRCM; and d_{ft} is the distance from the compression face to the lower edge of the jacket.

The effective stress of SRG is given by Tetta et al. (2018b):

$$f_{fed} = D_f f_{fed,max} \leq f_{fu,jac} \tag{3-5}$$

where D_f is the stress distribution coefficient; and $f_{fed,max}$ is the maximum design stress of the jackets.

Regarding the SRG strengthened beams with detachment failure (Chen and Teng, 2003a), the maximum design stress of the SRG is calculated as:

$$f_{fed,max} = 0.427\beta_l\beta_w\sqrt{\frac{E_f\sqrt{f_c}}{nt_f}} \tag{3-6}$$

The effective bond length and the concrete width ratio of the jacket, β_l and β_w are given as

$$\beta_l = \begin{cases} 1, \lambda \geq 1 \\ sin\left(\frac{\pi\lambda}{2}\right), \lambda < 1 \end{cases} \tag{3-7}$$

$$\beta_w = \sqrt{\frac{2 - w_f/(s_f sin\alpha)}{1 + w_f/(s_f sin\alpha)}} \tag{3-8}$$

where λ is the maximum bond length parameter, given by:

$$\lambda = L_{max}/L_e \tag{3-9}$$

where L_{max} and L_e are the available bond length and the effective bond length, respectively, given by the following:

$$L_{max} = \begin{cases} h_f/sin\alpha \text{ , for U-shaped jackets} \\ h_f/2sin\alpha \text{ , for side bonding jackets} \end{cases} \tag{3-10}$$

$$L_e = \sqrt{\frac{E_f n t_f}{\sqrt{f_c}}} \tag{3-11}$$

The expression of the stress distribution coefficient (D_f) for side bonding and U-shaped jackets is:

$$D_f = \begin{cases} \frac{2}{\pi\lambda}\left(\frac{1-cos\left(\frac{\pi\lambda}{2}\right)}{sin\left(\frac{\pi\lambda}{2}\right)}\right), \lambda \leq 1 \\ 1 - \frac{\pi - 2}{\pi\lambda}, \lambda > 1 \end{cases} \tag{3-12}$$

According to (Chen and Teng, 2003b), the expression of the stress distribution coefficient (D_f) for fully wrapped jackets is:

$$D_f = \frac{1 + z_t/z_b}{2} \tag{3-13}$$

Regarding the SRG strengthened beam with fibre rupture failure, the maximum design stress of the SRG is calculated as:

$$f_{fed,max} = f_{fu,jac} \tag{3-14}$$

where $f_{fu,JAC}$ is the ultimate stress of jackets. It is worth noting that Eq. (14) was originally proposed for only fully wrapped jackets exhibiting the fibre rupture failure mode (Spinella, 2019). However, recent studies have reported the possibility for U-shaped jackets also experiencing this failure mode (Tetta et al., 2018b). Therefore, this study endeavours to extend its applicability to both fully wrapped and U-shaped jackets. Considering the limitation of the data, further validation is necessary to confirm its effectiveness. According to Kang and Ary (2012), the strength of FRCM can be calculated by the following formula when jacket debonding failure does not occur:

$$f_{fu,JAC} = E_f \varepsilon_{SRG} \leq f_{fu,f} \tag{3-15}$$

where ε_{SRG} represents the effective strain of FRCM, considering only the fibres distributed along the main direction of the textile (Vertical); and $f_{fu,f}$ is ultimate stress of fibres. According to the strengthening configuration, ε_{SRG} can be calculated as:

$$\varepsilon_{SRG} = \begin{cases} 0.035\left(\dfrac{f_c^{2/3}}{\rho_f E_f}\right)^{0.65} \varepsilon_{fu,f}, \text{ for fully wrapped jackets} \\ 0.020\left(\dfrac{f_c^{2/3}}{\rho_f E_f}\right)^{0.55} \varepsilon_{fu,f}, \text{ for U-shaped jackets} \end{cases} \quad (3\text{-}16)$$

In Eq. (3-16), E_f and f_c' are expressed in GPa and MPa, respectively. SRG is the ultimate strain of fibres.

Substituting Eq. (3-3) and Eq. (3-4) into Eq. (3-2), the final expression for the shear strength of the strengthened beam is obtained:

$$\begin{aligned} V &= R_c V_c + R_f V_{JAC} \\ &= R_c 0.12k\left(100\rho_{long} f_c\right)^{1/3} b_w d + R_f 2nt_f b_w h_{fe} f_{fed} \end{aligned} \quad (3\text{-}17)$$

Based on regression analysis of the data, the influence factors of *a/d* on the beam and SRG jacket (R_c and R_f) are:

$$R_c = \begin{cases} (2.47/\chi)^{\eta}, \ a/d \le 2.5 \\ 0.86\eta^{1.25}, a/d > 2.5 \end{cases} \quad (3\text{-}18)$$

$$R_f = \begin{cases} 1.39\sqrt{R_c}, a/d \le 2.5 \\ 0.7{R_c}^{3/4}, a/d > 2.5 \end{cases} \quad (3\text{-}19)$$

Where $\chi = a/d, \eta = 2.5/\chi$.

Table 3.5. Experimental database of SRG strengthened RC beams and predicted shear strength.

	b_w (mm)	d (mm)	a/d	f_c (MPA)	t_f (mm)	w_f/s_f	ρ_f (%)	E_f (GPA)	$\varepsilon_{fu,f}$	V_{exp} (kN)	V_{pre} (kN)	V_{pred}/V_{exp}
Present study												
A-GL-U2	102	177	2.0	22.2	0.084	1.00	0.329	190	0.015	74.9	62.2	0.83
A-GH-U1	102	177	2.0	22.1	0.169	1.00	0.331	190	0.015	66.5	62.2	0.94
A-GH-W1	102	177	2.0	22.7	0.169	1.00	0.331	190	0.015	73.4	62.7	0.85
B-GL-U2	102	177	3.5	20.5	0.084	1.00	0.329	190	0.015	44.8	41.5	0.93
B-GH-U1	102	177	3.5	22.2	0.169	1.00	0.331	190	0.015	45.8	42.6	0.93
Thermou et al. (2019)												
BUL1	200	270	2.2	23.3	0.084	1.00	0.084	190	0.015	140.2	135.7	0.97
BUL2	200	270	2.2	23.3	0.084	1.00	0.168	190	0.015	136.6	160.2	1.17
BUML1	200	270	2.2	23.3	0.084	1.00	0.084	190	0.015	146.0	171.4	1.17
Wakjira & Ebead (2020)												
BS1-L	180	334	3.1	34.0	0.084	1.00	0.187	190	0.015	157.1	180.3	1.15
BS1-H	180	334	3.1	34.0	0.169	1.00	0.376	190	0.015	187.7	209.6	1.12
BS2-L	180	334	2.6	34.0	0.084	1.00	0.376	190	0.015	237.5	218.7	0.92
BS2-H	180	334	2.6	34.0	0.084	1.00	0.376	190	0.015	260.8	224.0	0.86
BS3-L	180	334	2.1	34.0	0.084	1.00	0.187	190	0.015	308.9	249.0	0.81
BS3-H	180	334	2.1	34.0	0.169	1.00	0.376	190	0.015	325.7	269.1	0.83
BS4-L	180	334	1.6	34.0	0.084	1.00	0.187	190	0.015	347.0	323.5	0.93
BS4-H	180	334	1.6	34.0	0.169	1.00	0.376	190	0.015	379.3	379.3	1.00
Wakjira & Ebead (2019a)												
B1-U-L	180	335	2.8	34.0	0.084	1.00	0.187	190	0.015	207.9	176.2	0.85
B1-U-H	180	335	2.8	34.0	0.169	1.00	0.376	190	0.015	200.8	187.5	0.93

B1-S-L	180	335	2.8	34.0	0.084	1.00	0.187	190	0.015	182.3	186.3	1.02
B1-S-H	180	335	2.8	34.0	0.169	1.00	0.376	190	0.015	172.8	207.9	1.20
Ombres & Verre (2021)												
BC-2L	200	263	3.4	14.4	0.084	1.00	0.168	197.0	0.020	91.8	105.0	1.14
BD-1L-3S	200	263	3.4	14.4	0.084	0.29	0.024	197.0	0.020	53.7	59.1	1.10
BD-1L-4S	200	263	3.4	14.4	0.084	0.43	0.036	197.0	0.020	63.7	65.2	1.02
BD-2L-3S	200	263	3.4	14.4	0.084	0.29	0.048	197.0	0.020	77.8	63.4	0.81
BD-2L-4S	200	263	3.4	14.4	0.084	0.43	0.072	197.0	0.020	53.1	71.6	1.35

Note: V_{exp} = the experimental shear strength; V_{pred} = the predicted shear strength

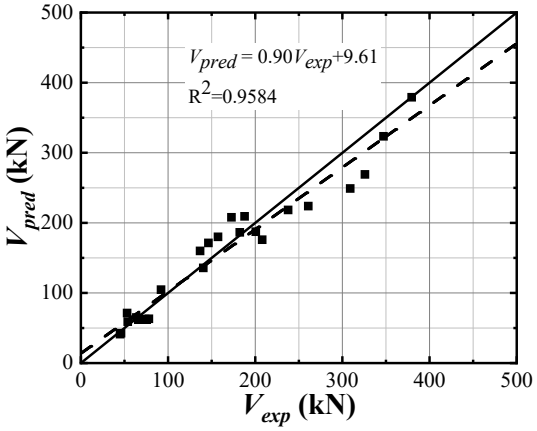

Fig. 3.14 Comparison between predicted and experimental shear strength.

Table 3.5 presents the shear strength of SRG-strengthened beams obtained using the proposed model, and the ratio of predicted to experimental results (V_{pre}/V_{exp}). A comparison between experimental and predicted shear strengths is illustrated in Fig 3.14. The results indicate that the proposed model accurately predicts the shear capacity, and the predicted values are conservative in most cases. The average and standard deviation (SD) of V_{pre}/V_{exp} are 0.99 and 0.15, respectively, with a correlation coefficient (R^2) between predicted and experimental shear capacities of 95.84%. In addition, the predicted shear strength values for the five beams tested in this study are consistently lower than the experimental results, a trend that contrasts with the more varied distribution observed in beams collected from other literature sources. This discrepancy may be attributed to the fact that the specimens tested in this study have the smallest effective depth and width in the entire database. Although the Eurocode 2 model accounts for size effects through the coefficient K, this factor may not fully capture the nonlinear scaling effects associated with smaller cross-sectional dimensions. Bazant and Planas (2019) emphasised that as beam size decreases, fracture energy dominates failure mechanisms, increasing crack tip energy release rates and enhancing arching action, which can lead to the underestimation of shear capacity in small beams by prediction models. Moreover, it is worth noting that the

validity of this model should be carefully evaluated for low-strength concrete, as empirical formulas may not reliably represent the actual behaviour of concrete with strengths below 17 MPa (Eurocode 2, 2005).

In this study, the influence of *a/d* is accounted for through the inclusion of correction factors R_c and R_f, as shown in Eqs. (3-18) and (3-19). These factors were derived from regression analysis of the experimental data, reflecting the distinct effects of *a/d* on the shear capacity of beams (arch or truss action) and the contribution of SRG jacketing. While the current model effectively incorporates these influences, the influence of *a/d* in other formulations remains less explored and warrants further investigation. Moreover, the high R^2 value observed between the predicted and experimental results not only indicates the model's ability to accurately capture the key parameters influencing shear strength but also reflects the limitations inherent to the dataset and assumptions. Considering the restricted dataset, further validation with a broader range of experimental configurations and material properties is required to fully assess and enhance the model's performance.

3.5 Conclusions

This chapter experimentally investigated the shear strengthening effectiveness of RC beams with different *a/d* ratios through external bonding of SRG under monotonic loading. Through a comparison with the performance of CFRCM and SRP-strengthened beams, the efficacy of the SRG system was analysed. The main conclusions drawn from this study are as follows:

- All systems effectively enhanced the strength capacity of shear deficient RC beams. For beams with *a/d=2.0* (Series A beams), the strength increased by 90-124% and 119-176% for SRG and SRP systems, respectively. The shear strength increases in CFRCM strengthened beams was 107-174%. For beams *a/d=3.5* (Series B beams), the strength increased by 164-170% and 221% for U-shaped SRG and SRP systems, respectively, while the shear strength increase in U-shaped CFRCM was 204-215%.
- As the shear span ratio increased, a decrease in the shear strength of the strengthening system was observed, while the proportion of shear contribution provided by the strengthening system increased. This is related to the dominant

shift in the load-carrying mechanism of the beam from an arch effect to a truss effect when transitioning from deep beams (Series A) to slender beams (Series B).

- Regarding the SRG systems, the utilization of UHTSS with a density of 3.14 cords/cm posed certain challenges in terms of the mortar's ability to penetrate the small gaps between successive cords. As a result, it is advisable to opt for textiles with lower density for similar applications. On the contrary, the implementation of UHTSS with a density of 3.14 cords/cm proved to be highly effective in the SRP jacketing application (i.e. resin matrix). In comparison, CFRCM and SRP systems demonstrate an advantage in shear strength enhancement, while the SRG system holds an advantage in improving ductility.
- All U-shaped jacketed beams exhibited shear-detachment failure independently of the type of jacket (SRG, SRP, CFRCM). However, in the case of SRP jacketing, detachment occurred by tearing off large parts of the concrete cover and concrete core due to the high adhesion offered by the resin matrix. The fully wrapped beams were able to modify the failure mode from brittle to ductile and demonstrated a high energy absorption capacity.
- The proposed analytical model, accounting for the influence of *a/d*, effectively predicts the shear capacity of SRG-strengthened, stirrup-free RC beams in the database. The average and standard deviation (STD) of V_{pre}/V_{exp} are 0.99 and 0.15. However, its applicability to low-strength concrete (below 17 MPa) should be approached with caution. Considering the limited dataset, further experiments are necessary to expand the database and validate the model.

Chapter 4

Effectiveness of SRG Jackets in Shear Strengthening of RC Beams under Fatigue Loading

Based on the existing literature, research on the fatigue response of shear-deficient RC beams strengthened with Steel Reinforced Grout (SRG) systems remains scarce. To further evaluate the performance of SRG strengthening systems, this chapter investigates the shear behaviour of SRG-strengthened beams under fatigue loading, providing valuable insights into failure modes and generating data to support fatigue design. For comparison, the performance of Carbon Fiber Reinforced Cementitious Matrix (CFRCM) and Steel Reinforced Polymer (SRP) strengthening systems is also evaluated.

A total of nine beams were tested: two control beams and seven U-shaped SRG-strengthened beams. The key research parameters include shear span ratio (2.0 or 3.5), UHTSS textile density (1.57 or 3.14 cords/cm), fibre type (UHTSS or carbon), and matrix type (resin or mortar). The results confirm the effectiveness of the strengthening systems and highlight the significant influence of the *a/d* ratio on fatigue behaviour. Beams with smaller *a/d* ratios experience higher shear stresses, accelerating fatigue damage and leading to earlier failure. Additionally, high-density UHTSS textiles

exhibited poor bonding with mortar, resulting in premature failure. A prediction method for the shear fatigue life of SRG-strengthened beams is also proposed based on fracture mechanics.

4.1 Experimental Programme

4.1.1 Specimen Details and Test Setup

The experimental program comprised 9 rectangular RC beams, divided into two series (A and B) based on their a/d ratios of 2.0 and 3.5, respectively. Series A included five beams, while Series B included four beams. Each series included one control sample, while the remaining beams in each series were strengthened with a U-shaped FRCM system. In this fatigue study, only U-shaped strengthened beams were considered. Because fully wrapped configurations, though effective, are impractical in real engineering applications. Fully wrapped beams were included in the static tests primarily to prevent premature debonding of the strengthening system and to evaluate the ultimate performance of this configuration under monotonic loading.

The geometric properties and material characteristics of the specimens remain consistent with those described in Chapter 3. The naming convention is also similar to that used in the static tests. However, to distinguish the fatigue study specimens, the symbol 'U' (indicating the U-shaped configuration) has been omitted. For instance, the specimen labelled A-C-3 in this chapter corresponds exactly to A-C-U3 in Chapter 3, both representing a beam strengthened with three layers of CFRCM. The detailed information for the beams tested in this chapter is provided in Table 4.1.

Table 4.1. Applied fatigue load range of beams.

Series	Beam	Type of strengthening	P_{max} (kN)	Applied fatigue load (kN)			
				P_l	P_h	Amplitude	Mean
A (a/d=2.0)	A-N	-	51.3	15.4	35.9	20.5	25.7
	A-GL-2	2-layed low density SRG	109.8	32.9	76.9	44.0	54.9
	A-GH-1	1-layed high density SRG	97.5	29.2	68.2	39.0	48.8
	A-PH-1	1-layed high density SRP	112.5	33.7	78.7	45.0	56.3
	A-C-3	3-layed CFRCM	120.2	36.0	84.1	48.1	60.1
B (a/d=3.5)	B-N	-	38.8	11.6	27.2	15.5	19.4
	B-GL-2	2-layed low density SRG	102.6	30.8	71.8	41.0	51.3
	B-GH-1	1-layed high density SRG	105.0	31.5	73.5	42.0	52.5
	B-PH-1	1-layed high density SRP	120.9	36.3	84.6	48.4	60.5

4.1.2 Test Setup and Procedure

As shown in Figure 4.1, All beams were tested under the three-point loading using a stiff steel reaction frame, in which a vertically positioned servo-hydraulic actuator with a capacity of 500 kN was employed. The beams were placed on two steel supports secured to a solid floor with threaded rods. Additional constraints were applied at the beam ends to prevent unexpected rotation during fatigue testing. Specifically, two wooden plates were positioned on each side of the supports and clamped against the beam to restrain lateral movement and ensure stability throughout cyclic loading. The beams were subjected to fatigue loading until failure, with a maximum cycle limit of 2 million cycles (Chaallal et al., 2010). If the beams did not fail under fatigue loading, they were then tested under monotonic loading.

During fatigue testing, all specimens were loaded at a frequency of 4 Hz (Banjara and Ramanjaneyulu, 2020; Garcez et al., 2021). This relatively low frequency was chosen to reduce the occurrence of hysteresis effects, lack of full recovery between successive cycles, and undesirable heating (Gagani et al., 2019). Moreover, it has been demonstrated in studies that the loading frequency of vehicles ranges from 0.159 to 8.724 Hz when traveling at speeds between 2 km/h and 110 km/h (Oudah and El-Hacha, 2012), while traditional RC building structures usually experience frequencies in the range of 1 to 5 Hz (Garcez et al., 2021). Therefore, the selection of 4 Hz can provide a more realistic simulation of traditional RC structures.

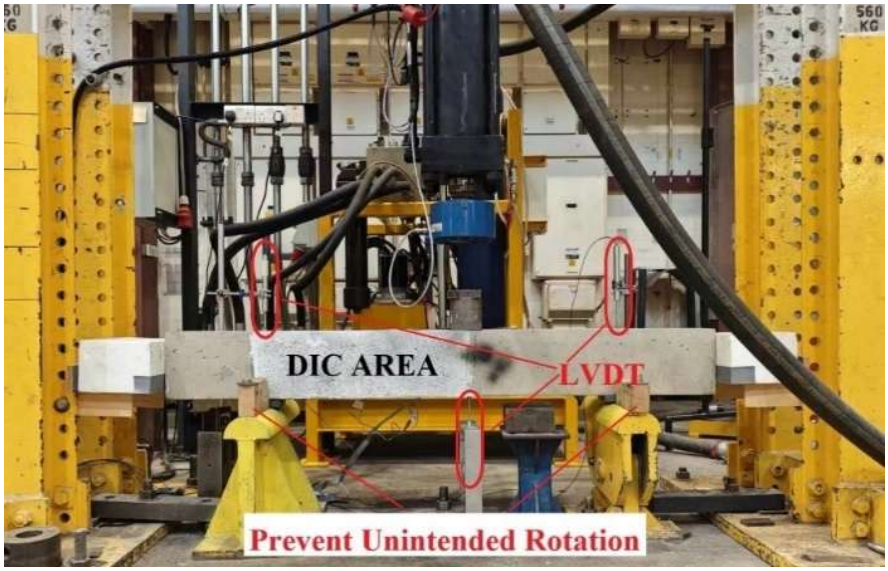

Fig. 4.1 Three-point bending test set-up of beams.

According to *fib* 2001 (2001), the range of applied fatigue loads (P_l to P_h) can be calculated as $P_l = P_{mean}(1 - \text{DAF})$ and $P_h = P_{mean}(1 + \text{DAF})$, where DAF represents the dynamic amplification factor and ranges from 0.25 to 0.4; P_{mean} corresponds to 50% of the total shear resistance (P_{max}) of the specimens. The value of P_{peak} for all specimens was obtained from previous studies on beams with the same strengthening configuration under static loading conditions (El-Saikaly and Chaallal, 2015), and detailed results of the static loading tests can be found in the Chapter 3. The DAF was selected as 0.4, lead to a fatigue load range of 30% to 70% P_{max} for each beam. Table 4.1 shows the applied fatigue load range and strengthening configuration of beams.

Similar to static tests, an external Linear Variable Differential Transducer (LVDT) was employed at the load application point to monitor the vertical deflection of the beam during loading. Two LVDTs were placed on the beams (on both sides) at the support location to ensure that there was no unexpected movement of the beam. Additionally, Digital Image Correlation (DIC) technology was utilised to capture the strain distribution of the beams tested. To achieve this, the shear critical region of each beam was painted with a speckle pattern using a special brush and black ink. A high-performance camera was placed to capture deflection changes of the speckled region at the rate of one photo every 8 cycles in the first 10,000 cycles, and the subsequent cycles were recorded every 1000 cycles. Subsequently, the high-resolution speckle images were analysed using DIC software.

4.2 Results and Discussion

Table 4.2 presents a summary of the test outcomes, including the concrete compressive strength of all beams on the test day (f_c), the fatigue life (N_f), the total deflection (δ) and the stiffness degradation (β) at the last cycle, as well as the failure mode. Due to limitations in the machine, the load for the first 30 cycles was slightly lower than setting. The symbols used in Table 4.2 correspond to the following failure modes: S represents shear failure, that is, the failure caused by diagonal tension, fibre rupture, etc; SD stands for shear-detachment failure, that is, shear failure occurs when detachment occurs either between the composite and the beam substrate or within the mortar layer. In general, the experimental results demonstrated that, apart from the

single-layer high-density SRG system, all jacketing increased the fatigue life of RC beams with shear defects.

Table 4.2. Summary of test results

Series	Specimens	f_c (MPa)	N (cycles)	δ (mm)	β (%)	Failure Mode
A	A-N	24.7	75	3.81	56.0	S
	A-GL-2	25.0	227	4.74	40.4	SD
	A-GH-1	25.1	29	3.79	22.9	SD
	A-PH-1	27.1	2,165	4.23	37.3	SD
	A-C-3	25.3	152,654	6.08	38.9	SD
B	B-N	24.4	12,525	1.61	30.4	S
	B-GL-2	26.7	21,935	3.71	26.9	SD
	B-GH-1	27.2	25	3.79	53.7	SD
	B-PH-1	26.0	60,895	7.01	44.8	SD

Note: S is shear failure; SD stands for shear-detachment failure.

4.2.1 Failure Modes and Crack Evolution Analysis

Figure 4.2 provides a comprehensive visualisation of both the final failure states and the strain evolution in the tested beams. The first column presents the physical condition of each beam at the end of testing, while the subsequent images show transverse strain fields obtained from DIC at two critical stages: the onset of visible damage and the point near or after failure. All beams demonstrated shear-dominated failure, and no fracture of the longitudinal steel reinforcement was observed upon removal of the protective layer.

The control beams, A-N and B-N, demonstrated an identical failure mode, characterised by a characteristic diagonal tension failure within the shear span between the points of load application and support. Although due to the different stress and strain responses of deep beams (A series) and slender beams (B series), the number of load cycles that B-N endures is much greater than that of A-N. Throughout the cyclic loading process, the gradual accumulation of damage led to a progressive decline in the shear bearing capacity of the A-N. This deterioration initiated the formation of diagonal cracks within the central region of the strengthening zone. Subsequently, in an exceptionally short span of time, the cracks swiftly propagated across the entire cross-section, ultimately culminating in the beam's failure during the 74^{th} cycle and12530^{th} cycle for A-N and B-N, respectively. DIC diagrams indicate that the control beams A-N and B-N, although lacking visible cracks at the 30th and 12,000th

cycles respectively, exhibited strain patterns in the mid-section of the shear-deficient region that closely resembled the final inclined shear crack.

The failure modes of reinforced beams in Series A are shown in Figs. 4.2(b-e). The beams strengthened by the SRG system (A-GL-2 and A-GH-1) exhibited similar failure modes. Upon multiple loading cycles, small cracks started to appear in the middle region of the SRG jacket, and as the cycles progressed, these cracks gradually expanded and formed a main crack perpendicular to the ground. Eventually, along this crack, a substantial detachment of the textile-mortar layer within the SRG jacket occurred, leading to the sudden failure of the beam. Furthermore, noticeable shear diagonal cracks were observed on the surface of the beam after removing the SRG system. This detachment-shear failure can be attributed to the significant disparity between the stiffness of the SRG system and the beam, which affects the stress distribution and causes differential responses between the strengthening system and the substrate, resulting in detachment. In addition, the beam reinforced with two layers of low-density SRG, BML, failed in the 213^{th} cycle, demonstrating the effectiveness of the SRG system in enhancing fatigue performance. On the other hand, the beam reinforced with one layer of high-density SRG, A-GH-1, failed after only 26 cycles, significantly fewer than A-N. This can be primarily attributed to the small gaps present in the high-density UHTSS, which hindered the infiltration of mortar, thus affecting the adhesion between the textile and mortar, ultimately leading to premature detachment of the jacket. Moreover, A-MH-1 experienced much higher loads than A-N, accelerating its accumulation of damage.

The SRP-strengthened beam (A-PH-1) experienced a resemble shear failure of the SRG system, but the detachment occurred between the SRP jacket and the substrate. It is noteworthy that A-PH-1 failed after 2164 cycles, which is significantly better than the SRG system. This indicates that the resin, the fine matrix, can penetrate the gaps in UHTSS more effectively than mortar, enhancing the adhesion between the textile and the matrix and significantly delaying the detachment of the strengthening system. This phenomenon also explains why detachment primarily occurs at the SRP-substrate interface rather than at the textile-matrix interface in the SRP system.

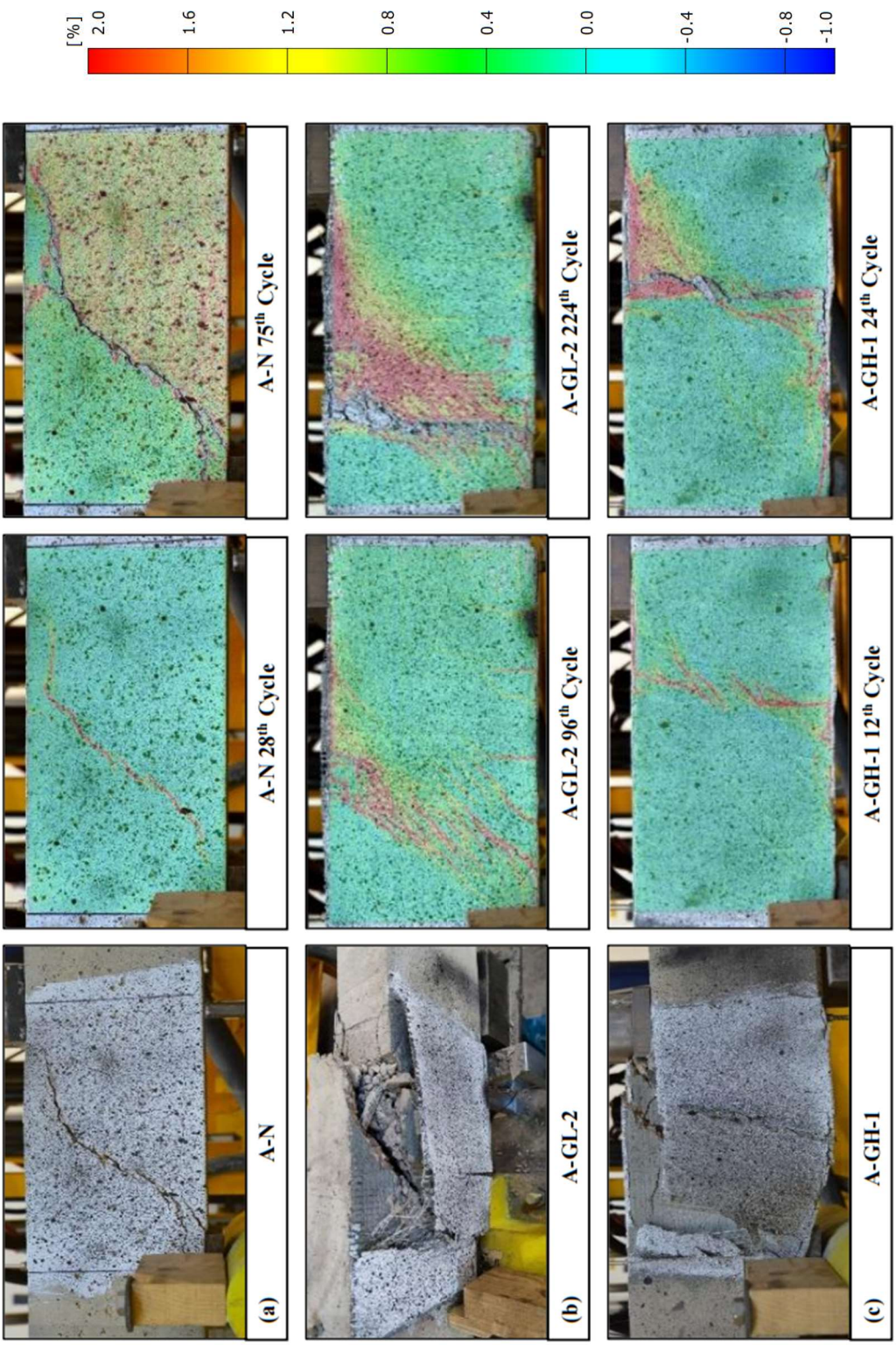
[%]
2.0
1.6
1.2
0.8
0.4
0.0
-0.4
-0.8
-1.0
A-N 75th Cycle
A-GL-2 224th Cycle
A-GH-1 24th Cycle
A-N 28th Cycle
A-GL-2 96th Cycle
A-GH-1 12th Cycle
(a) A-N
(b) A-GL-2
(c) A-GH-1

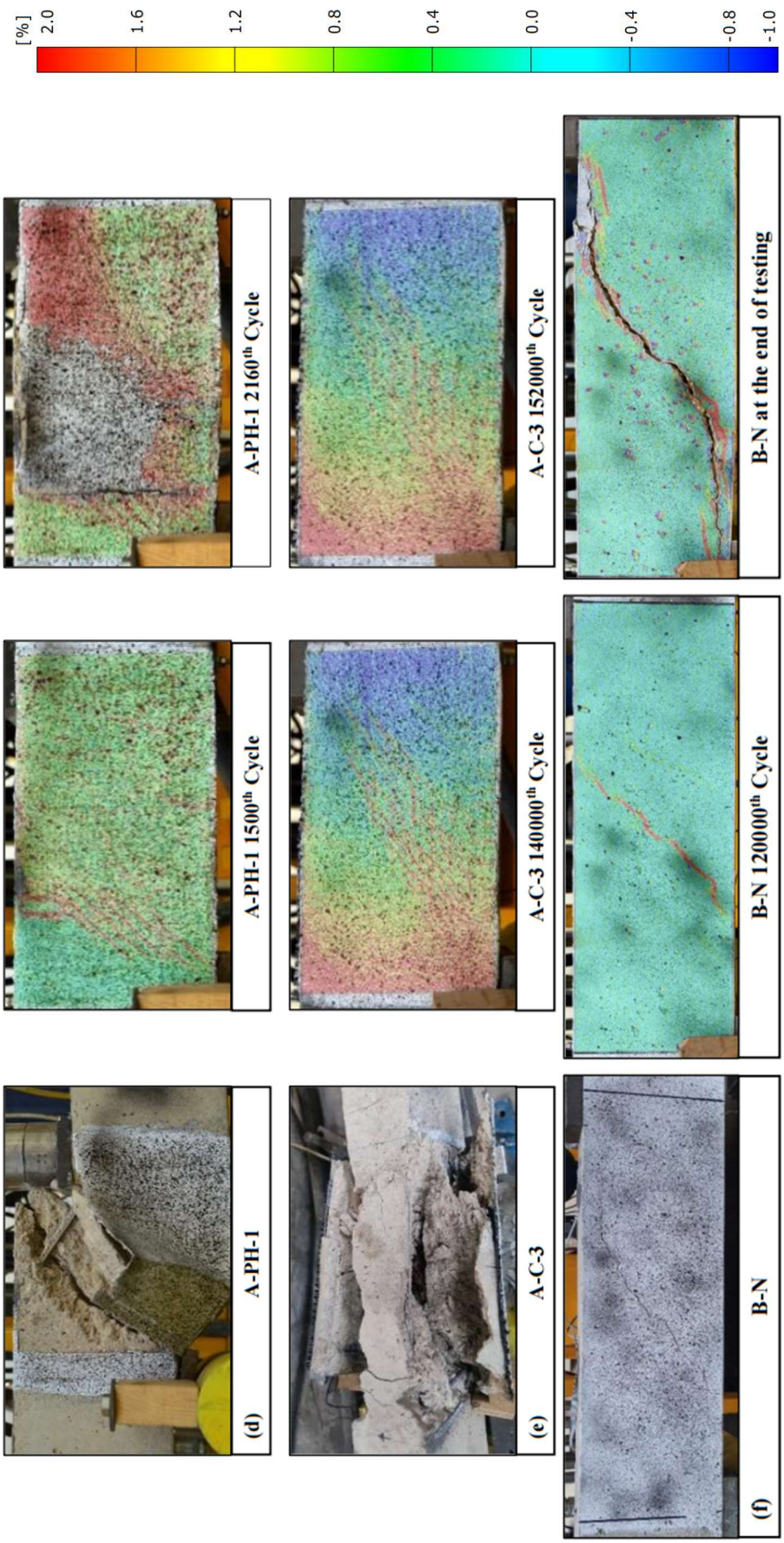
[%]
2.0
1.6
1.2
0.8
0.4
0.0
-0.4
-0.8
-1.0
A-PH-1 2160th Cycle
A-C-3 152000th Cycle
B-N at the end of testing
A-PH-1 1500th Cycle
A-C-3 140000th Cycle
B-N 120000th Cycle
(d) A-PH-1
(e) A-C-3
(f) B-N

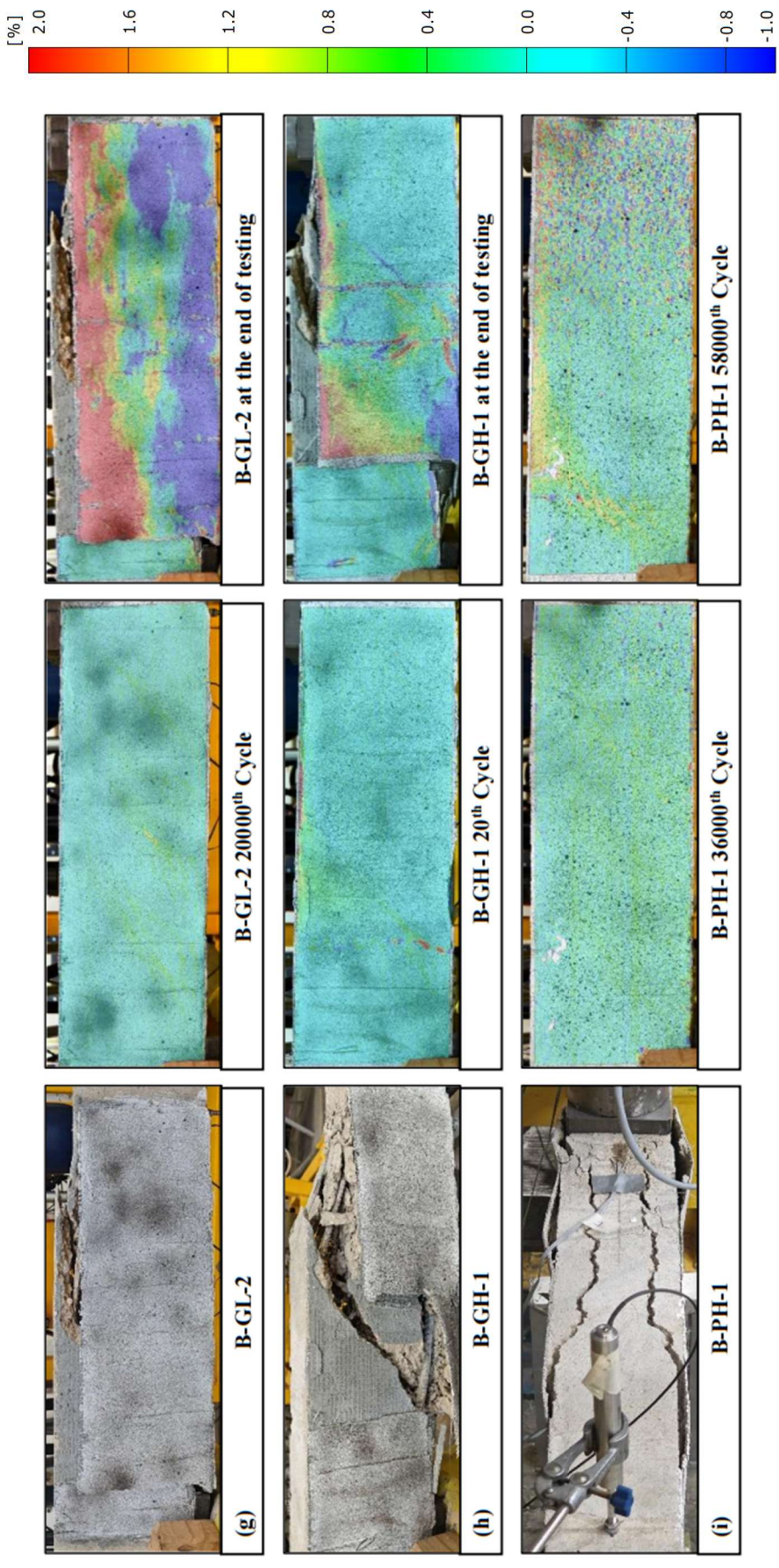

Fig. 4.2. Failure modes and transverse strain contours in the critical shear span at failure of the beams: (a) A-N; (b) A-GL-2; (c) A-GH-1; (d)A-PH-1; (e) A-C-3; (f) B-N; (g) B-GL-2; (h) B-GH-1; (i) B-PH-1.

In the case of the CFRCM system in series A, A-C-3 failed after 152,647 cycles. Unlike the SRP and SRG systems, CFRCM jacket's surface did not exhibit prominent cracks during cycling. However, it experienced cracks on the upper surface of the beam's strengthening region. Around the 80,000th cycle, distinct cracks emerged on both sides of the protective layer, spanning almost the entire region. Over time, these cracks gradually widened, and at the 152,647th cycle, the CFRCM jacket suddenly detached, resulting in beam failure. During detachment, a significant portion of the beam's cover layer was peeled off, exposing the undamaged longitudinal reinforcements. Although the three-layer CFRCM system had higher stiffness compared to the SRP and SRG systems, considering the substantial difference in fatigue life, it can be concluded that CFRCM demonstrates the most effective enhancement in fatigue performance.

For the strengthened beams in Series B (Figs. 4.2(g-i)), shear failure occurred for all cases with detachment of the jacket from the substrate (including part of the concrete cover layer). The failure modes of SRG strengthened beams in series B mirrored those of the corresponding specimens with $a/d = 2.0$. In the SRP-strengthened beam B-PH-1, significant detachment of the SRG jacketing, along with a substantial portion of the protective layer from the substrate, was observed around 53,000 cycles. Despite this, the beam did not completely fail and continued to bear the designated load with noticeable increased beam's deflection was evident. Ultimately, the beam experienced complete failure at 60,895 cycles. The specimen strengthened with a single layer of high-density SRG system, B-GH-1, still failed prematurely due to early detachment, occurring as early as the 28th cycle. In contrast, both B-ML-2 and B-PH-1 significantly improved the fatigue life of the beams. Additionally, regardless of whether it was from Series A or Series B, the SRP system exhibited extensive peeling of the concrete cover layer at failure. This phenomenon was less common in the SRG-reinforced systems, where failure primarily involved separation between the mortar and the UHTSS textile. This observation further underscores the superior adhesive properties of the resin in bonding the substrate to the UHTSS.

In the DIC results, all strengthened beams exhibited more distributed strain patterns compared to the control specimens, indicating that the composite systems effectively reduced stress concentrations at crack initiation zones. This contributed to a more

uniform stress distribution and delayed the onset of failure. Furthermore, beams in Series B showed significantly lower strain levels prior to failure than those in Series A. The smaller inclination angle between the principal strain direction and the fibre alignment in Series B resulted in reduced tensile demand along the fibres, thereby mitigating stress accumulation and delaying jacket debonding.

4.2.2 Fatigue Behaviour

Figure 4.3 presents the load-displacement response, as well as the displacement (δ) at P_h, stiffness degradation (β) with an increase in a number of cycles under the fatigue of the control beam and the strengthened beams. The left plots show the load-deflection behaviour for various cycle intervals up to the cycle just before failure. Since the applied load reached a stabilised state by the 30th cycle, the load-displacement curves for all specimens, except A-GH-1, were plotted starting from the 30th cycle. Due to the premature failure of A-GH-1 after only 29 cycles, its curve was plotted starting from the 18th cycle. On the right plots, δ and β for each cycle are automatically determined and computed using Python. The stiffness (K) is calculated as the ratio of the load range ($P_h - P_l$) to the corresponding displacement range ($\delta_{max} - \delta_{min}$) (Banjara and Ramanjaneyulu, 2019). As the number of cycles increases, the stiffness decreases, and β can be defined as:

$$\beta = \frac{K_1 - K_n}{K_1} \times 100\% \tag{4-1}$$

Where K_n is the stiffness of each cycle, K_1 is the stiffness of the first cycle.

The overall response of all tested beams exhibits a typical accumulation pattern of damage under fatigue loading, resembling the behaviour of typical reinforced concrete (RC) beams in the several previous studies (i.e., Xia et al., 2022; Al-Rousan and Issa, 2011). The specimens demonstrated an accelerated rate of damage propagation, characterised by three distinct stages in the overall response:

- Initial stage: during the initial cycles, the deflection and strain of various components, including the longitudinal reinforcement, strengthening system, and concrete, underwent a rapid increase due to the emergence of a significant number of initial cracks;

- Stable stage: the response shifted into a stable phase marked by a notable deceleration in the accumulation of damage. During this stage, the rate of increase in deflection and the degradation of stiffness decelerated. This stable phase persisted until the commencement of the final, brief stage preceding failure;
- Final stage: the tested beams experienced a sudden and marked surge in both deflection and stiffness degradation, ultimately leading to failure.

These three stages represent the characteristic fatigue response of the beams as they undergo progressive structural degradation. As shown in the load–deflection curves in Fig. 4.3, the initial, stable, and final stages are indicated in red, blue, and green, respectively, to illustrate their temporal evolution. Moreover, as the beams approach failure, there is a clear increase in deflection and a significant reduction in stiffness, as reflected in the decreasing slope of the ascending load segments.

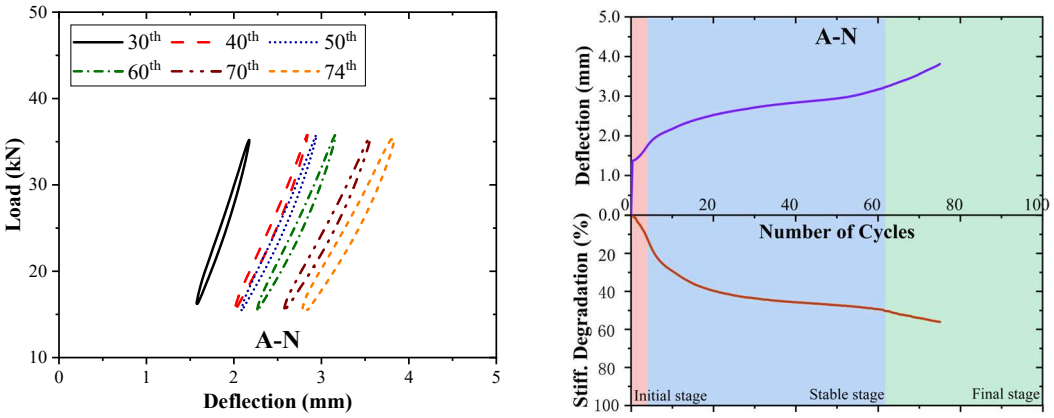

(a) Fatigue behaviour of A-N

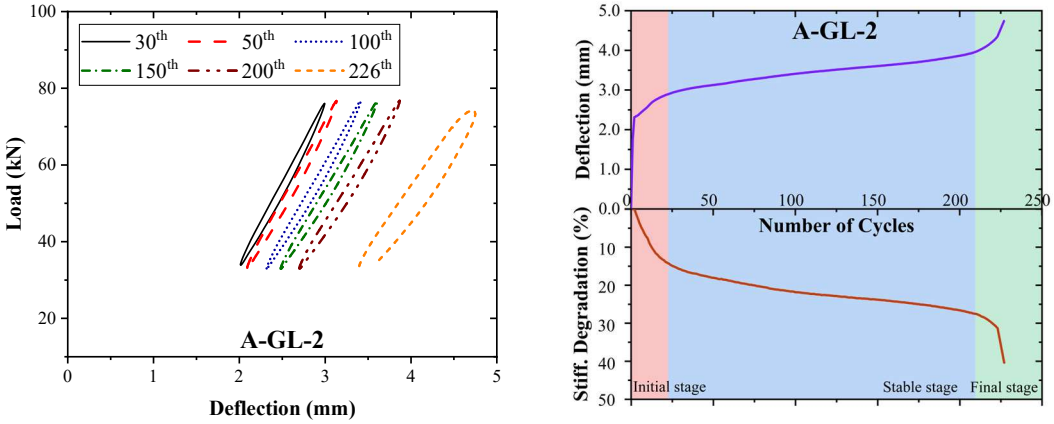

(b) Fatigue behaviour of A-GL-2

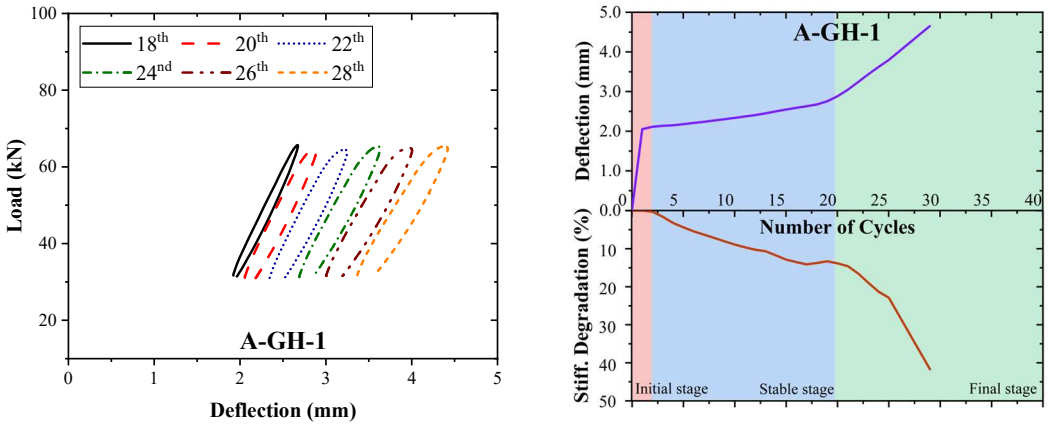

(c) Fatigue behaviour of A-GH-1

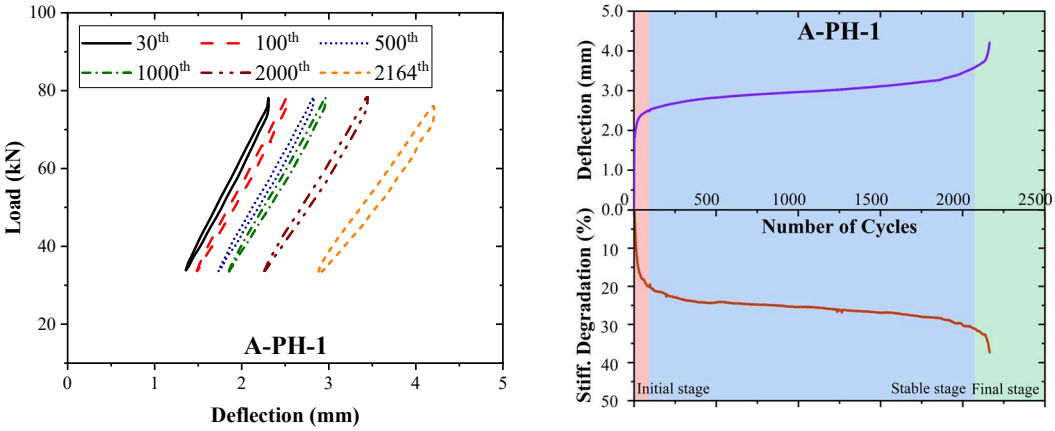

(d) Fatigue behaviour of A-PH-1

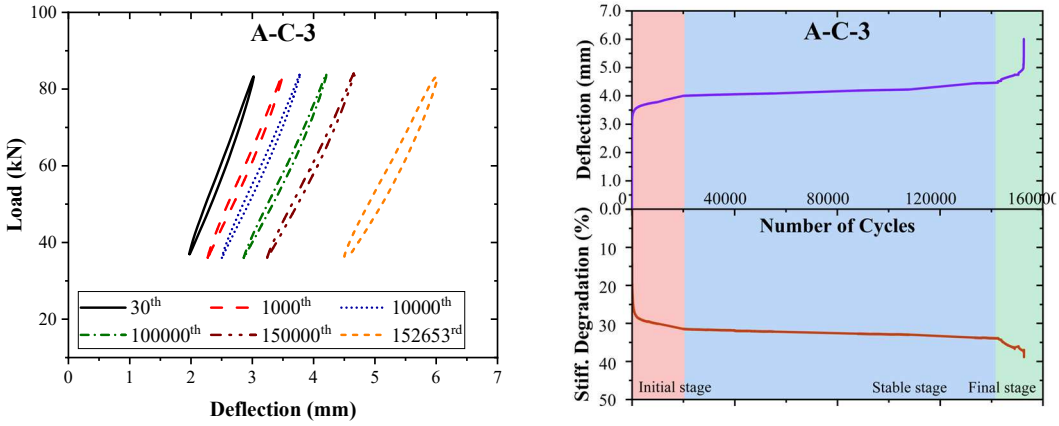

(e) Fatigue behaviour of A-C-3

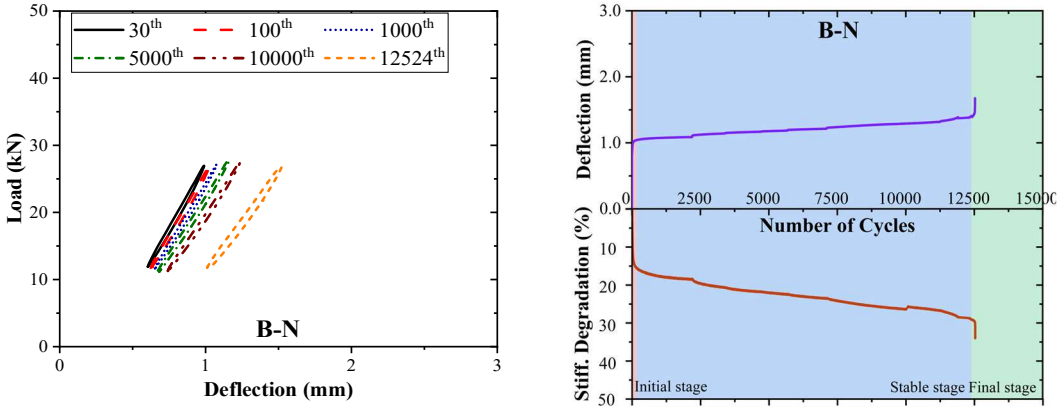

(f) Fatigue behaviour of B-N

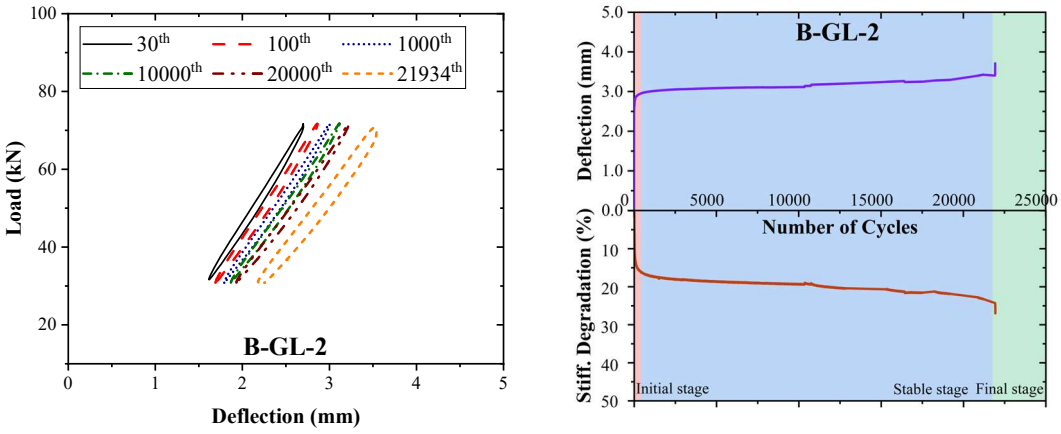

(g) fatigue behaviour of B-GL-2

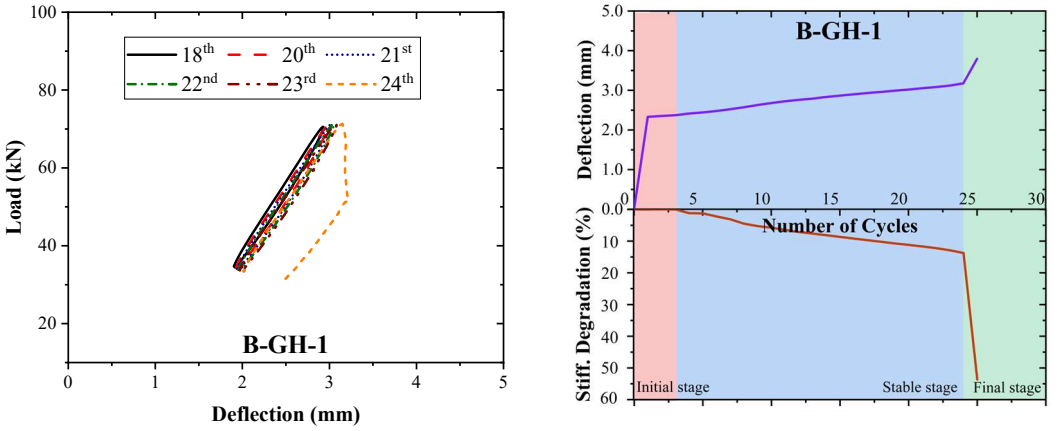

(h) fatigue behaviour of B-GH-1

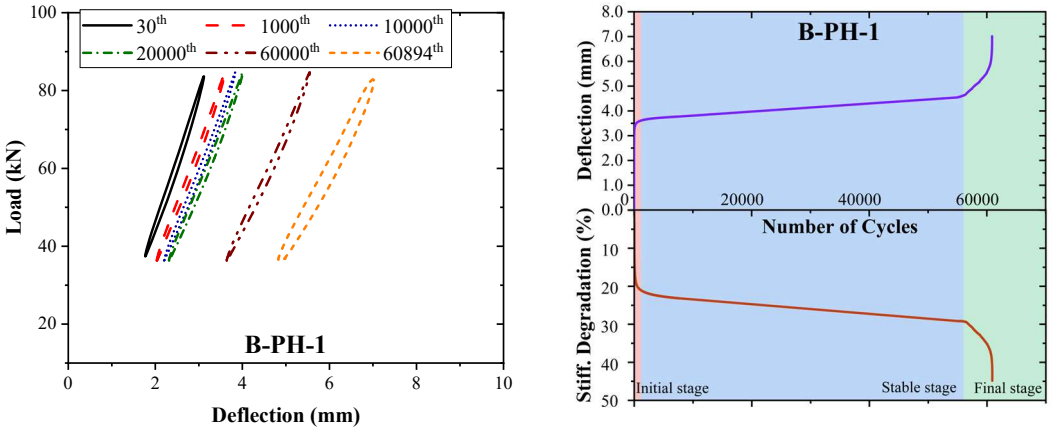

(i) fatigue behaviour of B-GH-1

Fig. 4.3. Fatigue behaviour of tested beams.

In series A (a/d = 2.0), the control beam A-N displayed substantial gaps in both the ascending and descending phases of the load-deflection curve, which indicates a higher level of damage in the control beam, emphasizing the importance of reinforcing systems. In contrast, the strengthened beams exhibited smaller gaps in their load-deflection curves. Particularly noticeable in A-PH-1 and A-C-3, their gaps remain minimal even when approaching failure, indicating that the strengthening systems

significantly enhance the toughness of the beams, thereby reducing the permanent deformation generated in each cycle. However, A-GH-1 demonstrated widder gaps in the load-deflection curve after 20 cycles. This behaviour can be attributed to premature separation between the high-density UHTSS and the mortar, resulting in accelerated damage accumulation and eventual failure of the BMH beam. The changes in deflection and load degradation with increasing cycles exhibited a similar pattern across all specimens. For instance, in the case of A-GL-2, δ increased from 1.74 mm in the first cycle to 2.80 mm in the 17th cycle, corresponding to a β of 12.5%. This period represented the initial stage of rapid stiffness degradation due to the generation of initial cracks. From cycle 18th until cycle 215th, BML entered the relatively stable second stage, with δ and β reaching 4.07mm and 28.5%, respectively. Finally, the beam underwent rapid deterioration within 13 cycles until it failed, with δ and β reaching 4.75 mm and 40.4%, respectively.

In Series B, the amplitudes of deflection and stiffness degradation during the final stage were higher compared to Series A. This suggests that an increase in the *a/d* ratio led to a slower rate of damage development during the stable stage, resulting in smoother curves and an extended fatigue life. Except for B-GH-1, all beams in Series B experienced significantly higher fatigue life compared to Series A. This phenomenon can be attributed to the fact that slender beams distribute a smaller portion of shear force in the reinforced area under the same load, thereby delaying shear failure to some extent. Although B-GH-1, similar to A-GH-1, failed due to noticeable premature detachment, their responses were significantly different. As shown in Fig. 4.3c, A-GH-1 exhibited detachment at the 18th cycle, with the degree of detachment gradually increasing, leading to a progressive increase in deflection and a decrease in stiffness until failure. In contrast, B-GH-1 showed no significant detachment before the 24^{th} cycle, but detachment suddenly appeared at the 24^{th} cycle, resulting in rapid failure. This difference in response can be attributed not only to the difference in adhesive force generated by the mortar but also to the fact that inclined cracks in the deep beams (Series A) are more inclined relative to the fibre alignment of the fabric (vertical direction), resulting in greater stress along the fibre direction and causing earlier detachment.

Moreover, when comparing the control beams, the strengthened beams demonstrate increased deflection and reduced stiffness degradation upon failure. This difference can be attributed to the improved beam ductility achieved through the implementation of strengthening systems, which enhanced the beam's ability to undergo greater deformations when subjected to seismic or other extreme loading conditions, thereby mitigating the risk of failure. The enhanced ductility of the beams contributes to their superior performance and structural integrity, highlighting the effectiveness of the strengthening techniques in enhancing the overall resilience and safety of the beams.

4.2.3 Strain Response of Strengthened Beams

Strain measurements obtained through Digital Image Correlation (DIC) have been shown to align well with those recorded by conventional strain gauges, confirming the reliability of DIC in structural applications (Dutton et al., 2014). Therefore, this study utilised DIC to capture the transverse strain variations in the strengthened beams. The strain for each sample, as shown in Fig. 4.4, represents the average of five equidistant points in the mid-section of the critical shear zone.

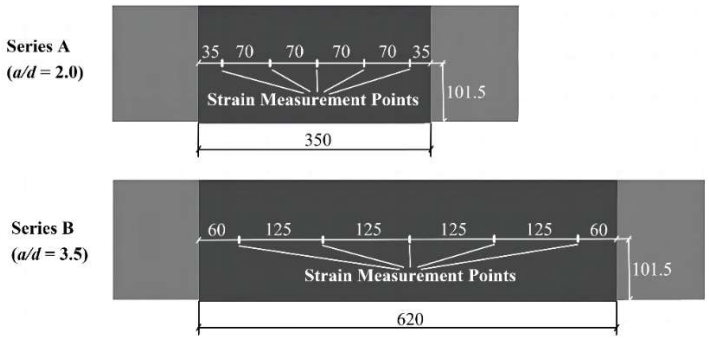

Fig. 4.4. Strain measurement points of strengthening system.

Figure 4.5 depicts the jacketing strain versus the number of cycles, and this strain includes the slippage of the strengthening system. Due to the limitations of the servo loading control system, the beams were sometimes loaded beyond failure until complete destruction. Consequently, the high-speed camera images captured at the point of failure may not accurately reflect the exact state at failure. Thus, the strain values at failure shown in Fig. 4.5 represent indicative trends rather than precise data. As shown in Fig. 4.5, the strain responses in all reinforcement systems exhibited a similar three-stage pattern, consistent with the deflection and stiffness degradation responses. Initially, during the early cycles, the strain increased rapidly, followed by a

relatively stable phase. Finally, just before failure, the strain increased sharply. When comparing the strain patterns of different reinforcement types within Series A and B, it is evident that the CFRCM system exhibited the highest strain, while the SRG system showed the least, demonstrating the superiority of the SRG system in controlling deformation. Furthermore, Series B displayed lower strain levels before failure compared to Series A, underscoring the impact of the shear span-to-depth ratio on beam response.

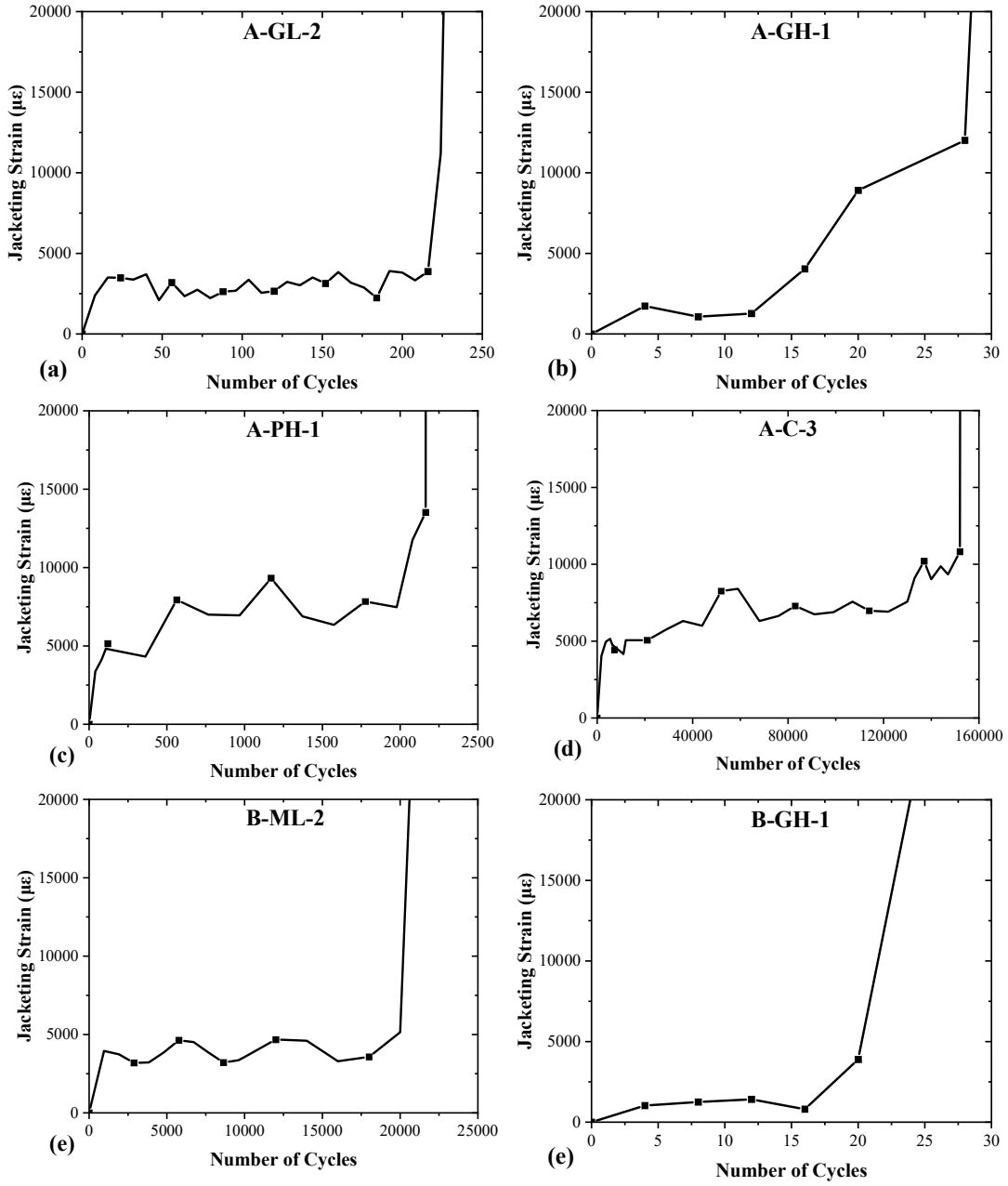

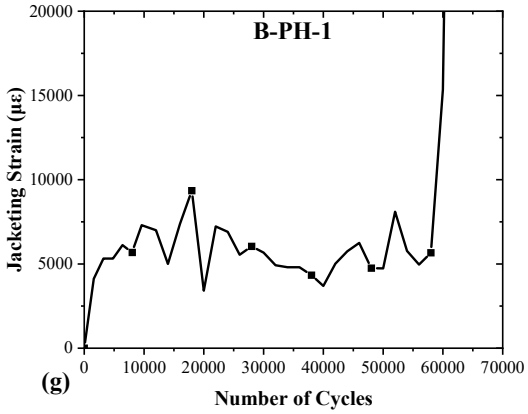

Fig. 4.5. Jacketing strain versus number of cycles.

4.2.4 Energy Dissipation

The energy dissipation (Ψ_d) was calculated for each cycle as the area enclosed by the load-deflection hysteresis loop during cyclic loading (D'Antino et al., 2015). To facilitate comparison, the cycle numbers for all beams were normalised, i.e., expressed as a ratio of the cycle number (N) to the total number of cycles (N_{tot}).

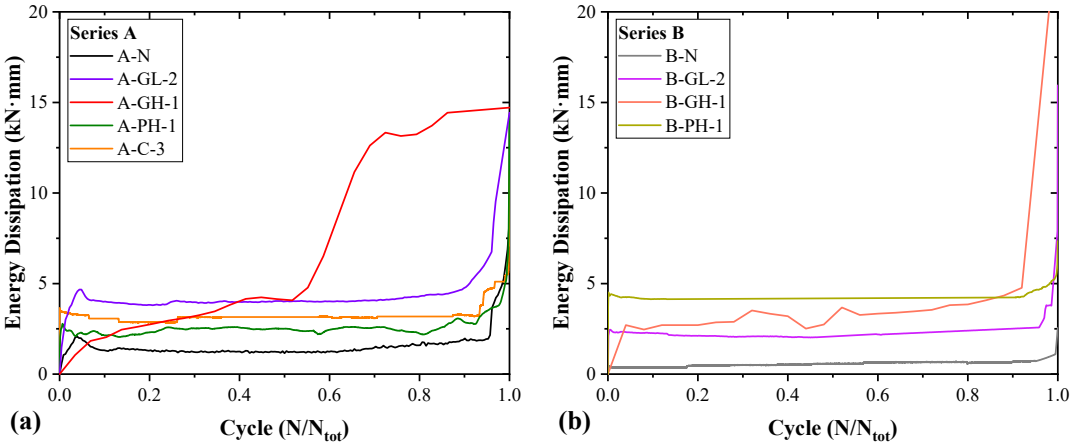

Fig. 4.6. Energy dissipation verse cycles curves: (a) Series A; (b) Series B.

The energy dissipation versus cycles for each beam is presented in Fig. 4.6. A three-stage trend similar to that observed in δ and β was noticed in the Ψ_d measurements of the tested beams. However, one notable exception was observed in the case of A-GH-1, which entered the third stage earlier in its overall fatigue life compared to the other specimens. This premature transition can be attributed to the inferior adhesion of the high-density SRG system again. Specifically, at 16 cycles (N/N_{tot}=0.55), A-GH-1 exhibited a certain degree of detachment, leading to a sudden dissipation of energy. Furthermore, the control beams A-N and B-N exhibited the lowest level of energy

dissipation among all the beams, due to the absence of a strengthening system, resulting in the lowest capacity for energy absorption. Additionally, control beams were subjected to the lowest applied load, and the fluctuations in P_h and P_l during the cyclic loading impact the value of the area enclosed in the load- deflection curve. In contrast, among the strengthened beams, both the SRP and CFRCM systems demonstrated lower energy dissipation compared to the SRG system, which indicates that these two systems effectively delayed the deterioration of the beam, resulting in longer fatigue life. When comparing the responses of Series A and Series B, it is clear that the increase in the *a/d* ratio (Series B) led to a more gradual development of damage and a smoother energy dissipation curve during the stable stage. This resulted in an extended fatigue life for the beams in Series B, except for the outlier B-GH-1.

4.3 Prediction of the Fatigue Life of SRG Jacketed Beams

4.3.1 *S-N* Curve

S-N curves are widely used to assess the fatigue life of concrete structures, where *S* refers to the cyclic stress level (Gallego et al., 2014, Xia et al., 2022). In the case of shear failure mode, the dominant factor leading to failure is no longer the longitudinal reinforcement, therefore, *S* can be calculated as follows (Mahal et al., 2013):

$$S = \frac{\sigma_h}{f_{fu}} = \frac{P_h}{P_{max}} \tag{4-2}$$

Where σ_h is the maximum applied fatigue stress; f_{fu} the ultimate strength of the beam. In general, the relationship between *S* and *N* can be considered as Gallego et al. (2014):

$$S = A - \alpha LogN \tag{4-3}$$

Where A and α are the parameters calculated by the least squares method based on the experimental data. Based on this, Mode Code 2010 proposed an S-N relationship equation for concrete without shear reinforcement (Walraven, 2010):

$$S = 1 - \frac{1}{10} LogN \tag{4-4}$$

Figure 4.7 illustrates the *S-N* relationship of the beams under fatigue loading. Although this method is the mainstream approach for fatigue life prediction (Gallego et al., 2014, Xia et al., 2022), it is evident that it is not suitable for this project. The

limited number of current tests is insufficient to determine whether the *S-N* curve can be applied to predict the fatigue durability of SRG shear-strengthened beams.

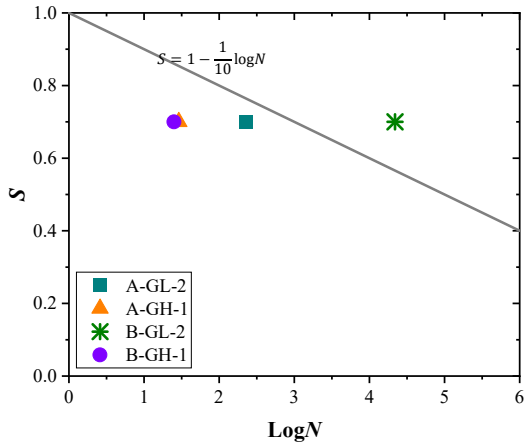

Fig. 4.7. S-N relationship of SRG strengthened beams.

4.3.2 Fracture Mechanics Model

In the linear elastic fracture mechanics, the Paris Law is a power law that relates the debonding growth rate per cycle, da/dN, to the stress intensity factor range, $\Delta K = K_{max} - K_{min}$ (D'Antino et al., 2015). Based on experimental observations of FRP-concrete double-lap shear specimens, Diab et al. (2009) proposed a fracture mechanics model grounded in the Paris Law, which links the debonding growth rate to the energy ratio for FRP strengthened concrete members:

$$\frac{da}{dN} = m_1 \left(\frac{G_F^{Fatigue}}{G_F} \right)^{n_1} \beta_F \tag{4-5}$$

where the coefficients m_1, n_1, and β are determined from experimental data; $G_F^{Fatigue}$ and G_F represent the energy release associated with the maximum load of the cycle and the fracture energy associated with the debonding phenomenon under quasi-static monotonic loading, respectively. The coefficient β_F accounts for the phenomenon of reduced crack propagation rate as the debonded area increases. Since $G_F^{Fatigue}$ has not been extensively studied, Carloni and Subramaniam (2013) noted that $G_F^{Fatigue}$ and G_F are directly related to the applied load during cyclic loading and the load-bearing capacity in quasi-static tests, respectively. They also observed that the strain distribution across the width of the FRP plate remains unchanged under fatigue loading.

Consequently, Carloni and Subramaniam (2013) refined this model to incorporate the effects of load amplitude and mean applied load:

$$\frac{da}{dN} = \overline{m_1}\left(\frac{\alpha\sqrt{\Delta P \cdot P_{mean}}}{P_{max}}\right)^{\overline{n_1}} \overline{\beta_F} \tag{4-6}$$

Where $\Delta P = P_h - P_l$; the coefficients $\overline{m_1}$ and $\overline{n_1}$ are derived from experimental data; the coefficients $\bar{\beta}$ is taken as 1 (D'Antino et al., 2015). The frequency factor α accounts for the dependence of fracture characteristics on loading frequency. According to D'Antino et al. (2015), the value of α is 1 at 5 Hz and 0.96 at 3 Hz; for this study at 4 Hz, α is approximately 1.

This model is based on the fracture mechanics properties of the strengthening system and the substrate, making it applicable to various RC elements, such as FRP-reinforced beams and joints (Li et al., 2021, Carloni and Subramaniam, 2013). In addition, D'Antino et al. (2015) have extended this model to predict the fatigue life of FRCM-concrete joints, and this study aims to extend it to the fatigue life prediction of SRG-strengthened beams for the first time. To simplify calculations, it is assumed that at the point of fatigue failure, the entire effective bond length (L_e) of the SRG system debonds, and the degradation of the effective bond length increases linearly with the number of fatigue cycles. At the point of sample failure:

$$\frac{da}{dN} = \frac{L_e}{N} \tag{4-7}$$

According to Chen and Teng (2003a), L_e can be calculated as

$$L_e = \sqrt{\frac{E_f n t_f}{\sqrt{f_c}}} \tag{4-8}$$

Where E_f is the elastic modulus of the fabric. Figure 4.8 illustrates the relationship between L_e/N and $\sqrt{\Delta P \cdot P_{mean}}/P_{max}$ of SRG strengthened beams. Due to the significant differences in adhesion between the high-density SRG and the substrate, and the low-density SRG and the substrate, their fatigue responses are notably different. Therefore, in the analysis of the relationship between L_e/N and $\sqrt{\Delta P \cdot P_{mean}}/P_{peak}$, these two groups are treated separately to predict fatigue life (N_{GH} for high-density and N_{GL} for low-density SRG strengthened beams). It is important to note that the model proposed by Diab et al. (2009) has not been extensively studied, and the data obtained

in this study are insufficient to fully characterise the coefficients and validate the equation. Consequently, the two fatigue life prediction expressions in Fig. 4.8 should be considered preliminary examples of this model's application, and further research and validation are necessary to establish the model's robustness. For instance, the relationship between degradation of the effective bond length and the number of fatigue cycles should exhibit a three-phase change consistent with stiffness reduction and deflection behaviour, so whether this degradation can be simplified to a linear relationship to achieve accurate predictive results remains a subject for further investigation.

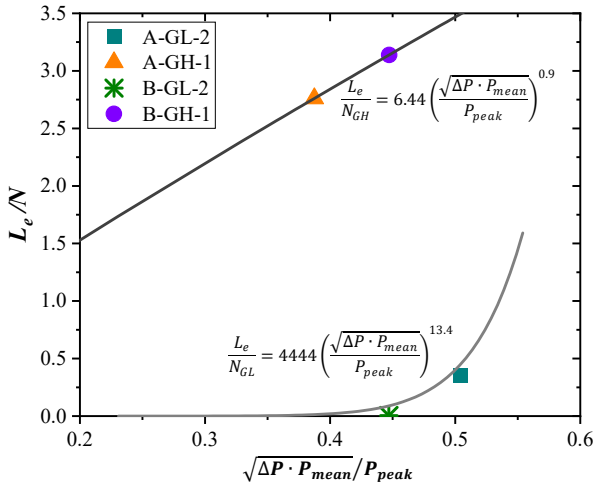

Fig. 4.8. Relationship between L_e/N and $\sqrt{\Delta P \cdot P_{mean}}/P_{peak}$ of SRG strengthened beams.

4.4 Conclusions

This chapter investigates the performance of RC beams reinforced with SRG, SRP, and CFRCM under fatigue loading. The experimental program involves testing 9 full-scale beams subjected to a 4Hz load ranging from 30% to 70% of P_{max}. Based on this study, the following conclusions can be drawn:

- Series A, the control beam failed after 75 cycles. Except for the high-density SRG system, all strengthening systems extended the fatigue life of shear-deficient RC beams. The high-density SRG reinforced beam failed after only 29 cycles due to poor adhesion from the prevention of mortar penetration by high-density UHTSS. In contrast, the SRP system showed significantly improved performance, failing after 2165 cycles compared to 227 cycles for the low-density SRG system. This

suggests that resin, as a dense matrix, is more effective for bonding with UHTSS, reducing stress concentration and enhancing fatigue performance. The CFRCM system exhibited the best strengthening effect, failing after 152,654 cycles, despite its higher stiffness compared to the other systems.

- In Series B, the control beam failed after 12,525 cycles. The high-density SRG system, similar to Series A, showed poor performance, failing after 25 cycles due to inadequate adhesion. The SRP system demonstrated significant improvement, with the beam failing after 60,895 cycles, highlighting the resin's effectiveness in bonding with UHTSS. The low-density SRG system also performed better in Series B than in Series A, with the beam failing after 21,935 cycles, showing that lower-density UHTSS allows better mortar penetration and adhesion.

- Comparing Series A and Series B reveals that the *a/d* ratio significantly impacts the fatigue performance of strengthened RC beams. The SRP system, with its excellent bonding properties, consistently outperformed the SRG system, especially under high cycle loads. The CFRCM system in Series A exhibited the highest fatigue life, indicating its potential for long-term structural reinforcement. In addition, similar trends were observed in terms of deflection, stiffness degradation, strain in the strengthening system, and energy dissipation of the tested beams with cycles increasing: in the first stage, initial cracks appeared, leading to rapid degradation of the beams; subsequently, the beams entered a long stable period with slow linear damage accumulation; finally, the degradation rate of the beams accelerated abruptly until failure.

- A prediction formula for the shear fatigue life of SRG strengthened beams based on the fracture mechanics is proposed. However, due to limited data, further validation of its effectiveness is necessary. This can be achieved through additional experimental fatigue testing on beams with varied configurations, as well as numerical simulation using calibrated finite element models to verify the consistency of predicted fatigue life against observed failure patterns and cumulative damage progression.

Chapter 5

Effectiveness of HPFRC Jackets under Monotonic and Fatigue in Shear Strengthening of RC Beams Loading

As a mortar-based composite, High-Performance Fibre Reinforced Concrete (HPFRC) has gained attention for structural strengthening and repair due to its excellent mechanical properties, durability, and resistance to environmental degradation. Unlike the FRCM systems discussed in Chapters 3 and 4, HPFRC jacketing enhances stiffness, strength, and crack control through fibre bridging mechanisms. However, based on the literature review, research on HPFRC-strengthened beams remains limited, particularly regarding their fatigue shear behaviour. To address this knowledge gap, this chapter analyses RC beams strengthened with HPFRC jackets under both static and fatigue loading conditions. The experimental program investigates 10 beams, focusing on two key parameters: the shear span-to-depth ratio (a/d = 2.0 and 3.5) and HPFRC thickness (10mm and 20mm).

The results show that under static loading, HPFRC jacketing increased the shear strength of RC beams by 95% to 130%, with the strengthening effect decreasing as the *a/d* ratio increased. Under fatigue loading, the HPFRC jackets significantly improved the beams' fatigue life. Similar to the observations in Chapter 4, the beams exhibited a three-stage behaviour in terms of deflection, stiffness degradation, and energy dissipation.

5.1 Experimental Programme

5.1.1 Specimen Details

The experimental investigation assessed ten RC beams under three-point bending conditions. Out of this set, five beams were subjected to monotonic loading tests, while the remaining five, identical in specifications, were tested under fatigue loading. Within the subset of five beams subjected to monotonic testing, three beams were characterised by a *a/d* of 2.0 (Group A), and the remaining two had a *a/d* of 3.5 (Group B). As shown in Fig. 5.1, the geometric properties of the specimens remain consistent with those described in Chapter 3 and 4. All beams, except for the two control beams, were strengthened in the shear-deficient regions using U-shaped HPFRC jacketing. When applying UHPFRC jackets, the near-surface mounted (NSM) technique is utilised. In this method, the concrete cover in the beam's strengthening area is removed, and grooves are created where the UHPFRC jacket is directly cast during the strengthening process. Compared to the externally bonded (EB) technique, the NSM approach offers several advantages, including enhanced protection of UHPFRC reinforcement from environmental degradation and a reduced risk of debonding between the strengthening material and the concrete substrate (Chellapandian et al., 2017).

Figure 5.1c illustrates two strengthened configurations: HPFRC jackets with 10 mm and 20 mm thicknesses. All the beams except the four control beams were strengthened in the shear critical zone. Grooves with a depth equal to the cover thickness (10 mm) in the shear critical area of the retrofitted beams were created (Fig. 5.2a). The grooved surface was then roughened, cleaned, and water-saturated before HPFRC was applied. Next, the jacket's mould was out in place in the critical zone, and the HPFRC was

poured (Figs. 5.2b and c). The mould was removed after two days, and the beams were covered with plastic film and cured until the testing time (Fig. 5.2d).

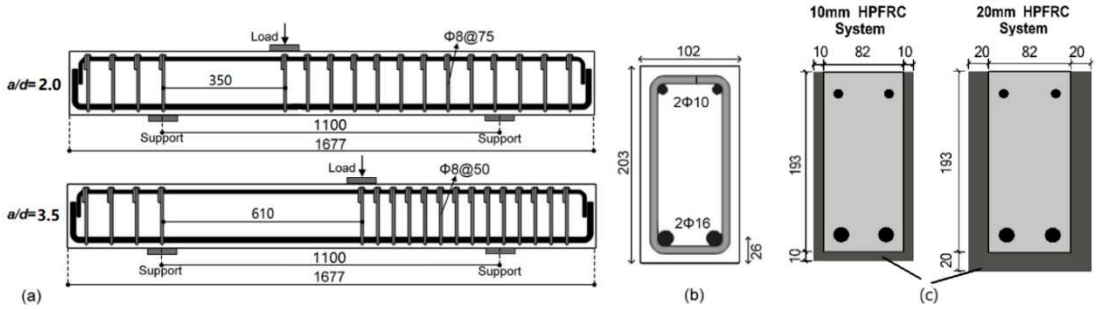

Fig. 5.1. Beam Details: (a) Layout of the reinforcement of the beams; (b) Cross section; (c) Strengthening configurations.

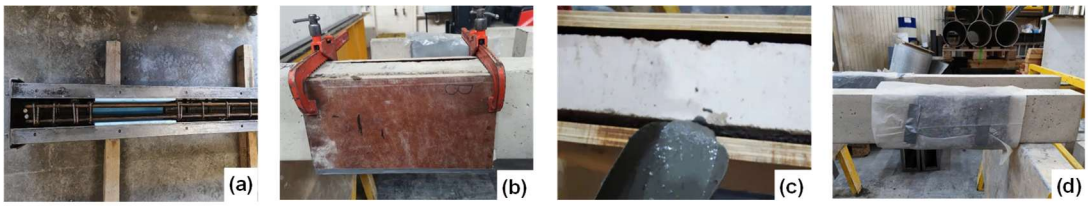

Fig. 5.2. Steps of the hybrid jacketing application: (a) create a grooved beam; (b) fix the jacketing mould; (c) pour HPFRC; (d) curing.

Table 5.1 summarises the tested beams under monotonic loading tests, which were labelled as 'X-UY'. 'X' denotes the beam group, where 'A' indicates the beam with a shear span of 2.0, while 'B' indicates the beam with a shear span of 3.5. 'U' refers to U-shaped jackets; 'Y' corresponds to the beam jacketing configuration, in which 'N' represents the control beam, '10' denotes beams with 10 mm HPFRC jacketing, and '20' corresponds to beams with 20 mm HPFRC jacketing. The specimens tested under the fatigue loading are identical; however, the symbol 'U' has been omitted in their naming for distinction.

Table 5.1. Details of the specimens.

	Name	**Jacketing Type**
Group A (a/d = 2.0)	A-N	Control beam
	A-U10	10 mm HPFRC
	A-U20	20 mm HPFRC
Group B (a/d = 3.5)	A-N	Control beam
	A-U10	10 m HPFRC

5.1.2 Material Properties

The properties of concrete and steel reinforcement are detailed in Section 3.2. In the HPFRC system, steel fibres were incorporated into the High-Performance Concrete (HPC) with a volume fraction of 1.66%. According to the manufacturer, the 28-day standard compressive strength and elastic modulus of the HPFRC can reach 106.5 MPa and 43 GPa, respectively. The geometric and mechanical properties of HPC (Kerakoll, 2024a) are detailed in Table 5.2, while Table 5.3 summarises the properties of the steel fibre (Kerakoll, 2024b), with all data sourced directly from the manufacturers.

Table 5.2. Properties of the HPC used according to the manufacturer.

	Mixture Density (kg/cm3)	f_{cm} **(MPa)**	f_f **(MPa)**	f_b **(MPa)**	E_f **(GPa)**
HPC	2270	110	14	2	34

f_{cm} = compressive strength (28 d); [2] f_f = flexural strength (28 d); [3] f_b = bond strength (28 d); [4] E_d = elastic modulus

Table 5.3. Properties of the HPC used according to the manufacturer.

	Shape	**Diameter (mm)**	**Length (mm)**	f_{fu} **(MPa)**	E_f **(GPa)**	ε_{fu} **(%)**
Steel Fibre	straight rigid	0.2	13	3100	200	1

$f_{fu,f}$ = tensile strength; ε_{fu} = fibre's strain to failure

5.1.3 Test Setup

All beams were tested under three-point bending using a rigid steel reaction frame equipped with a vertically positioned servo-hydraulic actuator with a capacity of 500 kN. The beams were placed on two steel supports, which were secured to a strong floor using threaded rods. Additional constraints were applied at the beam ends to prevent unexpected rotation during fatigue testing. Vertical displacements during loading were monitored using a LVDT positioned at the loading point, while two additional LVDTs were placed on the supports to monitor settlement. Furthermore, Digital Image Correlation (DIC) technology was employed to capture strain distribution in the shear-critical regions of the tested beams.

Static Loading Test: Consistent with Chapter 3, the tests were conducted under displacement control at a rate of 0.02 mm/s. A high-speed camera captured images of the critical shear regions every 2 seconds to enable subsequent DIC analysis.

Fatigue Loading Test: Following the method described in Chapter 4, the beams were subjected to cyclic loading until failure, with an upper limit of 2 million cycles. If a beam did not fail under fatigue loading, a subsequent monotonic loading test was performed until failure. The fatigue load range for each beam was set between 30% and 70% of Pmax at a frequency of 4 Hz. For Digital Image Correlation (DIC), images were captured at a frequency of one image every 8 cycles during the initial 10,000 cycles and subsequently recorded every 1,000 cycles. High-resolution speckle images were analysed using DIC software to assess strain distribution. The fatigue loading parameters were selected to minimise hysteresis effects, avoid undesirable heating, and realistically simulate the loading conditions of conventional reinforced concrete structures. Further details and justification are provided in Section 4.1.2.

5.2 Results and Discussion

5.2.1 Static Tests

Table 5.4 summarises the test results such as the peak load (P_{max}) and the corresponding displacement (δ_{max}); the strength increase of the retrofitted beams ($\Delta P_{max} = (P_{RET} - P_{CON})/P_{CON}$; where P_{RET} and P_{CON} are the peak load of the retrofitted and the corresponding control beam); the ultimate load P_u=(80%P_{max}) and the corresponding displacement δu; the shear strength of the critical shear span (V; for the control specimen it is equal to V_{CON}; for the retrofitted specimens it is equal to V_{RET}); the shear strength provided by the HPFRC system V_{FRC}(= $V_{RET} - V_{CON}$; where V_{RET} and V_{CON} are the shear strength of the retrofitted and the corresponding control beam); the displacement ductility (μ_δ); and the failure mode. The 'SH' in failure mode corresponds to shear failure.

Table 5.4. Summary of monotonic loading test results.

Series	Beam	f_c (MPa)	P_{max} (kN)	ΔP_{max} (%)	P_u (kN)	δ_{max} (mm)	δ_d (mm)	V (kN)	V_{FRC} (kN)	V_{FRC}/V (%)	μ_δ	Failure Mode
A	A-N	26.4	51.3	-	41.1	2.50	3.96	35.0*	-	-	-	SH
	A-U10	30.6	113.7	122	91.0	4.93	6.30	77.5$	42.5	55	1.72	SH
	A-U20	28.4	117.8	130	94.2	4.34	6.53	80.3$	45.3	56	2.04	SH
B	B-N	24.2	38.8	-	31.2	1.41	1.50	16.9*	-	-	-	SH
	B-U10	26.7	75.5	95	60.4	4.34	5.43	32.9$	16.0	49	2.06	SH

* V_{CON}; $ V_{RET}.

The displacement ductility (μ_δ) of a structural element quantifies its deformation capacity and is defined as the ratio of displacement at ultimate load (δ_u) to the displacement corresponding to the yield load (δ_y) (Shang et al., 2020). In accordance with the recommendations outlined in ASCE/SEI Standard 41-06 (2007), the displacement ductility was conceptually formalised by approximating the experimental load-deflection curve with a bilinear model. As depicted in Fig. 5.3, the yield point for non-ideal elasto-plastic elements was identified based on the energy equivalence method, which subsequently facilitated the derivation of the displacement ductility for the tested samples (Shang et al., 2020). The ductility indices were not calculated for control beams A-N and B-N because they did not exhibit ductile behaviour.

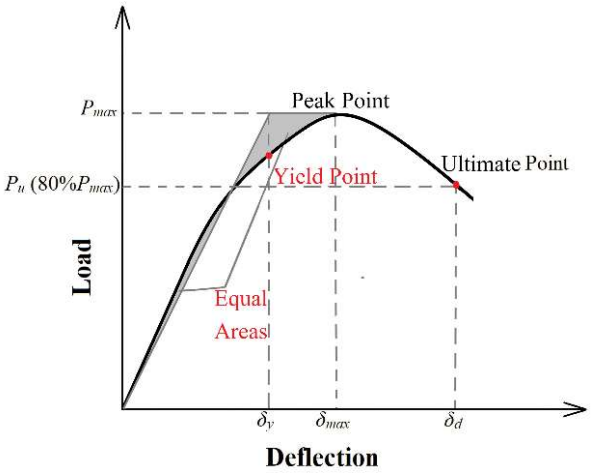

Fig. 5.3. Determination of yield and ultimate point.

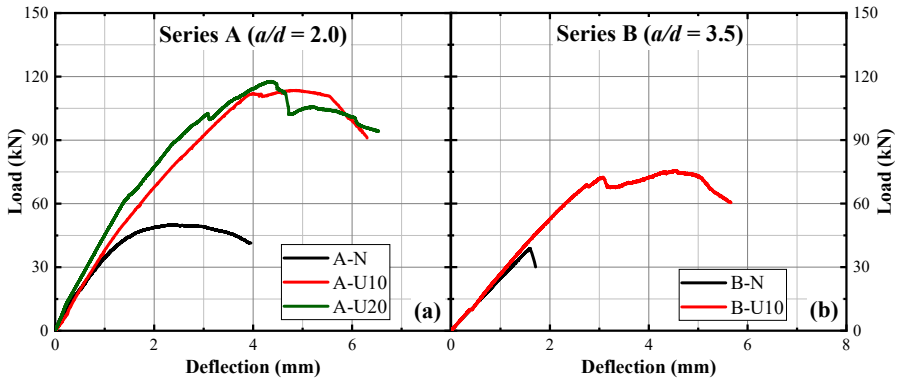

Fig. 5.4. Load-deflection curves under monotonic loading: (a) Series A; (b) Series B.

The load-deflection curves for 5 tested beams under monotonic loading are shown in Fig. 5.4. Regarding series A (a/d = 2.0), the control beam failed in shear at a peak

load of 51.3kN (corresponding displacement of 2.5mm). The HPFRC jacketing has substantially increased the peak load capacity of RC beams. Specifically, beams A-U10 and A-U20 demonstrated peak load increases of 122% and 130%, respectively, compared to the control beam A-N. This marked improvement is attributed to the fibre 'bridging effect', which facilitates the distribution of stress across developing cracks, thereby fortifying the structural integrity and delaying the onset of failure. Furthermore, the greater peak load observed for the 20 mm HPFRC jacketing (A-U20) compared to the 10 mm jacketing (A-U10) can be technically explained by improved fibre distribution and reduced fibre aggregation in thicker jackets, resulting in enhanced mechanical interlock and more effective crack bridging. Additionally, the increased jacket thickness notably improved the stiffness of beam A-U20 by increasing its effective moment of inertia and restraining deformation more effectively.

In Series B (a/d = 3.5), the 10mm HPFRC jacketing (B-U10) led to a 48% increase in peak load. With the escalation of the a/d ratio (from 2 to 3.5), there was a noticeable decline in V, ΔP_{max} and V_{JAC}/V, highlighting the diminished reinforcement efficacy of HPFRC as a/d increased. This phenomenon occurs because the beam changes from a deep to a slender shape, shifting the main way it supports weight from an arch-like structure to more of a truss system, which decreases its ability to resist shear forces (Tetta et al., 2018a; Wakjira and Ebead, 2020). In detail, for Series A beams (a/d = 2, deep beams), arching action dominates after the formation of diagonal cracks. The majority of the load is directly transferred from the point of application to the support via the diagonal strut, indicating that the diagonal strut primarily bears the load (Wakjira and Ebead, 2020). The influence of arching action diminishes with an increase in the a/d ratio, thereby reducing the contribution of concrete to shear strength. In addition, the larger shear span increases the likelihood of shear damage, impairing the bond between the jacket and substrate, facilitating detachment (Wakjira and Ebead, 2020). Compressive struts in deep beams (a/d = 2) can effectively transfer loads directly to the supports, enabling the HPFRC jacket to bridge and restrain diagonal cracking with greater efficiency. In contrast, slender beams (a/d = 3.5) exhibit more dispersed shear cracking and elevated shear stress concentrations near the supports, which can weaken the bond at the jacket–substrate interface and lead to premature debonding. These phenomena are supported by the localised strain patterns captured

in Fig. 5.5 through Digital Image Correlation (DIC), which clearly highlight regions of early damage initiation.

As shown in Fig. 5.4, all strengthened beams demonstrated a pseudo-ductile behaviour and maintained the peak load while the beam deformed due to 'bridging effect'. This observation suggests the HPFRC system's pivotal role in augmenting the energy absorption and dissipation capabilities of the beams, directly impacting beams seismic performance resilience. This 'pseudo-ductile behaviour' is characterised by a gradual reduction in load-carrying capacity after the peak load, instead of a sudden brittle failure, due to the strain-hardening properties of HPFRC. The fibres embedded in the HPFRC matrix bridge developing cracks, enabling the material to sustain load beyond initial cracking. This enhances energy absorption capacity and promotes a more controlled and ductile failure mode (Bandelt and Billington, 2016). Such behaviour is particularly advantageous in seismic applications, where improved energy dissipation and deformation capacity are critical for structural resilience. From Table 5.4, the displacement ductility range of the strengthened beams lies between 1.72 and 2.06. Furthermore, the ductility increases with the augmentation of the UHPFRC jacket thickness and the ratio of *a/d*. This observation not only underscores the enhanced potential of the reinforcement system attributable to the increased thickness, but also validates the influence of altered load transfer mechanisms, resulting from variations in *a/d*, on ductility.

Figure 5.5 provides a comprehensive visualisation of both the final failure states and the corresponding strain evolution of the tested beams. The first column shows the physical condition of each specimen at the end of testing, while the subsequent images present the horizontal and vertical strain fields captured via Digital Image Correlation (DIC) at peak load. These DIC results offer valuable insights into the shear behaviour of HPFRC-strengthened beams, revealing more uniformly distributed strain fields in critical regions—highlighting the capacity of HPFRC to redistribute stresses and delay the onset of localised failure. As illustrated in Fig. 5.5, damage in all beams was localised within the shear-critical region. The control beams (A-N and B-N) exhibited typical diagonal tension failure along the shear span connecting the load and support points (Figs. 5.5(a, d)).

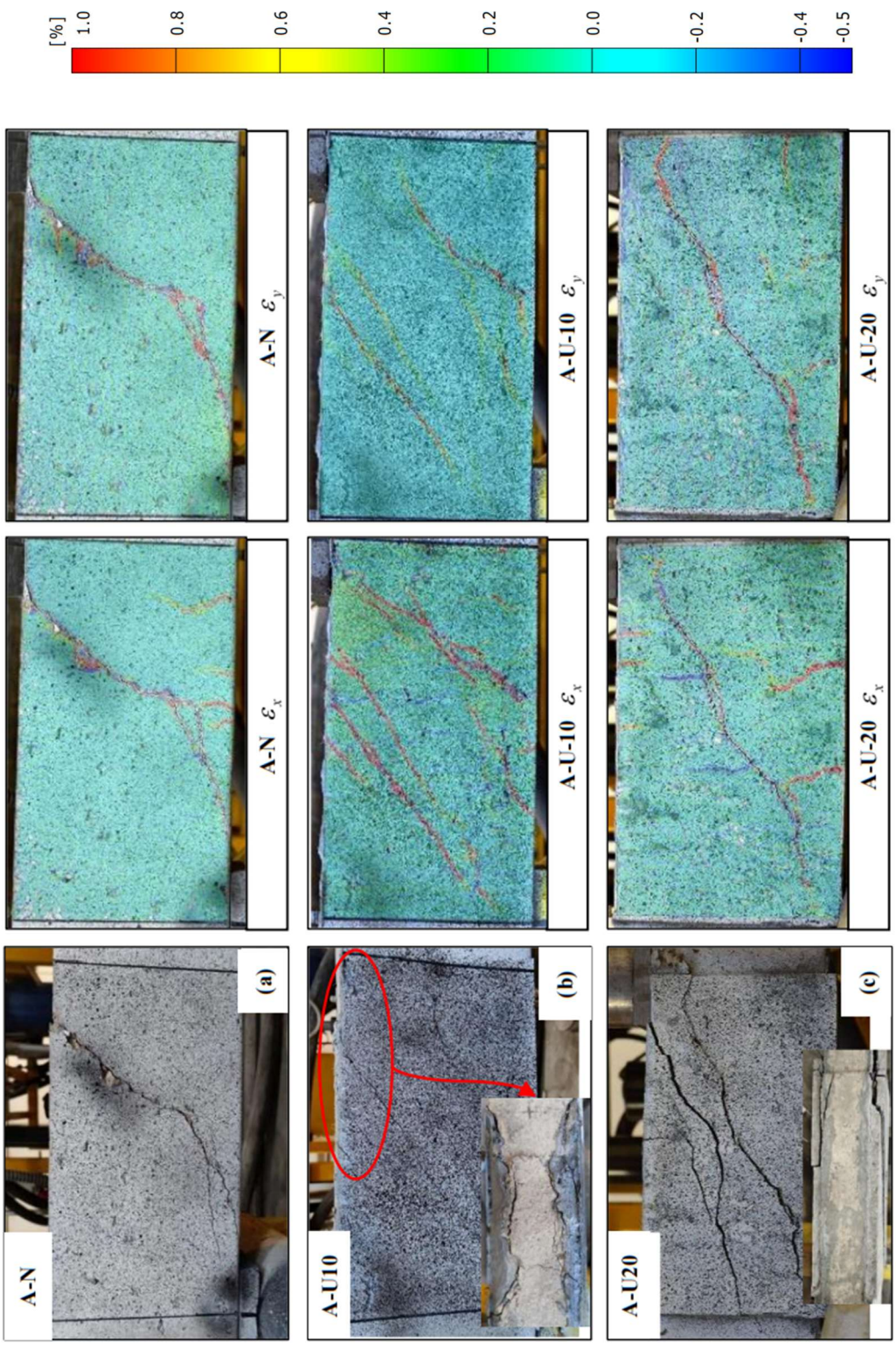
[%]
1.0
0.8
0.6
0.4
0.2
0.0
-0.2
-0.4
-0.5
A-N ε_y
A-U-10 ε_y
A-U-20 ε_y
A-N ε_x
A-U-10 ε_x
A-U-20 ε_x
A-N
(a)
A-U10
(b)
A-U20
(c)

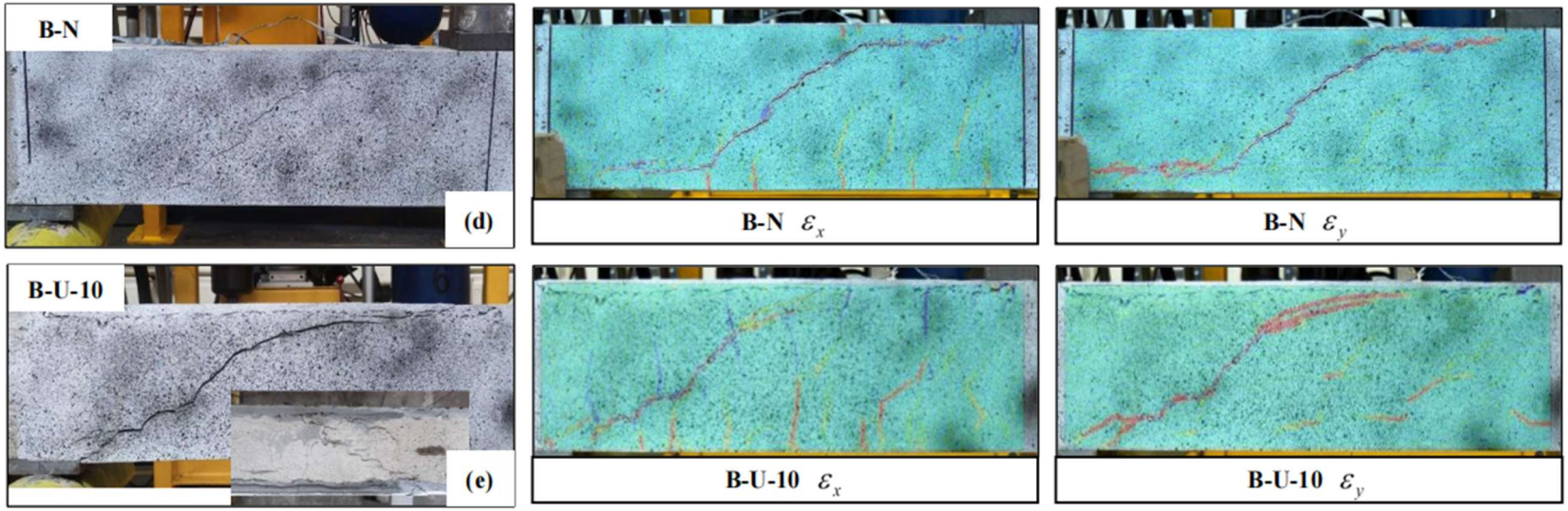

Fig. 5.5. Failure modes and strain contours in the critical shear span at failure under monotonic loading: (a) A-N; (b) A-10; (c) A-20; (d) B-N; (e) B-10.

In series A, the HPFRC-reinforced beams, A-U10 and A-U20 demonstrated similar failure modes (Figs. 5.5(c, d)), namely shear detachment failure with several diagonal shear cracks forming in the critical region. The observed gradual failure further corroborates that the strengthened beams exhibit pseudo-ductility. Additionally, the enhancement in ductility optimises the stress-strain transfer mechanism within the beams, resulting in multiple cracks on the HPFRC surface, as opposed to a single crack. The 20mm HPFRC system displayed enhanced crack visibility and jacket detachment. Despite improved adhesion due to superior fibre distribution within the 20mm HPFRC jacket, the marked stiffness contrast with the substrate resulted in a divergent load-stress response, exacerbating detachment issues relative to A-U10.

In the context of a higher *a/d* (3.5), B-U10 mirrored the control beam's failure mode. This is because the beam's changes to slender beams, leading to uneven stress distribution and a predisposition for cracks to propagate along singular paths of weakness (Mangalathu and Jeon, 2018). Consequently, the capacity of HPFRC to induce multiple cracking is mitigated, diminishing its potential to alter failure dynamics significantly.

5.2.2 Fatigue Tests

Fatigue test results are summarised in Table 5.5, including the concrete compressive strength of all beams on the test day (f_c), the fatigue life (N), the total deflection (δ), the stiffness degradation (β) at the last cycle and the energy dissipation (Ψ_d) at the last cycle, as well as the failure mode. Furthermore, as previously stated, the fatigue load range encompasses a span of 30% to 70% of P_{max}. Consequently, based on the outcomes of static testing, the loads applied to each beam are also delineated in Table 5.5.

Table 5.5. Summary of fatigue loading test results.

Series	Beam	P_l (kN)	P_h (kN)	f_c (MPa)	N (cycles)	δ (mm)	β (%)	Ψ_d (kN·mm)	Failure Mode
A	A-N	15.4	35.9	24.7	75	3.81	56.0	8.5	SH
	A-10	34.1	79.6	23.7	90	4.34	25.2	11.8	SH
	A-20	35.3	82.5	31.2	951	6.99	47.8	13.6	SH
B	B-N	11.6	27.2	24.4	12525	1.61	30.4	2.56	SH
	B-10	22.7	52.9	26.9	48786	4.79	48.8	7.42	SH

The results indicate that HPFRC jacketing enhanced the fatigue life and maximum deflection of shear-deficient beams, irrespective of their classification as Series A or B. Sample A-10 showed a fatigue life similar to that of the control beam, but it also demonstrated a 20% increase in the number of cycles. However, given the significantly higher load applied to A-10 in comparison to the control beam, it can be contended that the HPFRC system in A-10 maintained its effectiveness. Within Series A, increasing the thickness of HPFRC from 10mm to 20mm resulted in a substantial improvement in the fatigue behaviour of the RC beams, with the fatigue life increasing by almost 10 times. This improvement is attributed to the superior fibre distribution achieved with the thicker jacket, which aligns with observations from static loading tests. Furthermore, as the *a/d* ratio increased from 2.0 to 3.5, the performance of the 10mm strengthening system also improved. In Series B, B-10 exhibited even more

significant improvements in fatigue life (4 times) and maximum deflection than A-10, which is not only due to the different load-carrying mechanisms arising from varying *a/d* but also because the extended coverage of HPFRC provides a more pronounced enhancement in fatigue performance.

Figure 5.6 presents the load-displacement response, as well as the displacement (δ) at cap P sub h and stiffness degradation (β) with an increase in a number of cycles under the fatigue of the control beam and the strengthened beams. The left plots show the load-deflection behaviour for various cycle intervals up to the cycle just before failure. As the applied loads stabilised by the 30th cycle, load-displacement curves for all specimens are shown from this cycle. Beam A-20 exhibited significant cracking during the 14th cycle but continued normal operation after the 15th; thus, its curve starts from the 14th cycle to capture this change. The various of δ and β with the number of cycles are demonstrated on the right plots. Similar to the fatigue response of FRCM-strengthened beams, the specimens exhibited an accelerated rate of damage propagation, characterised by three distinct stages throughout the loading process: the initial stage, the stable stage, and the final stage.

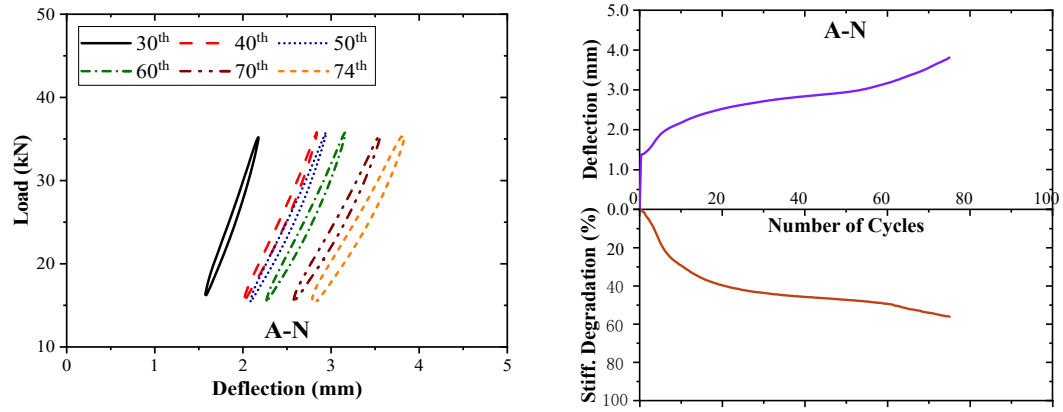

(a) Fatigue behaviour of A-N

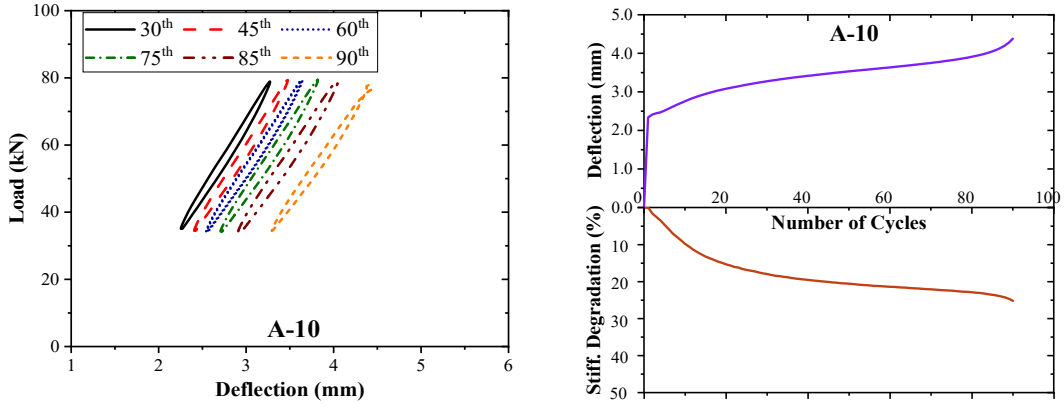

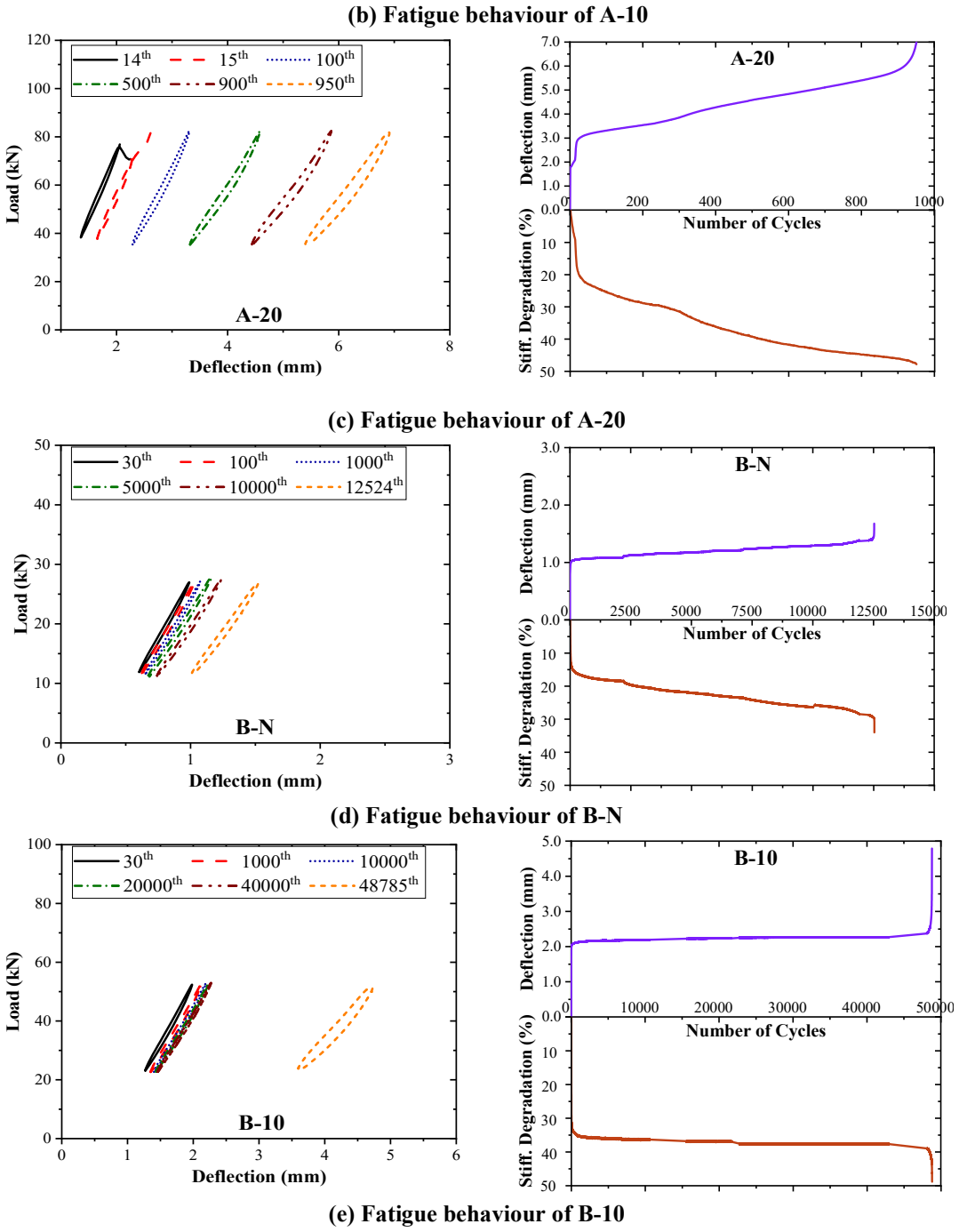

Fig. 5.6. Fatigue behaviour of HPFRC strengthened beams.

In Series A, a notable decrease in the slope of the load-deflection curves was observed for the control beam A-N, with β reaching 56.0% at failure. However, the application of HPFRC significantly slowed down the rate of stiffness degradation in the beams, with β values of 25.2% and 47.8% for A-10 and A-20 at failure, respectively. This indicates that the rate of damage accumulation in the strengthened beams decreased, enabling better resistance to structural deformation. A-20 beam exhibited a more pronounced increase in deflection and stiffness degradation during the 'stable

stage' compared to other beams, due to premature crack formation that expedited the damage progression and thus partially negated the fatigue performance enhancement provided by HPFRC. This phenomenon may be attributed to imperfections in the reinforcement process. In Series B, the amplitudes of deflection and stiffness degradation during the final stage were higher for B-N and B-10 compared to Series A. This suggests that an increase in the *a/d* led to a slower rate of damage development during the stable stage, resulting in smoother curves and an extended fatigue life.

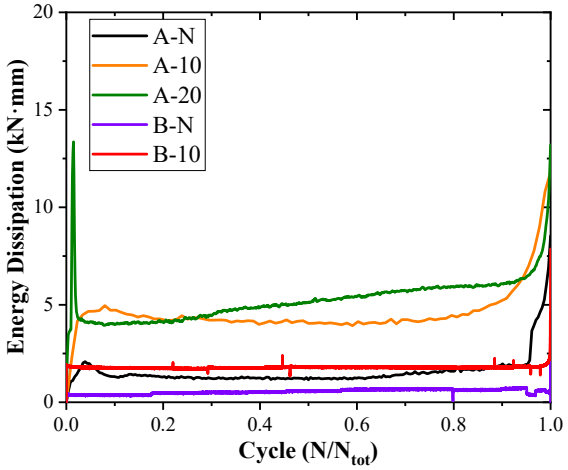

Fig. 5.7. Energy dissipation verse cycles curves.

The energy dissipation (Ψ_d) versus normalised cycles for each beam is presented in Figure 5.7. The energy dissipation (Ψ_d) was calculated for each cycle as the area enclosed by the load-deflection hysteresis loop during cyclic loading. To facilitate comparison, the cycle numbers for all beams were normalised, i.e., expressed as a ratio of the cycle number (N) to the total number of cycles (N_{tot}). A three-stage trend similar to that observed in δ and β was noticed in the Ψ_d measurements of the tested beams. A consistent three-stage trend was observed in the Ψ_d measurements. An exception was beam A-20, which showed an early spike in Ψ_d at the 14th cycle, coinciding with the onset of diagonal cracking at the transition between the initial and stable phases. This premature energy release is likely due to local imperfections in reinforcement. Nonetheless, the beam withstood loading until the 951st cycle, demonstrating the HPFRC jacket's effectiveness in crack bridging and fatigue life extension. Overall, all strengthened beams dissipated more energy than the control, while those with higher shear span-to-depth ratios exhibited lower per-cycle energy loss, suggesting enhanced fatigue resistance.

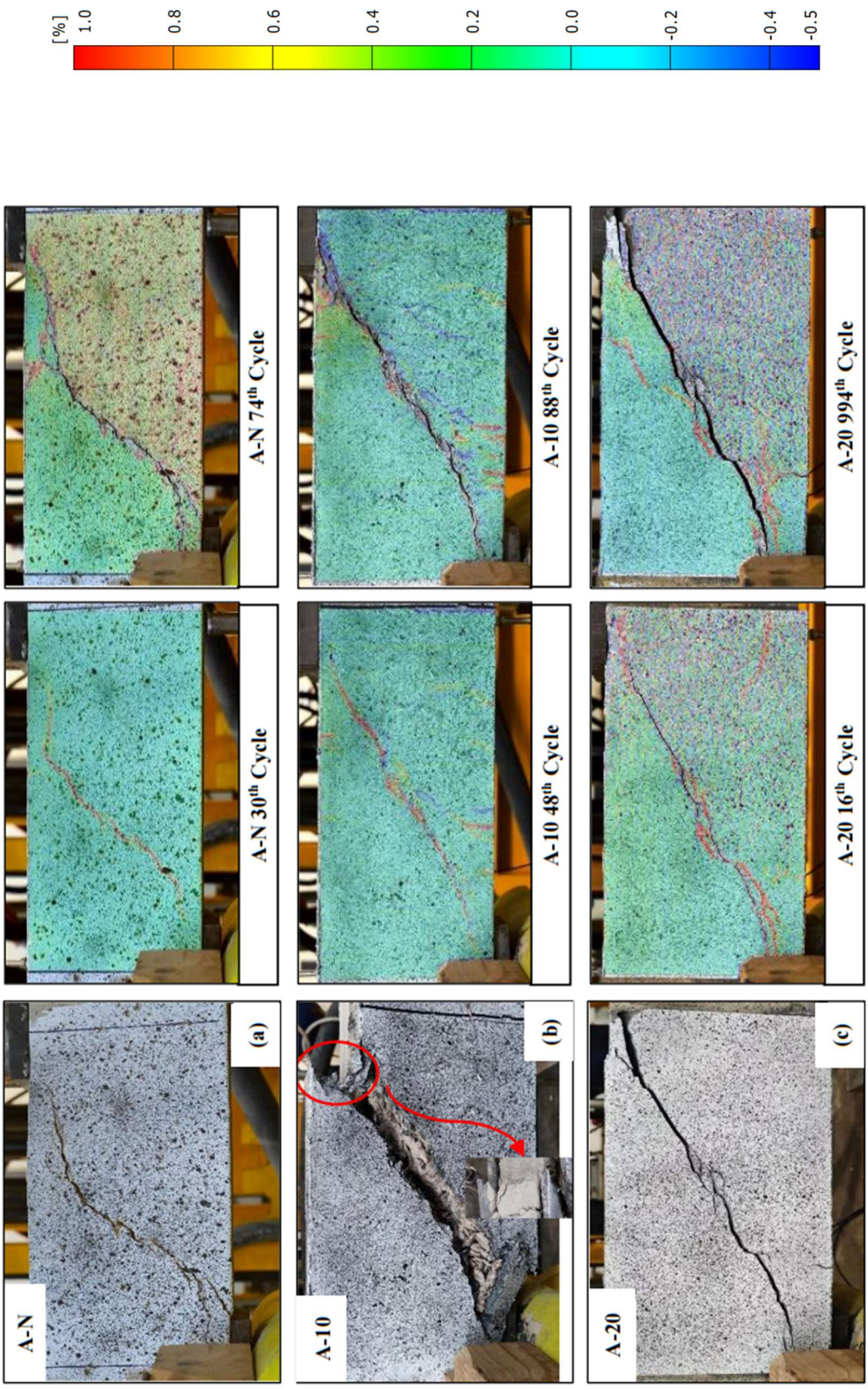
[%]
1.0
0.8
0.6
0.4
0.2
0.0
-0.2
-0.4
-0.5
A-N 74th Cycle
A-10 88th Cycle
A-20 994th Cycle
A-N 30th Cycle
A-10 48th Cycle
A-20 16th Cycle
(a)
(b)
(c)
A-N
A-10
A-20

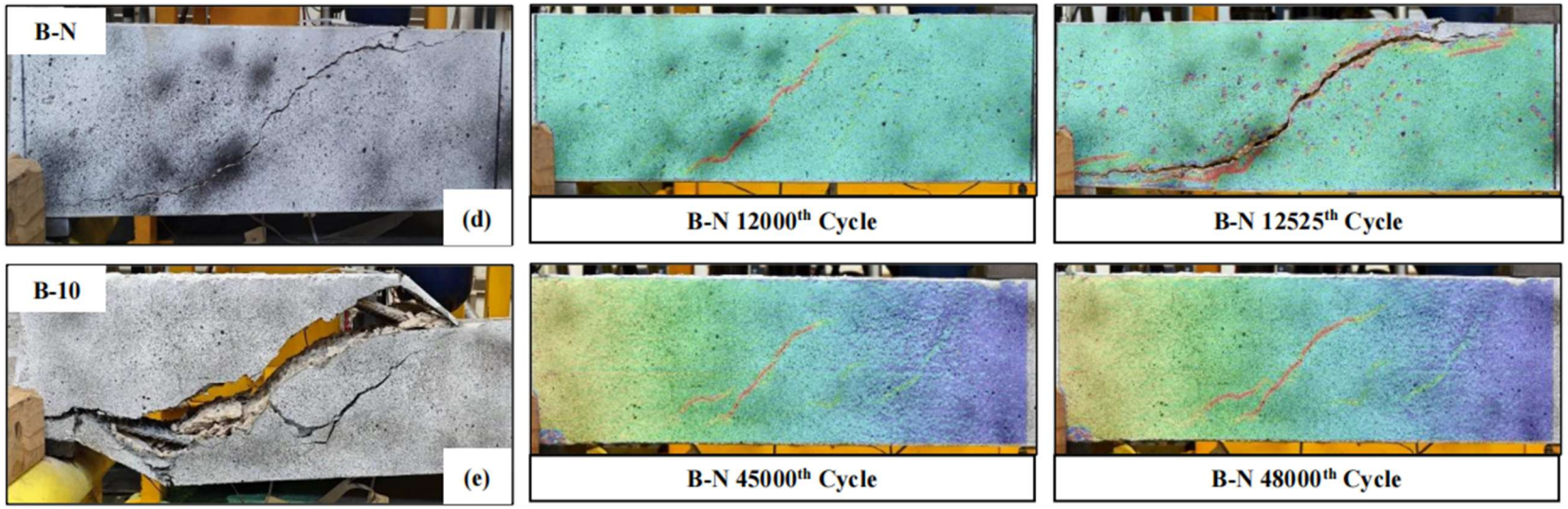

Fig. 5.8. Failure modes and transverse strain contours in the critical shear span at failure under fatigue loading: (a) A-N; (b) A-10; (c) A-20; (d) B-N; (e) B-10.

As shown in Figs. 5.8(a-e), all tested beams experienced shear failure. Both the control and strengthened beams in Series A and B exhibited an identical failure mode, characterised by typical diagonal tensile failure within the shear span between the load application point and the support points. As the number of cycles increased, the gradual accumulation of damage led to a progressive decline in the shear capacity of the specimens. This degradation culminated in the formation of a through-diagonal crack within the shear insufficient zone, ultimately resulting in beam failure. Prior to failure, a significant increase in beam deflection was observed. Additionally, due to the stiffness difference between the strengthening system and the substrate, their stress-strain responses varied, leading to partial jacketing detachment at failure (as shown in Fig. 5.8b).

To gain a deeper understanding of the damage progression in the tested beams, vertical strain (ε_y) distributions were analysed using Digital Image Correlation (DIC) at different cycles. Among them, although lacking visible cracks at the initial cycle, exhibited strain patterns in the mid-section of the shear-deficient region that closely resembled the final inclined shear crack. The presence of HPFRC optimised strain distribution, making it more dispersed compared to control beams. Increasing HPFRC thickness and the shear span-to-depth ratio also enhanced ductility, as indicated by the overall increase in vertical strain.

5.3 Fatigue life Prediction of the HPFRC Jacketed Beams

S-N curves are widely used to assess the fatigue life of concrete structures (Mahal et al., 2013, Gallego et al., 2014, Xia et al., 2022):

$$S = A - \alpha \mathrm{Log}N \tag{5-1}$$

where *S* refers to the cyclic stress level. A and α are the parameters calculated by the least squares method based on the experimental data. Since no stirrups were arranged in the reinforcement zone of the tested beams, the stress amplitude of the stirrups cannot be calculated. Therefore, '*S*' can be represented by the fatigue shear strength attenuation coefficient of the inclined section (Mahal et al., 2013, Gallego et al., 2014, Xia et al., 2022):

$$S = \frac{\sigma_{max}}{f_{fu}} = \frac{P_h}{P_{ref}} \tag{5-2}$$

where σ_{max} is the maximum applied fatigue stress; f_{fu} is the ultimate strength of the RC beam; P_h is the applied maximum fatigue load; P_{ref} is the design static shear ultimate strength of beams.

Currently, research on predicting the shear strength of HPFRC/UHPFRC jacketed beams is limited, with existing models primarily focused on bottom-bonded strengthening configurations (Noshiravani and Brühwiler, 2014, Ji and Liu, 2020). As shown in Fig. 5.9, the bottom bonding system exhibits delayed cracking upon failure, resulting in the formation of an intermediate crack-induced debonding (ICD) zone between the crack initiation point and the support. Within this zone, high shear stress leads to the development of numerous diagonal flexural-shear cracks, while the pry-

out stress also reaches its maximum, causing premature detachment of the strengthening system's ICD zone.

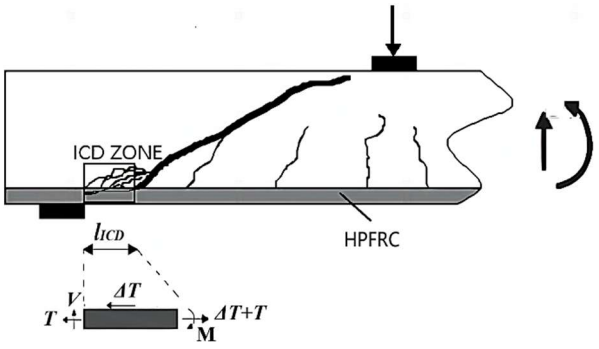

Fig. 5.9. Fatigue shear failure diagram for bottom bonded HPFRC-RC beam.

Based on these, Ji and Liu (2020) proposed a prediction model that considers the length of the ICD zone and the bending moment of the UHPFRC layer. However, in the U-shaped configuration, the side parts integrated with the bottom part prevent the formation of such a zone, rendering this model inapplicable. Furthermore, the relevant design codes primarily focus on the specification of HPFRC/UHPFRC as structural elements, with a lack of guidance on their use as reinforcement systems. Yin et al. (2018) have applied the shear design model for HPFRC proposed by the JSCE (2006) to bottom bonding jacketing. Therefore, this paper adapts this model for predicting the shear strength of the U-shaped HPFRC reinforcement system. Since no stirrups are present in the strengthened area, P_{ref} comprises shear strength contributions from concrete (V_c) and FRC jacket (V_{JAC}):

$$P_{ref} = V_c + V_{FRC} \tag{5-3}$$

where V_c is the shear strength of the substrate, V_{jac} is the shear strength of the strengthening system. the shear strength contributed by the concrete beam is typically calculated using the model in EC2 (2005):

$$V_C^{EC2} = 0.18k\left(100\rho_{long}f_c\right)^{1/3}b_w d \tag{5-4}$$

where, f_c is the compressive strength of concrete obtained from cylinders; d is the depth of the cross-section; ρ_{long} is the area ratio of the tensile reinforcement; and $k = 1 + \sqrt{(200/d)} \leq 2.0$ (with d in mm) is a factor that considers the size effect.

In U-shaped jackets, V_{FRC} is combined with 3 parts: 2 side parts and 1 bottom part. The shear strength of each component is determined by isolating the shear contribution from the cementitious matrix and fiber, as per JSCE (2006):

$$V_{FRC} = V_m + V_F = 0.18\sqrt{f_{cf}}b_{wj}d_j + f_{vdf}b_{wj}z \quad (5\text{-}5)$$

where V_m is shear strength contributions from concrete in HPFRC; V_F is shear strength contributions from fibre in HPFRC; b_{wf} and h_f are the width and hight of each part, respectively; f_{cf} is the compressive strength of HPFRC; $f_{vdf} = 0.3f_{cf}^{2/3}$ is the design average tensile strength perpendicular to diagonal cracks; $z = d_{FRC}/1.15$ is the distance from the location of the compressive stress resultant to centroid of tensile reinforcement for each part; $d_{FRC} = 0.9h_{FRC}$ is the effective depth of each part.

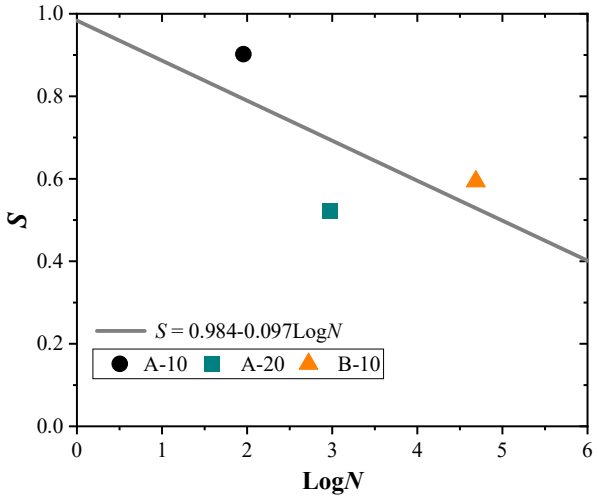

Fig. 5.10. *S-N* relationship of HPFRC strengthened beams**.**

According to the calculation results, the *S-N* relationship of HPFRC-strengthened beams is depicted in Fig. 5.10, alongside the *S-N* expression derived from the three tested beams. It is worth noting that analysing the *S-N* relationship requires a substantial amount of data (Akbari Hadad and Nanni, 2020). However, as this study is the first investigation into the shear fatigue behaviours of HPFRC-strengthened beams, further analysis is limited by the lack of additional data. Moreover, based on the *S-N* expression, it is expected that an increase in *S* would lead to a gradual decrease in *N*. While this trend holds true for Series A alone, as observed in Fig. 5.10, it appears to be mitigated when considering specimen B-10. This deviation can be attributed to the varying fatigue responses associated with different shear span ratios. Therefore, in the

future, with a sufficient amount of data, distinct *S-N* expressions could be derived by grouping the data based on shear span ratios.

5.4 Conclusions

The experimental study presented in this chapter investigated the static and fatigue performance of RC beams strengthened with U-shaped HPFRC jacketing, focusing on the effects of HPFRC thickness (10mm and 20mm) and shear span-to-depth ratio (*a/d* = 2.0 and 3.5). Key findings are summarised as following:

- **Static Loading:** HPFRC jacketing increased the shear strength of RC beams by 95% to 130%. Strengthening effects were more pronounced with increased HPFRC thickness, especially in deeper beams (*a/d* = 2.0), while a reduced enhancement was observed as the *a/d* ratio increased. The strengthened beams exhibited partial detachment but maintained a shear failure mode, with fibre bridging contributing to crack control.
- **Fatigue Loading:** HPFRC significantly improved the fatigue life of RC beams, extending the number of cycles by up to 951 cycles in beams with *a/d* = 2.0, and up to 48,786 cycles in beams with *a/d* = 3.5. The typical diagonal tension failure mode persisted across all specimens. The beams experienced three distinct phases of deflection, stiffness degradation, and energy dissipation, related to damage accumulation.
- **Fatigue Life Prediction Model:** A predictive model for fatigue life was developed based on maximum fatigue load and ultimate shear strength under static loading. Further validation with additional data is required to refine the model's accuracy.

Chapter 6

Shear Strength Prediction of FRCM Strengthened Beams using Machine Learning Approach

The predictive accuracy of existing models for the shear capacity of FRCM-strengthened RC beams remains limited, as highlighted in Chapters 2. Analytical models derived from regression analyses often fail to capture critical parameters such as shear span-to-depth ratio, mortar thickness, and the interaction between internal and external reinforcements. These oversights result in inconsistent predictions that undermine their practical applicability. Similarly, traditional empirical models are constrained by their dependence on specific experimental datasets, limiting their generalizability to diverse structural and material configurations.

Machine learning (ML) provides a powerful alternative for addressing these limitations. Unlike traditional regression-based or empirical models, ML algorithms can adaptively learn complex relationships between input variables and shear performance, yielding significantly higher predictive accuracy and robustness. Furthermore, ML methods enable interpretability through tools like SHAP (Shapley Additive Explanations) and PDP (Partial Dependence Plots), which elucidate the

relative importance of input parameters and provide insights into the underlying mechanisms affecting shear capacity.

In this chapter, a comprehensive study was conducted to address the shortcomings of traditional models using ML techniques. A database of 174 FRCM-strengthened RC beams was compiled, combining 162 beams from the database established in Chapter 2 with 12 beams tested in Chapter 3. Two beams from the original dataset were excluded due to construction defects reported by Younis et al. (2017) and Aljazaeri and Myers (2017), resulting in a final dataset of 172 specimens. Using this comprehensive database, nine different ML models were developed and evaluated to determine the most effective algorithm for predicting the shear capacity of FRCM-strengthened beams. These models were compared with the seven traditional empirical models outlined in Section 2.3.1, representing one of the first large-scale comparative analyses of predictive models for this purpose.

To bridge the gap between research and practical applications, a user-friendly graphical user interface (GUI) was developed, enabling engineers and practitioners to utilise the optimised ML models for shear strength prediction in FRCM systems. This chapter not only demonstrates the potential of ML in improving predictive accuracy for FRCM-strengthened beams but also establishes a framework for future analytical approaches and design optimization in structural strengthening using mortar-based composites.

6.1 Background and Literature Review

With the further development of artificial intelligence, machine learning (ML) has become an important tool to help solve many problems in the field of civil engineering (Abdalla and Hawileh, 2011; Abdalla et al., 2015; Wakjira et al., 2022a). Contrary to most empirical models, it can determine the relationship between input variables and target value without assuming basic mathematical and physical models in advance. Several studies, such as Abuodeh et al. (2020), Li et al. (2018), Naderpour et al. (2018), Tanarslan et al. (2012), have used ML to study the shear strength prediction of FRP strengthened beams. However, the research on the performance of the FRCM strengthened beams using ML is limited. Wakjira et al. (2022b) used seven different ML models, such as kernel ridge regression (KR), support vector regression (SVR),

regression tree (RT), random forest (RF), gradient tree boosting regression (GTBR), K-nearest neighbours (KNN), and extreme gradient boosting (XGBoost), to predict the flexural bearing capacity of FRCM strengthened beams. Their database contained 132 beams, and was based on beam geometry, mechanical properties of concrete and stirrups, performance of FRCM (fibre's type and elastic modulus), and reinforcement areas of internal and external FRCM reinforcement. The prediction results show that all ML models have good prediction effects compared with existing traditional design models. Wakjira et al. (2022) also studied the ML model's prediction effect of on the shear strength of FRCM strengthened beams. Compared with the previous research on flexural properties, they added input variables such as the strengthening configuration of the FRCM jacket and the tensile strength of the fibre. The results showed that XGBoost performed best in the six ML models used (i.e. the same models used in study).

Furthermore, Ombres et al. (2024) explored the application of ANN to predict the bond strength of SRG systems, proposing an analytical formula for bond capacity based on ANN methods. Similarly, Ke et al. (2024) employed a genetic algorithm-enhanced backpropagation neural network (GA-BPNN) to predict the shear capacity of near-surface-mounted (NSM) FRP-strengthened beams. Building on parameter analysis of GA-BPNN and existing models, they developed a design-oriented strength model for calculating shear capacity in NSM FRP-reinforced beams, further optimised through genetic algorithms. Nguyen et al. (2024) further utilised ANN models to create a predictive tool specifically for assessing the shear strength of RC beams strengthened with FRCM composites, and they also illustrated the E_f as the most critical factor influencing shear capacity in these beams. It can be observed that research on FRCM-strengthened beams remains limited, with most studies primarily focusing on ANN models and flexural strength prediction. This highlights the need for broader comparative studies across various ML models to enhance shear strength prediction accuracy for FRCM-strengthened beams.

ML models are often considered as 'black boxes', lacking explanation for the contribution of physical variables and eigenvalues. Several factors, however, can impact ML decisions, including the database, model selection, feature selection, and hyperparameter tuning. If prediction results are not adequately explained, users may

not trust them. Hence, elucidating the characteristics of the constructed model is imperative to enhance transparency and comprehension, especially in the context of model verification, regulatory compliance, ethical considerations, trustworthiness assessment, and model diagnostics (Rengasamy et al., 2022). In this regard, Lundberg and Lee (2017) proposed a method called 'Shapley Additive Explanations (SHAP)' to interpret the output of ML models, focusing on feature importance. In addition to SHAP, Partial Dependence Plots (PDP) provide insights into the relationship between individual input features and the predicted outcome by illustrating how a single variable impacts model predictions, averaging out other features' effects (Goldstein et al., 2015). This study uses PDPs to further interpret the influence of critical parameters on shear strength predictions, enhancing model transparency and comprehensibility. The details of this study are presented in the following.

6.2 Database and Input Parameters

Table 6.1 summarises the input parameters used in existing analytical models (Section 2.3.1) and in machine learning studies aimed at predicting the shear strength of beams strengthened with externally bonded reinforcement (i.e., FRP and FRCM systems). Almost all models incorporate parameters such as b_w, d, f_c and f_{yw}, as these are directly related to the beam's cross-sectional dimensions and material strength, which fundamentally govern shear capacity. Specifically, b_w and d represent the width and effective depth of the beam, determining the shear area and lever arm length, respectively. Increasing either parameter enhances the beam's ability to resist shear forces. However, Traditional models often overlook the influence of the a/d ratio, yet this parameter has a marked impact on shear behaviour. Studies demonstrate that a/d dictates the transition between deep and slender beam behaviour, affecting how shear forces are transferred through the beam (Chaallal et al., 2002; Li et al., 2001). A lower a/d typically results in arch action, enhancing shear capacity, whereas a higher a/d shifts the response towards truss action, reducing shear strength. In this study, the mean yield strength of stirrups (f_{yw}), rather than the design yield strength, is used in machine learning and tradition models to evaluate the actual material performance in an experimental context. The mean yield strength more closely reflects real-world data, and most existing studies report only the mean values, making it a practical choice for consistent comparisons.

The ratios of longitudinal reinforcement ($\rho_{long,b}$), stirrups (ρ_w), and fibres (ρ_f) play a dual role: they capture the interaction effects between the FRCM jacket and internal reinforcement while also directly influencing the overall shear capacity. Specifically, $\rho_{long,b}$, ρ_w, and ρ_f determine the reinforcement's contribution to shear resistance, with ρ_f summarizing information about fibre quantity, width, and thickness (i.e., n, w_f/s_f, t_f), thus reducing feature complexity. In addition, the interaction between the FRCM jacket and the internal reinforcement, particularly stirrups, is a crucial factor in predicting shear strength accurately. However, current models lack detailed analysis on this interaction.

In terms of fibre properties, ultimate strain ε_{fu} and the modulus of elasticity E_f of the fibres are selected because they define the deformation capacity and stiffness of the FRCM. Although most traditional models include effective strain ε_{eff} to account for possible FRCM detachment, this value is typically derived from ultimate strain, and no universally accepted model exists for directly calculating ε_{eff} in FRCM systems. It is noteworthy that even if the ε_{eff} was considered as a percentage of ε_{fu} (e.g. $0.5\varepsilon_{fu}$ as in the model proposed in Triantafillou and Papanicolaou (2006)), the distinct features of machine learning algorithms are likely to render this assumption negligible in terms of its impact on the final results. Therefore, ultimate strain ε_{fu} is chosen as a more reliable and consistent input in this study. Additionally, the fibre type and strengthening configuration (SC) significantly affect the load transfer efficiency between the fibre layer and the substrate. Study conducted by Gonzalez-Libreros et al. (2017a) shows that a fully wrapped configuration provides higher shear capacity than side-bonded configurations due to increased confinement and reduced detachment risk. However, due to the complexity of anchorage (such as anchorage method, material properties, and construction conditions can all impact effectiveness), its inclusion could introduce substantial uncertainty into the model. Additionally, studies, such as Escrig et al. (2015) and Tetta et al. (2016), have reached varied conclusions regarding the limited impact of anchorage on shear performance. To reduce overall model uncertainty and avoid potential overfitting due to an excessive number of parameters, end-anchorage was not included as an input variable in this study. Unlike FRP systems, the mortar used in FRCM systems possesses inherent thickness and strength, contributing to shear

Table 6.1. Input parameters in current analytical models and past ML research on FRP and FRCM systems

		Current analytical models					Past ML Research					
		Fibre properties		Composite properties			FRP					FRCM
		Model 1, 2, 3 (Thermou et al., 2019, Triantafillou and Papanicolaou, 2006, Escrig et al., 2015)	Model 4 (Tetta et al., 2018b)	Model 5 (ACI, 2013)	Model 6 (Younis et al., 2017)	Model 7 (Ombers, 2017)	Yousif et al. (2010)	Perera et al. (2010)	Naderpour et al. (2017)	Li et al. (2018)	Abuodeh et al. (2018)	Wakjira et al. (2022b)
Beam Details	b_w	√	√	√	√	√	√	√		√	√	√
	d	√	√	√	√	√	√		√	√	√	√
	f_c	√	√	√	√	√	√	√	√	√	√	√
	h		√				√	√				
	L						√				√	
	a/d					√	√		√	√	√	
Inner Reinforcement Details	$\rho_{long,b}$	√	√	√	√	√		√				
	A_{sl}						√			√	√	√
	$f_{y,L}$										√	
	ρ_w											√
	A_w											
	A_w/s	√	√	√	√	√	√	√			√	
	f_{yw}	√	√	√	√	√	√	√			√	
Externally Bonded Reinforcement Details	w_f					√					√	
	h_f	√	√				√		√		√	
	w_f/s_f		√		√		√		√	√	√	
	t_f		√				√		√	√	√	
	n		√		√							
	A_f											√
	ρ_f	√	√	√	√	√		√				
	ε_{fu}	√	√						√	√		
	E_f	√	√				√	√	√	√	√	√
	f_{fu}						√				√	
	t_{cm}											
	f_{cm}				√	√						
	E_{FRCM}			√	√	√						
	ε_{FRCM}			√	√	√						

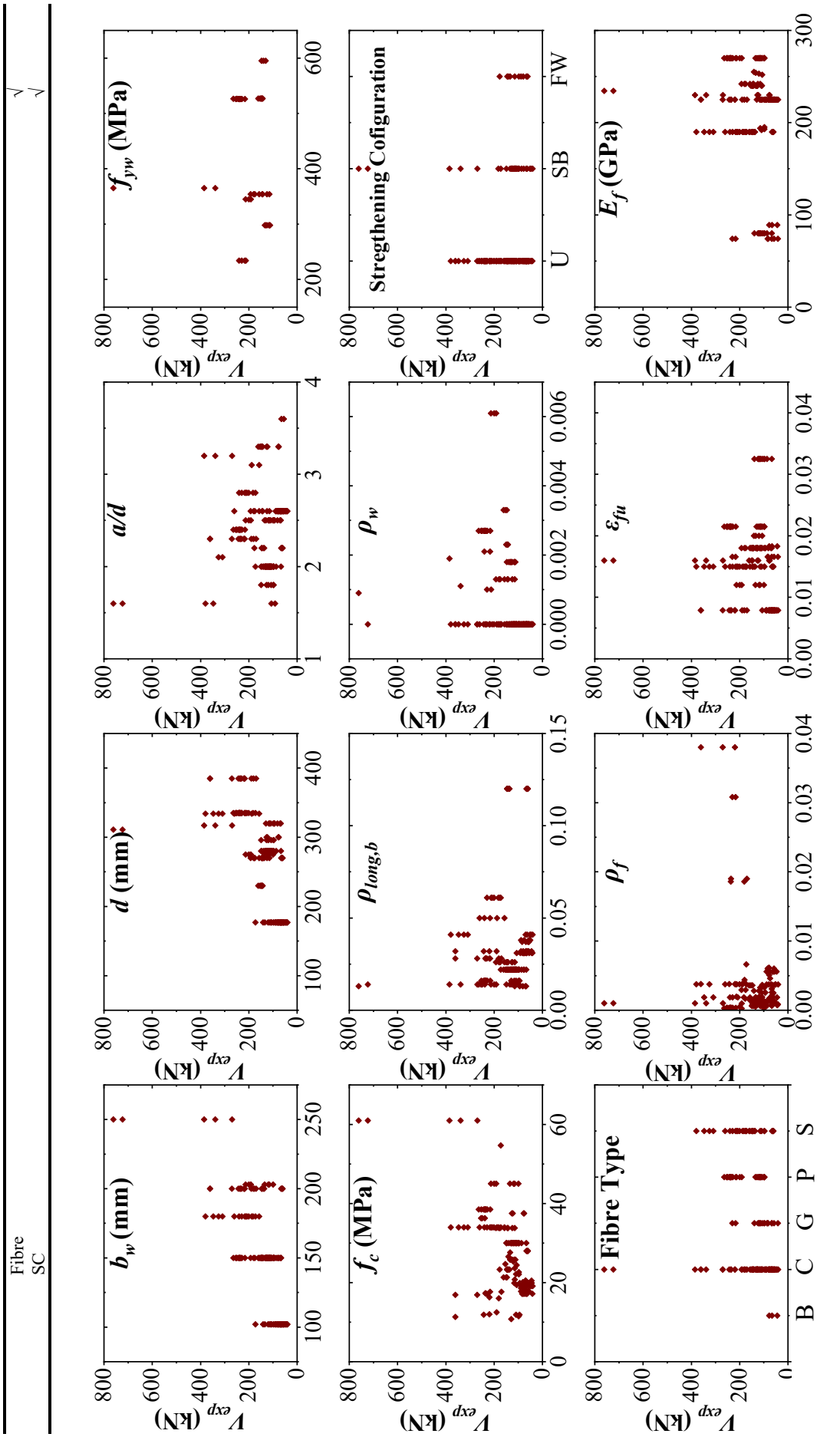
Fibre
SC
V_{exp} (kN)
b_w (mm)
d (mm)
a/d
f_{yw} (MPa)
f_c (MPa)
$\rho_{long,b}$
ρ_w
Stregthening Cofiguration
U
SB
FW
ρ_f
ε_{fu}
E_f (GPa)
Fibre Type
B
C
G
P
S

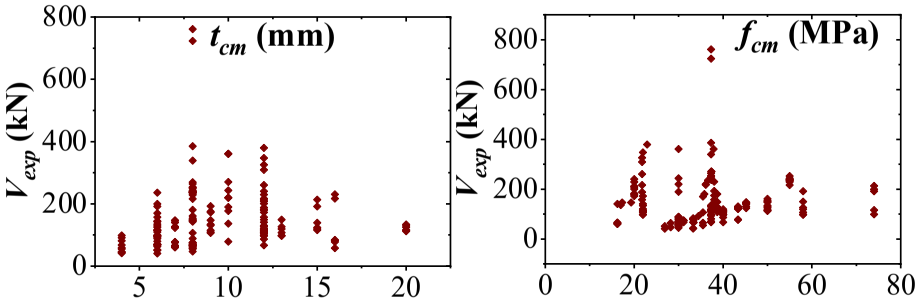

Fig. 6.1. Correlation between the input parameters and the shear capacity.

Table 6.2. Statistical measurements of the experimental data

	Parameter	μ	SD	Min	Q1	Median	Q3	Max
Beam Details	b_w (mm)	152.12	37.70	102	102	150	180	250
	d (mm)	271.58	65.62	177	177	280	320	385
	a/d	2.42	0.43	1.60	2.00	2.40	2.60	3.60
	f_c (MPa)	27.88	10.39	10.8	19.4	28	34	61
Inner Reinforcement Details	$\rho_{long,b}$	0.031	0.023	0.013	0.016	0.022	0.032	0.120
	ρ_w	0.00071	0.0013	0	0	0	0.0013	0.0061
	f_{yw} (MPa)	410.87	124.11	234	321	365	526	595
Externally Reinforcement Detail	ρ_f	0.0035	0.0065	0.0003	0.0008	0.0017	0.0037	0.0380
	ε_{fu}	0.0162	0.0062	0.0079	0.0120	0.0160	0.0183	0.0325
	E_f (GPa)	212.21	56.05	74	190	225	242	270
	t_{cm} (mm)	9.50	3.59	4	7	8	12	20
	f_{cm}(MPa)	37.02	12.52	16.2	30.0	37.3	43.4	74
	V_{exp} (KN)	151.89	99.21	40.73	88.44	126.47	192.5	761.35
	SC	U, SB, FW						
	Fibre	B, C, G, P, S						

Note: μ = mean, SD = standard deviation, Q1 = first quartile, Q3 = third quartile.

strength—a factor often overlooked in existing research. Hence, this study innovatively incorporates t_{cm} and f_{cm} as parameters to further refine the predictive accuracy. Therefore, the model incorporates 14 eigenvalues: b_w, d, a/d, f_c, f_{yw}, $\rho_{long,b}$, ρ_w, ρ_f, ε_{fu}, E_f, t_{cm}, f_{cm}, fibre type and SC. The objective is to predict the shear strength of FRCM-reinforced beams, with the experimental shear strength (V_{exp}) serving as the target value for training the model to generate the corresponding predicted value (V_{pre}).

Descriptive statistics of the database is presented in Table 6.2, detailed parameters of all samples are available in the database, and Fig. 6.1 illustrates the statistical distribution of the database in terms of input parameters versus experimental shear capacity (V_{exp}). In the collected data, there are three reinforcement configurations: U-shaped (U), side bonded (SB) and fully wrapped (FW), and five fibre types: basalt (B), carbon (C), glass (G), PBO (P) and steel (S).

6.3 Machine Learning Models

This section outlines the nine ML models used in this study to predict the shear capacity of FRCM strengthened RC beams, as described below.

6.3.1 Linear Regression

Linear regression (LR) model is a supervised machine learning algorithm, which evaluates the correlation between dependent and independent variables and determines their linear relationship (Liang and Song, 2009). Linear regression is mainly fitted by the least squares method, but it may be fitted by other methods, including minimizing the 'lack of fit' in some other specifications or minimizing the penalty version of the least squares loss function in ridge regression. Since the study includes 14 predictors, the model is called multiple linear regression (MLR), in which a hyperplane in the model is fitted to a 14-dimensional space with 14 independent features. The dependent variable, Y, is defined as (Liang and Song, 2009):

$$Y = \beta_0 + \sum_{i=1}^{N_t} \beta_j X_i \tag{6-1}$$

where X_i is the independent variables, and β_j is the partial regression coefficient, β_0 is the intercept term, and N_t is the number of predictors.

6.3.2 *K* Nearest Neighbour

K Nearest Neighbour (KNN) regression is a nonparametric algorithm, which, in an intuitive way, approximates the correlation between independent variables and continuous outcomes by averaging the observed values in the same neighbourhood, where *K* is the number of nearby points of a test point *X* (Wakjira et al., 2022b). In practice, the algorithm first measures the distance between *X* and the training data points and arranges them in ascending order of distance. Finally, the target values of *K* training data points closest to *X* are selected for weighted averaging to obtain the target value of *X*. The KNN model in this paper is developed by setting *K* as 3, and Fig. 6.2 shows the details of data processing of KNN algorithms.

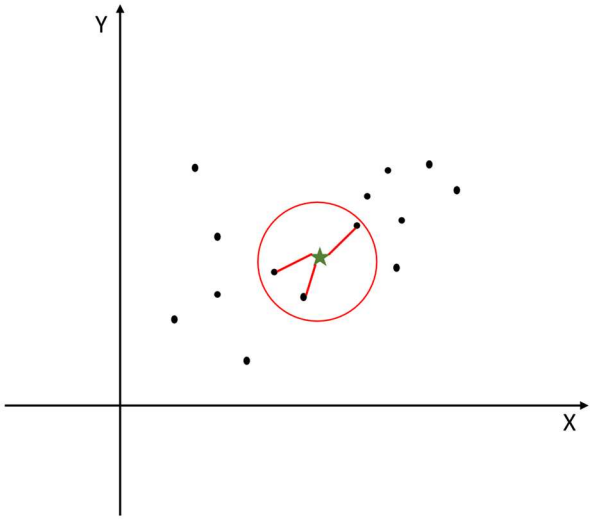

Fig. 6.2. 3-NN model.

6.3.3 Support Vector Machines

Support Vector Machine (SVM) is a machine learning method created by Vapnik based on Statistical Learning Theory (STL) (Wakjira et al., 2022b). The algorithm used for regression is called Support Vector Regression (SVR), which solves the regression problem as a set of linear equations, provides a faster training process, and higher stability and modelling accuracy. According to Vapnik (1999), for training samples $\{(x_1, y_1), (x_2, y_2) \ldots (x_n, y_n)\}$, the linear regression function established by SVR in the high-dimensional feature space is:

$$= \beta_0 + \sum_{i=1}^{N_t} \beta_j X_i \tag{6-2}$$

$$f(x) = \omega^T \varphi(x) + b \tag{6-3}$$

where $\varphi(x)$ is a nonlinear mapping function (hyperplane), ω is the weight vector, and b is the bias term.

After considering the linear insensitive loss function (boundary), ε, relaxation variables, ξ_i, and regularization parameter, C, the regression Eq. 6-4 is solved as:

$$f(x) = \sum_{i=1}^{n} (\alpha_i - \alpha_i') K(x_i, x) + b \tag{6-4}$$

where α_i and α_i' are Lagrange multipliers ($0 \leq \alpha_i, \alpha_i' \leq C$); k is a kernel function, including linear kernel, polynomial kernel, hyperbolic tangent (sigmoid) kernel and radial basis function (RBF) kernel. The kernel was chosen due to its capability of capturing intricate, nonlinear associations among input features, demonstrating superior performance compared to other kernel alternatives (such as linear and polynomial kernels) in preliminary evaluations (Burges, 1998). In this study, the RBF kernel is used, and the expression is:

$$K(x_i, x_j) = e^{\frac{-1}{2\sigma^2}\|x_i - x_j\|^2} \tag{6-4b}$$

where σ is the width of the kernel. Fig. 6.3 exhibits a schematic view of the SVR model.

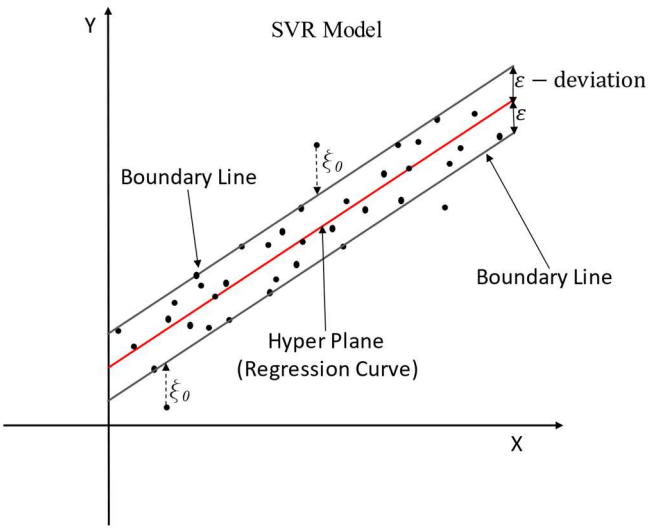

Fig. 6.3. SVR model.

6.3.4 Artificial Neural Network

Artificial neural network (ANN) is an approach simulating the function of human brain, which is composed of many interconnected artificial neurons (Chou and Tsai, 2012, Hammoudi et al., 2019, Liu et al., 2021). In the study, each processing element has multiple input parameters, and only one output is sent. Multilayer perceptron (MLP), as a type of ANN, is used: the first layer is for receiving input; the last layer is for generating output; the middle layers have no connection with the external world and are called the hidden layers. Each neuron is connected to each neuron in the next layer, and there is an input value and a weight, W_{ij}, between them. Figure 6.4 shows the MLP model with only one hidden layer.

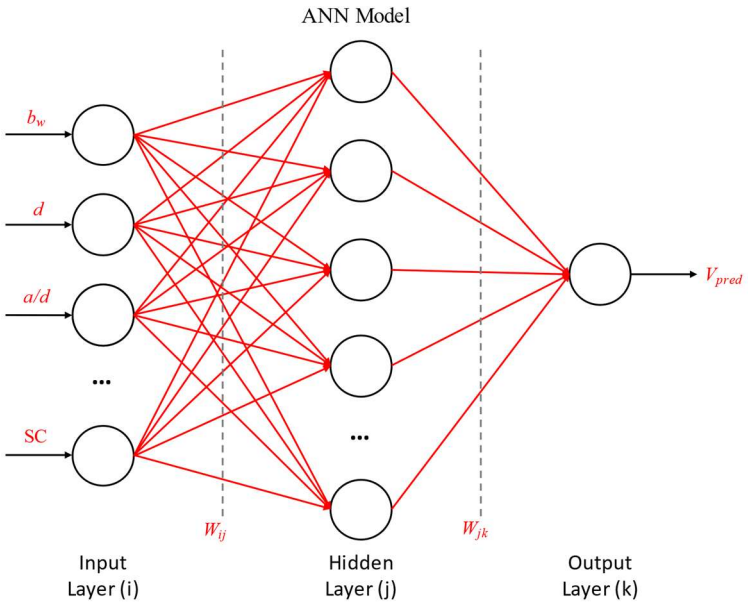

Fig. 6.4. MLP model.

6.3.5 Decision Tree

Decision tree (DT) is a supervised rule-based nonparametric algorithm that generates a tree model from training data, similar to a flow chart (Fig. 6.5). It predicts the value of target variable by learning simple decision rules inferred from data characteristics. The tree can be regarded as a piecewise constant approximation. which devices the feature space into several disjoint regions with smaller similar response values (Wakjira et al., 2022b).

Compared with other models, DT has the advantages of easy interpretation and visualization. However, this model will create biased trees when some categories are

dominant and is prone to overfitting. Ensemble models can reduce the occurrence of these issues. The models introduced later in this paper all are ensemble models combined with multiple decision trees, such as XGboost and random forest (Topçu et al., 2009).

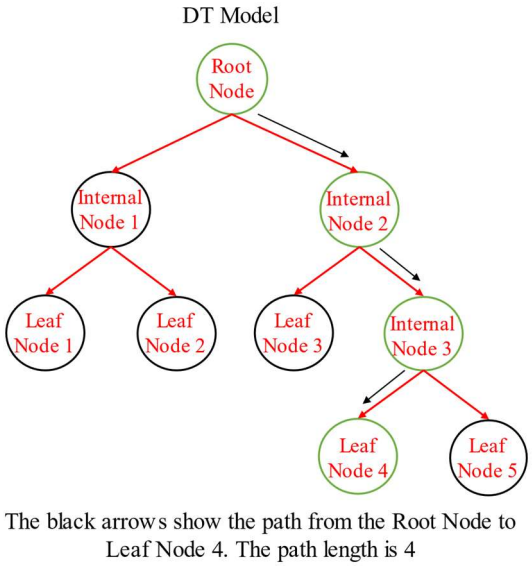

Fig. 6.5. DT model.

6.3.6 Random Forest

Random Forest (RF) is an application of bagging algorithm to create an ensemble of decision trees. This algorithm constructs multiple DTs in parallel to generate independent outputs and finally calculates their mean value to generate the final output, thus improving the prediction accuracy. In addition, there is a positive correlation between the accuracy and the number of trees. Moreover, RF as a bagging algorithm, has two selection processes when constructing trees: one is to select random sample data from training with guidance method, and the other is to select random feature attributes from the original at tribute data set (Mai et al., 2021). This makes the RF model insensitive to outliers and noise data and overcomes the problem of overfitting in DT to some extent. Figure 6.6 shows a simple schematic diagram of the RF algorithm, where its final prediction is made by averaging the predictions of each DT predictor:

$$Y = \frac{1}{T}\sum_{i=1}^{T} Y_i(X') \tag{6-5}$$

where $Y_i(X')$ is the output of each individual decision trees, which is trained on X' unknown instances, and T is the number of DT trees.

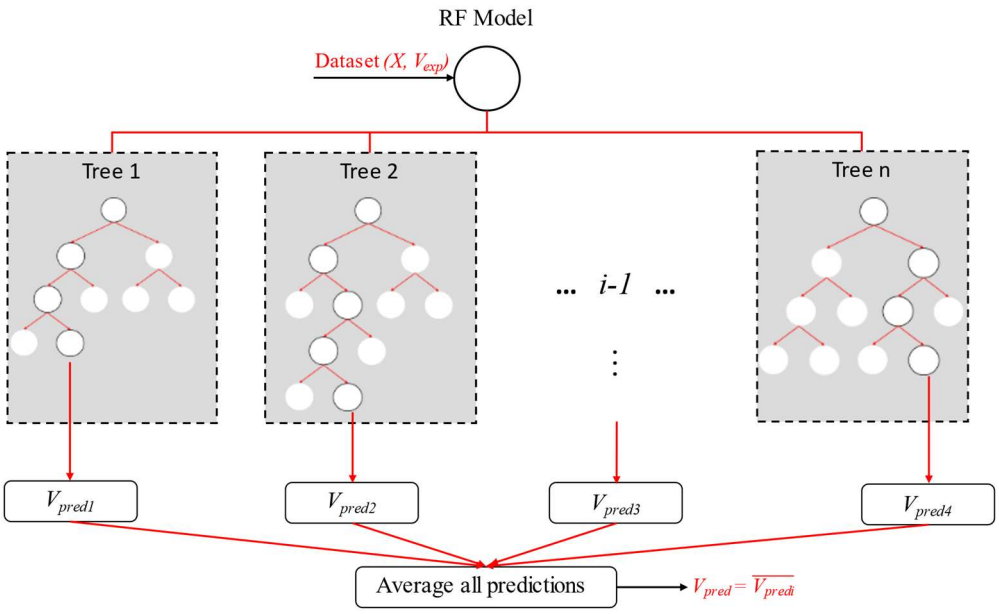

Fig. 6.6. RF model.

6.3.7 Extreme Gradient Boosting

Extreme gradient boosting (XGBoost) is a tree enhancement system, which combines multiple weak learning models, uses the 'greedy' method to learn each base tree, and continuously forms new decision trees to fit the residuals of previous predictions, constantly reduces the residuals between the predicted value and the real value, thus improving the prediction accuracy. To fix the limitation of weak learners, fit the first learner to the complete input dataset, and then fit the rest of models to the residual. According to Younis et al. (2022), the XGBoost can be expressed as Eq. 6-6:

$$Y = \sum_{i=1}^{T} L\left(Y_{i-1} + f_i(X)\right) + \Omega(f) \tag{6-6}$$

where Y_{i-1} is the prediction result after the *i-1* iteration, $f_i(x_i)$ is the calculated residual from *i* DT tree, and $\Omega(f)$ is the regularization as shown in Eq. 6-6b:

$$\Omega(f) = \gamma N + \frac{1}{2}\lambda\|\omega\|^2 \tag{6-6b}$$

where N represents the total number of leaf nodes and ω is the score of each leaf node. γ and λ are controlling factors employed to avoid overfitting (Dong et al., 2020).

Figure 6.7 shows the learning method of this algorithm, and it is worth noting that XGBoost does not use any weighted sampling technology when DT tree splitting. XGBoost is considered easier to use for small datasets running on CPUs than deep learning algorithms.

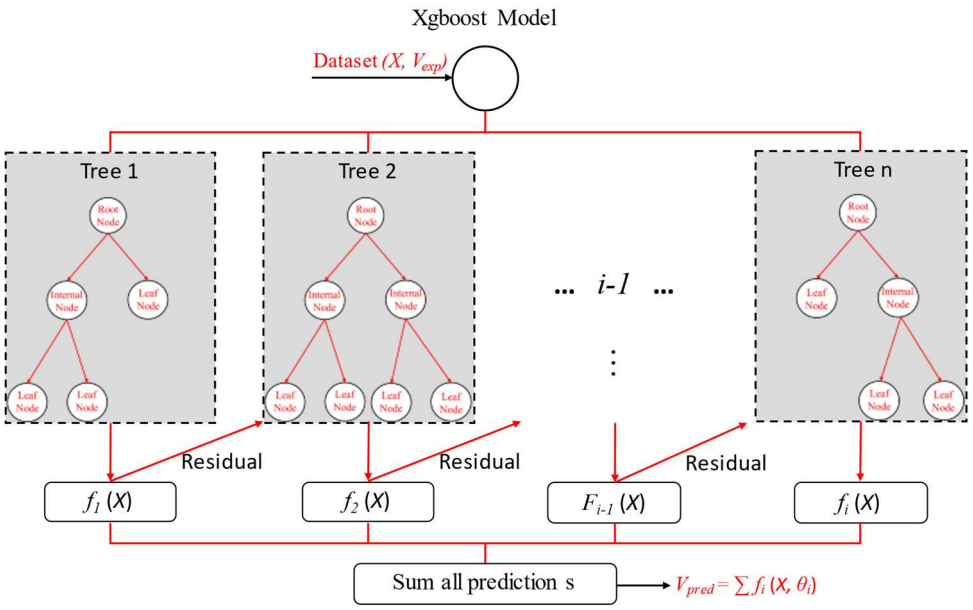

Fig. 6.7. XGBoost model.

6.3.8 Light Gradient Boosting

Light Gradient Boosting (LGBoost) is a multiple decision tree algorithm developed by Microsoft Research Institute (Yan et al., 2022). The main difference between LGBoost and XGBoost is the tree structure. When splitting trees, LGBoost uses gradient based one-sided sampling (GOSS), which selects segmentation based on all instances with large gradient (i.e., large error) and random samples of instances with small gradient (Ke et al., 2017). To maintain the accuracy of information, GOSS keeps the instances with large gradients and randomly discards the instances with small gradients. Therefore, GOSS has achieved a good balance between improving the speed and maintaining the accuracy of the learning decision tree by reducing the number of data instances. In addition, LGBoost also creates an exclusive function bundle (EFB): in a sparse feature space, many features are almost exclusive, which means that they rarely take non-zero values at the same time; EFB bundles these functions to reduce dimensions to improve efficiency while maintaining a high level of accuracy (Ke et al., 2017). These two features enable LGBoost to implement a highly optimised

histogram-based decision tree learning algorithm, which has great advantages in efficiency and memory consumption.

6.3.9 CatBoost

CatBoost is a gradient enhancement algorithm that uses dynamic enhancement to avoid overfitting (Yegulalp, 2017). Its main difference from XGBoost and LGBoost is also the splitting on each DT. CatBoost provides a new technology called Minimum Variance Sampling (MVS), which is a weighted sampling version of random gradient lifting. In this technique, weighted sampling occurs at the tree level rather than at the split level. The observation results of each tree are sampled in a way that maximizes the accuracy of the split score, and finally a balanced tree grows. The tree is symmetric, and in each layer, the feature with the least loss is selected to segment the pair, and it is used for nodes in all layers.

The models chosen for this study cover a range of different types, allowing for a comprehensive selection of the best-performing model for the current database. A summary of the models' advantages, disadvantages, and characteristics is provided in Table 6.3.

Table 6.3. Summary of Machine Learning Models.

	Advantages	**Disadvantages**	**Characteristics**
LR	Simple and interpretable; efficient for linear relationships; low computational cost	Limited to linear relationships; low accuracy with complex or nonlinear data	Provides a baseline for comparison
KNN	Nonparametric and intuitive; performs well with local patterns in small datasets	Sensitive to outliers and high-dimensional data; computationally intensive with large datasets	Captures local non-linear patterns
SVR	Effective for high-dimensional spaces; robust with appropriate kernel choice; works well with non-linear patterns	Computationally demanding; sensitive to kernel and parameter selection	Good for high-dimensional data
ANN	Models complex, nonlinear relationships; adaptive learning and suitable for large datasets	Prone to overfitting; requires substantial data and tuning; limited interpretability	Flexible for complex patterns

DT	Easy to interpret and visualise; fast for training and prediction	Prone to overfitting; biased with imbalanced data; lacks accuracy for complex patterns	Rule-based, interpretable model
RF	Reduces overfitting; robust to outliers and noise; suitable for high-dimensional data	Limited interpretability due to multiple trees; slower than single trees; higher memory usage	Aggregates DTs for better accuracy
XGBoost	High accuracy; reduces bias and variance; effective for complex interactions	Tuning can be challenging; higher memory use; may overfit if not properly regularised	Fast, suitable for complex data
LGBoost	Optimised for large datasets; efficient memory usage; faster training than XGBoost	Less interpretable; sensitive to data preprocessing and parameter tuning	Fast and memory-efficient
CatBoost	Handles categorical features natively; avoids overfitting with minimal tuning; robust to noisy data	Slightly lower adoption; slower training than LGBoost; performance varies based on data balance	Native categorical feature support

6.4 Model Development

All algorithms except XGBoost, LGBoost and CatBoost used in this study are implemented using the Scikit-learn module in Python, and XGBoost, LGBoost and CatBoost are based on their own packages, respectively. The dataset is randomly split into two parts, 70% (119 samples) for the training dataset and 30% (52 samples) for the test dataset. Afterwards, all input variables are standardised to eliminate the effect of internal composition differences on the results. All models are trained using the same randomly assigned train-test dataset. In addition, the hyperparameter values of an algorithm determine the predictive performance and generalization ability of the model, so the choice of hyperparameters is vital. And grid search is often used as a hyperparameter tuning technique, with the *K*-fold cross-validation algorithm at its core. This study uses 10-fold cross-validation (K=10): the training dataset is divided into 10 independent equal sizes without replacement groups, and each time uses 1 group of training data sets as the validation dataset, while the remaining 9 groups are used for training; the cross-validation is repeated 10 times, and a total of K performance metrics are generated each time, and the average is taken as the final score of the model under the current hyperparameters. Relying on this final score, the hyperparameters for

optimal performance of the model are found. Table 6.4 describes the optimised hyperparameters in all ML models, parameters not listed are the same as the default values in Scikit-learn, XGBoost, LGBoost and CatBoost.

Table 6.4. Optimised hyperparameters in all ML models.

	Parameters
LR	-
KNN	$K = 3$
SVR	Kernel = RBF, Regularization parameter (C) = 500, Gamma = 0.07
ANN	Hidden layer sizes = (8, 8, 16), Maximum number of iterations = 10000, Initial learning rate = 0.1
DT	Maximum depth = 6, Maximum features = 5
RF	Maximum features = 6, Number of estimators = 18, Number of jobs = 20
XGBoost	Learning rate = 0.1, Number of estimators = 900, Maximum depth = 3, Minimum child weight = 1, seed = 0, Subsample = 0.7, Colsample by tree = 0.9, gamma = 0.1, regression alpha = 0.05, regression lambda = 0.05
LGBoost	Learning rate = 0.08, Maximum depth = 3, Number of estimators = 1800, subsample = 0.6, Colsample by tree = 0.8
CatBoost	Iterations = 4000, Learning rate = 0.2, L2 leaf regularization = 1, Bagging temperature = 0.1, Depth = 4, Random subspace method = 0.1, One-hot maximum size=2, Fold length multiplier = 1.2, Border count = 128

Each machine learning model evaluates its performance by calculating the five statistical parameters of the actual and predicted shear capacity provided by FRCM strengthened beams (V_{exp} and V_{pre}): linear regression coefficient (α), bias (b), coefficient of determination (R^2), mean absolute error (MAE), root mean square error (RMSE), mean of V_{pre}/V_{exp} (μ_p) and Coefficient of Variation (CoV) of V_{pre}/V_{exp}.

6.5 Results and Discussion

In this section, the prediction ability of the developed ML models (LR, KNN, SVR, ANN, DT, RF, XGBoost, LGBoost and CatBoost) to the shear strength of FRCM strengthened beams is studied. In addition, this paper also compares the prediction effect of the existing traditional models (models 1-7 (Triantafillou and Papanicolaou, 2006; Escrig et al., 2015; Thermou et al., 2019; Tetta et al., 2018b; ACI, 2013; Younis et al., 2017; Ombres, 2015b)) with the developed ML models.

6.5.1 Performance of Machine Learning Models

Figure 6.8. illustrates the relationship between V_{pre} and V_{exp} obtained by the nine ML models, in which the purple points represent the data in the training set, the green ones represents the data in the test set, the black dotted line represents the perfect match between V_{pre} and V_{exp}, and the red solid line represents the real or actual linear matching effect of all data. The performance of the 9 ML models for the training, test and total data is presented in Table 6.5 based on the selected statistical indices. As shown in Fig. 6.8a, the LR model shows a poor prediction effect (α = 0.69, R^2 = 0.77), which indicates that the relationship between the selected 14 eigenvalues and the shear strength of the FRCM strengthened beam is not a simple linear relationship. While the rest of the models, except KNN, show good predictive performance (R^2 > 93.9%, Table 6.5). Among the single models (LR, KNN, SVR, DT), DT has the best performance considering both test and training sets (R^2 are 0.96 and 0.96, respectively), and the predicted values are well concentrated around the 45-degree diagonal indicating a small dispersion. The MAE values for training and testing are 11.215 kN and 16.751 kN, respectively, and the RMSE is 19.072 kN and 21.056 kN. These low error metrics indicate that the model provides accurate predictions with minimal deviation from the experimental values, highlighting its reliability.

Regardless of training set and test set, the ensemble models (ANN, RF, XGBoost, LGBoost and CatBoost) show better correlation (R^2 > 96%) and stability than other models. Among them, XGBoost emerges as the most suitable based on its overall performance. It achieves the highest R^2 and the lowest MAE and RMSE values (98.98%, 5.36kN and 10.07kN, respectively), underscoring its superior prediction accuracy and stability. While ANN and CatBoost also deliver commendable results, they fall short of XGBoost's benchmarks. Furthermore, models like LGBoost, known for their analysis speed, do not exhibit a significant advantage in this context due to the modest size of the research database.

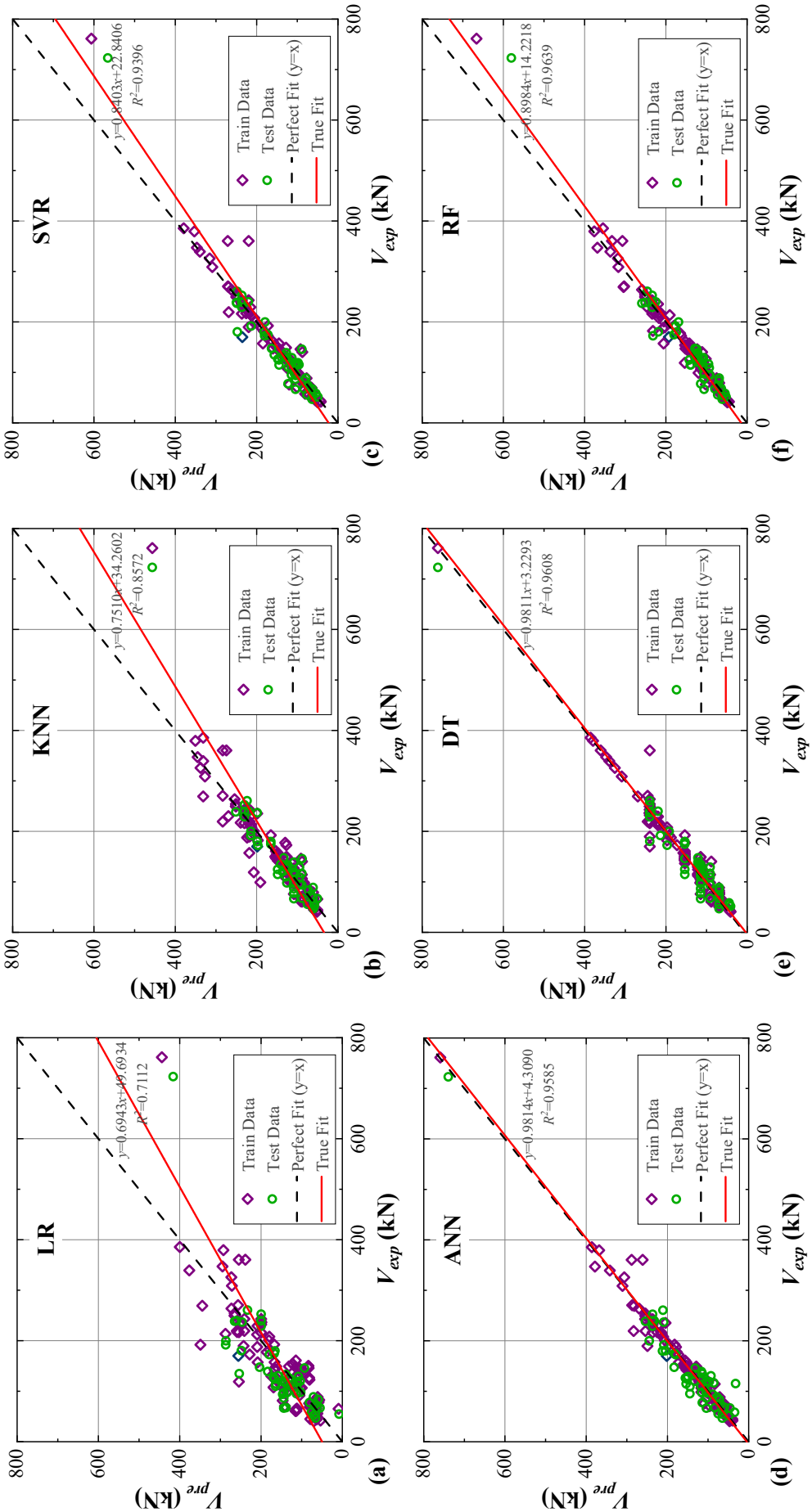
LR
y=0.6943x+49.6934
R²=0.7112
(a)
KNN
y=0.7510x+34.2602
R²=0.8572
(b)
SVR
y=0.8403x+22.8406
R²=0.9396
(c)
ANN
y=0.9814x+4.3090
R²=0.9585
(d)
DT
y=0.9811x+3.2293
R²=0.9608
(e)
RF
y=0.8984x+14.2218
R²=0.9639
(f)
Train Data
Test Data
Perfect Fit (y=x)
True Fit
V_pre (kN)
V_exp (kN)
0
200
400
600
800

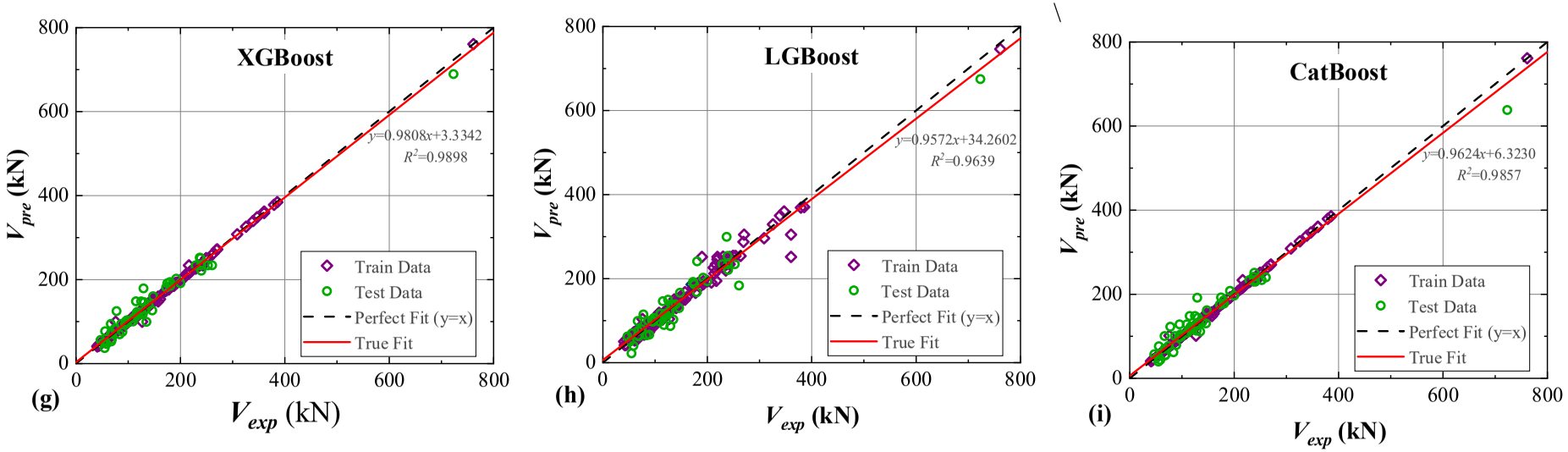

Fig. 6.8. Comparison between experimental,V_{exp}, and predicted, V_{pre}, shear strength for: (a) LR; (b) KNN; (c) SVR; (d) ANN; (e) DT; (f) RF; (g) XGBoost; (h) LGBoost; (i) Catboost.

Table 6.5. Results of the assessment of the ML models based on the selected statistical indices.

	Training Data							Test Data							Total Data						
	α	b	μ_p %	R^2 %	CoV %	MAE (kN)	RMSE (kN)	α	b	μ_p %	R^2 %	CoV %	MAE (kN)	RMSE (kN)	α	b	μ_p %	R^2 %	CoV %	MAE (kN)	RMSE (kN)
LR	0.74	41.43	106.21	73.55	31.15	33.04	50.49	0.61	65.82	114.89	66.35	30.66	37.70	59.22	0.69	49.69	108.85	71.12	31.06	34.46	53.30
KNN	0.79	31.22	102.31	85.83	19.22	19.29	37.80	0.66	40.86	109.84	87.58	19.66	21.62	42.30	0.75	34.26	101.81	85.72	19.36	20.00	29.22
SVR	0.86	19.59	101.61	94.31	12.68	9.51	25.00	0.80	29.28	104.67	93.34	17.14	17.47	29.30	0.84	22.84	102.30	93.96	14.35	11.94	26.38
ANN	0.97	4.84	97.19	96.84	10.67	9.83	17.49	1.00	3.14	117.94	93.83	22.81	20.78	25.68	0.98	4.31	102.01	95.90	15.55	13.16	20.33
DT	0.96	5.91	103.34	96.23	13.33	11.22	19.07	1.02	-2.17	101.03	95.96	20.08	16.75	21.06	0.98	3.23	101.84	96.12	15.70	12.94	19.70
RF	0.93	10.08	100.66	97.46	9.05	9.50	16.22	0.82	23.03	102.13	94.46	16.51	16.52	26.78	0.90	14.33	101.19	96.35	11.86	11.63	20.03
XGBoost	1.00	0.45	100.22	99.81	3.94	2.11	4.30	0.95	9.02	101.57	97.16	16.32	12.81	17.07	0.98	3.33	100.81	98.98	9.75	5.36	10.07
LGBoost	0.97	5.40	101.75	97.30	9.60	9.36	16.13	0.94	8.18	101.67	94.28	19.41	17.15	23.85	0.96	6.30	101.71	96.39	13.35	12.73	18.82
CatBoost	1.00	0.27	98.23	99.83	3.81	1.21	4.09	0.88	18.31	103.99	96.26	17.27	13.96	20.96	0.96	6.32	101.20	98.58	10.37	5.09	12.05

Figure 6.9 illustrates a boxplot of the 10-fold cross-validation accuracy for the training set, where K = 10 represents the number of folds in the cross-validation process. In each iteration, one of the 10 parts serves as the validation set, while the remaining nine parts are used for training, with this process repeated 10 times. The accuracy is calculated as the mean of accuracies obtained across all folds. The boxes show the interquartile range, the horizontal line in the middle refers to the median, the triangles are the mean, the diamonds indicate outliers, and the upper and lower whiskers show 1.5 times exceeding the difference between first and third quartiles, respectively. In the training set, the individual cross-validation training accuracy ranged between 53.5% and 96.5%, excluding LR and outliers. The average accuracy across all models ranges from 54.7% to 82.6%. Among them, the LR model has the largest dispersion and the lowest accuracy. Models KNN, ANN and DT also showed lower accuracy (average = 70.2%, 75.1%, and 73.1%). On the other hand, XGBoost and LGBoost showed the best accuracy (average = 82.6% and 82.0%).

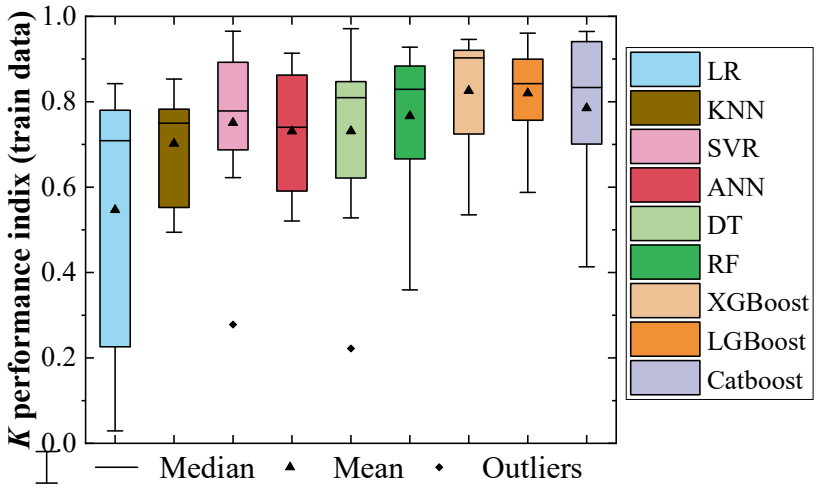

Fig. 6.9. 10-fold cross-validation performance for training data

6.5.2 Robustness and Stability Analysis of Boosting Algorithms

To mitigate potential biases from single dataset splits, a robustness and stability evaluation of the models was essential. Building on the analysis in the previous section, which showed that XGBoost delivered the best performance, and given the similarities between XGBoost, LGBoost, and CatBoost, this section further evaluates the robustness and stability of these three models. The dataset was randomly split 100 times, with 70% used for training and 30% for testing in each iteration. Key metrics

between V_{exp} and V_{pre} — R^2, MAE, RMSE, μ_p and CoV of V_{exp}/V_{pre} —were recorded after each modelling. Additionally, training time (TT) was measured to assess computational costs. Table 6.6 summarises the statistical results from these trials.

Table 6.6. Results of the robustness and stability analysis of boosting algorithms.

	Parameter	μ	SD	Min	Q1	Median	Q3	Max
XGBoost	R^2 (%)	96.97	3.11	78.75	97.05	97.67	98.15	99.1
	μ_p (%)	100.98	1.29	97.94	100.19	100.87	101.53	106.41
	CoV (%)	12.41	4.94	8.28	10.19	11.16	12.47	39.68
	MAE (kN)	7.2	1.16	5.16	6.45	6.99	7.65	11.25
	RMSE (kN)	16.42	5.78	9.5	13.61	15.28	17.19	46.1
	TT (s)	1.64	0.28	0.97	1.5	1.64	1.78	2.29
LGBoost	R^2 (%)	92.2	6.55	67.67	93.53	94.52	95.51	96.54
	μ_p (%)	102.01	1.22	98.67	101.21	109.97	102.61	106.82
	CoV (%)	15.20	1.41	12.62	14.56	15.21	15.72	24.96
	MAE (kN)	14.37	1.19	11.99	13.61	14.25	15.05	18.42
	RMSE (kN)	26.37	9.14	18.59	21.18	23.41	25.44	56.87
	TT (s)	0.105	0.028	0.075	0.083	0.094	0.12	0.175
CatBoost	R^2 (%)	93.84	8.46	69.06	95.81	97.37	97.97	99.05
	μ_p (%)	100.93	1.28	98.72	100.10	100.72	101.51	105.73
	CoV (%)	12.65	3.21	7.96	10.41	11.31	13.00	27.96
	MAE (kN)	7.4	1.95	4.59	6.08	6.78	7.81	13.8
	RMSE (kN)	21.29	12.69	9.76	14.24	16.21	20.48	55.63
	TT (s)	3.05	0.24	3.05	3.36	3.51	3.62	4.25

XGBoost exhibited the highest robustness, with an average R^2 of 96.97% and the lowest variability across dataset splits (SD = 3.11%), indicating consistent performance regardless of data partitioning. Its CoV was also the lowest at 12.41%, reflecting stable predictions across various test sets. Moreover, XGBoost achieved a good balance between accuracy and efficiency, with an average training time of 1.64 seconds, further emphasizing its superiority in both predictive power and computational cost. LGBoost, while offering the fastest training time (0.105 seconds on average), delivered the least accurate predictions (μ_p = 102.01%) and exhibited the highest CoV (15.20%). This suggests LGBoost is more sensitive to data splits and provides reduced stability compared to XGBoost. In addition, CatBoost had the longest training time (3.05 seconds) and greater variability, signalling lower stability than XGBoost.

In conclusion, XGBoost proved to be the most reliable and robust model, offering a well-balanced performance between accuracy and computational efficiency. While

LGBoost's speed is advantageous, its high variability makes it less suitable for smaller datasets. However, it may become more applicable as the dataset grows. CatBoost's strength lies in its ease of use, with minimal parameter tuning required, but its higher computational cost and lower stability make it less favourable than XGBoost in this context.

6.5.3 Comparison of the Proposed and Existing Models

In this section, the predicting ability between the proposed ML models and the existing analytical models mentioned in Chapter 2 is compared. Since XGBoost demonstrated the best performance among the ML models in terms of accuracy, stability, and computational efficiency, it was selected as the representative model for comparison with existing analytical models. In Models 1-7, the strengthened beams with anchorage systems and/or flexural failure are not considered in the analysis due to limitations imposed by the analytical models (Gonzalez-Libreros et al., 2017a). Therefore, the numbers of specimens used in this comparison is 105. In addition, since many of the studies included in the database do not provide information on the elastic modulus of the FRCM composite, only 58 beams are used in case of Models 5-7. To facilitate comparison, XGBoost's results are also listed. Figure 6.10 illustrates the relationship between V_{exp} and V_{pre} obtained by Models 1-7 and XGBoost, and their calculated α, b, R^2, RMSE, and MAE values are presented in Table 6.7.

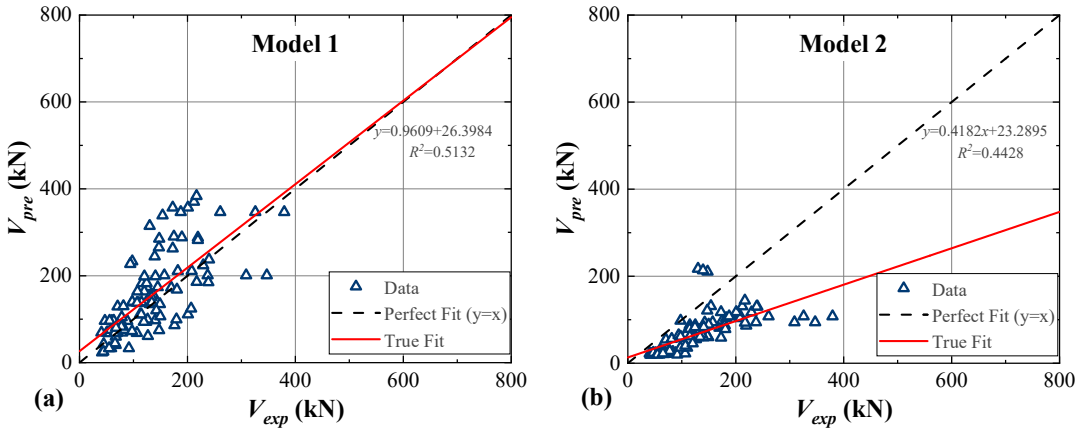

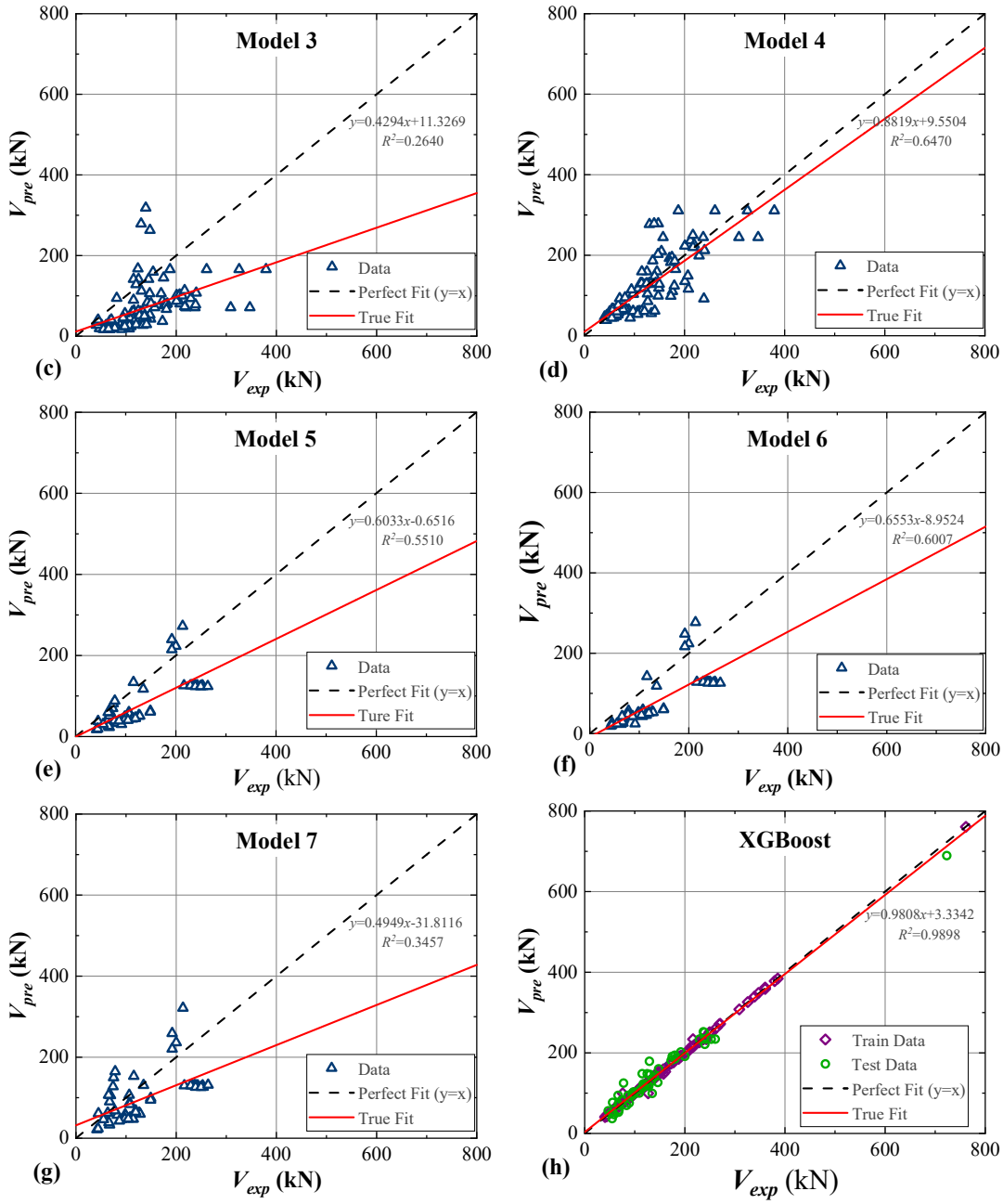

Fig. 6.10. Comparison between experimental,V_{exp}, and predicted, V_{pre}, shear strength for: (a) Model; (b) Model 2; (c) Model 3; (d) Model 4; (e) Model 5; (f) Model 6; (g) Model 7; (h) XGBoost.

As shown in Fig. 6.10, all analytical models show greater dispersion and worse prediction effects than XGBoost. Within the subset of models based on fibre properties (Models 1-4), Model 4, anchored in the jacket's effective stress, registers the highest R^2 at 64.7% yet remains less precise than XGBoost. Model 1, achieving the analytical models' closest regression coefficient to 1, demonstrates poor stability due to its high CoV, MAE, and RMSE. Furthermore, many data points in Models 1 and 4 are significantly overestimated (Figs. 6.10 (a, d)), which raises safety concerns in practical

engineering applications. Models 2 and 3, link the effective strain of fibre with $f_c^{2/3}/\rho_f E_f$, rank as the least precise, frequently underestimating shear strength. This limitation in Model 1's prediction accuracy is expected, as it simplistically assumes ε_{eff} to be $0.5\varepsilon_{fu}$, without adjusting for configuration variations or detachment effects. When initially proposed, Model 1 was based on a limited data, and its authors suggested treating this value as indicative until further testing becomes available (Triantafillou and Papanicolaou, 2006). Models 2 and 3 improved upon Model 1 by linking ε_{eff} to $f_c^{2/3}/\rho_f E_f$, but this relationship is grounded in studies of FRP's effective bond length and lacks adequate validation for FRCM applications (Escrig et al., 2015). Moreover, these models were derived from limited experimental data, which likely contributes to their reduced accuracy on broader datasets. Similar issues exist with Model 4, which was initially designed for FRP systems.

Table 6.7. Results of the assessment of Models 1-7 and XGBoost based on the selected statistical indices

	α	b	μ_p %	R^2 %	CoV %	MAE (kN)	RMSE (kN)
Model 1	0.96	26.40	118.09	51.32	38.93	47.93	67.39
Model 2	0.42	23.29	51.52	44.28	45.49	66.26	80.62
Model 3	0.43	11.33	53.01	26.40	72.40	73.27	88.79
Model 4	0.88	9.78	96.09	64.70	31.93	30.98	61.17
Model 5	0.60	-0.65	59.13	55.10	42.45	59.65	70.94
Model 6	0.66	-8.95	56.34	60.07	38.85	61.17	70.26
Model 7	0.49	-31.81	78.33	34.57	53.72	57.55	68.46
XGBoost	0.98	3.33	100.81	98.98	9.75	5.36	10.07

Moreover, Models 5-7, based on FRCM composite properties, also display limited accuracy, heightening the risk in engineering applications. Model 5 sets the composite's effective strain at 0.04, based on minimal testing, and the guidelines indicate that this value requires further validation (ACI549, 2013). The results in Fig 11(e) suggest that this strain limit may be too low for practical applications (μ_p= 59.13%, CoV = 42.45%). Model 7 builds on Model 5 by adding the mortar's shear contribution, effectively doubling the contribution without an explanation for this adjustment. While Model 7 somewhat reduces the tendency to underestimate (μ_p= 100.31%, CoV = 53.72%), it introduces a new issue, with many data points now showing a tendency to overestimate. In Model 6, the brittle nature of cement-based composites leads to non-uniform and locally high tensile stresses across shear cracks

in FRCM, resulting in partial failure before complete failure of the composite. Consequently, FRCM jackets exhibit lower efficiency than FRP jackets, and Model 6 accounts for this by introducing an 'effectiveness coefficient' of 0.5. However, the overall accuracy remains unsatisfactory, as shown as shown by its error indices (μ_p= 56.34%, CoV = 38.85%), in Fig. 6.10f , where Model 6 performs similarly to Models 5 and 7. The XGBoost model markedly enhances prediction accuracy compared to all traditional models, notably reducing CoV, MAE, and RMSE across all analytical models, showcasing the superiority of ML models.

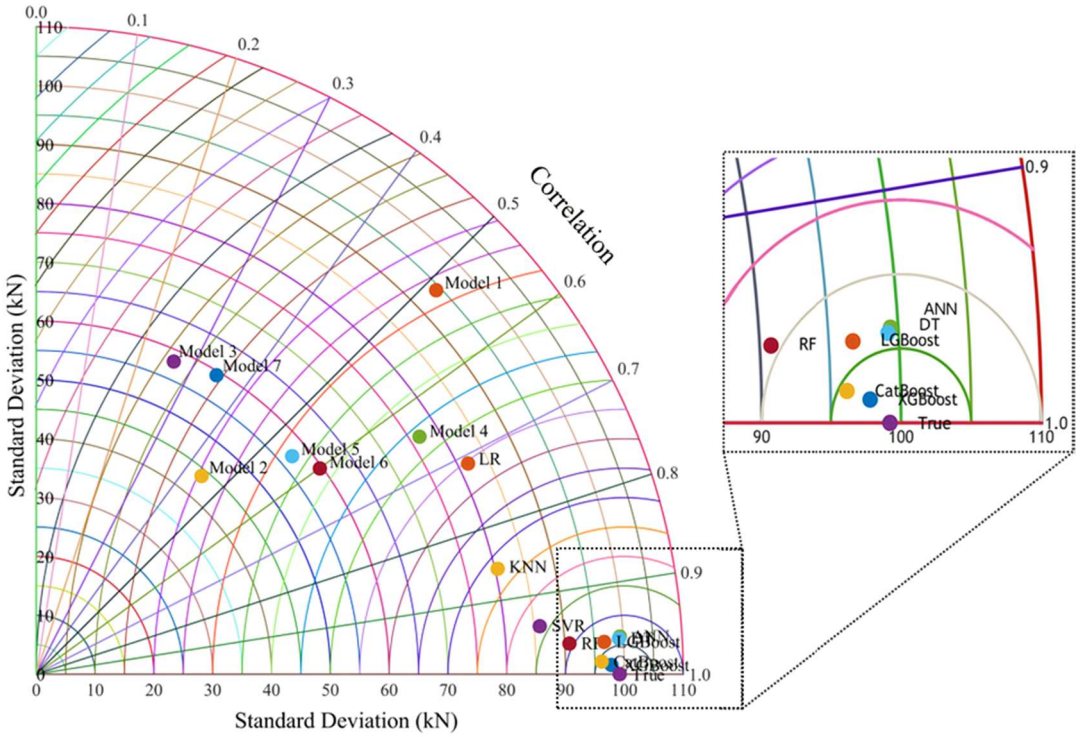

Fig. 6.11. Taylor diagram visualization for the predicted shear strength using the ML models and the empirical models.

For a further detailed comparison, the Taylor diagram shown in Fig. 6.11 has been developed which graphically indicates the accuracy of the models in predicting the shear strength. According to Taylor (2001), in Taylor diagrams:

- The horizontal distance of each model point from the origin represents the standard deviation of the model's predictions relative to the experimental values, showing how well each model captures the variability in the data. Ideally, a model with a standard deviation close to that of the experimental data

(represented by the purple 'True' point) is preferable, as it suggests that the model can replicate the range of observed responses.

- The radial line from the origin through each model point indicates the correlation coefficient between predicted and experimental values. Higher correlation (closer to 1) implies a stronger linear relationship, showing that the model's predictions align more closely with experimental trends.
- The distance from each model point to the 'True' point reflects the Root Mean Square Error (RMSE), which captures the overall prediction error. A smaller RMSE distance indicates higher model accuracy, as it reflects less deviation from the actual observed values.

The graph clearly demonstrates the effectiveness of the development models and visualises a series of points on the polar diagram. All machine learning models (shown in the zoomed section except LR) are clustered closer to the 'True' point compared to traditional empirical models (Models 1–7), indicating that ML models generally provide higher accuracy in predicting shear strength. In addition, the XGBoost and CatBoost show the best performance, as they are closest to the 'True' point. This implies that these models not only capture the variability in the data well (similar standard deviation) but also maintain a high correlation with experimental values and low RMSE, making them the most accurate predictors in this context.

6.6 Interpretations of XGBoost

6.6.1 Shapley Additive Explanations (SHAP) Interpretations

Previous studies were unable to address the interpretability of the ML models, but post interpretation is necessary for complex models. Therefore, this part uses the emerging SHAP method to reveal the potential reasoning behind the prediction and the interaction between each variable and the results for all data. In this method, the SHAP value, that is, the average marginal contribution of each factor, is allocated to each factor. The factor with the largest absolute SHAP value is considered the most important. In addition, because XGBoost has the best prediction effect, this paper uses the SHAP method to explain the output of XGBoost model.

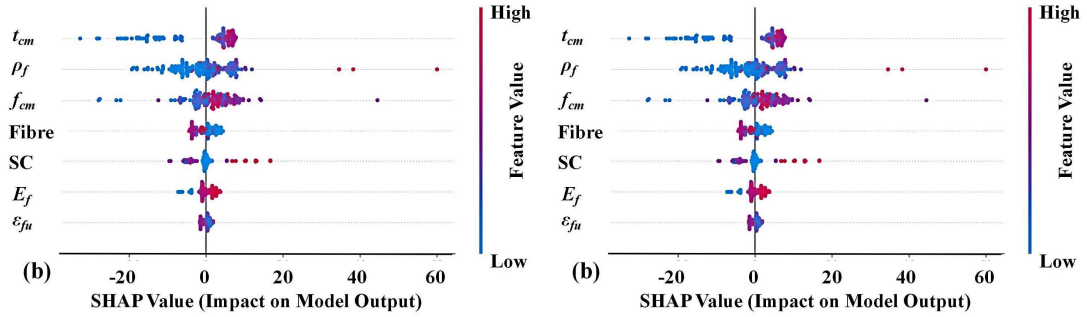

Fig. 6.12. SHAP global explanation on XGBoost: (a) Beam's properties; (b) FRCM solution properties

Figure 6.12 depicts the global interpretation of the XGBoost model, where the eigenvalues are represented by colour. Blue represents the lower values, whereas red represents higher values. Fig. 6.12a shows the influence of beam characteristics on the prediction effect, in which d, f_c and ρ_w play a major role. Like the experimental observation results, for these three inputs and f_{yw}, the larger value can positively affect the shear strength of the strengthened beam, while the lower value would exert a negative influence. On the other hand, a/d and $\rho_{long,b}$ have the opposite effect. For the properties of FRCM composites (Fig. 6.12b), t_{cm}, ρ_f and f_{cm} are the three main contributing factors. It is worth mentioning that, in the development of the model, U-shaped, side bonded and fully wrapped jackets are represented by '1', '2' and '3'. The results in SHAP show that the use of fully wrapped configuration improves the shear capacity of the reinforcement beam, because it can prevent jacket's detachment to a certain extent.

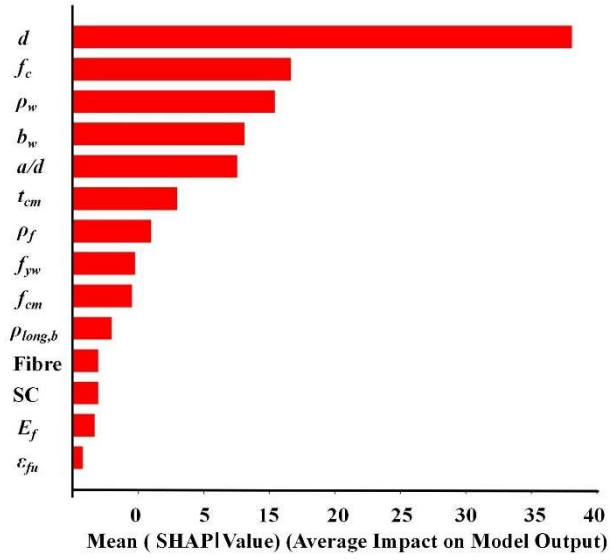

Fig. 6.13. Mean absolute SHAP values of XGBoost.

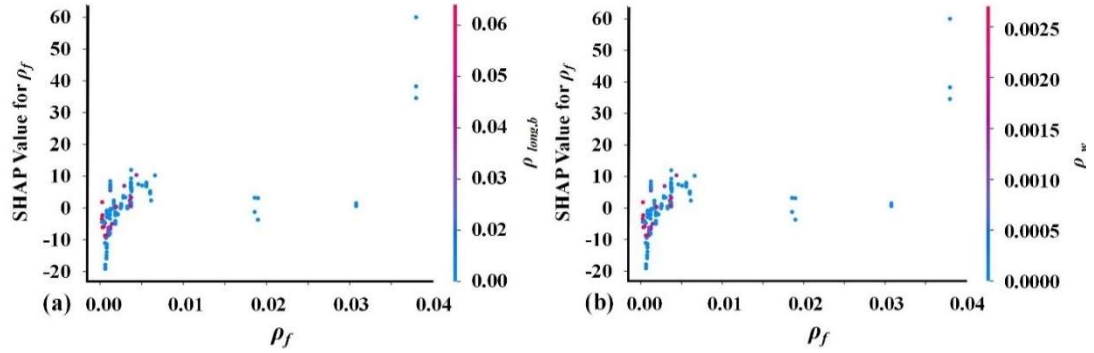

Fig. 6.14. SHAP dependency and interaction plots of XGBoost: (a) ρ_f vs $\rho_{long,b}$; (b) ρ_f vs ρ_w

Figure 6.13 depicts a graph illustrating the average SHAP values for each input value, arranged in descending order of importance. In the graph, the input parameters appear in y-axis, while their corresponding mean absolute SHAP values are presented in the x-axis, where *d* shows the highest average SHAP value. However, as the highest-ranking parameter in FRCM performance, t_{cm} only ranks sixth in the overall ranking. Some studies have confirmed the importance of mortar's effect for the performance of FRCM systems, but the related mechanisms and in-depth research, especially in terms of shear strengthening, are still very limited (Ombres, 2015a; Minafò and La Mendola, 2018). In addition, Fig. 6.14 shows SHAP dependency and interaction plots for selected pairs of input parameters. In these plots, the x-axis represents the value of the ρ_f, the y-axis corresponds to the SHAP values, and the colour scale represents the values of the second parameter involved in the interaction (i.e., $\rho_{long,b}$ in Fig. 6.14a and ρ_w in Fig. 6.14b). Figure 6.14 reveals that as ρ_f increases, the distribution of SHAP values exhibits a trend towards higher magnitudes, albeit without a clear linear relationship. Additionally, samples with higher SHAP values for ρ_w and $\rho_{long,b}$ are predominantly found within the lower SHAP value distributions for ρ_f. This suggests a minor negative interaction between the internal and external reinforcement within the XGBoost model, although this phenomenon is not pronounced.

In summary, the SHAP value analysis in this study elucidates key determinants of shear strength in FRCM-strengthened beams, such as *d*, f_c, ρ_w, f_{ywd}, and ρ_f, alongside the unexpected yet substantial role of the t_{cm}, challenging prevailing assumptions. Furthermore, the interaction between internal and external reinforcements has been corroborated to some extent. These findings hold the potential to inform future

research, guiding enhancements in the engineering practices and design guidelines for FRCM-reinforced beams.

6.6.2 Partial Dependence Plots (PDP) Analysis

To complement the SHAP analysis and further investigate the influence of input variables on the target value, Partial Dependence Plots (PDP) were used. PDP are a technique used in machine learning to visualise the relationship between a target response and selected input features, while averaging the effect of all other features. PDP shows the marginal effect of a specific input variable on the predicted outcome, providing insights into how changes in that feature influence the model's predictions. The horizontal axis represents the values of the specific feature being analysed, while the vertical axis shows the corresponding partial dependence (it indicates the effect of the feature on the predicted shear strength).

Figure 6.15 presents the PDPs for the XGBoost model used in the present study to predict the shear strength of FRCM-strengthened RC beams. It is important to note that the observed curves are not smooth; rather, they are derived from discrete data points available in the training dataset, inherently leading to non-continuous results. The reason for these curves being non-smooth also lies in the nature of the XGBoost model and the type of data used. XGBoost is a tree-based algorithm, which results in discontinuous decisions and step-like responses when predicting outcomes, especially when compared to models like neural networks.

As shown in Fig. 6.15, the shear strength of FRCM strengthened beams significantly increases with an increase in b_w, d, f_c. This trend is consistent with fundamental mechanics principles. Increasing the width and effective depth of the beam section results in a larger shear area and an increased lever arm, respectively, both of which enhance shear capacity. These observations align with traditional shear design equations, where shear strength is directly related to cross-sectional dimensions. Conversely, shear strength decreases as the a/d increases. This phenomenon occurs because the beam changes from a deep to a slender shape, shifting the main way it supports weight from an arch-like structure to more of a truss system, which decreases its ability to resist shear forces (Tetta et al., 2018a; Wakjira and Ebead, 2020).

FRCM parameters, such as p_f, E_f, and ε_{fu}, show a generally positive impact on shear strength, though their influence is less pronounced compared to geometric parameters. This is because the effectiveness of FRCM strengthening on overall beam capacity is shaped by complex interactions with the beam's inherent parameters, such as substrate compressive strength, stirrup configuration, and longitudinal reinforcement (Gonzalez-Libreros et al., 2017a). These factors may influence the contribution of FRCM parameters. Moreover, traditional models often overlook these interactions, which can substantially impact the prediction results. Notably, as mentioned in Chapter 2, side bonded configurations are more prone to detachment, which affects strengthening effectiveness, whereas fully wrapped configurations provide better resistance to detachment and thus superior strengthening. Additionally, they also claimed that basalt and carbon textiles have been shown to offer better strengthening compared to PBO. There two phenomena are also reflected in the PDP results.

Furthermore, Fig.6.15 also highlights the limitations posed by the current dataset, which lacks sufficient data to provide a smooth, continuous curve across all parameter ranges. This limitation could be addressed by expanding the experimental database with additional tests or by generating data using reliable finite element models once they are developed.

6.7 XGBoost Based Shear Strength Prediction Tool of FRCM Strengthened Beam

This study presents an XGBoost-based predictive model for estimating the shear strength of RC beams strengthened with FRCM systems. The model was trained on a comprehensive experimental database integrating diverse test results from the literature, utilizing 14 input parameters representing geometric dimensions, reinforcement ratios, matrix characteristics, and textile configuration details. XGBoost was selected due to its superior capability in handling nonlinear interactions, multicollinearity, and sparse data—conditions commonly encountered in structural retrofitting scenarios. Model development followed rigorous machine learning protocols, including 10-fold cross-validation for hyperparameter optimisation. To evaluate robustness and generalisation, the dataset was randomly split 100 times into training and testing subsets. XGBoost consistently achieved high predictive accuracy

and minimal performance variability, confirming its reliability under stochastic conditions.

A comprehensive benchmarking campaign was conducted against eight machine learning algorithms (e.g., support vector regression, decision trees, neural networks) and seven analytical models proposed in existing design codes and scholarly literature. Results indicated that XGBoost achieved the highest predictive accuracy and robustness across all metrics. To improve interpretability and enhance engineering relevance, SHAP and DPD methods were employed, confirming that variables such as the shear span-to-depth ratio and textile reinforcement index contributed consistently with theoretical expectations.

This work constitutes the first application of machine learning to predict the shear behaviour of FRCM-strengthened RC beams, thereby filling a critical research gap. Prior ML-based structural models have largely focused on flexural behaviour or FRP-based systems, with limited attention to shear-critical cases involving mortar-based composites. The integration of interpretable machine learning, robust validation, and a physically grounded parameter set represents a methodological innovation, offering a reproducible and extensible framework for future structural modelling in retrofitting applications.

To bridge academic innovation and engineering practice, the trained XGBoost model was embedded in a user-friendly graphical user interface (GUI). This tool allows engineers to input the 14 key variables and instantly retrieve shear strength predictions, bridging the gap between advanced modelling and engineering practice. The tool is freely accessible at https://github.com/13y37ith/XGBoost-Based-Shear-Strength-Prediction-Tool-of-FRCM-Strengthened-Beams, promoting broader use in academic research and preliminary design. Given that the model is trained exclusively on experimental data, predictions should be considered informed estimates and validated through additional testing when applied to novel strengthening configurations, as illustrated in Fig. 6.16.

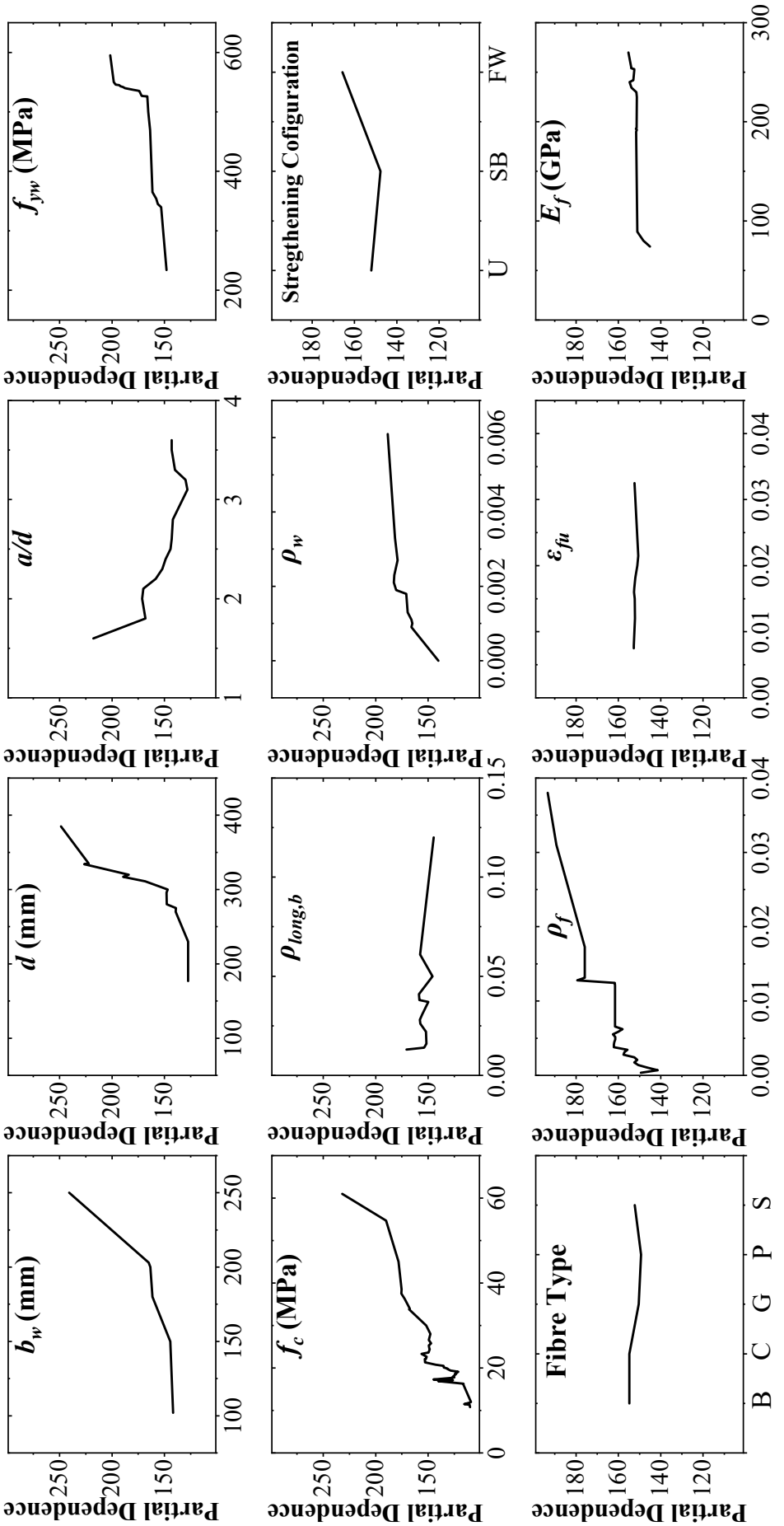
Partial Dependence
b_w (mm)
d (mm)
a/d
f_{yw} (MPa)
f_c (MPa)
$\rho_{long,b}$
ρ_w
Stregthening Cofiguration
U SB FW
ρ_f
ε_{fu}
E_f (GPa)
Fibre Type
B C G P S

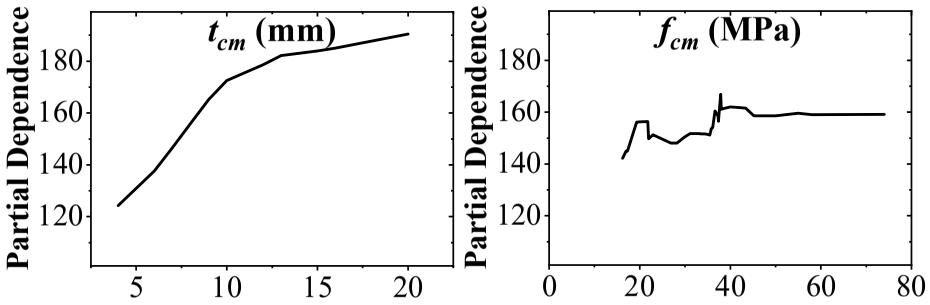

Fig. 6.15. Partial dependence verse input parameters of XGBoost

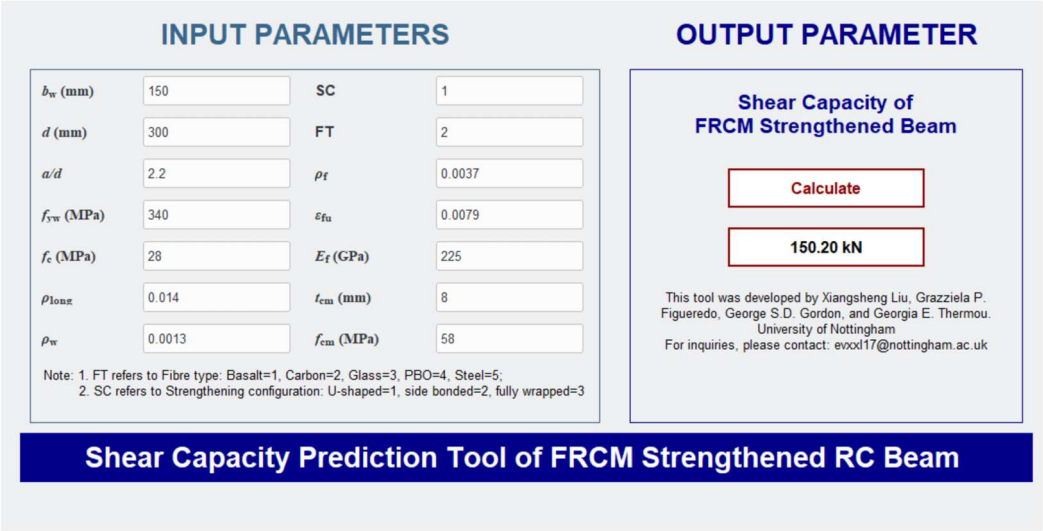

Fig. 6.16 Case Study of Shear Strength Calculation Using the Developed Tool.

6.8 Conclusions

This Chapter introduces nine ML models—Linear Regression (LR), K-Nearest Neighbour (KNN), Support Vector Regression (SVR), Artificial Neural Network (ANN), Decision Tree (DT), Random Forest (RF), Extreme Gradient Boosting (XGBoost), Light Gradient Boosting (LGBoost), and CatBoost—to estimate the shear capacity of FRCM-reinforced RC beams. Utilising a dataset of 175 samples. 14 variables are used as input value, encompassing structural, material, and reinforcement attributes, to construct these models. Key insights from this research include:

- ML models demonstrate potent capabilities in predicting shear capacities, with XGBoost outperforming others in effectiveness, stability, and accuracy, evidenced by its high R^2, CoV, MAE and RMS (98.98%, 9.75%, 5.36kN, and 10.07kN, respectively).
- Robustness and stability analysis showed that XGBoost outperformed LGBoost and CatBoost, with the highest average R^2 (96.97%) and lowest average CoV (12.41%), indicating strong stability across random dataset splits. XGBoost balanced predictive accuracy with computational efficiency, while LGBoost, despite its speed, showed higher variability, and CatBoost had higher computational costs with moderate stability.
- Comparative analysis with existing empirical models reveals the superior precision of ML approaches, notably the XGBoost model, which significantly reduces prediction errors.
- SHAP analysis identifies beam depth, concrete compressive strength, and stirrup reinforcement ratio as paramount influences on shear capacity. Surprisingly, mortar thickness emerges as a notable factor, despite limited existing research on its impact.
- PDP analysis shows that in the XGBoost model, the shear strength of FRCM-strengthened beams significantly increases with b_w, d, f_c, while decreasing with a/d. FRCM parameters (p_f, E_f, and ε_{fu}) positively impact shear strength, though their influence is secondary to beam geometry.

- Given the limitations of the current dataset, potential discrepancies between experimental and real-world beams, possible variations in mortar thickness during application, and other factors, findings in this study should be interpreted with caution. Expanding the database through additional testing or reliable finite element modelling could help validate and refine these insights for practical applications.

Chapter 7

Finite Element Modelling of SRG Strengthened RC beams

This chapter focuses on the finite element modelling (FEM) of Steel SRG strengthened RC beams. A critical evaluation of existing FE models, identifying their strengths and inherent limitations is carried out. These models frequently simplify SRG as a homogeneous composite, overlooking key factors such as mortar thickness and UHTSS textile density, which are essential for accurately predicting the shear response of high-density SRG systems under complex loading conditions. A refined FEA model is introduced to overcome these shortcomings, employing a micro-modelling approach for SRG systems. The model distinguishes between the mortar matrix and UHTSS textile, representing them as separate components. Three-dimensional solid elements are utilised for the mortar, while embedded truss elements simulate the steel cords. A novel bond-slip constitutive model is also developed to more accurately represent the interface behaviour and gradual detachment mechanisms.

The refined model is validated using experimental data from eight RC beams presented in Chapter 3, encompassing fully wrapped and U-shaped SRG configurations. The model's accuracy is evaluated by comparing its predictions for ultimate load, displacement, and failure modes with experimental results. Furthermore, its capacity to replicate complex behaviours, including stiffness degradation caused by minor detachment and distinct post-peak responses, is rigorously examined. By

addressing the limitations of existing models and introducing a robust framework for SRG-strengthened RC beams, this chapter contributes to the advancement of reliable and precise numerical tools for structural analysis.

Finite element validation under fatigue loading was not conducted in this chapter due to limited available experimental data and the inherent complexity of accurately simulating fatigue-induced failure mechanisms. Experimental investigations of SRG-strengthened beams subjected to fatigue remain scarce, precluding rigorous validation. Moreover, fatigue failure involves complex, time-dependent bond degradation processes between the strengthening system and concrete substrate, which are inadequately captured by bond-slip constitutive models originally developed under monotonic loading. Thus, the applicability of static bond-slip relationships to fatigue conditions remains uncertain. Given these limitations, fatigue modelling is identified as an essential focus for future research, necessitating targeted experimental studies and the development of dedicated fatigue-oriented finite element models.

7.1 Presentation of Existing FE Models of SRG Strengthened Elements

In Chapter 3, the effectiveness of SRG systems for shear strengthening of beams has been thoroughly validated, and their potential for altering failure modes is further demonstrated. However, research involving finite element modelling (FEM) of SRG-strengthened beams remains relatively scarce. The first notable study, conducted by Bencardino and Condello (2015), aimed to evaluate the effectiveness of various bilinear bond-slip laws for simulating the FRP-concrete interface in SRG-strengthened beams. These bond-slip laws are summarised in Table 7.1. Using the general-purpose finite element software Abaqus (2011), they simulated an SRG-strengthened beam subjected to flexural loading. The concrete, internal reinforcement, and external strengthening were modelled using tetrahedral, truss, and shell elements, respectively. The concrete material selected was of the damage-plastic type, with tensile cracking and compressive crushing identified as the primary failure mechanisms. The compressive behaviour followed Hognestad's simplified stress-strain equation, while the tensile response remained linear elastic until failure. The longitudinal and transverse reinforcement were modelled with bilinear elastic-plastic constitutive laws. Although SRG materials are naturally orthotropic, the model assumed their

mechanical behaviour to be isotropic. In modelling the SRG, mortar and fabric were treated as a homogeneous composite, and mortar thickness was neglected. Nonlinear analyses faced convergence difficulties, especially as cracks initiated, prompting the use of Explicit Dynamic to resolve quasi-static problems. The results indicated that the bond-slip law developed by Lu et al. (2005) successfully predicted the structural behaviour of SRG-strengthened beams, with a peak load error of just 2.6%.

Bencardino and Condello (2016) subsequently applied this model in Abaqus to simulate five flexural insufficient beams. Experimental results were used to calibrate the numerical simulations and assess their accuracy. The study parameters included matrix types (i.e. mortar matrix for SRG and resin matrix for SRP) and strengthening configuration (U-shaped and fully wrapped). The first specimen served as the control, while two specimens were U-shaped SRG/SRP jacketed beams. The final two specimens were strengthened by fully wrapped SRG/SRP jackets. The bond-slip models for the strengthening system and the substrate were based on Lu et al.'s model. The results demonstrated that the numerical failure modes were consistent with the experimental failure modes, with an average error in the ultimate load of approximately 6.5%. However, the load error reached up to 14%, and the displacement errors were as high as 32.8%, with the load-deflection curve after peak load not being reproduced in the simulation.

Table 7.1. Bond-slip laws between strengthening system and substrate (Bencardino and Condello, 2015).

Model	$K_0(\mathrm{N/mm^3})$	$\tau_{max}(\mathrm{N/mm^2})$	$G_f(\mathrm{N/mm})$	β_w
Obaidat et al. (2013)	$0.16G_a/t_a + 0.47$	$1.46f_{ct}^{1.033}G_a^{0.165}$	$0.52f_{ct}^{0.26}G_a^{-0.23}$	-
Monti et al. (2003)	$\frac{E_a E_c}{2.5(t_a E_c + 50E_a)}$	$1.8\beta_w f_{ct}$	$0.297 f_{ct}\beta_w^2$	$\sqrt{\frac{1.5(2 - b_f/b_w)}{1 + b_f/100}}$
Lu et al. (2005)	76.92	$1.5\beta_w f_{ct}$	$0.308\beta_w^2\sqrt{f_{ct}}$	$\sqrt{\frac{2.25 - b_f/b_w}{1.25 + b_f/b_w}}$
CNR-DT200 R1 (2013)	$\frac{0.6}{t_a/G_a + 25/G_c}$	$2G_f/0.25$	$0.77\beta_w\sqrt{f_c f_{ct}}$	$\sqrt{\frac{2 - b_f/b_w}{1 + b_f/b_w}} \geq 1$

K_0 = initial stiffness; τ_{max} = shear bond strength; G_f = fracture energy; G_c = shear modulus of concrete; t_a = ideal thickness of adhesive; G_a = the young modulus of adhesive, E_a = shear modulus of adhesive; β_w = width ratio factor; b_f = width of strengthening system.

Ombres and Verre (2019a) also employed this FE model to simulate three SRG-strengthened bending beams, with a primary focus on anchorage type as a critical

parameter. Their simulations demonstrated good agreement with experimental results, achieving a peak load prediction error of 10.5%. Additionally, the predicted cracking patterns at beam failure showed high accuracy. In 2021, they extended their analysis to include six U-shaped SRG shear-strengthened beams, reporting that the predicted ultimate loads and corresponding deflections were within 5% of the experimental values. The predicted cracking patterns also closely matched the experimental observations (Ombres and Verre, 2021).

Furthermore, Katsamamakas et al. (2021) utilised the ATENA (Cervenka Consulting, 2018) software to simulate nine shear-strengthened beams. They introduced a novel approach for modelling shear-strengthened, under-reinforced RC beams with SRG jackets. Their methodology incorporated embedded truss elements to represent external steel cords and reinforcement, while mortar and concrete were modelled using three-dimensional solid elements. In this approach, the SRG was assumed to be perfectly bonded to the beam, with no consideration for bond-slip effects. Within the SRG, the fully wrapped jacket with sufficient anchorage length was assumed to achieve perfect bonding between the steel tendons and mortar. For the U-shaped wrapped jacket, fib MC2010 (reference) guidelines were used to model bond-slip behaviour. Their results showed that the average load prediction error was less than 1%, the average displacement error was under 10%, but the maximum error reached 89%. Despite this, the correlation between numerical and experimental energy absorption was satisfactory, with an average error of 4.2%.

It is evident that numerical simulations of SRG-strengthened beams remain limited, with most studies concentrated on flexural strengthening. Additionally, Abaqus-based finite element models frequently treat the mortar and fabric as a composite material using shell elements in two-dimensional models. However, previous findings from this study have demonstrated that textile density and mortar thickness play a significant role in the shear strengthening performance of SRG systems. Specifically, high-density SRG systems are prone to premature delamination, resulting in diminished shear strengthening efficiency. Accordingly, Chapter 7 seeks to evaluate the performance of existing Abaqus finite element models in simulating high-density SRG-strengthened beams. Furthermore, it introduces refinements to the model to establish a more robust and reliable framework for simulating the shear response of SRG-strengthened RC beams.

7.2 Evaluation of Existing Models

To evaluate the performance of the existing model, numerical analyses were conducted on a control beam (A-N) and high-density SRG-strengthened reinforced concrete beams (Group A, $a/d = 2.0$) with U-shaped (A-GH-U1) and fully wrapped (A-GH-W1) configurations. The experimental results for these beams are provided in Chapter 3.

7.2.1 Geometry

All tested beams were modelled using three-dimensional (3D) finite element (FE) analysis. Considering the beams' geometric, mechanical, and loading asymmetry, the entire beam structure was modelled. A view of the FE mesh is given in Fig. 7.1.

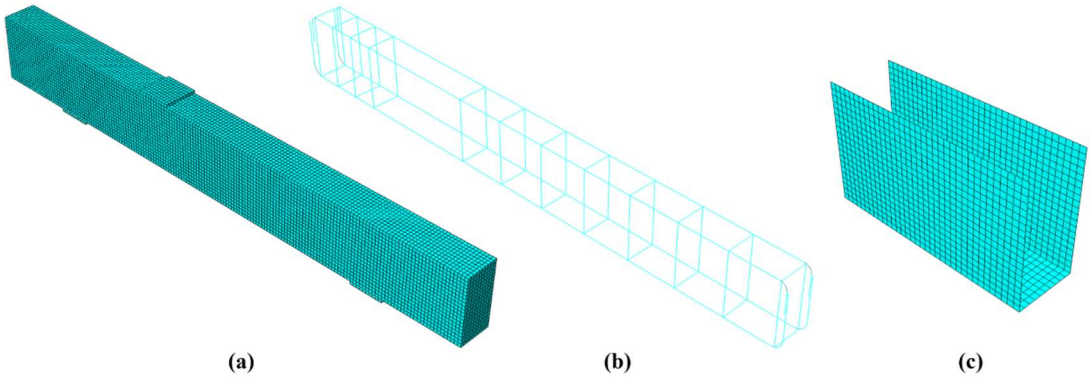

Fig. 7.1. 3D Finite Element mesh: (a) overview; (b) steel cage; (c) U-shaped SRG jackets.

For the concrete, 8-node brick elements (C3D8) were employed, which are solid continuum elements featuring eight nodes with three translational degrees of freedom per node and linear interpolation in each direction. Internal steel reinforcement was modelled using T3D2 linear truss elements. The external reinforcement system was modelled using a macro-modelling (MA) approach, which treats the steel fabric and inorganic matrix layer as a homogeneous composite without distinguishing individual components. The concrete-to-external reinforcement interface was modelled using a general contact definition to capture the bonding behaviour accurately. Nonlinear finite element analysis was performed using a displacement-controlled approach to effectively capture the softening branch of the load-midspan deflection curve and the debonding process.

The concrete was modelled using 8-node brick elements (C3D8), which are solid continuum elements characterised by eight nodes with three translational degrees of

freedom per node and linear interpolation in each direction. Internal steel reinforcement was represented using T3D2 linear truss element. The external SRG reinforcement system was modelled using a macro-modelling (MA) approach, which simplifies the system by treating the UHTSS textile and inorganic matrix as a single homogeneous composite material, without distinguishing individual components. Given the significantly smaller thickness of the SRG jackets compared to the beam width, shell elements with linear interpolation functions (S4R) were employed. These elements are well-suited for structures where one dimension (thickness) is much smaller than the other dimensions (Ombres and Verre, 2019b). The concrete-to-external reinforcement interface was modelled using a general contact definition to capture the bonding behaviour accurately. Nonlinear finite element analysis was performed using a displacement-controlled approach to effectively capture the softening branch of the load-midspan deflection curve and the debonding process.

7.2.2 Material Models

7.2.2.1 Concrete

The behaviour of concrete was simulated using the Concrete Damage Plasticity (CDP) model, which has demonstrated superior capability in capturing both elastic and plastic characteristics compared to the smeared cracking (SCM) and brittle cracking (BCM) models (Godat et al., 2020). The CDP model incorporates two primary failure mechanisms: concrete crushing under compression and cracking under tension. Given its robustness, the CDP model was selected for this study.

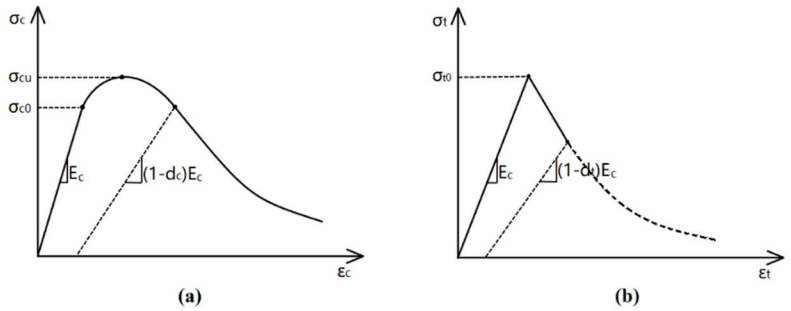

Fig. 7.2. Behaviour of concrete under uniaxial load: (a) compression; (b) tension.

The uniaxial responses of concrete under compressive and tensile loading are depicted in Fig. 7.2. The response of concrete under uniaxial compression was modelled using the well-known stress-strain relationship proposed by Hognestad

(1951), as specified in the Code for Design of Concrete Structures (GB50010, 2010). The constitutive relationship is established using the following equations:

$$\sigma_c = (1 - d_c)E_c\varepsilon_c \tag{7-1}$$

$$d_c = \begin{cases} 1 - \dfrac{\rho_c n_c}{n_c - 1 + x_c{}^n} & x_c \le 1 \\ 1 - \dfrac{\rho_c}{\alpha_c(x_c - 1)^2 + x_c} & x_c \ge 1 \end{cases} \tag{7-2}$$

$$\rho_c = \frac{f_c}{E_c\varepsilon_{c,r}} \tag{7-3}$$

$$n_c = \frac{E_c\varepsilon_{c,r}}{E_c\varepsilon_{c,r} - f_c} \tag{7-4}$$

$$x_c = \frac{\varepsilon_c}{\varepsilon_{c,r}} \tag{7-5}$$

Where σ_c represents the compressive stress of concrete; ε_c presents the strain when compressive stress reaches σ_c; σ_{cu} (=f_c) is the ultimate compressive stress; and $\varepsilon_{c,r}$ is the compressive strain corresponding to σ_{cu}. If the calculated $\varepsilon_{c,r}$ is less than 0.002, it is taken as 0.002. ρ_c is the parameter values of the descending section of the stress–strain curve under uniaxial compression; ε_{cu} denotes the ultimate compressive strain of the concrete; d_c is the damage evolution parameters of concrete under uniaxial compression. The coefficient n_c is used to account for material properties; when its calculated value exceeds 2.0, it is capped at 2.0.

The tensile behaviour of concrete is modelled with a linear elastic branch up to its tensile strength (f_t). After cracking initiates, the response transitions into a linear softening phase. The post-cracking behaviour under direct strain is modelled using tensile hardening, which defines the post-failure stress-strain relationship of cracked concrete. The constitutive relationship of concrete under uniaxial tension is shown below:

$$\sigma_t = (1 - d_t)E_c\varepsilon_t \tag{7-6}$$

$$d_t = \begin{cases} 1 - \rho_t(1.2 - 0.2x_t{}^5) & x_t \le 1 \\ 1 - \dfrac{\rho_c}{\alpha_t(x_t - 1)^{1.7} + x_t} & x_t \ge 1 \end{cases} \tag{7-7}$$

$$\rho_t = \frac{f_t}{E_c\varepsilon_{t,r}} \tag{7-8}$$

$$x_t = \frac{\varepsilon_t}{\varepsilon_{t,r}} \tag{7-9}$$

Where σ_t represents the tensile stress of concrete; ε_t presents the strain when tensile stress reaches σ_t; σ_{tu} (=f_t) is the ultimate tensile stress; and $\varepsilon_{t,r}$ is the tensile strain corresponding to σ_{tu}; ε_{tu} denotes the ultimate tensile strain of the concrete; d_t is the damage evolution parameters of concrete under uniaxial tensile. Based on the ACI 318 (2008), Poisson's ratio for concrete was taken as 0.2 for the beams considered, and the tensile strength f_t and elastic modulus E_c of concrete were calculated using the following equations:

$$E_c = 4700\sqrt{f_c} \tag{7-10}$$

$$f_t = 0.35\sqrt{f_c} \tag{7-11}$$

The CDP model employs five key plastic damage parameters in this framework: the dilation angle set at 38°, the flow potential eccentricity assigned a value of 0.1, the ratio of initial biaxial compressive yield stress to initial uniaxial compressive yield stress defined as 1.16, the ratio of the second stress invariant on the tensile meridian to that on the compressive meridian specified as 0.667, and a viscosity parameter with a value of zero.

7.2.2.2 Inner Reinforcement

The steel reinforcement demonstrates elastoplastic behaviour with strain hardening. Its linear elastic phase is described by an elastic modulus (210 GPa) and a Poisson's ratio (0.3). The yield and ultimate strain values characterise the steel reinforcement, with the average values derived from tests on three samples summarised in Table 7.2. A perfect bond was assumed using the embedded region interaction model in Abaqus. The concrete beam was modelled as the host region, while the reinforcement was defined as the embedded region.

Table 7.2. Mechanical properties of the internal steel reinforcement

Diameter	f_y (MPa)	f_u (MPa)	ε_y	ε_u
16 mm	528	619	0.0028	0.03
10 mm	538	626	0.0051	0.04
8 mm	326	505	0.0302	0.09

f_y = yield stress; f_u = ultimate stress; ε_y = yield strain; ε_u = ultimate strain.

7.2.2.3 SRG System

As shown in Fig. 7.1c, shell elements were employed to model the SRG system. In this model, the contribution of the mortar was neglected (Katsamamakas et al., 2021). Shell elements are particularly suited for modelling structures where the thickness is significantly smaller than the other dimensions (Taie et al., 2024). In this study, the high-density SRG layer, with a thickness of 0.169 mm (excluding the mortar thickness), was significantly thinner than the other dimensions, justifying this modelling approach. Although the mechanical behaviour of SRG systems is inherently orthotropic, with strain predominantly aligned in the transverse direction, this characteristic was not considered in the model. Instead, a brittle, elastic isotropic representation was employed. The material parameters for the high-density SRG system, as reported by Thermou et al. (2021), included an elastic modulus of 172,900 MPa, a Poisson's ratio of 0.3, and an ultimate tensile strength of 3011 MPa.

As shown in Fig. 7.1c, shell elements were utilised to model the SRG system, with the contribution of the mortar matrix omitted (Katsamamakas et al., 2021). Shell elements are well-suited for modelling structures with a thickness significantly smaller than their other dimensions (Taie et al., 2024). In this study, the high-density SRG system, with a thickness of 0.169 mm (excluding the Mortar's thickness), was significantly smaller compared to its other dimensions. While SRG systems inherently exhibit orthotropic mechanical behaviour (Ombres and Verre, 2019b), with strain primarily oriented in the transverse direction, this feature was simplified in the model by adopting a brittle, elastic isotropic representation. The material parameters for the high-density SRG system, as reported by Thermou et al. (2021), included an elastic modulus of 172,900 MPa, a Poisson's ratio of 0.3, and an ultimate tensile strength of 3011 MPa.

7.2.2.4 Bond-Slip Model at SRG-Concrete Interface

To simulate the SRG-concrete interface, a cohesive surface was defined. This model identifies potential separation zones and describes their interaction through the relative displacement at each contact point, following the traction-separation approach. The traction-separation model is assumed to be bilinear, exhibiting an initial linear elastic behaviour before damage initiation, which is modelled by a linear softening branch.

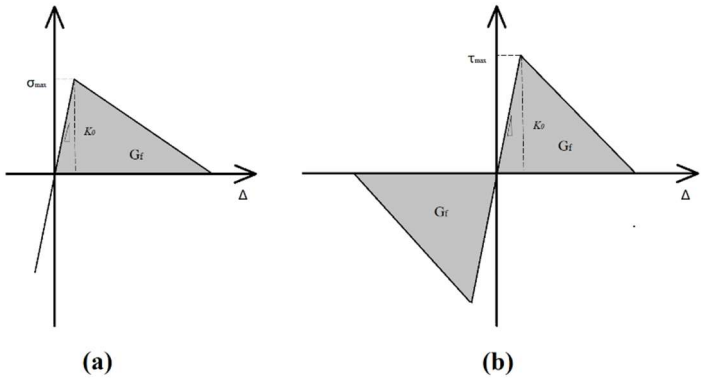

Fig. 7.3. Traction-separation response: (a) model I; (b) model II and III.

As illustrated in Fig. 7.3, this model accounts for two failure modes in two-dimensional modelling: opening (Mode I) and sliding (Mode II) (Bencardino and Condello, 2016). The first mode is driven by normal stress, while the second is governed by shear stress. The local behaviour at the SRG-concrete interface is represented using the bilinear bond-slip law proposed by Lu et al. (2015). This law is expressed through the following relationship:

$$\tau = \begin{cases} \tau_{max} s/s_0 & s < s_0 \\ \tau_{max}\left(s_f - s\right)/s_f - s_0 & s_0 < s < s_f \\ 0 & s > s_f \end{cases} \tag{7-12}$$

$$s_0 = 0.0195\beta_w f_{ct} \tag{7-13}$$

$$s_0 = G_f/\tau_{max} \tag{7-14}$$

$$k_0 = \tau_{max}/s_0 \tag{7-15}$$

where τ and s represent the local interface shear stress and relative slip, respectively; s_0 corresponds to the slip at which the bond strength is achieved; s_f is the slip value at which the interface shear stress reduces to zero. The definitions and equations for τ_{max}, k_0 and G_f are provided in Table 7.1.

7.2.3 Solution Approach

Modelling brittle materials like concrete and masonry often encounters challenges due to structural instability caused by crack propagation or strain softening (Bencardino and Condello, 2016). These phenomena hinder convergence in traditional static solution methods, such as the Newton-Raphson or arc-length techniques. The difficulties arise from localised damage, where displacement increments near the damaged zone dominate the response, making the global displacement norm insufficient to accurately capture the failure process.

To address these challenges, the explicit dynamic method is employed for quasi-static problems, as recommended by Chen et al. (2015). This nonlinear analysis approach integrates the equations of motion in the time domain using the central difference method, where the discrete mass matrix plays a critical role in ensuring computational efficiency and accuracy. In this specific finite element procedure, two key parameters govern the analysis: the kinetic energy-to-internal energy ratio and the variable mass scaling factor. To obtain a solution analogous to static conditions, the kinetic energy-to-internal energy ratio during the analysis must not exceed 5% (Chen et al., 2015). The variable mass scaling function adjusts the mass of elements at the beginning of each step and periodically throughout the analysis. In this study, a mass scaling value of 0.00005 was applied, resulting in accurate predictions for the static response.

To ensure the reliability of the finite element results, a mesh refinement study was performed using mesh sizes of 1, 5, 10, 15, 20, 25, 30, and 40 mm for the concrete domain, internal reinforcement, and SRG jackets. Very fine meshes (1–5 mm) yielded only marginal improvements in predicting ultimate load and mid-span deflection (within 1–2%) while significantly increasing computational time, often exceeding 10 hours. In contrast, coarse meshes (25–40 mm) led to notable accuracy loss, with peak load deviations up to 21% compared to the 5 mm reference, and failed to capture localised failure mechanisms such as jacket debonding. Meshes in the 10–25 mm range provided a good balance between accuracy and efficiency, with deviations within 3–5% compared to 5 mm meshes and computation times of 3–5 hours. As circular-section models exhibited greater sensitivity to mesh coarseness and showed larger deviations under identical conditions, square-section specimens with a 10 mm mesh were primarily adopted in this study to achieve more accurate and computationally efficient results.

7.2.4 Model Validity

To assess the reliability of the proposed finite element (FE) model, the load–midspan deflection curves predicted by the simulations were compared with the corresponding experimental results, as presented in Fig. 7.4.

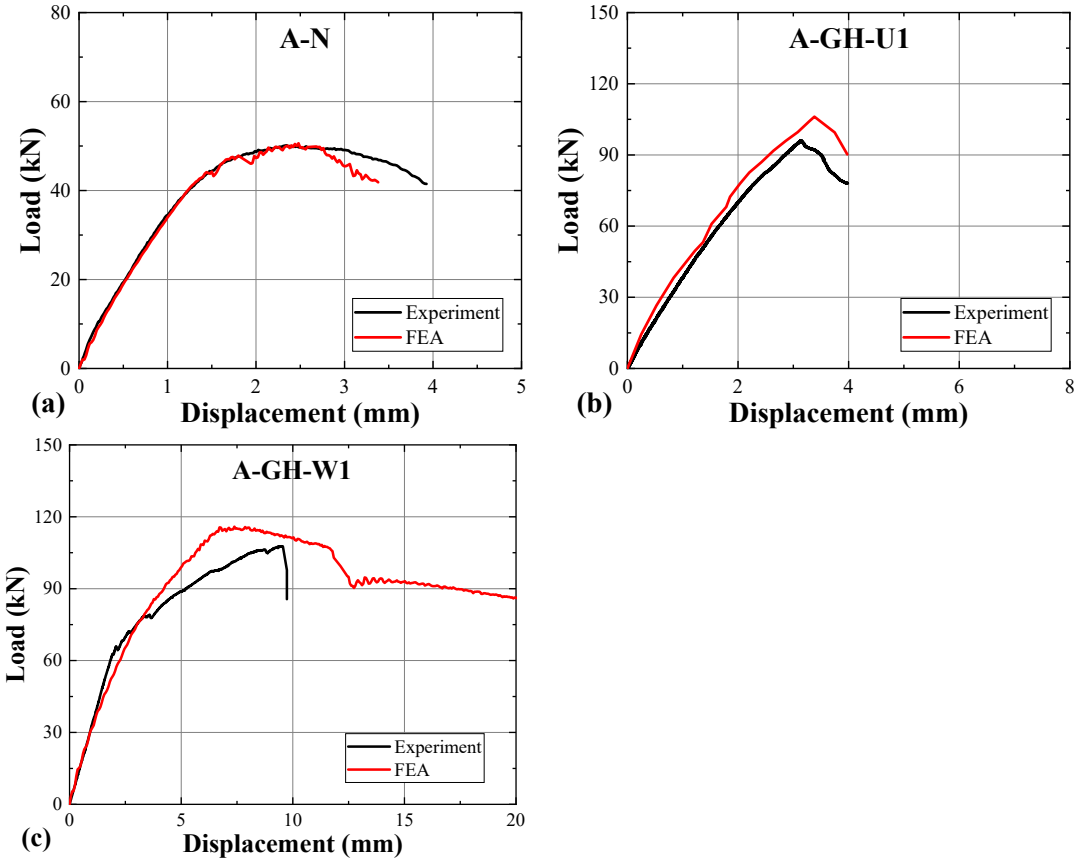

Fig. 7.4. Comparison between experimental and numerical force–displacement curves: (a) A-N; (b) A-GH-U1; (c) A-GH-W1

Figure 7.4a depicts the experimental and numerical load–deflection responses for the control beam (A-N) in Group A, demonstrating excellent alignment between the two datasets. Figures 7.4b and 7.4c illustrate the comparison between experimental and simulated responses for high-density SRG shear-strengthened beams within the same group. For the U-shaped SRG-strengthened beam (A-GH-U1), the numerical predictions closely matched the experimental response, although the FE model slightly overestimated the peak load by approximately 17.9%. In contrast, the fully wrapped SRG-strengthened beam (A-GH-W1) revealed significant discrepancies between the numerical and experimental responses.

These discrepancies are primarily attributed to the limitations of the macro-modelling approach used in this section. Specifically, modelling the SRG system as a homogeneous composite with shell elements neglects critical local mechanisms, such as interfacial bond degradation, mortar compaction, and stress concentration around textile cords. Additionally, the simplified representation does not account for variations in UHTSS textile density and mortar thickness, both of which have been

shown to substantially influence load transfer, cracking behaviour, and failure modes. As such, the roughness observed in the validations highlights the inherent constraints of conventional macro-modelling when simulating high-density SRG systems, further justifying the refined micro-modelling approach introduced in subsequent sections.

7.3 Proposed model Considering Mortar Thickness

7.3.1 Geometry

To address the limitations of existing FE models, which do not account for the influence of mortar thickness and UHTSS textile density, this study develops an enhanced model to more accurately simulate the shear behaviour of SRG-strengthened beams. Concrete and reinforcement were modelled using C3D8 and T3D2 elements, respectively, consistent with the methodologies outlined in the section 7.2.

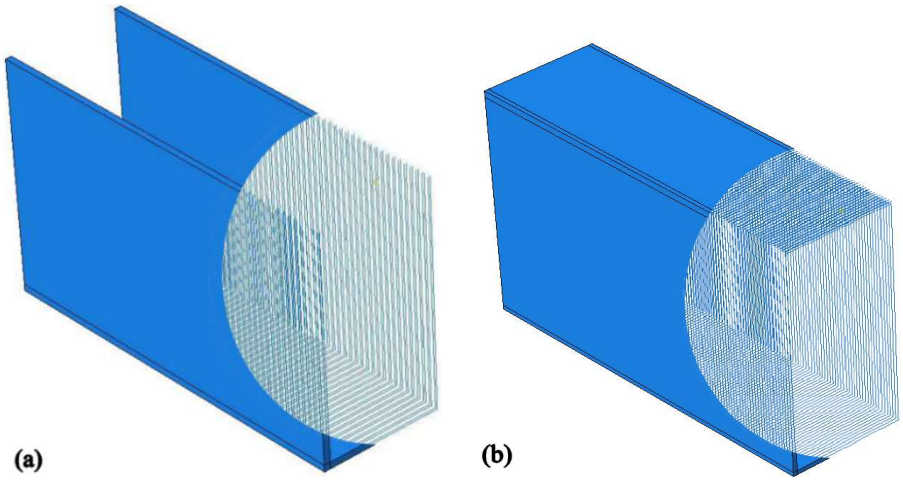

Fig. 7.5. Modelling the SRG system in ABAQUS by MI approach: (a) U-shaped; (b) fully wrapped.

For the SRG system, a micro-modelling (MI) approach was employed (Verre, 2022), where the mortar and UHTSS textile were modelled as separate components. The mortar, having mechanical properties similar to concrete, was modelled using C3D8 solid elements. The UHTSS textile, which consists of high-strength steel cords in the transverse direction and fibreglass micromesh in the longitudinal direction, was represented in the model with each steel cord modelled individually using T3D2 elements. The fibreglass micromesh, which serves to hold the steel cords in place and does not contribute to the composite's strength, was omitted from the model. Figure 7.5 illustrates the finite element resolution for the external reinforcement. Notably, the configuration mirrors the experimental setup: in U-shaped jackets, each textile layer is

modelled as discrete and independent (Fig. 7.5a); in fully wrapped jackets, the textile layers are represented as continuous and uninterrupted (Fig. 7.5b).

7.3.2 Material Models

The constitutive models for concrete, longitudinal steel bars, and stirrups are consistent with those outlined in Section 7.2.2. In the SRG system, the mortar matrix is treated similarly to concrete due to its comparable mechanical properties, and the same compressive and tensile constitutive relationships are applied. The mechanical properties of the mortar are detailed in Table 3.3. According to ACI 318-08 (2008), the ultimate tensile strength of the mortar matrix (f_{cmt}) is derived from its ultimate compressive strength (f_{cm}) using Equation (7-16).

$$f_{cmt} = 0.62\sqrt{f_{cm}} \tag{7-16}$$

To ensure the accuracy of the FE results, five tensile specimens of each type of UHTSS textiles were prepared and tested (Fig. 7.6). The tests were conducted under tensile loading, with axial strain recorded using a video gauge. Displacement control was applied at a rate of 1.25 mm/s, and both ends of the specimens were firmly clamped. Table 7.3 presents the experimentally determined values for elastic modulus, tensile strength, and ultimate strain, while Fig. 7.7 illustrates the corresponding stress-strain curves obtained from the tests.

Fig. 7.6. Test setup of tensile tests on the UHTSS textile.

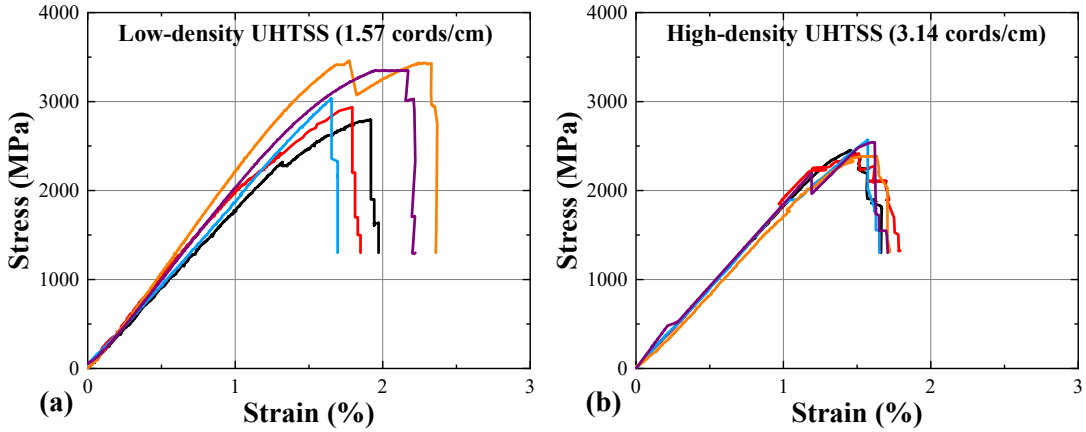

Fig. 7.7. Load-displacement curves: (a) low density UHTSS textile (1.57 cords/cm); (b) high density UHTSS textile (3.14 cords/cm).

Table 7.3. Mechanical Properties of UHTSS.

	E_f (GPa) (CoV)	$f_{fu,f}$ (MPa)(CoV)	ε_{fu} (%) (CoV)
1.57 cords/cm	200.6 (0.09)	3116.3 (0.08)	2.0 (0.10)
3.14 cords/cm	184.8 (0.02)	2474.8 (0.03)	1.7 (0.03)

7.3.3 Modelling of interface performance

In the SRG system, the fabric is assumed to be perfectly bonded to the matrix (embedded region), with no allowance for fabric-matrix interface sliding (Mercedes et al., 2021). The bond-slip behaviour between the mortar and the substrate is modelled using the constitutive law proposed by Feng et al. (2022) for FRCM systems applied to beams. The shear strength (τ) and interface slip (s) are defined as follows:

$$\tau = \begin{cases} \tau_{max} s/s_0 & s < s_0 \\ \tau_{max} s_0 (s_u - s)/(s_u - s_o) & s_0 < s < s_u \end{cases} \quad (7\text{-}17)$$

$$\tau_{max} = \sigma_{cm}(a_s \times e^{\chi/b_s} + c_s) \quad (7\text{-}18)$$

$$s_0 = \sigma_{cm}\left(-0.013e^{\chi/-0.89} + 0.016\right) + \left(-29310.74e^{\chi/1084419.4} + 29310.8\right) \quad (7\text{-}19)$$

$$s_u = \sigma_{cm}\left(0.0044e^{\chi/-0.99} + 0.0092\right) + \left(-0.76e^{\chi/-0.82} + 0.44\right) \quad (7\text{-}20)$$

where s_u represents the ultimate interface slip, σ_{cm} denotes the uniaxial compressive strength of mortar, χ is the interface roughness parameter, and a_s, b_s, and c_s are fitting parameters. According to Tian et al. (2019), for $f_{cm} \approx 40$ MPa, the fitting parameters for various roughness levels are listed in Table 7.4. Experimental results indicate that the interface of high-density SRG with concrete is relatively weak. Therefore, the constitutive data corresponding to the minimum bond strength is used for high-density SRG, while the data set corresponding to a roughness of 1.32 is selected for low-density SRG systems.

Table 7.4. Fitting parameters in the bond-slip law.

χ	a_s	b_s	c_s
0.57	-0.1048	-0.9590	0.0849
1.32	-0.1048	-0.9590	0.0849
3.33	-0.1048	-0.9590	0.0849

7.3.4 Model Validity

To validate the model, numerical analyses were conducted on the two control beams and six SRG-strengthened beams presented in Chapter 3, with results compared against experimental data. Figure 7.8 presents the typical failure modes obtained from finite element analysis (FEA) and highlights their consistency with the experimentally observed failure modes and DIC damage assessments discussed in Sections 3.11 and 3.12. The agreement between the numerical and experimental results demonstrates the reliability of the FEA model in predicting the failure behaviour of the tested beams.

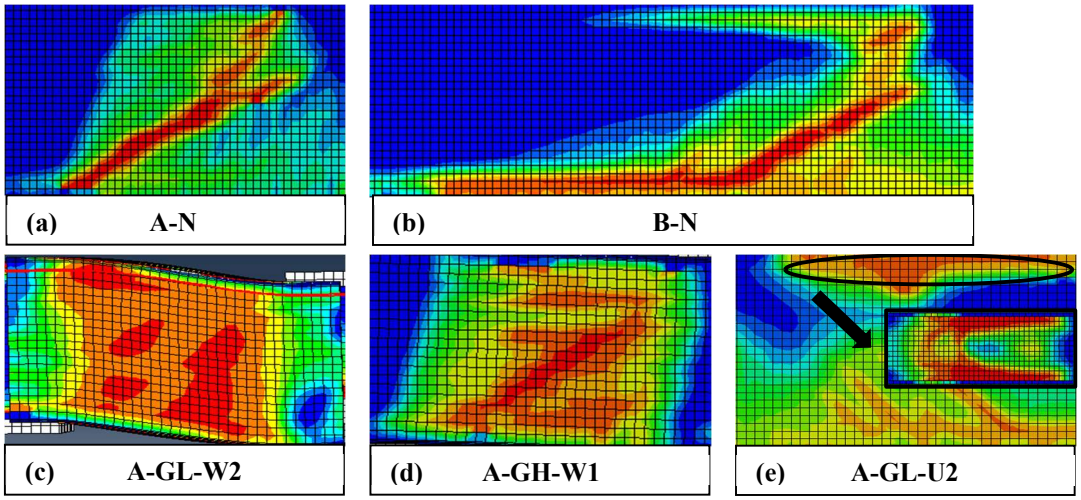

Fig. 7.8. Failure modes: (a) A-N; (b) B-N; (c) A-GL-W2; (d) A-GH-W1; (e) A-GL-U2.

For the control beams (A-N and B-N), both exhibited characteristic shear cracking, closely aligning with experimental observations. In the case of fully wrapped beams, the ductile failure mode of A-GL-W2, characterised by extensive damage areas, corresponds well to the patterns captured in DIC analysis (Fig. 7.8c). This suggests that the fully wrapped configuration optimised the stress-strain response and effectively reduced stress concentrations. Conversely, the high-density textile in A-GH-W1 resulted in poor adhesion, causing sudden debonding and leading to detachment-shear failure. This failure mode was marked by significant stress concentrations compared to A-GL-W2 (Fig. 7.8d). For U-shaped SRG-strengthened

beams, as exemplified by A-GL-U2 (Fig. 7.8e), no substantial damage was observed on the mortar surface. However, the top view revealed pronounced stress concentrations in the beam's cover layer. This pattern aligns with the experimentally observed detachment at the top surface and subsequent delamination of the cover layer during failure.

Table 7.5 presents a comparison of the ultimate loads obtained from experimental tests ($P_{max,t}$) and finite element analysis (FEA) results ($P_{max,f}$). The results show excellent agreement between the experimental and numerical predictions, with an average $P_{max,f}/P_{max,t}$ ratio of 99.6% and a coefficient of variation (COV) of 0.032. Similarly, the midspan deflections corresponding to the peak loads ($\delta_{max,t}$ for experimental results and $\delta_{max,f}$ for FEA) are consistent, with an average $\delta_{max,f}/\delta_{max,t}$ ratio of 107.5% and a COV of 0.091.

Table 7.5. Summary of test results

Series	Beam	$P_{max,t}$ (kN)	$P_{max,f}$ (kN)	$P_{max,f}/P_{max,t}$ (%)	$\delta_{max,t}$ (mm)	$\delta_{max,f}$ (mm)	$\delta_{max,f}/\delta_{max,t}$ (%)
A	A-N	51.3	49.5	0.96	2.50	2.44	0.98
	A-GL-U2	109.8	105.9	0.96	3.53	3.60	1.02
	A-GH-U1	97.5	97.4	1.00	3.15	3.59	1.14
	A-GL-W2	114.8	121.6	1.06	24.30	27.28	1.12
	A-GH-W1	107.7	106.8	0.99	9.51	8.79	0.92
B	B-N	38.8	39.8	1.03	1.41	1.78	1.26
	B-GL-U2	102.6	101.7	0.99	4.70	5.10	1.09
	B-GH-U1	105.0	103.0	0.98	5.17	5.53	1.07

The load-displacement curves, shown in Fig. 7.9, further validate the alignment between the experimental and FEA results. Specimens A-N and B-N, serving as the control beams for Groups A and B, exhibit differences of only 4% and 3% between $P_{max,f}/P_{max,t}$, respectively. It is noted that the load-deflection curve for A-N is detailed in Section 7.2.4. In Group A, the fully wrapped strengthened specimens demonstrate a strong agreement between FEA predictions and experimental results. For instance, the ultimate loads for A-GL-W2 and A-GH-W1 differ by only 6.00% and 1.00%, respectively, from the experimental values. The predicted load-displacement curves closely follow the experimental trends, effectively capturing the significant stiffness reduction observed around 70 kN due to minor detachment. Furthermore, the FEA results successfully replicate the post-peak behaviours of these specimens. A-GL-W1 exhibits a plateau-like response after reaching the peak load, with both numerical and

experimental curves maintaining a consistent trend without a significant decline (Fig, 7.9c). In contrast, A-GH-W1 demonstrates a sudden drop following the peak load caused by detachment, which is accurately reflected in the FEA results (Fig, 7.9d).

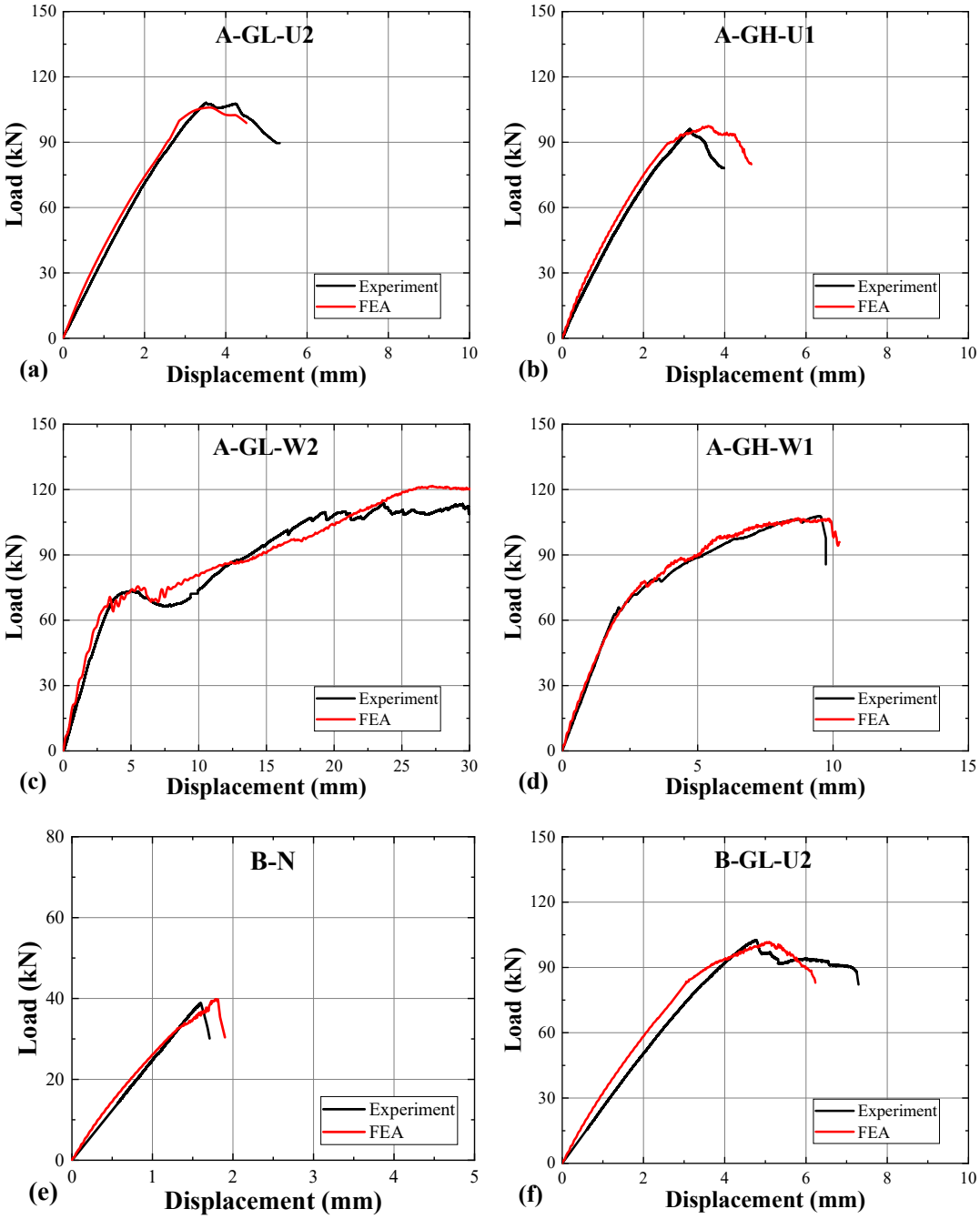

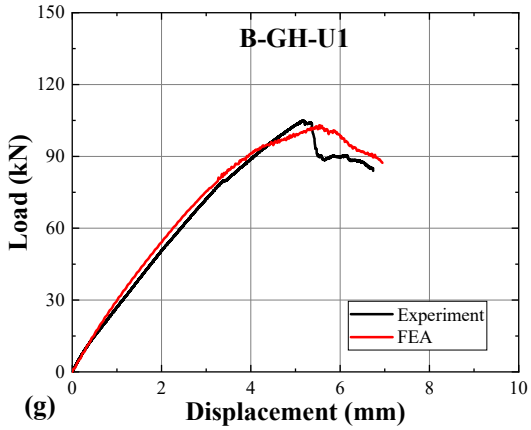

Fig. 7.9. Experimental versus numerical load–deflection response of the tested beams: (a)A-GL-U2; (b) A-GH-U1; (c)A-GL-W1; (d)A-GH-W1; (e)B-N; (f)B-GL-U2; (g)B-GH-U1.

For U-shaped SRG-strengthened specimens, the numerical load-displacement curves for all four samples from Groups A and B (A-GL-U2, A-GH-U1, B-GL-U2 and B-GH-U1) exhibit similar bilinear responses. These responses include an initial ascending branch leading to peak strength, followed by a sharp descending branch. The differences between $P_{max,f}$ and $P_{max,t}$ for these specimens are minimal, at 4%, 0.1%, 2%, and 1%, respectively, demonstrating the reliability of the FEA model in predicting the structural performance of strengthened beams. Nevertheless, the FEA model shows limitations in accurately simulating the post-peak pseudo-ductility observed in U-shaped strengthened beams in Group B (B-GL-U2 and B-GH-U1). This pseudo-ductility in experiments may arise from the increased shear span (620 mm) and reduced shear force, which result in a gradual detachment process of the SRG system rather than a sudden failure as observed in Group A. This behaviour involves complex interfacial mechanisms, such as progressive bond degradation, interfacial slip, and friction, which lead to a slow reduction in load capacity after the peak. However, the simplified bilinear bond-slip model used in the FEA does not adequately represent these gradual degradation processes, instead predicting an abrupt load drop after the peak, failing to replicate the experimentally observed gradual reduction.

7.4 Conclusions

This chapter provides a comprehensive review of existing finite element (FE) models for SRG-strengthened beams and evaluates their performance. The findings reveal that modelling SRG as a homogeneous composite neglects critical factors such

as mortar thickness and UHTSS textile density, which significantly influence bonding and stress distribution. These limitations hinder the accurate simulation of shear responses for high-density SRG systems. To address these shortcomings, the existing FE models were refined by adopting a micro-modelling (MI) approach. Embedded truss elements were introduced to represent external steel cords, while three-dimensional solid elements were employed to simulate the mortar matrix. Additionally, a novel bond-slip constitutive model was implemented, specifically designed to capture the adhesive behaviours between mortar and concrete.

The proposed FE model was validated using experimental data from eight RC beams presented in Chapter 3. The validation demonstrated the model's capability to accurately predict both the failure modes and the strengthening performance of the tested beams. The average ratios of $P_{max,f}/P_{max,t}$ and $\delta_{max,f}/\delta_{max,t}$ were 99.6% and 107.5%, respectively. For fully wrapped beams, the numerical analysis effectively captured the stiffness reduction observed around 70 kN due to minor detachment. Moreover, it accurately reproduced distinct post-peak behaviours: for A-GL-W1, the numerical and experimental load-deflection curves exhibited a plateau-like response with no sharp decline after the peak load; while for A-GH-W1, a sudden drop due to detachment was well-represented. For U-shaped SRG-strengthened beams in both Group A and Group B, the model successfully simulated the characteristic bilinear detachment-shear failure mode observed in all samples.

Chapter 8

Conclusions and Recommendations for Future Work

The degradation of existing structures due to aging, environmental conditions, insufficient maintenance, or the need to meet current design standards pose significant risks to their structural integrity, particularly for critical infrastructure such as bridges. Structural strengthening interventions are essential to prolong service life and ensure the safety and reliability of these systems. Fibre-reinforced polymers (FRPs) have gained widespread adoption as a strengthening solution due to their high strength-to-weight ratio and design flexibility. However, the resin-based matrices used in FRPs exhibit significant limitations, including poor high-temperature performance, low fire resistance, and environmental toxicity, which restrict their applicability in certain scenarios.

In recent years, mortar-based composites have emerged as an advanced and sustainable alternative for retrofitting deficient masonry and concrete structures. These materials offer several advantages, including compatibility with concrete or masonry substrates, excellent performance under high temperatures, high corrosion resistance, minimal cross-sectional modification, and ease of application. Given these attributes, mortar-based composites present a promising alternative to FRP systems for structural strengthening.

This study evaluates the application of mortar-based composite jackets for shear strengthening of reinforced concrete (RC) beams using a combination of experimental testing, machine learning (ML), and finite element analysis (FEA).

8.1 Conclusions

8.1.1 Experimental Investigations

The experimental component of this study focuses on two mortar-based composite systems: Steel-Reinforced Grout (SRG) and High-Performance Fiber-Reinforced Concrete (HPFRC).

For SRG systems, the shear performance of strengthened beams under both static and fatigue loading was evaluated. Additionally, for comparative purposes, the performance of Carbon-FRCM (CFRCM) and SRP (Steel Reinforced Polymer) systems was also studied. The main parameters investigated include shear span-to-depth ratio, textile type, number of textile layers, strengthening configuration, substrate type, and UHTSS textile density. A total of 17 beams were tested under static loading, while 9 beams were tested under fatigue loading. Based on the experimental data, two predictive models were developed: a shear strength model considering the influence of the shear span-to-depth ratio and a fatigue life prediction model based on fracture mechanics. Notably, this is the first study to systematically compare SRG with other strengthening systems and to investigate the shear performance of SRG-strengthened beams under fatigue loading. Unlike SRG, HPFRC does not incorporate textiles, resulting in distinct performance characteristics. Therefore, its investigation was conducted separately in Chapter 5. The study on HPFRC-strengthened beams under static and fatigue loading focused on two key parameters: shear span-to-depth ratio and HPFRC jacket thickness. The main conclusions from Chapters 3, 4, 5 are summarised as following:

- The experimental results confirm that all mortar-based strengthening systems effectively enhanced the shear capacity of RC beams. For SRG systems, the shear capacity increased by 90–124% in beams with a shear span-to-depth ratio (a/d) of 2.0 and 164-170% in beams with a/d =3.5. For CFRCM systems, the increases ranged from 107% to 215%, while SRP systems exhibited similar performance

with increases of 119-221%. These findings demonstrate the significant potential of mortar-based composite systems for addressing shear deficiencies in RC beams.

- The shear span-to-depth ratio significantly influenced the performance of all strengthening systems. As the *a/d* ratio increased, the overall shear strength contribution of the strengthening systems decreased. However, the proportion of the shear capacity provided by the external strengthening systems increased. This trend reflects a shift in the load-carrying mechanism from an arch effect in deep beams (*a/d* =2.0) to a truss effect in slender beams (*a/d* = 3.5).
- Fully wrapped SRG jackets were particularly effective in altering the failure mode of the strengthened beams from brittle shear failure to ductile flexural failure. These configurations demonstrated higher energy absorption and improved ductility, making them an ideal choice for applications requiring enhanced structural resilience. However, in U-shaped configurations, detachment failure remained the predominant mode across all strengthening systems (SRG, CFRCM, and SRP). For SRP systems, the high adhesion of the resin matrix resulted in detachment involving large portions of the concrete cover and core, demonstrating the strong bond achieved by this system.
- The density of the UHTSS textile in SRG systems was found to be a critical factor influencing performance. High-density textiles (3.14 cords/cm) posed challenges in mortar penetration, leading to poor adhesion and premature failure under fatigue loading. In contrast, low-density textiles (1.57 cords/cm) provided better mortar penetration and adhesion, enhancing the overall performance of the SRG system.
- Under fatigue loading, SRG, SRP, and CFRCM were all effective shear strengthening systems. For beams with *a/d* = 2.0, the CFRCM system exhibited the highest fatigue life, surviving up to 152,654 cycles, followed by the SRP system with 2165 cycles and the low-density SRG system with 227 cycles. Beams with *a/d* = 3.5 showed similar trends, with the SRP and CFRCM systems consistently outperforming SRG systems. The experimental results also revealed three distinct phases of fatigue behaviour: an initial rapid degradation stage with crack formation, a stable phase with slow damage accumulation, and a final stage of accelerated degradation leading to failure.

- Predictive models were developed to estimate the shear capacity and fatigue life of SRG strengthened beams. The proposed model incorporating the influence of the *a/d* ratio accurately predicted shear capacity, achieving an average V_{pre}/V_{exp} ratio of 0.99 with a standard deviation of 0.15. A fatigue life prediction model for SRG-strengthened beams based on fracture mechanics was also proposed, although further validation with additional data is required to confirm its reliability.
- For HPFRC systems, shear strength improvements ranged from 95% to 130%, with thicker jackets (20 mm) and lower *a/d* ratios yielding more pronounced strengthening effects. Under fatigue loading, HPFRC significantly extended fatigue life, reaching up to 48,786 cycles for beams with *a/d* = 3.5. The study developed a fatigue life prediction model based on the maximum fatigue load and ultimate shear strength under static loading, providing a framework for evaluating HPFRC systems' durability.

8.1.2 Design Guidelines for the Shear Strength of FRCM Strengthened Beams

To evaluate predictive models for FRCM systems, a database comprising 218 beams was established in Chapter 2. This database was used to assess the performance of seven traditional empirical models, revealing their limited accuracy in predicting the shear capacity of FRCM-strengthened beams. To address these shortcomings, this study employed machine learning techniques in Chapter 6 to develop predictive models.

Unlike traditional regression-based or empirical models, ML algorithms adaptively learn complex relationships between input variables and shear performance, achieving significantly higher accuracy and robustness. Using the database and the additional test results from Chapter 3, nine ML models were developed and evaluated to identify the most effective algorithm for predicting the shear capacity of FRCM-strengthened beams. Additionally, tools like SHAP (Shapley Additive Explanations) and PDP (Partial Dependence Plots) were employed to interpret the ML models, providing insights into the relative importance of input parameters and the underlying mechanisms affecting shear capacity.

In chapter 6, nine ML models—Linear Regression (LR), K-Nearest Neighbour (KNN), Support Vector Regression (SVR), Artificial Neural Network (ANN), Decision Tree (DT), Random Forest (RF), Extreme Gradient Boosting (XGBoost), Light Gradient Boosting (LGBoost), and CatBoost — were introduced to predict the shear capacity of FRCM-reinforced RC beams using a dataset of 175 samples. Fourteen input variables, representing structural, material, and reinforcement properties, were used to construct and evaluate the models. The following main conclusions can be drawn.

- The results demonstrated the exceptional predictive capabilities of ML models, with XGBoost achieving the highest accuracy and stability. XGBoost outperformed other models with a R^2 of 98.98%, CoV of 9.75%, MAE of 5.36 kN, and RMSE of 10.07 kN.
- Robustness and stability analyses revealed that XGBoost consistently performed better than LGBoost and CatBoost. It achieved the highest average R^2 (96.97%) and the lowest CoV (12.41%) across random dataset splits. While LGBoost offered faster computational times, its predictions were more variable, and CatBoost, despite its moderate stability, required greater computational resources.
- A comparison with traditional empirical models showed that ML approaches significantly outperformed these conventional methods. In particular, XGBoost demonstrated superior predictive accuracy and reduced errors, making it a more reliable tool for estimating shear capacity.
- SHAP analysis identifies beam depth, concrete compressive strength, and stirrup reinforcement ratio as paramount influences on shear capacity. Surprisingly, mortar thickness emerges as a notable factor, despite limited existing research on its impact.
- PDP analysis shows that in the XGBoost model, the shear strength of FRCM-strengthened beams significantly increases with b_w, d, f_c, while decreasing with a/d. FRCM parameters (p_f, E_f, and ε_{fu}) positively impact shear strength, though their influence is secondary to beam geometry.
- To bridge the gap between research and practical applications, a user-friendly graphical user interface (GUI) was developed, enabling engineers and

practitioners to utilise the optimised ML models for shear strength prediction in FRCM systems.

8.1.3 Finite Element Analysis for SRG Strengthened Beams

For SRG systems, the finite element analysis in Chapter 7 addresses a critical gap identified in the literature review. Existing models typically treat the mortar and textile as a single composite material. However, experimental findings from Chapter 3 reveal that UHTSS textile density significantly influences the bonding performance of mortar, a factor not captured by these models. Subsequent model evaluations confirmed that this approach struggles to simulate premature delamination observed in high-density, fully wrapped SRG systems.

To overcome this, the proposed model separates the mortar and textile components, improving the accuracy of the simulations. The results demonstrate the model's capability to predict both failure modes and the strengthening performance of SRG systems under practical conditions. The average ratio of numerical to experimental peak load was 99.6%. Notably, for fully wrapped beams, the model accurately simulated the stiffness reduction around 70 kN due to minor detachment and replicated the post-peak behaviour: A-GL-W1 showed a plateau-like response, while A-GH-W1 exhibited a sudden load drop due to detachment, consistent with experimental data. For U-shaped SRG beams, the model effectively captured the bilinear detachment-shear failure mode across all samples. The load prediction error was under 1%, and displacement error averaged less than 10%, validating the accuracy and reliability of the enhanced model. These results underscore the robustness of the approach in replicating the structural behaviour of SRG-strengthened beams.

8.2 Recommendations for Future Work

This study demonstrates that mortar-based composites, particularly SRG and HPFRC jackets, are highly effective solutions for shear strengthening of reinforced concrete beams. Building on the findings of this research, several areas warrant further investigation to deepen understanding and expand the applicability of these materials.

- To minimize interference, no stirrups were placed in the strengthened regions in this study. However, the interaction between internal reinforcement, such as stirrups, and external reinforcement, such as mortar-based composite jackets,

remains insufficiently understood. Future studies should explore how these reinforcements interact mechanically to contribute to shear resistance, potentially uncovering synergies that could optimise strengthening designs.

- Detachment failure was the most common failure mode observed in U-shaped configurations of mortar-based composites, limiting their shear strengthening effectiveness. Investigating the influence of various anchorage systems, including variations in anchor geometry, materials, or embedment depth, could help mitigate detachment failures and improve the performance and reliability of these systems.
- Current research, including this study, on HPFRC-strengthened RC beams has been predominantly experimental. Future work should also focus on developing analytical models to better understand their mechanical behaviour and employing advanced numerical simulations, such as finite element modelling, to enhance predictive accuracy and broaden practical applications.
- The performance of mortar-based composites under complex conditions also merits further exploration. This study examined their behaviour under conventional conditions at room temperature, but their effectiveness under more challenging scenarios, such as high temperatures, fire exposure, or corrosive environments, remains unclear. Extending research to include these conditions could enhance the resilience and applicability of mortar-based composites in diverse and demanding engineering contexts.
- Training accurate ML models requires extensive datasets, which are difficult to generate solely through experimental work. To address this limitation, mathematical or numerical methods could be used to expand the available data. For example, the FEA model developed in this study, once validated with additional experimental data, could generate realistic datasets for ML training, improving predictive accuracy and robustness.
- Future research should also focus on optimizing FEA models to better capture the behaviour of mortar-based composites under varying conditions, such as different textile densities or adhesive interactions. Further refinements in these models could provide a more accurate representation of real-world performance, contributing to better design and analysis practices.

- Broader applications of mortar-based composites in structural retrofitting should be investigated, including their use for improving both structural and energy efficiency in existing concrete or masonry buildings. Evaluating their performance in real-world engineering projects would provide critical insights into their practical utility and long-term sustainability.
- The integration of new materials into mortar-based composites presents an additional opportunity for advancement. Incorporating nanomaterials or ultra-high-performance additives into the mortar matrix could further improve mechanical properties, durability, or bonding performance. Research into scalable production methods for such enhanced composites would be essential to facilitate their adoption in large-scale construction projects.
- Further development of new mortar-based composites for application in the shear strengthening of RC beams should be considered. For instance, combining UHTSS textiles with HPFRC/UHPFRC warrants investigation to evaluate their mechanical performance, durability, and bonding characteristics, potentially unlocking novel strengthening solutions with superior properties.

By addressing these areas, future research can significantly advance the understanding and application of mortar-based composites, unlocking their full potential for improving structural resilience and sustainability across a wide range of engineering applications.

References

ABAQUS Finite Element Code. (2011). Hibbitt, Karlsson and Sorensen, Inc., RI.

Abdalla, J. A., Attom, M. F. & Hawileh, R. (2015). Prediction of minimum factor of safety against slope failure in clayey soils using artificial neural network. *Environmental Earth Sciences,* 73**,** 5463-5477.

Abdalla, J. A. & Hawileh, R. (2011). Modeling and simulation of low-cycle fatigue life of steel reinforcing bars using artificial neural network. *Journal of the Franklin Institute,* 348**,** 1393-1403.

Abuodeh, O. R., Abdalla, J. A. & Hawileh, R. A. (2020). Prediction of shear strength and behavior of RC beams strengthened with externally bonded FRP sheets using machine learning techniques. *Composite Structures,* 234**,** 111698

ACI 318-08. (2008). Building code requirements for structural concrete (ACI 318-08) and commentary. In: American Concrete Institute.

ACI 318-19. (2022). Building Code Requirements for Structural Concrete. In: American Concrete Institute.

ACI 549R-13. (2013). Guide to design and construction of externally bonded fabric-reinforced cementitious matrix (FRCM) systems for repair and strengthening concrete and masonry structures. In: American Concrete Institute.

ACI 554-18. (2018). Guide to Design with Fiber-Reinforced Concrete In: American Concrete Institute.

Akbari Hadad, H. & Nanni, A. (2020). Fatigue behavior of FRCM-strengthened RC beams. *Journal of Composites for Construction,* 24**,** 04020074.

Akbari Hadad, H., Nanni, A., Ebead, U. A. & El Refai, A. (2018). Static and fatigue performance of FRCM-strengthened concrete beams. *Journal of Composites for Construction,* 22**,** 04018033.

Al-Jaberi, Z. & Myers, J. J. (2023). Prediction of compressive strength and evaluation of different theoretical standards and proposed models of brick columns confined with FRP, FRCM, or SRG system. *Case Studies in Construction Materials,* 18**,** e01875.

Al-Rousan, R. & Issa, M. (2011). Fatigue performance of reinforced concrete beams strengthened with CFRP sheets. *Construction and Building Materials,* 25**,** 3520-3529.

Al-Salloum, Y. A., Elsanadedy, H. M., Alsayed, S. H., & Iqbal, R. A. (2012). Experimental and numerical study for the shear strengthening of reinforced concrete beams using textile-reinforced mortar. *Journal of Composites for Construction*, 16(1), 74-90.

Aljazaeri, Z. R. & Myers, J. J. (2017). Strengthening of reinforced-concrete beams in shear with a fabric-reinforced cementitious matrix. *Journal of Composites for Construction,* 21**,** 04017041.

Amin, M., Zeyad, A. M., Tayeh, B. A. & Agwa, I. S. (2021). Effects of nano cotton stalk and palm leaf ashes on ultrahigh-performance concrete properties incorporating recycled concrete aggregates. *Construction and Building Materials,* 302**,** 124196.

Ary, M. I. & Kang, T. H.-K. (2012). Shear-strengthening of reinforced & prestressed concrete beams using FRP: part I—review of previous research. *International Journal of Concrete Structures and Materials,* 6**,** 41-47.

ASCE 2007. Seismic rehabilitation of existing buildings (ASCE/SEI 41–06). *american society of civil engineers*.

Attar, H. S., Esfahani, M. R. & Ramezani, A. (2020). Experimental investigation of flexural and shear strengthening of RC beams using fiber-reinforced self-consolidating concrete jackets. *Structures,* 2020, 46-53.

Awani, O., El-Maaddawy, T. & El Refai, A. (2016). Numerical simulation and experimental testing of concrete beams strengthened in shear with fabric-reinforced cementitious matrix. *Journal of Composites for Construction,* 20**,** 04016056.

Azam, R. & Soudki, K. (2014). FRCM strengthening of shear-critical RC beams. *Journal of Composites for Construction,* 18**,** 04014012.

Azam, R., Soudki, K., West, J. S. & Noël, M. (2018a). Behavior of shear-critical RC beams strengthened with CFRCM. *Journal of Composites for Construction,* 22**,** 04017046.

Baggio, D., Soudki, K., & Noel, M. (2014). Strengthening of shear critical RC beams with various FRP systems. *Construction and Building Materials*, *66*, 634-644.

Bandelt, M. J. & Billington, S. L. (2016). Bond behavior of steel reinforcement in high-performance fiber-reinforced cementitious composite flexural members. *Materials and structures,* 49**,** 71-86.

Banjara, N. K. & Ramanjaneyulu, K. (2020). Effect of Deficiencies on Fatigue Life of Reinforced Concrete Beams. *ACI Structural Journal,* 117.

Basunbul, I. A., Gubati, A. A., Al-Sulaimani, G. J., & Baluch, M. H. (1990). Repaired reinforced concrete beams. *Materials Journal,* 87(4), 348-354.

Bazant, Z. P. & Planas, J. (2019). *Fracture and size effect in concrete and other quasibrittle materials*, Routledge.

Bazant, Z. P., & Yu, Q. (2005). Designing against size effect on shear strength of reinforced concrete beams without stirrups: I. Formulation. *Journal of Structural Engineering*, *131*(12), 1877-1885.

Bencardino, F., & Condello, A. (2015). SRG/SRP–concrete bond–slip laws for externally strengthened RC beams. *Composite Structures*, 132, 804-815.

Bencardino, F., & Condello, A. (2016). 3D FE analysis of RC beams externally strengthened with SRG/SRP systems. *Fibers*, 4(2), 19.

Brückner, A., Ortlepp, R., & Curbach, M. (2008). Anchoring of shear strengthening for T-beams made of textile reinforced concrete (TRC). *Materials and Structures*, 41, 407-418.

BS EN. (1999a). EN 1542. Products and Systems for the Protection and Repair of Concrete Structures–Test Methods–Measurement of Bond Strength by Pull-Off. *CEN Bruxelles, Belgium.*

BS EN. (1999b) EN 12190. Products and systems for the protection and repair of concrete structures. Test methods. Determination of compressive strength of repair mortar. *British Standards Institution: London, UK*.

BS EN. (2005). EN 196-1. Methods of testing cement–Part 1: Determination of strength. *European Committee for standardization,* 26.

BS EN. (2005) EN 2561. Carbon fibre reinforced plastics. Undirectional laminates. Tensile test parallel to the fibre direction. *British Standards Institution: London, UK*.

BS EN. (2013). EN 12390-13. Testing hardened concrete–Part 13: determination of secant modulus of elasticity in compression. *British Standards Institution: London, UK*.

Buttignol, T. E. T., Sousa, J. & Bittencourt, T. (2017). Ultra High-Performance Fiber-Reinforced Concrete (UHPFRC): a review of material properties and design procedures. *Revista IBRACON de estruturas e materiais,* 10**,** 957-971.

Bywalski, C., Drzazga, M., Kamiński, M. & Kaźmierowski, M. (2020). A New Proposal for the Shear Strength Prediction of Beams Longitudinally Reinforced with Fiber-Reinforced Polymer Bars. *Buildings,* 10**,** 86.

Cakir, F., Aydin, M. R., Acar, V., Aksar, B. & Akkaya, H. C. (2023). An experimental study on RC beams shear-strengthened with Intraply Hybrid U-Jackets Composites monitored by digital image correlation (DIC). *Composite Structures,* 323**,** 117503.

Carloni, C. & Subramaniam, K. V. (2013). Investigation of sub-critical fatigue crack growth in FRP/concrete cohesive interface using digital image analysis. *Composites Part B: Engineering,* 51, 35-43.

Carpinteri, A., Ferro, G., & Monetto, I. (1999). Scale effects in uniaxially compressed concrete specimens. *Magazine of Concrete Research*, *51*(3), 217-225.

Çetin, K., Mylonakis, G., Sextos, A., Stewart, J. & Irmak, T.（2020). Seismological and Engineering Effects of the M 7.0 Samos Island (Aegean Sea) Earthquake.

Cervenka Consulting. (2018). ATENA Program Documentation. Prague, Czech Republic.

Chaallal, O., Boussaha, F. & Bousselham, A. (2010). Fatigue performance of RC beams strengthened in shear with CFRP fabrics. *Journal of Composites for Construction,* 14**,** 415-423.

Chaallal, O., Shahawy, M. & Hassan, M. (2002). Performance of reinforced concrete T-girders strengthened in shear with carbon fiber-reinforced polymer fabric. *Structural Journal,* 99**,** 335-343.

Chellapandian, M., Prakash, S. S. & Sharma, A. (2017). Strength and ductility of innovative hybrid NSM reinforced and FRP confined short RC columns under axial compression. *Composite Structures,* 176**,** 205-216.

Chen, G. M., Teng, J. G., Chen, J. F., & Xiao, Q. G. (2015). Finite element modeling of debonding failures in FRP-strengthened RC beams: A dynamic approach. *Computers & Structures*, *158*, 167-183.

Chen, J.-F. & Teng, J. (2003a). Shear capacity of FRP-strengthened RC beams: FRP debonding. *Construction and Building Materials,* 17**,** 27-41.

Chen, J.-F. & Teng, J. (2003b). Shear capacity of fiber-reinforced polymer-strengthened reinforced concrete beams: Fiber reinforced polymer rupture. *Journal of Structural Engineering,* 129**,** 615-625.

Chou, J.-S. & Tsai, C.-F. (2012). Concrete compressive strength analysis using a combined classification and regression technique. *Automation in Construction,* 24**,** 52-60.

CNR-DT 200 R1/2013. Guide for the design and construction of externally bonded FRP systems for strengthening existing structures – materials, RC and PC structures, masonry structures. Italian National Research Council, Rome, Italy; 2013.

Czaderski, C. & Motavalli, M. (2004). Fatigue behaviour of CFRP L-shaped plates for shear strengthening of RC T-beams. *Composites Part B: Engineering,* 35**,** 279-290.

D'Antino, T., Carloni, C., Sneed, L. & Pellegrino, C. (2015). Fatigue and post-fatigue behavior of PBO FRCM-concrete joints. *International Journal of Fatigue,* 81**,** 91-104.

Department for Communities and Local Government. (2012). Annual report and accounts 2011 to 2012. GOV.UK.

Diab, H., Wu, Z. & Iwashita, K. (2009). Theoretical solution for fatigue debonding growth and fatigue life prediction of FRP-concrete interfaces. *Advances in structural engineering,* 12**,** 781-792.

Dong, J. F., Wang, Q. Y., & Guan, Z. W. (2012). Structural behaviour of RC beams externally strengthened with FRP sheets under fatigue and monotonic loading. *Engineering Structures*, *41*, 24-33.

Dutton, M., Take, W. A. & Hoult, N. A. (2014). Curvature monitoring of beams using digital image correlation. *Journal of Bridge Engineering,* 19**,** 05013001.

Ebead, U. (2015). Inexpensive strengthening technique for partially loaded reinforced concrete beams: Experimental study. *Journal of materials in civil engineering,* 27**,** 04015002.

Ebead, U. & Wakjira, T. FRCM/stirrups interaction in RC beams strengthened in shear using NSE-FRCM. IOP Conference Series: Materials Science and Engineering, 2018. IOP Publishing, 112001.

Eberhard, M. O., Baldridge, S., Marshall, J., Mooney, W. & Rix, G. J. (2010). The mw 7.0 Haiti earthquake of January 12, 2010: USGS/EERI advance reconnaissance team report. *US Geological Survey Open-File Report,* 1048**,** 58.

El-Saikaly, G. & Chaallal, O. (2015). Extending the fatigue life of reinforced concrete T-beams strengthened in shear with externally bonded FRP: Upgrading versus repairing. *Journal of Composites for Construction,* 19**,** 04014027.

Elghazy, M., El Refai, A., Ebead, U., & Nanni, A. (2018). Fatigue and monotonic behaviors of corrosion-damaged reinforced concrete beams strengthened with FRCM composites. *Journal of Composites for Construction*, *22*(5), 04018040.

Escrig, C., Gil, L., Bernat-Maso, E. & Puigvert, F. (2015). Experimental and analytical study of reinforced concrete beams shear strengthened with different types of textile-reinforced mortar. *Construction and building materials,* 83**,** 248-260.

E.C. for Standardization. (2005) Eurocode 2: design of concrete structures–Part 1-1: general rules and rules for buildings: EN 1992-1-1. CEN, Brussels.

Feng, R., Liu, P., Zhang, J., Wang, F., Xu, Y., & Zhu, J. H. (2022). Bending behaviour of corroded RC continuous beams with C-FRCM strengthening system. *Journal of Building Engineering*, *60*, 105229.

Ferrier, E., Bigaud, D., Clement, J. & Hamelin, P. (2011). Fatigue-loading effect on RC beams strengthened with externally bonded FRP. *Construction and Building Materials,* 25**,** 539-546.

fib Bulletin 90. (2019). Externally applied FRP reinforcement for concrete structures, International Federation for Structural Concrete (*fib*).

fib Model Code. (2010) Design code for concrete structures, International Federation for Structural Concrete (*fib*).

fib Model Code. (2001). Externally bonded FRP reinforcement for RC structures. *Bulletin,* 14**,** 138.

Gagani, A. I., Monsås, A. B., Krauklis, A. E. & Echtermeyer, A. T. (2019). The effect of temperature and water immersion on the interlaminar shear fatigue of glass fiber epoxy composites using the I-beam method. *Composites Science and Technology,* 181**,** 107703.

Gallego, J. M., Zanuy, C. & Albajar, L. (2014). Shear fatigue behaviour of reinforced concrete elements without shear reinforcement. *Engineering Structures,* 79**,** 45-57.

Garcez, M. R., Meneghetti, L. C. & Teixeira, R. M. (2021). The effect of FRP prestressing on the fatigue performance of strengthened RC beams. *Structural Concrete,* 22**,** 6-21.

Garg, V., Bansal, P. P. & Sharma, R. (2019). Retrofitting of Shear-Deficient RC Beams Using UHP-FRC. *Iranian Journal of Science and Technology, Transactions of Civil Engineering,* 43**,** 419-428.

GB 50010. (2010). Design Code for Concrete Structures. China Construction Industry Press: Beijing, China, 2011.

Godat, A., Chaallal, O., & Obaidat, Y. (2020). Non-linear finite-element investigation of the parameters affecting externally-bonded FRP flexural-strengthened RC beams. *Results in Engineering*, 8, 100168.

Godat, A., Hammad, F. & Chaallal, O. (2020). State-of-the-art review of anchored FRP shear-strengthened RC beams: A study of influencing factors. *Composite Structures,* 254**,** 112767.

Goldstein, A., Kapelner, A., Bleich, J. & Pitkin, E. (2015). Peeking inside the black box: Visualizing statistical learning with plots of individual conditional expectation. *journal of Computational and Graphical Statistics,* 24**,** 44-65.

Gonzalez-Libreros, J. H., Sabau, C., Sneed, L. H., Pellegrino, C. & Sas, G. (2017a). State of research on shear strengthening of RC beams with FRCM composites. *Construction and Building Materials,* 149**,** 444-458.

Gonzalez-Libreros, J. H., Sneed, L., D'antino, T. & Pellegrino, C. (2017b). Behavior of RC beams strengthened in shear with FRP and FRCM composites. *Engineering Structures,* 150**,** 830-842.

Graeff, Â.G., Pilakoutas, K., Neocleous, K., Peres, M.V.N.N. (2012). Fatigue resistance and cracking mechanism of concrete pavements reinforced with recycled steel fibres recovered from post-consumer tyres. *Engineering Structures,* 45, 385-395.

Hammoudi, A., Moussaceb, K., Belebchouche, C. & Dahmoune, F. (2019). Comparison of artificial neural network (ANN) and response surface methodology (RSM) prediction in compressive strength of recycled concrete aggregates. *Construction and Building Materials,* 209**,** 425-436.

He, W., Wang, X., Monier, A., & Wu, Z. (2020). Shear behavior of RC beams strengthened with side-bonded BFRP grids. *Journal of Composites for Construction*, 24(5), 04020051.

Hognestad, E. (1951). Study of combined bending and axial load in reinforced concrete members. *University of Illinois. Engineering Experiment Station. Bulletin; no. 399*.

Huang, Y., Grünewald, S., Schlangen, E. & Luković, M. (2022). Strengthening of concrete structures with ultra high performance fiber reinforced concrete (UHPFRC): A critical review. *Construction and Building Materials,* 336**,** 127398.

Hung, C.-C. & Chen, Y.-S. (2016). Innovative ECC jacketing for retrofitting shear-deficient RC members. *Construction and building materials,* 111**,** 408-418.

ISO, E. (2009). 6892-1. Metallic materials-Tensile testing-Part 1: Method of test at room temperature. *International Organization for Standardization*.

ISO, U. (2019). 15630-1. Steel for the reinforcement and pre-stressing of concrete—Test Methods—Part 1: Reinforcing Bars, Wire Rod And Wire. *Aenor: Madrid, Spain*.

Jabbar, A. M., Hamood, M. J. & Mohammed, D. H. (2021). The effect of using basalt fibers compared to steel fibers on the shear behavior of ultra-high performance concrete T-beam. *Case Studies in Construction Materials,* 15**,** e00702.

Jen, Yi-Ming, and Chih-Wei Ko. (2010). Evaluation of fatigue life of adhesively bonded aluminum single-lap joints using interfacial parameters. *International Journal of Fatigue,* 32.2, 330-340.

Ji, H. & Liu, C. (2020). Ultimate shear resistance of ultra-high performance fiber reinforced concrete-normal strength concrete beam. *Engineering structures,* 203**,** 109825.

Jo, M.-S., Kim, H.-G., Kim, D.-H., Lim, S.-A., Kong, H. & Kim, K.-H. (2024). Evaluation of Behavior Characteristics of Reinforced Concrete Beam Shear Strengthening with Different FRCMs. *Buildings,* 14**,** 3949.

Jongvivatsakul, P., Attachaiyawuth, A. & Pansuk, W. (2016). A crack-shear slip model of high-strength steel fiber-reinforced concrete based on a push-off test. *Construction and Building Materials,* 126**,** 924-935.

Jongvivatsakul, P., Bui, L. V., Koyekaewphring, T., Kunawisarut, A., Hemstapat, N. & Stitmannaithum, B. (2019). Using steel fiber-reinforced concrete precast panels for strengthening in shear of beams: an experimental and analytical investigation. *Advances in Civil Engineering,* 2019.

JSCE. (2006). Recommendation for design and construction of ultra high strength fiber reinforced concrete structures. Japan Society of Civil Engineers Tokyo (Japan).

JSCE. (2007). Standard specifications for concrete structures-2007. Japan Society of Civil Engineers Tokyo (Japan).

Kang, S.-T., Lee, Y., Park, Y.-D. & Kim, J.-K. (2010). Tensile fracture properties of an Ultra High Performance Fiber Reinforced Concrete (UHPFRC) with steel fiber. *Composite structures,* 92**,** 61-71.

Kang, T. H.-K. & Ary, M. I. (2012). Shear-strengthening of reinforced & prestressed concrete beams using FRP: Part II—Experimental investigation. *International Journal of Concrete Structures and Materials,* 6**,** 49-57.

Kani, G. (1964). The riddle of shear failure and its solution. *Journal Proceedings,* 1964, 441-468.

Katsamakas, A. A., Papanikolaou, V. K., & Thermou, G. E. (2021). A FEM-based model to study the behavior of SRG-strengthened R/C beams. *Composite Structures*, 266, 113796.

Ke, G., Meng, Q., Finley, T., Wang, T., Chen, W., Ma, W., Ye, Q. & Liu, T.-Y. (2017). Lightgbm: A highly efficient gradient boosting decision tree. *Advances in neural information processing systems,* 30.

Ke, Y., Zhang, S., Jedrzejko, M., Lin, G., Li, W. & Nie, X. (2024). Strength models of near-surface mounted (NSM) fibre-reinforced polymer (FRP) shear-strengthened RC beams based on machine learning approaches. *Composite Structures,* 337**,** 118045.

KERAKOLL. (2024a). *Technical Data Sheet: Geolite Magma;* [Online]. Available: https://products.kerakoll.com/en-gcc/p/geolite-magma [Accessed 15 October 2024].

KERAKOLL. (2024b). *Technical Data Sheet: Steel Fibre;* [Online]. Available: https://products.kerakoll.com/en/p/steel-fiber [Accessed 15 October 2024].

Larbi, A. S., Contamine, R., Ferrier, E., & Hamelin, P. (2010). Shear strengthening of RC beams with textile reinforced concrete (TRC) plate. *Construction and Building Materials*, 24(10), 1928-1936.

Laterza, M., D'amato, M., Casamassima, V.M. (2017). Stress-life curves method for fatigue assessment of ancient brick arch bridges. *International Journal of Architectural Heritage,* 11, 843-858.

Li, A., Diagana, C. & Delmas, Y. (2001). CRFP contribution to shear capacity of strengthened RC beams. *Engineering Structures,* 23**,** 1212-1220.

Li, K., Zhao, D., Wang, X., Feng, H. & Zou, X. (2021). Investigation of crack growth in CFRP-concrete interface under fatigue loading. *Structures,* 2021. Elsevier, 356-367.

Li, W. & Leung, C. K. (2016). Shear span–depth ratio effect on behavior of RC beam shear strengthened with full-wrapping FRP strip. *Journal of Composites for Construction,* 20**,** 04015067.

Li, W., Ren, X. & Hu, C. Artificial Neural Network Model for FRP Shear Contribution of RC Beams Strengthened with Externally Bonded FRP Composites. 4th Annual International Conference on Material Engineering and Application (ICMEA 2017), 2018. Atlantis Press, 166-169.

Liu, D., Zhang, W., Tang, Y. & Jian, Y. (2021). Prediction of hydration heat of mass concrete based on the SVR model. *Ieee Access,* 9**,** 62935-62945.

Lu, W. Y., Lin, I. J., Hwang, S. J. & Lin, Y. H. (2003). Shear strength of high-strength concrete dapped-end beams. *Journal of the Chinese Institute of Engineers,* 26**,** 671-680.

Lu, T., Li, W., Zhou, T., Mansour, M., Zheng, K., Wang, P., Ke, L., & Yu, J. (2024) Comparative analysis of shear behavior and mechanism of concrete beams with strip-shaped CFRP or conventional steel stirrups. *Case Studies in Construction Materials,* 20, e03140.

Lu, X. Z., Teng, J. G., Ye, L. P., & Jiang, J. J. (2005). Bond–slip models for FRP sheets/plates bonded to concrete. *Engineering structures*, 27(6), 920-937.

Lundberg, S. M. & Lee, S.-I. (2017). A unified approach to interpreting model predictions. *Advances in neural information processing systems,* 30.

Mahal, M., Blanksvärd, T. & Täljsten, B. (2013). Examination at a material and structural level of the fatigue life of beams strengthened with mineral or epoxy bonded FRPs: the state of the art. *Advances in Structural Engineering,* 16**,** 1311-1327.

Mai, H.-V. T., Nguyen, T.-A., Ly, H.-B. & Tran, V. Q. (2021). Prediction compressive strength of concrete containing GGBFS using random forest model. *Advances in Civil Engineering,* 2021.

Mandor, A. & El Refai, A. (2022). Strengthening the hogging and sagging regions in continuous beams with fiber-reinforced cementitious matrix (FRCM): Experimental and analytical investigations. *Construction and Building Materials,* 321**,** 126341.

Mangalathu, S. & Jeon, J.-S. (2018). Classification of failure mode and prediction of shear strength for reinforced concrete beam-column joints using machine learning techniques. *Engineering Structures,* 160**,** 85-94.

Marcinczak, D. & Trapko, T. (2019a). DIC (Digital Image Correlation) method in the research of RC beams strengthened with PBO-FRCM materials. E3S Web of Conferences. EDP Sciences, 03008.

Marcinczak, D. & Trapko, T. The impact of the anchorage on the shear capacity of reinforced concrete beams. IOP Conference Series: Materials Science and Engineering, 2019b. IOP Publishing, 012003.

Marcinczak, D., Trapko, T. & Musiał, M. (2019). Shear strengthening of reinforced concrete beams with PBO-FRCM composites with anchorage. *Composites Part B: Engineering,* 158**,** 149-161.

Mazumdar, S. K., & Mallick, P. K. (1998). Static and fatigue behavior of adhesive joints in SMC-SMC composites. *Polymer composites,* 19(2), 139-146.

Mercedes, L., Escrig, C., Bernat-Masó, E., & Gil, L. (2021). Analytical approach and numerical simulation of reinforced concrete beams strengthened with different FRCM systems. *Materials*, *14*(8), 1857.

Minafò, G. & La Mendola, L. (2018). Experimental investigation on the effect of mortar grade on the compressive behaviour of FRCM confined masonry columns. *Composites Part B: Engineering,* 146**,** 1-12.

Monti, G., Renzelli, M., & Luciani, P. (2003). FRP adhesion in uncracked and cracked concrete zones. In *Fibre-Reinforced Polymer Reinforcement for Concrete Structures*: (In 2 Volumes) (pp. 183-192).

Mujika, F. (2007). On the effect of shear and local deformation in three-point bending tests. *polymer testing*, 26.7, 869-877.

Naderpour, H. & Alavi, S. (2017). A proposed model to estimate shear contribution of FRP in strengthened RC beams in terms of Adaptive Neuro-Fuzzy Inference System. *Composite Structures,* 170**,** 215-227.

Naderpour, H., Poursaeidi, O. & Ahmadi, M. (2018). Shear resistance prediction of concrete beams reinforced by FRP bars using artificial neural networks. *Measurement,* 126**,** 299-308.

National Research Council (CNR). (2004). Guide for the design and construction of externally bonded FRP systems for strengthening existing structures, CNR-DT200, Rome, Italy.

Nguyen, T.-H., Tran, N.-L., Phan, V.-T. & Nguyen, D.-D. (2024). Prediction of shear capacity of RC beams strengthened with FRCM composite using hybrid ANN-PSO model. *Case Studies in Construction Materials,* 18**,** e02183.

Noshiravani, T. & Brühwiler, E. (2014). Analytical model for predicting response and flexure-shear resistance of composite beams combining reinforced ultrahigh performance fiber-reinforced concrete and reinforced concrete. *Journal of Structural Engineering,* 140**,** 04014012.

Nunes, S., Pimentel, M. & Sousa, C. Mechanical and Fracture Behaviour of an HPFRC. Fibre Reinforced Concrete: Improvements and Innovations II: X RILEM-fib International Symposium on Fibre Reinforced Concrete (BEFIB) 2021 10, 2022. Springer, 174-185.

Obaidat, Y. T., Heyden, S., & Dahlblom, O. (2013). Evaluation of parameters of bond action between FRP and concrete. *Journal of Composites for construction*, 17(5), 626-635.

Ombers, L. (2015a). Analysis of the bond between fabric reinforced cementitious mortar (FRCM) strengthening systems and concrete. *Composites Part B: Engineering,* 69**,** 418-426.

Ombres, L. (2015b.) Structural performances of reinforced concrete beams strengthened in shear with a cement based fiber composite material. *Composite Structures,* 122**,** 316-329.

Ombres, L., Aiello, M. A., Cascardi, A. & Verre, S. (2024). Modeling of steel-reinforced grout composite system-to-concrete bond capacity using artificial neural networks. *Journal of Composites for Construction,* 28**,** 04024034.

Ombres, L., & Verre, S. (2019a). Flexural strengthening of RC beams with steel-reinforced grout: Experimental and numerical investigation. *Journal of Composites for Construction*, 23(5), 04019035.

Ombres, L., & Verre, S. (2019b). Numerical modeling approaches of FRCMs/SRG confined masonry columns. Frontiers in Built Environment, 5, 143.

Ombres, L. & Verre, S. (2021). Shear strengthening of reinforced concrete beams with SRG (Steel Reinforced Grout) composites: Experimental investigation and modelling. *Journal of Building Engineering,* 42**,** 103047.

Oudah, F. & El-Hacha, R. (2012). Fatigue behavior of RC beams strengthened with prestressed NSM CFRP rods. *Composite Structures,* 94**,** 1333-1342.

Paramasivam, P., Ong, K. C. G., & Lim, C. T. E. (1994). Ferrocement laminates for strengthening RC T-beams. *Cement and Concrete Composites,* 16(2), 143-152.

Perera, R., Barchín, M., Arteaga, A. & De Diego, A. (2010). Prediction of the ultimate strength of reinforced concrete beams FRP-strengthened in shear using neural networks. *Composites Part B: Engineering,* 41**,** 287-298.

Pino, V., Akbari Hadad, H., De Caso y Basalo, F., Nanni, A., Ali Ebead, U., & El Refai, A. (2017). Performance of FRCM-strengthened RC beams subject to fatigue. *Journal of Bridge Engineering*, *22*(10), 04017079.

Ramezani, A. & Esfahani, M. R. (2023). Shear strengthening of RC beams using FRCM system made with industrial wastes. *Structures,* 1833-1847.

Ren, G., Yao, B., Huang, H. & Gao, X. (2021). Influence of sisal fibers on the mechanical performance of ultra-high performance concretes. *Construction and Building Materials,* 286**,** 122958.

Rengasamy, D., Mase, J. M., Kumar, A., Rothwell, B., Torres, M. T., Alexander, M. R., Winkler, D. A. & Figueredo, G. P. (2022). Feature importance in machine learning models: A fuzzy information fusion approach. *Neurocomputing,* 511**,** 163-174.

Roberts, T.M., Hughes, T.G., Dandamudi, V., Bell, B. (2006). Quasi-static and high cycle fatigue strength of brick masonry. *Construction and Building Materials,* 20, 603-614.

Ruano, G., Isla, F., Pedraza, R. I., Sfer, D. & Luccioni, B. (2014). Shear retrofitting of reinforced concrete beams with steel fiber reinforced concrete. *Construction and Building Materials,* 54**,** 646-658.

Ryall, M. (2008). Loads and load distribution, ICE Manual of Bridge Engineering: *Second Edition ICE Publishing,* 23–48.

Said, A., Elsayed, M., Abd El-Azim, A., Althoey, F. & Tayeh, B. A. (2022). Using ultra-high performance fiber reinforced concrete in improvement shear strength of reinforced concrete beams. *Case Studies in Construction Materials,* 16**,** e01009.

Sakr, M. A., Sleemah, A. A., Khalifa, T. M. & Mansour, W. N. (2018). Behavior of RC beams strengthened in shear with ultra-high performance fiber reinforced concrete (UHPFRC). MATEC web of conferences. EDP Sciences, 09002.

Sakr, M. A., Sleemah, A. A., Khalifa, T. M. & Mansour, W. N. (2019). Shear strengthening of reinforced concrete beams using prefabricated ultra-high performance fiber reinforced concrete plates: Experimental and numerical investigation. *Structural Concrete,* 20**,** 1137-1153.

Savino, V., Lanzoni, L., Tarantino, A. M. & Viviani, M. (2018). Simple and effective models to predict the compressive and tensile strength of HPFRC as the steel fiber content and type changes. *Composites Part B: Engineering,* 137**,** 153-162.

Shang, X. Y., Yu, J. T., Li, L. Z. & Lu, Z. D. (2020). Shear strengthening of fire damaged RC beams with stirrup reinforced engineered cementitious composites. *Engineering Structures,* 210**,** 110263.

Sharafisafa, M., Aliabadian, Z., & Shen, L. (2020). Crack initiation and failure development in bimrocks using digital image correlation under dynamic load. *Theoretical and Applied Fracture Mechanics*, 109, 102688.

Sohail, M. G., Kahraman, R., Al Nuaimi, N., Gencturk, B. & Alnahhal, W. (2021). Durability characteristics of high and ultra-high performance concretes. *Journal of Building Engineering,* 33**,** 101669.

Spinella, N. (2019). Modeling of shear behavior of reinforced concrete beams strengthened with FRP. *Composite Structures,* 215**,** 351-364.

Tamura, H., Tamon, U., Hitoshi, F., & Fujima, S. (2009). Effect of adhesive thickness on bond behaviour of carbon fiber sheet under static and fatigue loading. I*n The Second Official International Conference of International Institute for FRP in Construction for Asia-Pacific Region,* 12, 241-246.

Tan, K.-H., Cheng, G.-H. & Zhang, N. (2008). Experiment to mitigate size effect on deep beams. *Magazine of Concrete Research,* 60**,** 709-723.

Tanarslan, H., Secer, M. & Kumanlioglu, A. (2012). An approach for estimating the capacity of RC beams strengthened in shear with FRP reinforcements using artificial neural networks. *Construction and Building Materials,* 30**,** 556-568.

Tanarslan, H. M., Yalçınkaya, Ç., Alver, N. & Karademir, C. (2021). Shear strengthening of RC beams with externally bonded UHPFRC laminates. *Composite Structures,* 262**,** 113611.

Taie, B., Mandor, A., & El Refai, A. (2024). Experimental and numerical investigation of two–span RC beams strengthened with fiber–reinforced cementitious matrix (FRCM). *Engineering Structures*, 300, 117246.

Taylor, K. E. (2001). Summarizing multiple aspects of model performance in a single diagram. *Journal of Geophysical Research: Atmospheres,* 106**,** 7183-7192.

Tetta, Z. C. & Bournas, D. A. (2016). TRM vs FRP jacketing in shear strengthening of concrete members subjected to high temperatures. *Composites Part B: Engineering,* 106**,** 190-205.

Tetta, Z. C., Koutas, L. N. & Bournas, D. A. (2015). Textile-reinforced mortar (TRM) versus fiber-reinforced polymers (FRP) in shear strengthening of concrete beams. *Composites Part B: Engineering,* 77**,** 338-348.

Tetta, Z. C., Koutas, L. N. & Bournas, D. A. (2016). Shear strengthening of full-scale RC T-beams using textile-reinforced mortar and textile-based anchors. *Composites Part B: Engineering,* 95**,** 225-239.

Tetta, Z. C., Koutas, L. N. & Bournas, D. A. (2018a). Shear strengthening of concrete members with TRM jackets: Effect of shear span-to-depth ratio, material and amount of external reinforcement. *Composites Part B: Engineering,* 137**,** 184-201.

Tetta, Z. C., Triantafillou, T. C. & Bournas, D. A. (2018b). On the design of shear-strengthened RC members through the use of textile reinforced mortar overlays. *Composites Part B: Engineering,* 147**,** 178-196.

Thermou, G. E., De Santis, S., de Felice, G., Alotaibi, S., Roscini, F., Hajirasouliha, I., & Guadagnini, M. (2021). Bond behaviour of multi-ply steel reinforced grout composites. *Construction and Building Materials*, 305, 124750.

Thermou, G., Papanikolaou, V., Lioupis, C. & Hajirasouliha, I. (2019). Steel-Reinforced Grout (SRG) strengthening of shear-critical RC beams. *Construction and Building Materials,* 216**,** 68-83.

Tian, J., Wu, X., Zheng, Y., Hu, S., Du, Y., Wang, W., & Zhang, L. (2019). Investigation of interface shear properties and mechanical model between ECC and concrete. *Construction and Building Materials*, *223*, 12-27.

Topçu, İ. B., Boga, A. R. & Hocaoglu, F. O. (2009). Modeling corrosion currents of reinforced concrete using ANN. *Automation in Construction,* 18**,** 145-152.

Tzoura, E. & Triantafillou, T. (2016). Shear strengthening of reinforced concrete T-beams under cyclic loading with TRM or FRP jackets. *Materials and Structures,* 49**,** 17-28.

Vapnik, V. N. (1999). An overview of statistical learning theory. *IEEE transactions on neural networks,* 10**,** 988-999.

Verre, S. (2022). Numerical Strategy for Column Strengthened with FRCM/SRG System. *Buildings*, 12(12), 2187.

Wakjira, T. G. & Ebead, U. (2019a). Experimental and analytical study on strengthening of reinforced concrete T-beams in shear using steel reinforced grout (SRG). *Composites Part B: Engineering,* 177**,** 107368.

Wakjira, T. G. & Ebead, U. (2019b). Internal transverse reinforcement configuration effect of EB/NSE-FRCM shear strengthening of RC deep beams. *Composites Part B: Engineering,* 166**,** 758-772.

Wakjira, T. G. & Ebead, U. (2020). Shear span-to-depth ratio effect on steel reinforced grout strengthened reinforced concrete beams. *Engineering Structures,* 216**,** 110737.

Wakjira, T. G., Ebead, U. & Alam, M. S. (2022a). Machine learning-based shear capacity prediction and reliability analysis of shear-critical RC beams strengthened with inorganic composites. *Case Studies in Construction Materials,* 16**,** e01008.

Wakjira, T. G., Ibrahim, M., Ebead, U. & Alam, M. S. (2022b). Explainable machine learning model and reliability analysis for flexural capacity prediction of RC beams strengthened in flexure with FRCM. *Engineering Structures,* 255**,** 113903.

Walraven, J. (2010). *Model code 2010-first complete draft-volume 2: Model code*, fib Fédération internationale du béton.

Wang, B., Wang, Z., Uji, K., Zhang, J. & Guo, R. (2020a). Experimental investigation on shear behavior of RC beams strengthened by CFRP grids and PCM. *Structures,* 1994-2010.

Wang, G., Yang, C., Pan, Y., Zhu, F., Jin, K., Li, K. & Nanni, A. (2019). Shear behaviors of RC beams externally strengthened with engineered cementitious composite layers. *Materials,* 12**,** 2163.

Wang, G., Zhu, F. & Yang, C. (2020b). Experimental study on Shear behaviors of RC beams strengthened with ECC layers. IOP Conference Series: *Materials Science and Engineering,* IOP Publishing, 042024.

Wei, J., Wu, C., Chen, Y. & Leung, C. K. (2019). Shear strengthening of reinforced concrete beams with high strength strain-hardening cementitious composites (HS-SHCC). *Materials and Structures,* 53**,** 1-15.

Williams, G., & Higgins, C. (2008). Fatigue of diagonally cracked RC girders repaired with CFRP. *Journal of Bridge Engineering*, *13*(1), 24-33.

Xia, J., Chen, K., Wu, Y., Xiao, W., Jin, W. & Zhang, J. (2022). Shear fatigue behavior of reinforced concrete beams produced with manufactured sand as alternatives for natural sand. *Journal of Building Engineering,* 62**,** 105412.

Xu, X., Crocombe, A. & Smith, P. (1996). Fatigue crack growth rates in adhesive joints tested at different frequencies. *The Journal of Adhesion,* 58**,** 191-204.

Yan, H., He, Z., Gao, C., Xie, M., Sheng, H. & Chen, H. (2022). Investment estimation of prefabricated concrete buildings based on XGBoost machine learning algorithm. *Advanced Engineering Informatics,* 54**,** 101789.

Yang, X., Dai, J. G. & Lu, Z. Shear behavior of RC beams strengthened with FRP grid reinforced engineered cementitious composites. 6th Asia-Pacific Conference on FRP in Structures, APFIS 2017, 2017.

Yang, X., Gao, W.-Y., Dai, J.-G. & Lu, Z.-D. (2020). Shear strengthening of RC beams with FRP grid-reinforced ECC matrix. *Composite Structures,* 241**,** 112120.

Yegulalp, S. Yandex open sources CatBoost machine learning library. Journal of Physics Conference Series, 2017. InfoWorld.

Yin, H., Shirai, K. & Teo, W. (2018). Prediction of shear capacity of UHPC–concrete composite structural members based on existing codes. *Journal of civil engineering and management,* 24**,** 607-618.

Younis, A. & Ebead, U. Characterization and application of FRCM as a strengthening material for shear-critical RC beams. MATEC Web of Conferences, 2018. EDP Sciences, 09004.

Younis, A., Ebead, U. & Shrestha, K. C. (2017). Different FRCM systems for shear-strengthening of reinforced concrete beams. *Construction and Building Materials,* 153**,** 514-526.

Younis, E. M., Zaki, S. M., Kanjo, E. & Houssein, E. H. (2022). Evaluating Ensemble Learning Methods for Multi-Modal Emotion Recognition Using Sensor Data Fusion. *Sensors,* 22**,** 5611.

Yousif, S. T. & A Al-Jurmaa, M. (2010). Modeling of ultimate load for RC beams strengthened with Carbon FRP using artificial neural networks. *Al-Rafidain Engineering Journal (AREJ),* 18**,** 28-41.

Zhang, H. Y., Yan, J., Kodur, V. & Cao, L. (2019). Mechanical behavior of concrete beams shear strengthened with textile reinforced geopolymer mortar. *Engineering Structures,* 196**,** 109348.

Zeiss. (2023). INSPECT Correlate 2023 [Computer software]. Carl Zeiss GOM Metrology GmbH, Oberkochen, Germany, 2023. Available at: https://www.zeiss.com.

Appendix

Table A. Database of mortar-based composite systems

Ref.	Name	Beam details							Mortar-based system details									Test Results		
		Shape	b_w	a/d	ρ_w	SC	TYPE	Anchors	t_{cf}	ε_{fu}	E_f	ρ_f	t_{cm}	f'_{cm}	E_{frcm}	ρ_{cm}	FM	V_{JAC}	V_{JAC} /V_{CON}
			mm		%						GPa		mm	MPa	GPa			kN		
Wakjira and Ebead, 2020	BS1-L	R	180	3.1	0.00	U	S	-	0.084	0.0150	190	0.0019	12	50	NR	0.133	SH	73.1	0.87
	BS1-H	R	180	3.1	0.00	U	S	-	0.169	0.0150	190	0.0038	12	50	NR	0.133	SH	103.7	1.23
	BS-L	R	180	2.6	0.00	U	S	-	0.084	0.0150	190	0.0019	12	50	NR	0.133	SH	125.5	1.12
	BS-H	R	180	2.6	0.00	U	S	-	0.169	0.0150	190	0.0038	12	50	NR	0.133	SH	148.8	1.33
	BS3-L	R	180	2.1	0.00	U	S	-	0.084	0.0150	190	0.0019	12	50	NR	0.133	SH	122.9	0.66
	BS3-H	R	180	2.1	0.00	U	S	-	0.169	0.0150	190	0.0038	12	50	NR	0.133	SH	139.7	0.75
	BS4-L	R	180	1.6	0.00	U	S	-	0.084	0.0150	190	0.0019	12	50	NR	0.133	SH	59.0	0.20
	BS4-H	R	180	1.6	0.00	U	S	-	0.169	0.0150	190	0.0038	12	50	NR	0.133	SH	91.3	0.32
Wang et al., 2020a	BGS	R	200	2.6	0.12	SB(T)	E-N-M	-	-	-	-	-	20	36.7	-	-	SH	13.50	0.04
Wang et al., 2020b	S/d1.5S1	R	150	1.5	0.19	SB(T)	E-PE	-	-	-	-	0.02	10	128	-	-	SH	27.10	0.10
	S/d1.5S2	R	150	1.5	0.19	SB(T)	E-PE	-	-	-	-	0.02	10	128	-	-	SH	51.20	0.18
	S/d2.5S1	R	150	2.5	0.19	SB(T)	E-PE	-	-	-	-	0.02	10	128	-	-	SH	22.20	0.13
	S/d2.5S2	R	150	2.5	0.19	SB(T)	E-PE	-	-	-	-	0.02	10	128	-	-	SH	39.95	0.24
Yang et al., 2020	a-N-E-Cast	R	150	2.3	0.00	SB(T)	E-PE	-	-	-	-	0.02	20	25	-	-	SH	16.81	0.77
	b-B-E-Cast	R	150	2.3	0.00	SB(T)	E-PE-R	-	-	-	-	0.02	20	25	-	-	SH	19.13	0.88
	c-N-E-Cast	R	150	3.0	0.00	SB(T)	E-PE	-	-	-	-	0.02	20	25	-	-	SH	11.29	0.51

Attar et al., 2020	R 0.44-NS-F0	R	150	4.5	0.00	U	E-N	-	-	-	-	0.0	50	-	-	-	SH	4.00	0.15
	R 0.44-NS-F0.5	R	150	4.5	0.00	U	E-N	-	-	-	-	0.005	50	-	-	-	SH	5.00	0.19
	R 0.44-NS-F1.0	R	150	4.5	0.00	U	E-N	-	-	-	-	0.01	50	-	-	-	SH	11.50	0.44
	R 0.44-NS-F1.5	R	150	4.5	0.00	U	E-N	-	-	-	-	0.015	50	-	-	-	SH	31.50	1.21
Thermou et al., 2019	AUH1	R	200	2.2	0.00	U	S	-	0.254	0.0150	190	0.0025	7	55	25	0.070	F	13.1	0.28
	AUML1	R	200	2.2	0.00	U	S	YES	0.084	0.0150	190	0.0008	7	55	25	0.070	F	16.3	0.34
	AFL1	R	200	2.2	0.00	F	S	-	0.084	0.0150	190	0.0008	7	55	25	0.070	F	18.1	0.38
	AFH1	R	200	2.2	0.00	F	S	-	0.254	0.0150	190	0.0025	7	55	25	0.070	F	13.6	0.29
	BUL1	R	200	2.2	0.00	U	S	-	0.084	0.0150	190	0.0008	7	55	25	0.070	SH	71.9	1.05
	BUL2	R	200	2.2	0.00	U	S	-	0.084	0.0150	190	0.0017	10	55	25	0.100	SH	68.3	1.00
	BUML1	R	200	2.2	0.00	U	S	YES	0.084	0.0150	190	0.0008	7	55	25	0.070	SH	77.7	1.14
	BFL1	R	200	2.2	0.00	F	S	-	0.084	0.0150	190	0.0008	7	55	25	0.070	F	77.5	1.13
	BFH1	R	200	2.2	0.00	F	S	-	0.084	0.0150	190	0.0017	10	55	25	0.100	F	109.1	1.60
Marcinczak et al., 2019	B_P1	T	150	2.4	0.27	U	PBO	YES	0.046	0.0215	270	0.0003	8	30	NR	0.060	SH	17.9	0.09
	B_P2	T	150	2.4	0.27	U	PBO	YES	0.046	0.0215	270	0.0003	8	30	NR	0.060	SH	44.7	0.23
	B_P3	T	150	2.4	0.27	U	PBO	YES	0.046	0.0215	270	0.0003	8	30	NR	0.060	SH	33.7	0.17
	B_WS1	T	150	2.4	0.27	U	PBO	YES	0.046	0.0215	270	0.0003	8	30	NR	0.060	SH	38.1	0.19
	B_WS2	T	150	2.4	0.27	U	PBO	YES	0.046	0.0215	270	0.0003	8	30	NR	0.060	SH	41.5	0.21
	B_WS3	T	150	2.4	0.27	U	PBO	YES	0.046	0.0215	270	0.0003	8	30	NR	0.060	SH	37.8	0.19
	B_W1	T	150	2.4	0.27	U	PBO	YES	0.046	0.0215	270	0.0003	8	30	NR	0.060	SH	54.5	0.27
	B_W2	T	150	2.4	0.27	U	PBO	YES	0.046	0.0215	270	0.0003	8	30	NR	0.060	SH	39.1	0.20
	B_W3	T	150	2.4	0.27	U	PBO	YES	0.046	0.0215	270	0.0003	8	30	NR	0.060	SH	30.7	0.15
Wakjira and Ebead, 2019a	B1-U-L	T	180	2.8	0.00	U	S	-	0.084	0.0150	190	0.0019	12	50	20	0.133	SH	86.4	0.71
	B1-U-H	T	180	2.8	0.00	U	S	-	0.169	0.0150	190	0.0038	12	50	20	0.133	SH	79.2	0.65
	B1-S-L	T	180	2.8	0.00	SB	S	-	0.084	0.0150	190	0.0019	12	50	20	0.133	SH	60.8	0.50
	B1-S-H	T	180	2.8	0.00	SB	S	-	0.169	0.0150	190	0.0038	12	50	20	0.133	SH	51.2	0.42
	B2-U-L	T	180	2.8	0.10	U	S	-	0.084	0.0150	190	0.0019	12	50	20	0.133	SH	60.8	0.36
	B2-U-H	T	180	2.8	0.10	U	S	-	0.169	0.0150	190	0.0038	12	50	20	0.133	SH	43.5	0.26

	B3-U-L	T	180	2.8	0.21	U	S	-	0.084	0.0150	190	0.0019	12	50	20	0.133	SH	43.9	0.22
	B3-U-H	T	180	2.8	0.21	U	S	-	0.169	0.0150	190	0.0038	12	50	20	0.133	SH	19.7	0.10
Jongvivatsakul et al., 2019	0F-8D12	R	150	2.8	0.11	SB(T)	E-S	YES	-	-	-	0.0	10	56.8	-	-	SH	48.80	0.90
	1F-8D12	R	150	2.8	0.11	SB(T)	E-S	YES	-	-	-	1.0	10	69.7	-	-	SH	45.90	0.85
	1.5F-8D12	R	150	2.8	0.11	SB(T)	E-S	YES	-	-	-	1.5	10	60.8	-	-	SH	57.15	1.05
	1.5F-4D12	R	150	2.8	0.11	SB(T)	E-S	YES	-	-	-	1.5	10	60.8	-	-	SH	55.30	1.02
	1.5F-6D12	R	150	2.8	0.11	SB(T)	E-S	YES	-	-	-	1.5	10	60.8	-	-	SH	47.20	0.87
	1.5F-6D10	R	150	2.8	0.11	SB(T)	E-S	YES	-	-	-	1.5	10	60.8	-	-	SH	46.90	0.87
	1.5F-8D10	R	150	2.8	0.11	SB(T)	E-S	YES	-	-	-	1.5	10	60.8	-	-	SH	54.70	1.01
Garg et al., 2019	EJ-UR	R	150	1.6	0.89	U	E-S	-	-	-	-	2.0	50	118	-	-	SH	-3.63	-
	EJ-O/R	R	150	1.6	0.89	SB(T)	E-S	-	-	-	-	2.0	50	118	-	-	SH	-1.26	-
Wang et al., 2019	SA-20-2	R	150	2.0	0.00	SB(T)	E-PVA	-	-	-	-	1.5	20	44.8	-	-	SH	57.00	0.84
	SA-20-3	R	150	3.0	0.00	SB(T)	E-PVA	-	-	-	-	1.5	20	44.8	-	-	SH	16.00	0.38
	SB-20-2	R	150	2.0	0.00	SB(T)	E-PVA	-	-	-	-	1.5	20	44.8	-	-	SH	52.50	0.57
	SB-20-3	R	150	3.0	0.00	SB(T)	E-PVA	-	-	-	-	1.5	20	44.8	-	-	SH	12.50	0.20
	SA-40-2	R	150	2.0	0.00	SB(T)	E-PVA	-	-	-	-	1.5	40	44.8	-	-	SH	27.00	0.40
	SA-40-3	R	150	3.0	0.00	SB(T)	E-PVA	-	-	-	-	1.5	40	44.8	-	-	SH	17.50	0.41
	SB-40-2	R	150	2.0	0.00	SB(T)	E-PVA	-	-	-	-	1.5	40	44.8	-	-	SH	82.50	0.89
	SB-40-3	R	150	3.0	0.00	SB(T)	E-PVA	-	-	-	-	1.5	40	44.8	-	-	SH	13.00	0.21
Wakjira and Ebead, 2019b	E-C-A	R	150	2	0.18	SB	C	-	0.047	0.018	240	0.0012	20	20	NR	0.175	SH	36.9	0.40
	E-G-A	R	150	2	0.18	SB	G	-	0.047	0.0325	80	0.0012	20	40	NR	0.175	SH	20.0	0.22
	E-P-A	R	150	2	0.18	SB	PBO	-	0.046	0.0215	270	0.0012	20	30	NR	0.175	SH	23.4	0.25
	E-C-UA	R	150	2	0.18	SB	C	-	0.047	0.018	240	0.0012	20	20	NR	0.175	SH	35.5	0.36
	E-G-UA	R	150	2	0.18	SB	G	-	0.047	0.0325	80	0.0012	20	40	NR	0.175	SH	16.3	0.17
	E-P-UA	R	150	2	0.18	SB	PBO	-	0.046	0.0215	270	0.0012	20	30	NR	0.175	SH	26.3	0.27
Zhang et al., 2019	Bi10-GM1-A	R	150	2.6	0.13	U	C	YES	0.110	0.0180	242	0.0015	6	43.4	NR	0.080	SH	57.5	0.68
	Bi10-GM1	R	150	2.6	0.13	U	C	-	0.110	0.0180	242	0.0015	6	43.4	NR	0.080	SH	40.0	0.47
	Bi7-GM1-A	R	150	2.6	0.13	U	C	YES	0.110	0.0180	242	0.0015	6	43.4	NR	0.080	SH	72.5	0.85

	Bi7-GM1	R	150	2.6	0.13	U	C	-	0.110	0.0180	242	0.0015	6	43.4	NR	0.080	SH	60.0	0.71
	Bi10-GM2-A	R	150	2.6	0.13	U	C	YES	0.110	0.0180	242	0.0029	9	43.4	NR	0.120	SH	107.5	1.26
	Bi10-GM2	R	150	2.6	0.13	U	C	-	0.110	0.0180	242	0.0029	9	43.4	NR	0.120	SH	90.0	1.06
	Bi10-GM3	R	150	2.6	0.13	U	C	-	0.110	0.0180	242	0.0044	12	43.4	NR	0.160	SH	30.0	0.35
	Uni10-GM1	R	150	2.6	0.13	U	C	-	0.110	0.0180	242	0.0015	6	43.4	NR	0.080	SH	95.0	1.12
Wei et al., 2020	S-20-2	R	150	2.0	0.00	SB(T)	E-N	-	-	-	-	-	20	56	-	-	SH	57.00	0.84
	S-20-3	R	150	3.0	0.00	SB(T)	E-N	-	-	-	-	-	20	56	-	-	SH	16.00	0.38
	S-40-2	R	150	2.0	0.00	SB(T)	E-N	-	-	-	-	-	40	56	-	-	SH	27.00	0.40
	S-40-3	R	150	3.0	0.00	SB(T)	E-N	-	-	-	-	-	40	56	-	-	SH	17.50	0.41
Sakr et al., 2019)	ST-1S-R	R	150	2.1	0.13	SB	E-S	YES	-	-	-	2.0	60	135.4	-	-	F	108.00	1.88
	ST-2S-R	R	150	2.1	0.13	SB(T)	E-S	YES	-	-	-	2.0	30	135.4	-	-	S	68.5	1.19
Marcinczak and Trapko, 2019b	B_P100_BZ	T	150	2.4	0.27	U	PBO	-	0.046	0.0215	270	0.0003	8	30	NR	0.053	SH	11.9	0.05
	B_P100_1	T	150	2.4	0.27	U	PBO	YES	0.046	0.0215	270	0.0003	8	30	NR	0.053	SH	27.3	0.12
	B_P100_2	T	150	2.4	0.27	U	PBO	YES	0.046	0.0215	270	0.0003	8	30	NR	0.053	SH	22.9	0.10
	B_P100_3	T	150	2.4	0.27	U	PBO	YES	0.046	0.0215	270	0.0003	8	30	NR	0.053	SH	22.8	0.10
Marcinczak and Trapko, 2019a	B1	T	150	2.4	0.27	U	PBO	YES	0.046	0.0215	270	0.0003	8	30	NR	0.048	SH	36.9	0.16
Azam et al., 2018a	S0-CM	R	250	3.2	0.00	SB	C	-	0.128	0.0160	230	NR	8	58	21	0.064	SH	125.6	0.87
	S50-CM	R	250	3.2	0.11	SB	C	-	0.128	0.0160	230	NR	8	58	21	0.064	SH	79.2	0.30
	S150-CM	R	250	3.2	0.19	SB	C	-	0.128	0.0160	230	NR	8	58	21	0.064	SH	78.5	0.26
Tetta et al., 2018a	CL1	R	102	2.6	0.00	U	C	-	0.062	0.0079	225	0.0012	4	38.7	NR	0.078	SH	28.9	0.97
	CL1_strips	R	102	2.6	0.00	U	C	-	0.062	0.0079	225	0.0009	6	38.7	NR	0.090	SH	33.7	1.13
	CH1	R	102	2.6	0.00	U	C	-	0.095	0.0079	225	0.0019	4	31.1	NR	0.078	SH	15.1	0.51
	CH1_CL1	R	102	2.6	0.00	U	C	-	0.079	0.0079	225	0.0031	6	38.7	NR	0.118	SH	37.6	1.27
	CH2	R	102	2.6	0.00	U	C	-	0.095	0.0079	225	0.0037	6	31.1	NR	0.118	SH	39.2	1.32
	CL3	R	102	2.6	0.00	U	C	-	0.062	0.0079	225	0.0036	8	35.5	NR	0.157	SH	37.9	1.28
	CH2_CH1	R	102	2.6	0.00	U	C	-	0.079	0.0079	225	0.0049	8	38.7	NR	0.157	SH	44.4	1.49
	CH3	R	102	2.6	0.00	U	C	-	0.095	0.0079	225	0.0056	8	26.9	NR	0.157	SH	45.4	1.53
	CH3_CL1	R	102	2.6	0.00	U	C	-	0.079	0.0079	225	0.0068	10	38.7	NR	0.196	SH	48.5	1.63

	G1	R	102	2.6	0.00	U	G	-	0.044	0.0166	74	0.0009	4	35.5	NR	0.078	SH	12.2	0.41
	G3	R	102	2.6	0.00	U	G	-	0.044	0.0166	74	0.0026	8	35.5	NR	0.157	SH	37.0	1.25
	G7	R	102	2.6	0.00	U	G	-	0.044	0.0166	74	0.0060	16	38.7	NR	0.314	SH	53.0	1.78
	B1	R	102	2.6	0.00	U	B	-	0.037	0.0183	89	0.0007	4	33.3	NR	0.078	SH	14.4	0.48
	B3	R	102	2.6	0.00	U	B	-	0.037	0.0183	89	0.0022	8	35.5	NR	0.157	SH	36.1	1.22
	B7	R	102	2.6	0.00	U	B	-	0.037	0.0183	89	0.0051	16	35.5	NR	0.314	SH	47.9	1.61
	CL1_1.6	R	102	1.6	0.00	U	C	-	0.062	0.0079	225	0.0012	4	33.3	NR	0.078	SH	26.1	0.40
	CL3_1.6	R	102	1.6	0.00	U	C	-	0.062	0.0079	225	0.0036	8	33.3	NR	0.157	SH	40.2	0.61
	CL1_3.6	R	102	3.6	0.00	U	C	-	0.062	0.0079	225	0.0012	4	33.3	NR	0.078	SH	29.4	1.15
	CL3_3.6	R	102	3.6	0.00	U	C	-	0.062	0.0079	225	0.0036	8	33.3	NR	0.157	SH	39.6	1.55
Ebead and Wakjira, 2018	C0	R	150	2.0	0.00	U	C	-	0.047	0.0180	240	0.0013	9	20	NR	0.120	SH	56.8	0.77
	P0	R	150	2.0	0.00	U	PBO	-	0.045	0.0215	270	0.0012	12	40	NR	0.160	SH	46.2	0.63
	G0	R	150	2.0	0.00	U	G	-	0.047	0.0325	80	0.0013	15	22	NR	0.200	SH	49.7	0.67
	C1	R	150	2.0	0.18	U	C	-	0.047	0.0180	240	0.0013	9	20	NR	0.120	SH	46.9	0.47
	P1	R	150	2.0	0.18	U	PBO	-	0.045	0.0215	270	0.0012	12	40	NR	0.160	SH	29.1	0.29
	G1	R	150	2.0	0.18	U	G	-	0.047	0.0325	80	0.0013	15	22	NR	0.200	SH	38.3	0.38
Younis and Ebead, 2018	C_Full	R	150	1.8	0.00	U	C	-	0.047	0.0180	240	0.0013	13	20	NR	0.173	F	75.3	1.02
	C_Intermittent	R	150	1.8	0.00	U	C	-	0.047	0.0180	240	0.0008	13	20	NR	0.114	SH	52.6	0.71
	P_Full	R	150	1.8	0.00	U	PBO	-	0.045	0.0215	270	0.0012	13	30	NR	0.173	SH	33.4	0.45
	P_Intermittent	R	150	1.8	0.00	U	PBO	-	0.045	0.0215	270	0.0008	13	30	NR	0.114	SH	24.2	0.33
	G_Full	R	150	1.8	0.00	U	G	-	0.047	0.0325	80	0.0013	13	40	NR	0.173	SH	45.5	0.62
	G_Intermittent	R	150	1.8	0.00	U	G	-	0.047	0.0325	80	0.0008	13	40	NR	0.114	SH	23.4	0.32
Azam et al., 2018b	S0-CM	R	250	1.6	0.00	SB	C	-	0.128	0.0160	234.5	NR	8	58	NR	0.064	SH	136.5	0.23
	S50-CM	R	250	1.6	0.09	SB	C	-	0.128	0.0160	234.5	NR	8	58	NR	0.064	SH	106.3	0.16
Sakr et al., 2018	ST-1S	R	150	2.1	0.13	SB	E-S	-	-	-	-	2.0	30	135.4	-	-	SH	19.00	0.33
	ST-2S	R	150	2.1	0.13	SB(T)	E-S	-	-	-	-	2.0	60	135.4	-	-	F	83.00	1.44
Yang et al., 2017	B	R	150	2.2	0.33	SB	E-N	-	-	-	-	-	20	72.60	-	-	SH	43.60	1.00
	C	R	150	2.2	0.33	SB	E-N	-	-	-	-	-	20	30.20	-	-	SH	45.34	1.04

	D	R	150	2.2	0.33	SB	E-N-R	-	-	-	-	-	20	30.20	-	-	SH	54.06	1.24
Gonzalez-Libreros et al., 2017b	S1-FRCM-F3-UA	R	150	3.3	0.23	U	C	YES	0.047	0.0180	240	0.0006	8	45.2	NR	0.107	SH	29.9	0.26
	S1-FRCM-F4-UN	R	150	3.3	0.23	U	S	-	0.047	0.0160	190	0.0006	8	45.2	NR	0.107	SH	34.5	0.30
	S1-FRCM-F4-UA	R	150	3.3	0.23	U	S	YES	0.047	0.0160	190	0.0006	8	45.2	NR	0.107	SH	34.9	0.30
	S-FRCM-F3-UN	R	150	3.3	0.33	U	C	-	0.270	0.0180	240	0.0036	8	45.2	NR	0.107	SH	24.3	0.19
	S-FRCM-F4-UN	R	150	3.3	0.33	U	S	-	0.270	0.0160	190	0.0036	8	45.2	NR	0.107	SH	17.5	0.13
	S-FRCM-F4-UA	R	150	3.3	0.33	U	S	YES	0.270	0.0160	190	0.0036	8	45.2	NR	0.107	SH	31.3	0.24
Younis et al., 2017	C–F–90	R	150	2.0	0.00	SB	C	-	0.047	0.0180	240	0.0013	12	20	NR	0.160	SH	75.1	1.02
	C–I–90	R	150	2.0	0.00	SB	C	-	0.047	0.0180	240	0.0008	12	20	NR	0.105	SH	52.3	0.71
	C–I–45	R	150	2.0	0.00	SB	C	-	0.047	0.0180	240	0.0007	12	20	NR	0.083	SH	33.7	0.46
	C–I–90–A	R	150	2.0	0.00	SB	C	YES	0.047	0.0180	240	0.0008	12	20	NR	0.105	SH	54.1	0.73
	C–I–45–A	R	150	2.0	0.00	SB	C	YES	0.047	0.0180	240	0.0007	12	20	NR	0.083	SH	36.3	0.49
	P–F–90	R	150	2.0	0.00	SB	PBO	-	0.045	0.0215	270	0.0012	12	30	NR	0.160	SH	33.6	0.45
	P–I–90	R	150	2.0	0.00	SB	PBO	-	0.045	0.0215	270	0.0008	12	30	NR	0.105	SH	23.9	0.32
	P–I–45	R	150	2.0	0.00	SB	PBO	-	0.045	0.0215	270	0.0006	12	30	NR	0.083	SH	39.3	0.53
	P–I–90–A	R	150	2.0	0.00	SB	PBO	YES	0.045	0.0215	270	0.0008	12	30	NR	0.105	SH	25.4	0.34
	P–I–45–A	R	150	2.0	0.00	SB	PBO	YES	0.045	0.0215	270	0.0006	12	30	NR	0.083	SH	40.5	0.55
	G–F–90	R	150	2.0	0.00	SB	G	-	0.047	0.0325	80	0.0013	12	40	NR	0.160	SH	45.4	0.61
	G–I–90	R	150	2.0	0.00	SB	G	-	0.047	0.0325	80	0.0008	12	40	NR	0.105	SH	23.4	0.32
	G–I–45	R	150	2.0	0.00	SB	G	-	0.047	0.0325	80	0.0007	12	40	NR	0.083	SH	-7.1	-9.60
	G–I–90–A	R	150	2.0	0.00	SB	G	YES	0.047	0.0325	80	0.0008	12	40	NR	0.105	SH	30.5	0.41
	G–I–45–A	R	150	2.0	0.00	SB	G	YES	0.047	0.0325	80	0.0007	12	40	NR	0.083	SH	12.8	0.17
Aljazaeri and Myers, 2017	BA-S-1	R	203	2.5	0.61	U	PBO	-	0.050	0.0120	270	0.0002	6	38	NR	0.030	SH	29.5	0.18
	BA-S-4	R	203	2.5	0.61	U	PBO	-	0.050	0.0120	270	0.0010	15	38	NR	0.074	SH	29.5	0.18
	BA-C-4	R	203	2.5	0.61	U	PBO	-	0.050	0.0120	270	0.0020	15	38	NR	0.148	SH	51.0	0.31
	BB-S-1	R	203	2.5	0.00	U	PBO	-	0.050	0.0120	270	0.0002	6	38	NR	0.030	SH	-12.5	-0.11
	BB-S-4	R	203	2.5	0.00	U	PBO	-	0.050	0.0120	270	0.0010	15	38	NR	0.074	SH	4.0	0.04
	BB-C-1	R	203	2.5	0.00	U	PBO	-	0.050	0.0120	270	0.0005	6	38	NR	0.059	SH	23.5	0.21

Tetta et al., 2016	CH2	T	200	2.3	0.00	U	C	-	0.950	0.0079	225	0.0190	6	37.4	NR	0.060	SH	47.0	0.38
	CL3	T	200	2.3	0.00	U	C	-	0.620	0.0079	225	0.0186	8	35.8	NR	0.080	SH	57.6	0.47
	CH4	T	200	2.3	0.00	U	C	-	0.950	0.0079	225	0.0380	10	36.1	NR	0.100	SH	96.5	0.78
	G7	T	200	2.3	0.00	U	G	-	0.440	0.0166	74	0.0308	16	33.7	NR	0.160	SH	94.2	0.77
	CH2_A100	T	200	2.3	0.00	U	C	YES	0.950	0.0079	225	0.0190	6	34.5	NR	0.060	SH	112.5	0.91
	CL3_A100	T	200	2.3	0.00	U	C	YES	0.620	0.0079	225	0.0186	8	37.9	NR	0.080	SH	114.0	0.93
	CH4_A50	T	200	2.3	0.00	U	C	YES	0.950	0.0079	225	0.0380	10	36.6	NR	0.100	SH	147.6	1.20
	CH4_A100	T	200	2.3	0.00	U	C	YES	0.950	0.0079	225	0.0380	10	33.4	NR	0.100	SH	237.5	1.93
	G7_A100	T	200	2.3	0.00	U	G	YES	0.440	0.0166	74	0.0308	16	37.4	NR	0.160	SH	107.2	0.87
Hung and Chen, 2016	B-E	R	250	3.3	0.21	U	E-PVA	-	-	-	-	-	40	63.2	-	-	SH	13.50	0.10
	B-M-6	R	250	3.3	0.21	U	E-PVA-R	-	-	-	-	-	40	28.1	-	-	SH	21.00	0.16
	B-M-1	R	250	3.3	0.21	U	E-PVA-R	-	-	-	-	-	40	62	-	-	SH	45.90	0.35
	B-E-6	R	250	3.3	0.21	U	E-PVA-R	-	-	-	-	-	40	49.6	-	-	SH	28.00	0.21
	B-E-1	R	250	3.3	0.21	U	E-PVA-R	-	-	-	-	-	40	53.4	-	-	SH	36.90	0.28
Awani et al., 2016	S0- FRCM-1	R	150	3.0	0.00	SB	C	-	1.000	0.0160	230	0.0133	12	74	22	0.160	SH	66.5	1.10
	S0- FRCM-2	R	150	3.0	0.00	SB	C	-	1.000	0.0160	230	0.0267	18	74	22	0.240	SH	87.2	1.45
	S1- FRCM-1	R	150	3.0	0.25	SB	C	-	1.000	0.0160	230	0.0133	12	74	22	0.160	SH	68.4	0.64
	S1- FRCM-2	R	150	3.0	0.25	SB	C	-	1.000	0.0160	230	0.0267	18	74	22	0.240	SH	72.1	0.67
	S- FRCM-1	R	150	3.0	0.50	SB	C	-	1.000	0.0160	230	0.0133	12	74	22	0.160	SH	67.6	0.51
	S- FRCM-2	R	150	3.0	0.50	SB	C	-	1.000	0.0160	230	0.0267	18	74	22	0.240	SH	73.6	0.55
Tetta and Bournas, 2016	SB_MCH2_20	R	102	2.6	0.00	SB	C	-	0.095	0.0079	225	0.0037	6	28.2	NR	0.118	SH	21.0	0.70
	SB_MCH2_150	R	102	2.6	0.00	SB	C	-	0.095	0.0079	225	0.0037	6	16.2	NR	0.118	SH	11.0	0.37
	SB_MCH3_20	R	102	2.6	0.00	SB	C	-	0.095	0.0079	225	0.0056	8	26.9	NR	0.157	SH	33.0	1.11
	SB_MCH3_150	R	102	2.6	0.00	SB	C	-	0.095	0.0079	225	0.0056	8	16.2	NR	0.157	SH	17.0	0.57
	UW_MCH2_20	R	102	2.6	0.00	U	C	-	0.095	0.0079	225	0.0037	6	31.1	NR	0.118	SH	39.0	1.31
	UW_MCH2_150	R	102	2.6	0.00	U	C	-	0.095	0.0079	225	0.0037	6	16.2	NR	0.118	SH	20.0	0.67
	UW_MCH3_20	R	102	2.6	0.00	U	C	-	0.095	0.0079	225	0.0056	8	26.9	NR	0.157	SH	45.0	1.51

	UW_MCH3_150	R	102	2.6	0.00	U	C	-	0.095	0.0079	225	0.0056	8	16.2	NR	0.157	SH	25.0	0.84
	UW_MCH3_100	R	102	2.6	0.00	U	C	-	0.095	0.0079	225	0.0056	8	17.3	NR	0.157	SH	45.0	1.51
	UW_MCH3_250	R	102	2.6	0.00	U	C	-	0.095	0.0079	225	0.0056	8	17	NR	0.157	SH	29.0	0.97
	UW_MCL3_20	R	102	2.6	0.00	U	C	-	0.062	0.0079	225	0.0036	8	38.7	NR	0.157	SH	38.0	1.28
	UW_MCL3_150	R	102	2.6	0.00	U	C	-	0.062	0.0079	225	0.0036	8	16.2	NR	0.157	SH	25.0	0.84
	UW_MG7_20	R	102	2.6	0.00	U	G	-	0.044	0.0166	74	0.0060	16	35.5	NR	0.314	SH	53.0	1.78
	UW_MG7_150	R	102	2.6	0.00	U	G	-	0.044	0.0166	74	0.0060	16	16.2	NR	0.314	SH	27.0	0.91
	FW_MCH2_20	R	102	2.6	0.00	F	C	-	0.095	0.0079	225	0.0037	6	28.2	NR	0.118	F	58.0	1.95
	FW_MCH2_150	R	102	2.6	0.00	F	C	-	0.095	0.0079	225	0.0037	6	16.2	NR	0.118	SH	48.0	1.61
	CH4_20	T	200	2.3	0.00	U	C	-	0.095	0.0079	225	0.0038	10	36.1	NR	0.100	SH	95.0	0.76
	CH4_150	T	200	2.3	0.00	U	C	-	0.095	0.0079	225	0.0038	10	22.9	NR	0.100	SH	66.0	0.53
	CH4_A100_20	T	200	2.3	0.00	U	C	Yes	0.095	0.0079	225	0.0038	10	33.4	NR	0.100	SH	236.0	1.90
	CH4_A100_150	T	200	2.3	0.00	U	C	Yes	0.095	0.0079	225	0.0038	10	19.3	NR	0.100	SH	119.0	0.96
Tzoura and Triantafillou, 2016	L1	T	150	2.5	0.00	U	C	-	0.048	0.0180	225	0.0006	4	21.8	NR	0.053	SH	10.6	0.18
	L2	T	150	2.5	0.00	U	C	-	0.048	0.0180	225	0.0013	6	21.8	NR	0.080	SH	13.4	0.24
	H1	T	150	2.5	0.00	U	C	-	0.096	0.0180	225	0.0013	4	21.8	NR	0.053	SH	24.2	0.42
	H2	T	150	2.5	0.00	U	C	-	0.096	0.0180	225	0.0026	6	21.8	NR	0.080	SH	37.1	0.65
	L2A15ha	T	150	2.5	0.00	U	C	YES	0.048	0.0180	225	0.0013	6	21.8	NR	0.080	SH	59.7	1.04
	L2A10	T	150	2.5	0.00	U	C	YES	0.048	0.0180	225	0.0013	6	21.8	NR	0.080	SH	85.7	1.96
	H1A15	T	150	2.5	0.00	U	C	YES	0.096	0.0180	225	0.0013	4	21.8	NR	0.053	SH	54.7	1.25
	H2A10	T	150	2.5	0.00	U	C	YES	0.096	0.0180	225	0.0026	6	21.8	NR	0.080	SH	51.6	1.18
	H2A10	T	150	2.5	0.00	U	C	YES	0.096	0.0180	225	0.0026	6	21.8	NR	0.080	SH	52.1	0.91
Azam and Soudki, 2014	SB-CT1	R	150	3.3	0.00	SB	C	-	0.128	0.0160	230	NR	7	58	NR	0.093	SH	16.0	0.26
	UW-CT1	R	150	3.3	0.00	U	C	-	0.128	0.0160	230	NR	7	58	NR	0.093	SH	14.1	0.23
	SB-CT2	R	150	3.3	0.00	SB	C	-	0.128	0.0160	230	NR	7	58	NR	0.093	SH	60.9	0.99
	UW-CT2	R	150	3.3	0.00	U	C	-	0.128	0.0160	230	NR	7	58	NR	0.093	SH	64.9	1.05
Ruano et al., 2014	1	R	150	1.7	0.30	U	E-S	-	-	-	-	-	30	26.3	-	-	SH	64.65	1.11
	2	R	150	1.7	0.30	U	E-S	-	-	-	-	-	30	26.3	-	-	SH	84.40	1.45

3	R	150	1.7	0.00	U	E-S	-	-	-	-	-	30	26.3	-	-	SH	28.40	0.49
7	R	150	1.7	0.30	U	E-S	-	-	-	-	-	30	85.7	-	-	SH	81.20	1.40
8	R	150	1.7	0.30	U	E-S	-	-	-	-	-	30	85.7	-	-	SH	80.05	1.38
9	R	150	1.7	0.00	U	E-S	-	-	-	-	-	30	85.7	-	-	SH	18.30	0.32
13	R	150	1.7	0.30	U	E-S	-	-	-	-	-	30	95.3	-	-	SH	73.15	1.26
14	R	150	1.7	0.30	U	E-S	-	-	-	-	-	30	95.3	-	-	SH	90.95	1.57
15	R	150	1.7	0.00	U	E-S	-				-	30	95.3	-	-	SH	67.95	1.17

Note: 1. ‘SC’ is jacket’s strengthening configuration: ‘U’ – U wrapped, ‘F’ – Fully wrapped, ‘SB’ – Side bonding (one side), ‘SB(T)’ – Side bonding (two sides).

2. Type: ‘B’ – BFRCM, ‘C’ – CFRCM, ‘G’ – GFRCM, ‘PBO’ – PBOFRCM, ‘S’ – SRG, ‘E-N’ – FRC (unknown fibre) without mesh/grid, ‘E-N-R’ – FRC (unknown fibre) with mesh/grid, ‘E-PE’ – FRC (PE fibre) without mesh/grid, ‘E-PE-R’ – FRC (PE fibre) with mesh/grid, ‘E-PVA’ – RC (PVA fibre) without mesh/grid, ‘E-PVA-R’ – FRC (PVA fibre) with mesh/grid, ‘E-S’ – FRC (steel fibre) without mesh/grid, ‘E-S-R’ – FRC (steel fibre) with mesh/grid,

3. ‘FM’ is failure mode: ‘F’ – flexural failure, ‘SH’ – shear failure.

4. f_c is cylinder compression strength. If the specimen uses cube compression strength, it shall be converted according to EC2 (2005).

5. Regarding ρ_f, it refers to the fibre reinforcement ratio of the textile in FRCM, and it refers to the volume fraction of fibre in mortar in ECC.

Publications

Papers in Journals

Liu, X., Figueredo, G. P., Gordon, G. S., & Thermou, G. E. (2025). Data-driven shear strength prediction of RC beams strengthened with FRCM jackets using machine learning approach. *Engineering Structures*, 325, 119485.

Liu, X., & Thermou, G. E. (2025). Effectiveness of SRG in shear strengthening of deep and slender concrete beams. *Structures*, 71, 108197.

Liu, X., & Thermou, G. E. (2024). Shear Performance of RC Beams Strengthened with High-Performance Fibre-Reinforced Concrete (HPFRC) Under Static and Fatigue Loading. *Materials*, 17(21), 5227.

Liu, X., & Thermou, G. E. (2023). A review on the shear performance of reinforced concrete (RC) beams strengthened with externally bonded mortar-based composites. *Structures*, 58, 105474.

Papers in Conference Proceedings

Liu, X., Karaghool, O., Thermou, G. E., & Yu, J. (2024). Experimental Investigation on Shear Performance of RC Beams Strengthened with High-Tensile-Strength Strain-Hardening Cementitious Composite (HTS-SHCC). In *1st International Conference on Engineering Structures*, Guangzhou, China, November.

Liu, X., & Thermou, G. E. (2023). SRG vs SRP Jacketing in Shear Strengthening of Reinforced Concrete Beams. In *International Symposium of the International Federation for Structural Concrete (fib)*, Istanbul, Turkey, June.

Liu, X., & Thermou, G. E. (2023). Shear Performance of RC Beams Strengthened with Ultra-High Performance Fibre Reinforced Concrete (UHPFRC). In *Earthquake Engineering & Dynamic for a Sustainable Future (SECED)*, Cambridge, UK, September.

Liu, X., Thermou, G. E., & Liu, T. (2022). Shear Performance of RC Beams Strengthened with Mortar-Based Composites. In *International Symposium of the International Federation for Structural Concrete (fib)*, Oslo, Norway, July.

Planned Journal Papers

Liu, X., Karaghool, O., Thermou, G. E., & Yu, J. Experimental Investigation on Shear Strengthening of RC Beams Using Different Fibre Reinforced Cementitious Composites.

Liu, X., & Thermou, G. E. Experimental Investigations on Fatigue Performance of Shear Deficient RC beams strengthened with FRCM jacketing.

Liu, X., Thermou, G. E., & Wang, F. Development of a Nonlinear FE Modelling Approach for SRG- Strengthened Beams.